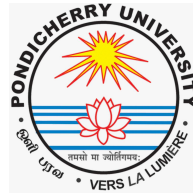# THE STRUCTURE, KINEMATICS AND EVOLUTION OF THE MAGELLANIC CLOUDS

A THESIS

SUBMITTED FOR THE DEGREE OF

DOCTOR OF PHILOSOPHY

THE DEPARTMENT OF PHYSICS
THE SCHOOL OF PHYSICAL, CHEMICAL
& APPLIED SCIENCES
PONDICHERRY UNIVERSITY
PUDUCHERRY - 605 014, INDIA

BY

INDU G

INDIAN INSTITUTE OF ASTROPHYSICS
BANGALORE - 560 034, INDIA

FEBRUARY 2014

DECLARATION

I hereby declare that the material presented in this thesis entitled **"The Structure, Kinematics and Evolution of the Magellanic Clouds"** is the result of investigations carried out by me at the Indian Institute of Astrophysics, Bangalore, under the supervision of Prof. Annapurni Subramaniam. The results reported in this thesis are new, and original, to the best of my knowledge, and has not been submitted in whole or part for the award of any degree, diploma, associateship, fellowship etc. of any University or Institute. In keeping with the general practice of reporting scientific observations, due acknowledgement has been made whenever the work described is based on the findings of other investigators.

Indu G

(Candidate)

Indian Institute of Astrophysics
Bangalore-560034, India

CERTIFICATE

This is to certify that the material presented in this thesis entitled **"The Structure, Kinematics and Evolution of the Magellanic Clouds"** submitted to Pondicherry University by **Ms. Indu G** for the award of the degree of Doctor of Philosophy, is based on the results of investigations carried out by her under my supervision and guidance, at the Indian Institute of Astrophysics. This thesis has not been submitted in whole or part for the award of any degree, diploma, associateship, fellowship etc. of any University or Institute.

Prof. Annapurni Subramaniam
(Supervisor)

Indian Institute of Astrophysics
Bangalore-560034, India

ACKNOWLEDGEMENTS

joyous and adventurous. I enjoyed the valuable company of Anantha, Avijeeth, Arun, Madhu, Manpreet, Ramesh, Sajal, Sasi, Sreeja, Suresh and Vineeth. I am grateful to my seniors, Amit, Anantha, Anusha, Bharat, Chandrasekhar, Girjesh, Ramya, Thapan, Veeresh and Vigeesh. I acknowledge Chiranjib Konar, Jessy Jose, Koshy George and Sumedh for their support and timely inputs. It is a pleasure to thank my juniors Ambily, Annu, Avinash, Estrella, Phanindra, Prasanna Deshmukh, Honey, Joby, Joice, Kishore, Mugundan, Nancy, Nirmal, Priyanka, Pradeep, Ramya, Shubham, Sangeetha, Mayuresh, Smitha, Sowmya, Sreejith, Sreekanth, Sreenivasa Prasanna, Subhmoy, Sudeep, Supria, Susmitha, Thanmoy, Vaibhav, Vaidhehi, Vidhya and Hariharan. You all made my days in Bhaskara memorable. Many thanks to Anantha, Arun, Chandrasekhar, Honey, Hema, Jayasree, Nirmal, Rathna, Sajal and Susmitha for all the help and support.

The most valuable ones - Drisya and Sindhuja - I hardly missed my family here since they were always with me. Their support cannot be covered with words.

The gratitude to my family is beyond the words could express. My parents P. N. Gopalakrishnan, and N. Nirmala for the trust, love and encouragement. My dear brother Madhu for giving me the right acceleration whenever I tried to move backwards. Finally my husband and my best friend Shaji, for being there for me always, showing me the right path whenever I was puzzled, spreading optimism and strength in all my eccentricities and miseries, through out my life. My little Nieva, who brought immense joy to my life. She gave clarity to my ideas, made me stressless and think freely than ever before.

TABLE OF CONTENTS

Abstract

The Large and Small Magellanic Clouds (LMC & SMC), along with the Magellanic Bridge and the Stream, comprise the Magellanic system. The presence of the Stream and the Bridge connecting the two Clouds suggest that these two galaxies might be interacting as a pair for a couple of Gyr. The Bridge in particular indicates that they have had a close encounter in the recent past. This system moves in the gravitational potential of the Milky Way (MW). The L&SMC form the nearest interacting binary to our Galaxy and the proximity allows us to understand the details of such interactions. Such interacting systems are numerous in the universe and this pair serves as the test bed to understand such systems. It is expected that the structure, kinematics, and evolution of the Clouds and the Galaxy are modified by their interactions. The details of these interactions have been studied over a time scale. It was long believed that the Clouds orbit our Galaxy and that the bursts of star formation episodes as well as the structural changes seen in both the Clouds are probably due to their perigalactic passage and tidal effects. On the other hand, the recent estimates of the proper motion of the Clouds find that the Magellanic System is probably passing close to the MW for the first time (Besla et al. 2007). Hence the interaction of the Clouds with the Galaxy is restricted to a recent past of a few hundred Myr. As we have a reliable estimate of the proper motion of the Clouds, we understand their orbits, velocity and the direction of motion. In the light of these new estimates, we study the effect of the interaction on the Clouds in the recent past. We study the recent star formation history, in the last 500 Myr, in the two Clouds which could reveal the effect due to their interaction with the Galaxy as well as their mutual interaction, at similar time scales. We also study the Atomic Neutral Hydrogen (H I) gas kinematics, which could identify signatures of the ongoing interaction between the three galaxies. The Magellanic System is introduced with a history of the Clouds and related features, and the back ground and motivation of this thesis study are outlined, in Chapter 1.

We made use of optical photometric data for estimating the recent star formation history. We used the photometric catalogues from the third phase of the Optical Gravitational Lensing Experiment (OGLE III) and the Magellanic Cloud Photometric Survey (MCPS) for this purpose. To analyse the gas kinematics we used the radio data from three different surveys - the combined data set of Australian Telescope Compact Array (ATCA) and Parkes telescopes, the all sky survey data sets from the Parkes Galactic All Sky Survey (GASS) and the Leiden Argentine Bonn Survey (LAB). The details of the data sets, various corrections applied to the data, including the correction for the transverse motion of the Clouds, as well as the methods adopted for the analysis are discussed in Chapter 2.

The star formation episodes of the Clouds are influenced by the LMC-SMC-MW interaction. The estimation of star formation history is proven to be a useful tool to decode the evolutionary history of the Clouds. We traced the age of the last star formation event (LSFE) in the inner L&SMC using the photometric data in V and I passbands from the OGLE III and the MCPS catalogues. The LSFE is estimated from the main sequence turn-off point in the colour magnitude diagram (CMD) of a sub region. After correcting for extinction, the turn-off magnitude is converted to age, which represents the LSFE in a region. The spatial distribution of the age of the LSFE shows that the star formation has shrunk to within the central regions in the last 100 Myr in both the galaxies. The location as well as the age of LSFE is found to correlate well with those of the star clusters in both the Clouds. The SMC map shows two separate concentrations of young star formation, one near the center and the other near the wing. We detected peaks of star formation at 0 - 10 Myr and 90 - 100 Myr in the LMC, and 0 - 10 Myr and 50 - 60 Myr in the SMC. The quenching of star formation in the LMC is found to be asymmetric with respect to the optical center such that most of the young star forming regions are located to the north and east. On deprojecting the data onto the LMC plane, the recent star formation appears to be stretched in the northeast direction and the H I gas is found to be distributed preferentially in the north. We found that the centroid is shifted to the north during the time interval 200 - 40 Myr, whereas it is found to have shifted to the northeast in the last 40 Myr. In the SMC, we detected a shift in the centroid of the population younger than 500 Myr and as young as 40 Myr in the direction of the LMC. The analysis of the recent star formation history of the L&SMC are presented in Chapters 3 and 4 respectively.

Kinematics of a galaxy is basically the study of its velocity field using either gaseous or stellar tracers. The observed radial/line of sight velocity field can be resolved to components of internal rotation, transverse motion, systemic motion, precession and nutation. We analysed the gas kinematics of the L&SMC using H I as tracer. The value of proper motion do play a crucial role in the kinematic analysis of a galaxy. The recent proper motion estimates of Piatek et al. 2008, Kallivayalil et al. 2006b, Kallivayalil et al. 2006a and Kallivayalil et al. 2013 are very different from the older values and the estimation of the H I velocity field is affected by this change, especially in the outer disk. Hence it is necessary to compute the H I velocity field of the Clouds using the new proper motion values. This study is a re-estimate of H I kinematics of the Clouds using the recent proper motion estimates. It has been recently realised that including the component of precession and nutation of the disk can change the estimated kinematics. Various features in the

gas, which are connected to the Magellanic Bridge, the Leading Arm & the Magellanic Stream have been identified in the literature, but their formation and the details of the gas flow in these features are not clearly understood.

The H I kinematics of the LMC disk is analysed considering the two recent and accurate proper motion estimates (Piatek et al. 2008 and Kallivayalil et al. 2013). The value of Position Angle (PA) of Line of Nodes (LON) of the LMC, estimated using ATCA/Parkes data ($126° \pm 23°$) is found to be similar to the recent estimate of the PA using stellar tracers. The effect of precession and nutation in the estimation of PA is found to be significant. The mean H I disk is found to be disturbed within $1.°0$ radius and beyond $2.°9$ radius. Most of the H I gas in the LMC ($\sim 87.9\%$ of the data points) is located in the disk. We detected 12.1% of the data points as kinematic outliers. Significant part of the type 1 as well as the slow type 2 H I gas are found to be similar to Arm E. We identified features similar to the well known Arm S, Arm W, Arm B and a new stream, Outer Arm, as part of the faster type 2 outlier component. The GASS data analysis brings out the details of the Magellanic Bridge and its connection to the LMC disk. We found that the arm B is connected to the Magellanic Bridge and the velocities suggest a possible gas infall through arm B, if the gas is in the plane of the LMC. We detected possible outflows from the western disk of the LMC and the southwest and southern parts of the Magellanic Bridge, likely to be due to ram pressure stripping. The analysis and results of the H I kinematics of the LMC is presented in Chapter 5.

In the case of the SMC, the estimation of the nutation (di/dt) of the SMC H I disk is done for the first time, using the mean H I velocity field. The SMC is found to undergo fast tumbling motion with a di/dt value $-416.39 \pm 19°$/Gyr. The H I kinematics of the SMC is analysed in detail for the first time covering almost the entire gaseous disk of the SMC, applying the recent high precision proper motion estimates (Piatek et al. 2008 and Kallivayalil et al. 2013). The rotation curve of the SMC is estimated to a larger radial extend using GASS data and the flat part of the rotation curve is detected for the first time. The turn over radius is found to be 4.1 kpc and the deprojected rotational velocity is 64 km s^{-1}. The dynamical mass estimated within the outermost data point at 5.7 kpc is $5.4 \times 10^9 \ M_\odot$, which is more than twice of the previous estimate (Stanimirović et al. 2004). This could be an indicator of the presence of a dark matter halo in the SMC. The PA of LON is estimated to be $67°.2 \pm 9°.2$, which is different from the stellar PA, located in the southeast quadrant, as suggested by previous studies (Stanimirović et al. 2004). We identified a few tidal features in the SMC disk as kinematical outliers. The gaseous feature which connects the SMC to the Magellanic Bridge is identified as a slow type 2

outlier. The inner SMC seems to be unperturbed, while the outer regions are strongly disturbed possibly by the tidal interaction with the LMC. The analysis and results are presented in Chapter 6.

In this thesis study we find that the star formation in the last 100 Myr is propagating radially inward in both the Clouds. The recent star formation in the LMC is dictated by the perigalactic passage. The lopsidedness in the gas distribution, and the northeast extension of the young stellar as well as cluster populations are the combined effect of the gravitational interaction of the MW and the movement of the LMC in the MW halo. The recent star formation in the SMC is due to the combined gravitational effect of the LMC and the perigalactic passage. Our study finds the PA of LON of the gaseous disk of the LMC is not mis-aligned with that of the stellar disk. In the case of the SMC, the PA estimate of the gaseous disk is flipped to another quadrant compared to the stellar disk estimate. The precession and nutation motion of the disk of the Clouds are found to be significant in understanding the kinematics. The disk of the SMC tumbles in a significantly high rate, which is probably due to its interaction with the LMC.

The valuable signatures of on going interactions of the LMC-SMC-MW system is detected and analysed in both the aspects of star formation history as well as gas kinematics. The star formation episodes and the kinematics of the LMC disk are strongly influenced by its hydrodynamic and tidal interaction with the MW. There are possible on going gas accretions and outflows in the LMC which are likely to be connected to the Magellanic Bridge, the Leading Arm and the Magellanic Stream. The star formation in the SMC is dictated by a combined gravitational effect of the MW and the LMC, while the gas distribution bears the signature of the LMC-SMC tidal interactions. These results and conclusions are summarised in Chapter 7. The Clouds of Magellan are unquestionably the test beds to understand the nuances of galaxy interactions at our door step.

List of Publications

- **Refereed Journals**

    - Recent Star Formation History of the Large and Small Magellanic Clouds, **Indu, G.**, Subramaniam, A., 2011, A&A, 535, A115

    - H I Kinematics of the Large Magellanic Cloud Revisited - Evidence of Ongoing Accretions and Outflows, **Indu, G.**, Subramaniam, A., 2013 (submitted to A&A, under revision)

    - Kinematics of the extended H I disk of the SMC - Evidence for a dark halo. (In preparation)

- **Conference proceedings**

    - **Indu, G.**, Subramaniam, A., 2011, ASInC, 3, 143
    - **Indu, G.**, Subramaniam, A., 2012, ASInC, 4, 139

LIST OF FIGURES

12

LIST OF TABLES

17

LIST OF ABBREVIATIONS

The following table describes various abbreviations used throughout the thesis.

Abbreviation	Description
ATCA	Australian Telescope Compact Array
CMD	Colour Magnitude Diagram
Dec	Declination
EW	eastwest
GASS	Parkes Galactic All Sky Survey
H I	Atomic Neutral Hydrogen
HST	Hubble Space Telescope
IMF	Initial Mass Function
LA	Leading Arm
LAB	Leiden Argentine Bonn Survey
LF	Luminosity Function
LG	Local Group
LMC	Large Magellanic Cloud
LON	Line of Nodes
LSFE	Last Star Formation Event
LSR	Local Standard of Rest
MB	Magellanic Bridge
MCs	Magellanic Clouds
MCPS	Magellanic Cloud Photometric Survey
MS	Magellanic Stream
MW	Milky Way
NE	northeast
NS	northsouth
NW	northwest
OGLE	Optical Gravitational Lensing Experiment
PA	Position Angle
RA	Right Ascension
RSFH	Recent Star Formation History
SE	southeast
SEHO	South East H I Over density
SFH	Star Formation History
SGS	Super Giant Shells
SMC	Small Magellanic Cloud
SW	southwest

CHAPTER 1

INTRODUCTION

The Clouds of Magellan, the two most exciting objects in the Local Group (LG), are subject to numerous observations and studies in the past decades. These gas rich binary systems, interacting with our Galaxy, occupy a prime position in understanding various aspects of galaxy-galaxy interaction and evolution.

1.1 History of the Clouds

The Magellanic Clouds (MCs) must be pre-historically familiar to human eyes, being two distinctive and fabulous members of the southern sky. They were called by various names by inhabitants of various continents in the southern hemisphere. They have been known as 'The Cape Clouds', 'The Upper and Lower Clouds of Mahu (Mist)', 'The Sacks of Coal', 'The Oxen of Tehama' etc. They were been the characters of folks or star lores all over the hemisphere spread then among various civilisations. The first known recorded mention of the Clouds is by the Persian astronomer Abd Al-Rahman al Sufi, in A.D. 964, in his 'Book of Fixed Stars' written in Arabic. The book was an attempt to create a synthesis of the most popular classical work of astronomy in his time. He noticed that they are visible from Southern Arabia, although not from more northern latitudes. These were the first galaxies other than the Milky Way (MW) to be observed from Earth. But it is a matter of dispute that the historians claim that in fact, the Arabs did not know of the MCs until the end of the 15th century, about the same time that they became known in the west. However, al Sufi does not claim that he observed these stars himself. He attributed this to the southern people of Arabia (region of Tehama). The 15th century Arab seafarer Ibn-Majed mentioned the Large Magellanic Cloud (LMC) as a nebula (for the first time) and named it al-Baqar. The next recorded observation was in 1503-4 by Amerigo Vespucci,

the Italian navigator and cartographer, in a letter about his third voyage. In this letter he mentions "three Canopes, two bright and one obscure"; "bright" refers to the two MCs, and "obscure" refers to the Coalsack. Later in 1522, the Venitian scholar Antonio Pigafetta, who assisted the Portuguese explorer Ferdinand Magellan and his crew on their voyage to the Indies, described about the Clouds in his writings after he returned to Spain, being one of the very few travellers who completed the historical circumnavigation. The writings of Pigafetta made the Clouds more popular to the common Western knowledge and the Clouds were named after Magellan posthumously some time in the 18th century. The Clouds served the navigators for hundreds and hundreds of years to fix the direction since there is no southern counter part for the Polaris. The Italian explorer Andrea Corsali of 15th century, who illustrated and named the constellation Crux for the first time also described about the MCs as two bright clouds with a regular circular path around the South Pole.

In early 17th century the ever great invention of the telescope, by Galileo Galilei resolved the so called Nebulae (galaxies) to be a multitude of stars packed so densely that they appeared from Earth to be clouds. In the middle of 18th century John Herschel following his father's trails explored the southern skies. In his own words "he packed up the 20 feet reflector, went and passed a year or two in the Cape, to pick up some nebulae in the south and for a peep at the MCs .. ". He gave the first authentic scientific examination of the Clouds, which he presented in his book which became famous in Europe as "the Cape Results" in 1847. One significantly long section of the book was dealing with "*Of The Two Nubecule*". He presented hand sketches of the Clouds which are evidently different in their complex details from the Bode's maps which were popular then. He created a catalogue of 919 objects in the *Nubecule Major* and 244 in the *Nubecule Minor*. Abbe in 1867 mentioned about the clouds that "The visible universe is composed of systems, of which the *Via Lactea*, (the Milky Way) the two Nubeculae, and the Nebulae are individuals and which are themselves composed of stars (either simple, multiple or in clusters) and of gaseous bodies of both regular and irregular outlines". The Latin word *Nubeculae Magellani*, or simply *Nubeculae* literally bears the meaning of "the Little Clouds". A more detailed discussion on the "knowns and unknowns" of the Clouds follows.

1.2 The Large Cloud

The LMC is known as an *astronomical treasure-house* as described by Robert Burnham, Jr. in his book named *Burnham's Celestial Handbook (1978)*. It is the 3rd nearest
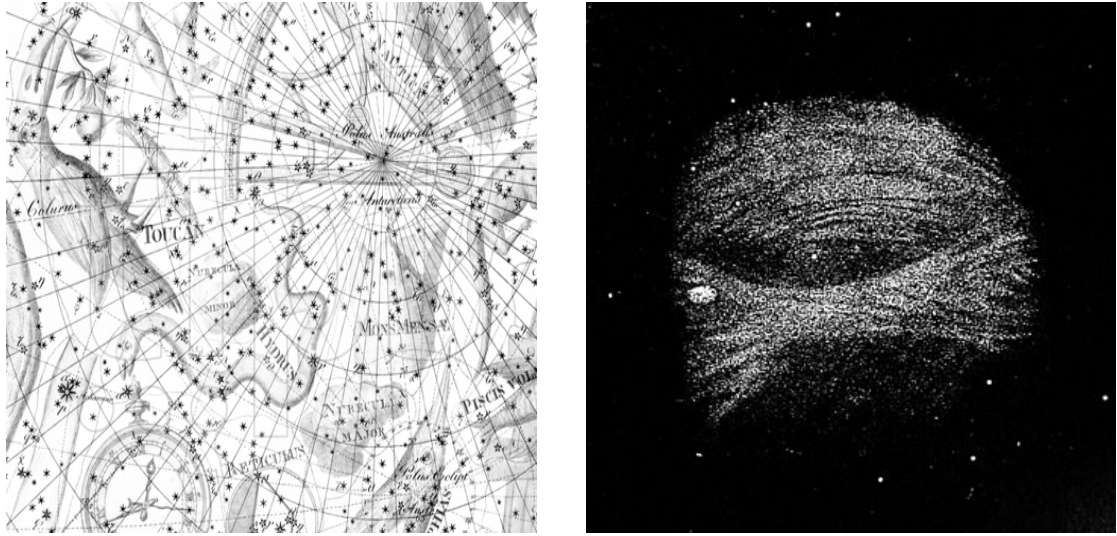
Figure 1.1: *Left*: A picture of the Uranographia published in 1801 by the German astronomer Johann Elert Bode (1747-1826); shows an area near the South Celestial Pole (upper right), the MCs (Nubecula Major and Nubecula Minor), along with several constellations. The constellations are represented by a mixture of contemporary and mythological figures. The Toucan (Toucana) at upper left, Hydrus (male water snake) at centre, Mons Mensae (Mensa) at centre right, and Reticulus (Reticulum) at bottom. *Copyright by: science photo library. Courtesy: Tipsimages. Right*: A hand sketch of the LMC *(Popular Science Monthly/Volume 3/June 1873/The Constitution of Nebulae)*

galaxy to the MW at a distance of about 50 kpc and the 4th largest galaxy in the LG. The basic parameters of the LMC are given in the 2nd column of Table1.1. The LMC has a prominent, off-centered and warped stellar bar and suspected spiral arms. Further it is a gas rich galaxy with active on going star formation. The LMC is a great celestial laboratory for the study of the formation and evolution of the stars in a low metallicity environment. It is home to the Tarantula Nebula (also known as 30 Doradus or NGC 2070), the most active star forming region in the LG. Supernova 1987a the nearest supernova in the recent years was also located in the LMC. The LMC has been long considered as a planar face on disk galaxy. But the studies on Cepheids (Nikolaev et al. 2004), red clump stars (Olsen & Salyk 2002), and RGB stars (van der Marel & Cioni 2001) confirmed the inclined geometry of the disk of the LMC with an angle of inclination of the order of $i \sim 35°$. The second parameter which defines the geometry of the disk plane of the galaxy is the Position Angle (PA) of Line Of Nodes (LON). A summary of these orientation measurements by various authors are given in Table 1 of Subramanian & Subramaniam (2013). The gas distribution and stellar population in the LMC are confined to a disk even though their radial extents are different. It is a kinematically cold disk system. A pressure

supported halo is proposed in the LMC by Minniti et al. (2003) using RR Lyrae stars as tracers. But further studies suggested that the RR Lyrae population follows the density distribution of the LMC disk rather than the halo (Subramaniam 2006, Alves 2004). This suggests that the RR Lyrae stars in the LMC might have formed in the LMC disk, instead of in the halo, and their large dispersions may be resulted from a combination of disk heating and MW tidal forces (Weinberg 2000). The LMC structure and kinematics definitely bear a signature of its tidal/hydrodynamical interaction with the MW and the SMC. van der Marel (2001) found that the LMC is elongated in the general direction of the Galactic center and is elongated perpendicular to the Magellanic Stream (MS) and the velocity vector of the LMC center of mass. He suggested that the elongation of the LMC has been induced by the tidal force of the MW. Mastropietro et al. (2009) analysed the effect of the ram pressure on the gas distribution and star formation in the LMC. The study by Indu & Subramaniam (2011) on the recent star formation history of the L&SMC shows that the recent star formation in both the clouds is dictated by the perigalactic passage. Besla et al. (2012) illustrated that the observed irregular morphology and internal kinematics of the Magellanic System (in gas and stars) are naturally explained by interactions between the LMC and the SMC, rather than gravitational interactions with the Galaxy. They also demonstrated that the off-center, warped stellar bar of the LMC and its one-armed spiral, can be naturally explained by a recent direct collision with its lower mass companion, the SMC. Even though there are on going debates on the details, the LMC is an ideal test bed to analyse the interaction and evolution of galaxies at our door step.

1.3 The Small Cloud

John Herschel in his book of 'Cape Results' points out that "the lesser cloud is less complex; but for that very reason is less interesting". But the studies in the last 150 years proven this to be wrong. Westerlund (1997) said that the structure of the SMC is more complex than that of the LMC. The basic parameters of the SMC are given in the 3rd column of Table 1.1. As suggested by the name, the mass and tidal radius of the SMC is lower than that of the LMC. It could be considered as the next nearest dwarf galaxy after the LMC. The SMC is a gas rich, metal poor galaxy with active on going star formation. The SMC is known to have a large line of sight depth as proposed by many studies (Mathewson et al. 1986, Mathewson et al. 1988 for the first time). The SMC is characterised by a less pronounced bar and an eastern extension called *Shapley Wing* (Shapley 1940). Shapley described it as a wing of faint stars, with radial extent almost

Figure 1.2: The LMC (*left*) and the SMC (*right*) in optical wavelength; long exposure images from APOD.

twice of then measured SMC radius, in the general direction of the LMC, and hence may be of some significance. By analysing H I distribution and kinematics of the LMC, Stanimirović et al. (2004) suggested tidal arm like tails which extents up to the Magellanic Bridge (MB). Subramanian & Subramaniam (2009) proposed a bulge in the SMC. Both the observational and theoretical studies suggests that the old and intermediate age stellar populations in the SMC are distributed in a regular smooth spheroidal/ellipsoidal component. While the young stars as well as gas is distributed in a rotating extended disk, irregular and highly disturbed. The explanation for the co-existence of these components are credited to the evolutionary history and the suggested merger events. As in the case of the LMC, the evolution, kinematics and structure of the SMC are also known to be influenced and continuously modified by the tidal/hydrodynamical interaction of both the MW and the LMC.

1.4 Magellanic Complexes

The interaction between the Galaxy and the MCs has resulted in several high-velocity complexes which are connected to the Clouds. The complexes are known as the Magellanic Bridge (MB), an Atomic Neutral Hydrogen (H I) connection between the Large and Small Magellanic Clouds, the Magellanic Stream (MS), a $10° \times 100°$ H I filament which trails the Clouds, and the Leading Arm (LA), a diffuse H I filament which leads the

Table 1.1: Fundamental parameters of the LMC and the SMC

	LMC	SMC
Type	SB(s)m	SB(s)mp
Optical center[†]	$5^h19^m38^s$; -69°27''5.2'	$0^h52^m12.5^s$; -72°49''43'
Mass[‡]	1.3×10^{10} M$_\odot$	2.4×10^9 M$_\odot$
Distance[*]	50.1 kpc	61.7 kpc

[†] J2000, de Vaucouleurs & Freeman (1972)

[‡] van der Marel et al. (2009)

[*] Cioni et al. (2000), van der Marel et al. (2002), Piatek et al. (2008)

Clouds. The mechanism responsible for the formation of these features remains under some debate. These three interactive features, collectively called as *Magellanic Complexes* are connected, but unique in their spatial and velocity distribution (Putman 2000). These Magellanic H I complexes make up a large fraction of the high-velocity H I concentrations in the southern sky which are known as high velocity clouds (HVCs). The three HVCs are also classified as Magellanic debris. Further the Clouds are known to have in a common envelope of H I which is considered as a supporting element to the theory that the Clouds are together for a significantly long time. The details of these three complexes are discussed below.

1.4.1 The Bridge or Inter-Cloud Region

As pointed out by Mary Putman, the LMC-SMC-MW interaction has created a variety of unique H I features which can be viewed in detail due to its proximity. The 21 cm line observations of the Clouds are done for the first time by Kerr et al. (1954) using a 36 feet paraboloid antenna owned by CSIRO Sydney. It was the first step to detect extra galactic H I. They estimated the H I mass of the clouds more or less accurately and from the radial velocity measurement suggested that the Clouds are rotating systems. They also tried to estimate the mass of the Clouds from the rotation curve. Later Hindman et al. (1963) mapped a 'gaseous bridge' like structure between the Clouds. The MB is a $\sim 10^8$ $M_\odot$ filament of H I which joins the two MCs and has a velocity gradient which proceeds from 125 km s^{-1} at the tail of the SMC or Shapleys Wing, to $\sim$ 300 km s^{-1} at the extended arm of the LMC. Tidal models predict that the Bridge was pulled from the SMC during a close encounter between the two Clouds 200 Myr ago (Gardiner &

Noguchi 1996). Later Putman (2000) by analysing HIPASS data observed an extension of the Bridge from the LMC and suggested that the Bridge is made of both the SMC and the LMC material. It is still a matter of debate. The Bridge is an H I feature which also contain stars.

1.4.2   Magellanic Stream

The presence of a velocity anomaly near the South Galactic Pole (SGP) was first noted by Dieter (1965). But the gas was not mapped, and the connection to the two MCs was not made. A subsequent study of the feature by van Kuilenburg (1972) showed a single narrow cloud about 35° in length, in their all sky high velocity H I survey using Dwingloo Telescope. (cf. Wannier & Wrixon 1972.) The feature has been called initially as the South-Pole complex. Wannier & Wrixon (1972) with a higher sensitivity and broader frequency range improved the picture considerably, increasing the observed length of the cloud to 60°. The large range in velocity of this feature (negative with respect to the Local Standard of Rest, LSR) was also noticed by all the above studies. Wannier & Wrixon (1972) concluded that the single cloud near the SGP has highly suggestive properties including velocity behaviour, shape and orientation. Mathewson et al. (1974) using 18 m reflector of Parkes observatory discovered that the feature is connected to the MCs. The feature is given the name Magellanic Stream, in their paper of the same name. Their observations was in a range covering both positive and negative velocities from -340 to $+380$ km s^{-1}. Models describing the formation of the MS had been produced since 1980. Following computing power, the initial models were very simple, non-self-gravitating, and with few particles. Most models predicted a feature leading the MCs. These early models were tidal models. Later on ram pressure models and models based on combination of tidal and ram pressure interaction came up. The MS is basically a continuous filament, bifurcated for most of its length into horse shoe shaped structures. The most recent observation by Nidever et al. (2013a) showed the length of the Stream to be 160°. The MS is a gaseous feature with no stars and dust observed with it yet. There are a number of theories put forward to explain the origin of the Stream, on the basis of either tidal or hydrodynamical or the combination of both interactions. Putman et al. (2003) explained the dual filamentary structure of the Stream to be relics of the gas stripped separately from the Bridge and the SMC. On the contrary there are also theories put forward discussing the MS gas fed by a filament connected to the South East H I Overdensity (SEHO) region in the LMC. The proposed mechanism was the blow-out of gas from Super Giant Shells (SGS) (Nidever et al. 2008), which contributes at least one
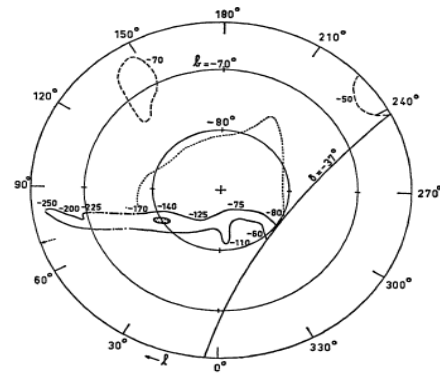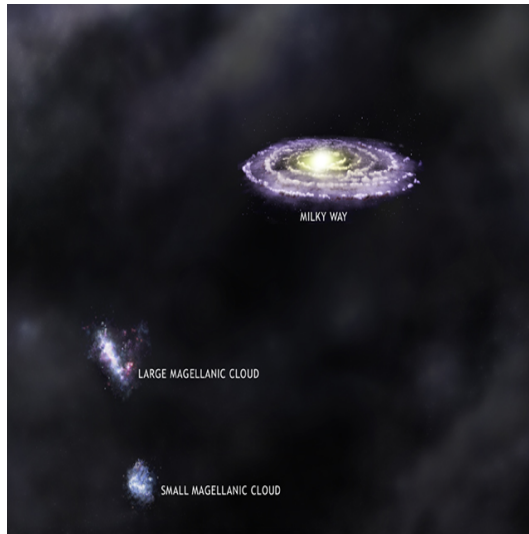
Fig. 4. A map of the South Pole Complex. The contour indicates a temperature above 0.5 °K. Velocities are given near the concentration in km/s. The dotted contours enclose regions where hydrogen near — 50 km/s was observed. The arrow at $l = 70°$ points to intermediate velocity material near $b = 55°$. Below $\delta = 37°$ no observations can be made from Dwingeloo

Figure 1.3: *Left*: An artistic view of the LMC-SMC-MW system *Right*: The South Pole complex observed and depicted by Dieter (1965)

half of the trailing stream gas.

1.4.3 Leading Arm

The LA consists of three complexes of gas, LA I, II & III. Pieces of these structures were first seen by van Kuilenburg (1972) and Wannier & Wrixon (1972). Although there was no direct connection, Mathewson et al. (1974) suggested a possible association of these features to the MCs, and this hypothesis was further explored by Mathewson et al. (1979), Morras (1982), and Bajaja et al. (1989) (cf. Nidever et al. 2008). In 1998, the HIPASS survey revealed a new stream of gas that lies in the opposite direction to the trailing MS and leads the motion of the Clouds (Putman et al. 1998). The existence of both leading and trailing streams supports a gravitational interaction scenario, whereby the streams are torn from the bodies of the MCs by tidal forces. One of the main pitfall of the proposed model of tidal origin for the MS was the lack of observational evidence of a predicted leading feature, which is a natural consequence of tidal interaction. Putman et al. (1998) observed a continuous feature connected to the Clouds and lie between the Clouds and the Galactic Center (GC). They detected it up to a length of $\sim 25°$. So, the LA Feature had its existence finally established in 1998 after 25 years of discovery of the MS. Furthermore, Lu et al. (1998) and Gibson et al. (2000) established the chemical similarity between the streams and MCs. The currently observed extent of the LA is $65°$ across the sky by Venzmer et al. (2012). They also observed a fourth arm segment called
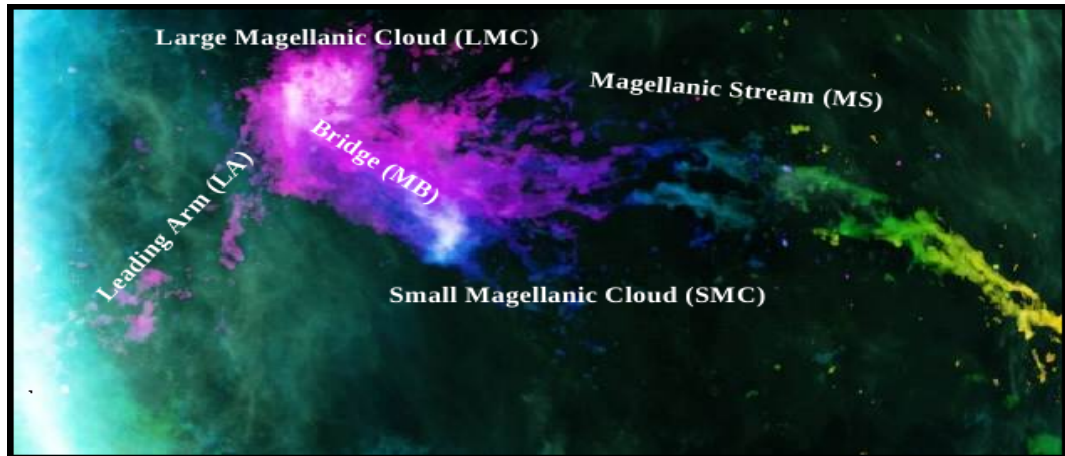
Figure 1.4: Magellanic System in H I, GASS map.

LA IV. McClure-Griffiths et al. (2008) found evidence of LA colliding with the Galactic disc.

Putman et al. (1998) suggested that the LA gas comes mainly from the SMC. Staveley-Smith et al. (2003) noted several H I features of the LMC (arms B, E, S, and W) and remarked that arm E pointed to the LA clouds, which lay beyond the coverage of their survey. Staveley-Smith et al. (2003) went on to say that deep, reprocessed HIPASS data show a continuous connection between arm E and the LA. Nevertheless, Staveley-Smith et al. (2003) concluded that the LA gas mainly arises from the SMC, and only some LMC gas 'leaks' into the LA. Brüns et al. (2005) showed that the first concentration of LA I is directly connected in position and velocity to the H I clouds close to the LMC, but claimed that it is associated with the Bridge. Further in 2008, with the Leiden Argentine Bonn (LAB) all sky H I survey, Nidever et al. (2008) found evidence suggestive of the possibility that most of the LA originates in the LMC, contrary to previous assertions that both the MS and the LA originate in the SMC and/or in the MB.

1.5   Magellanic System

The word Magellanic System, refers to the Clouds and the three H I complexes together. As we discussed, the system bears vivid signatures of the LMC-SMC-MW interaction. The proximity opens a path for the detailed understanding of this interaction. All sky survey data sets like Parkes Galactic All Sky Survey (GASS) covered the Magellanic System to ever possible larger extents, with significant kinematic/spatial resolution to show deep in to these beautiful features. Figure 1.4 shows the H I map of the Magel-

lanic System, using GASS data. To summarise the Magellanic Complexes are known to be the results of the LMC-SMC-MW interaction. But the origin of the gas/stars present in these features, the type of interaction and its details, time scales of their formation, all are topics currently under debate. Therefore, detailed studies with data sets of more wider coverage and better resolution are desired to understand the Magellanic System.

1.6 The Era of New Proper Motion Estimates

The Clouds were known to be satellites for the Galaxy for a considerably long period of time in the past. All the scientific analysis and the related interpretations about the Clouds in almost every aspects, like interaction, evolution, star/cluster formation history, kinematics, structure and structural peculiarities, were based on this belief. One of the strong element related to this satellite scenario was *the multiple perigalactic passage*, which possibly explained many structural, evolutionary, and kinematical features of not only the Clouds, but also the MW. But the Hubble Space Telescope observations in 2006, and the re-estimation of the proper motions of the L&SMC opened a new era in the history of the Clouds (Kallivayalil et al. 2006a, Kallivayalil et al. 2006b). The studies suggested that the 3D velocities of the Clouds are substantially higher (by $\sim$ 100 km s^{-1}) than previously estimated and now approach the escape velocity of the MW. The important implication of this study was *the first passage scenario* (Besla et al. 2007). It states that the LMC and SMC are either currently on their first passage towards the MW or they have a highly eccentric orbit with a significantly larger orbital period. It also drastically limits the time scale over which the Clouds and the MW can have interacted, making it highly unlikely that the Clouds have undergone multiple perigalactic passage. This forces a major reassessment on the studies of star formation history, kinematics and also on the proposed formation mechanisms for the MS, which depend strongly on the assumption that the Clouds have undergone multiple pericentric passages.

1.7 Star Formation History

The study of galaxy evolution is known to pursue on two distinct and complimentary fronts, the high redshift universe and the local galactic neighbourhood. The evolutionary studies of the high redshift galaxies is basically by cosmological simulations, from the time of first light and the birth of galaxies. The high red shift universe provide numerous sample galaxies, but the details like morphology, kinematics, chemical composition

are not accessible. On the contrary, in the LG, even though the number of samples are limited, the properties can be accurately measured using direct methods and analysing resolved stellar populations. A galaxy's star formation history (SFH) is a detailed analysis of how, when, and where the galaxy formed its stars. By analysing the SFH one should be able to resolve the puzzles like - whether the galaxy formed stars continuously, or there were bursts of star formation and quiescent periods? What is the rate of star formation? Whether the stars are formed in cluster environment or not? How efficient is the chemical enrichment and what fraction of the enriched material is transferred to subsequent generations of stars? Whether the star formation episodes are spatially uniform or localized according to the morphology of the galaxy? Is there any directionally propagating star formation present? Are the star formation triggered internally or externally? What are the possible internal or external triggering mechanisms? Is there any signatures of past interactions/mergers with nearby galaxies? Addressing the above mentioned puzzles in detail using the tool of SFH will eventually point to the constraints of the structural, chemical, and evolutionary history of the galaxy. To summarise the evolution of a galaxy is encoded in its SFH.

The fundamental method for measuring the SFH of a stellar population is the analysis of a colour magnitude diagram (CMD) that includes both the bright giant stars and the faint dwarf stars, observed photometrically. The location of the main sequence turn-off, and the subgiant branch stars, could infer the age and metallicity of the stellar population while the colour of the red giant branch stars can disentangle the estimates of age and metallicity. In 1950s the method was restricted to star clusters in the Galaxy (Sandage 1953) and in the Clouds (e.g., Arp 1958, Hodge 1960, Westerlund 1961, Tifft 1963). 1970s replaced the photographic plates with CCDs which improved the analysis significantly. But the global SFH of a galaxy demands the estimation of the SFHs of its heterogeneous, complex and mixed field star population. In 1980s the improved understanding of the stellar evolution and stellar initial mass function (IMF) as well as the more advanced computational techniques made it possible to reconstruct the SFH of field populations. The key to disentangling the complex mix of stellar populations lies in the quantitative comparison of observed CMDs to synthetic CMDs estimated by populating theoretical isochrones with an adopted IMF and an input model SFH (Harris & Zaritsky 2009). One of the earliest method is called the "R method", which is a statistical comparison of observed and synthetic CMDs using the main sequence luminosity function and ratios of star counts in age sensitive regions of the CMD, such as the red giant branch and the subgiant region (Bertelli et al. 1992). All modern synthetic CMD methods are

generalizations of the R method, with a library of synthetic CMDs, with various age and metallicity ranges.

The Clouds of Magellan are optimal targets for the SFH analysis due to various reasons. Their proximity help to estimate CMDs of resolved stellar populations well down the main sequence and the on going star formation enables the analysis of the SFH to very young populations were the greatest temporal as well as spatial resolution is achievable. Further the Clouds are ideal laboratories at our door step to understand the effect of galaxy-galaxy interaction on the star formation episodes. The estimation of the SFH of the admixture of the field stellar population of the Clouds was carried out by various studies (e.g., Holtzman et al. 1999, Olsen 1999, Dolphin et al. 2001, Smecker-Hane et al. 2002). The Hubble Space Telescope (HST) observations with stars fainter than the ancient main sequence turn-off helped to reveal the presence of older populations in the Clouds. But many of the previous studies were spatially restricted to localised fields in the Clouds. The reconstruction of the spatially resolved SFH of the L&SMC covering almost the entire area is done by Harris & Zaritsky (2004) and Harris & Zaritsky (2009). They analyse the SFH from populations as old as 16 Gyr in the LMC and 10 Gyr in the SMC to populations as young as a few Myr. But since the analysis covers a larger time span it compromises the temporal resolution to identify any propagating star formation.

1.7.1 Recent Star Formation History of the L&SMC

The study of Star Formation History (SFH) form a useful tool to understand the formation and evolution of the Clouds. The star formation episodes can be presumably triggered due to LMC-SMC-MW interactions, which may restrict the time scales of this mergers/interactions. Also the pattern of propagation of star formation may reveal the directional details of interaction. Therefore the analysis of SFH leads to the spatial and temporal information of the mutual interactions of the Clouds as well as their interaction with the Galaxy. As discussed previously the new proper motion measurements restricted the interactions of the Clouds with the Galaxy to a very recent past of the order of a few 100 Myr. Also the predicted close encounter of the LMC with the SMC is around 200 Myr ago. Therefore the analysis of the Recent Star Formation History (RSFH) is exclusively important, since it may lead to the details of the recent LMC-SMC-MW interaction. As we discussed earlier the RSFH enables the highest spatial and temporal resolution achievable, since the brightest part of the main sequence is analysed and only a short range in age is covered. The age-metallicity degeneracy does not play a very significant role in the RSFH, and also it is favourable in observational aspects due to the above reasons.

1.8   Kinematics of galaxies

Kinematics of a galaxy is defined as the measurement and analysis of the velocity distribution of its visible matter including stars and gas. The kinematics is closely related to the galaxy's morphology, structure and the gravitational potential it holds. It also possess imprints of the interactions and evolution of the galaxy. The first attempt to estimate the kinematical model of a galaxy was done by Lindblad for the MW by measuring the radial velocities of globular clusters using the aid of Doppler shifts. This attempt produced new insights in to the properties of the Galaxy (Lindblad 1927). Lindblad's idea pointed to the first approximation of the dynamically inferred mass estimate of the MW and also tried to explain its apparent structure. He noted the most fundamental/crude idea behind the classification scheme of galactic morphology, that the degree of flattening of systems depends on whether its motion were dominated by rotational or random velocities. Nevertheless in the kinematical aspect, the disk galaxies are classified as rotationally supported systems while the elliptical and spheroidals are pressure supported systems in general.

One of the important physical parameter derived from the astronomical spectra of a celestial object is the radial velocity along the line of sight. It is measured as the Doppler shift of absorption or emission lines produced by the chemical elements of the object. The velocity dispersion is measured as an estimate of the spread/broadening of the line profile. For high red shift galaxies and distant galaxies observed as point objects, for which only the integrated spectra is accessible, one could derive only a single estimate of the rotational/dispersion velocity. But the stellar as well as gaseous distribution of the galaxies in the Galactic neighbourhood are resolvable and one could analyse the velocity distribution across these galaxies. The LMC and SMC being objects of large angular extents in the sky, are ideal for such detailed kinematical analysis.

1.8.1   Atomic Neutral Hydrogen (H I)

The major constituent of the visible universe is Hydrogen. It is obvious that one of the most significant and widely used spectral line arises from H I. A great advance in dynamical studies of the MW and other galaxies came from the discovery that the gas in these system emits at radio wavelength. In 1932 Karl Jansky established the emission of the broad radio spectrum, but the major break through came from the discovery of the strong spectral line at 21 cm wavelength. It was predicted by H. C. van de Hulst in 1944, and was observationally confirmed in 1951 (Ewan and Purcell at Harward, Christiansen

in Australia, Muller and Oort in the Netherlands). This emission line is formed from a hyperfine transition in the H I atom caused by the spin reversal of the single proton. The radio emission formed the ideal tool for studying the large scale kinematics of the Galaxy/galaxies. This distinctive line enabled astronomers to measure the line of sight motions of atomic Hydrogen via Doppler shifts. Radiation at such long wavelength is entirely unaffected by dust extinction, so the limitation to study kinematics in optical wavelength ceases to be a problem (cf. Binney & Merrifield 1998). The first H I map of the MW was produced by Oort et al. (1958), shown in figure 1.5. The H I distribution in the MCs was first analysed in 1960s (McGee 1964, Hindman 1964, McGee & Milton 1966) and continued till date by various studies (e.g., Mathewson et al. 1988, Luks & Rohlfs 1992, Kim et al. 1998, Kim et al. 2003, Stanimirović et al. 2004). Early radio observations were done using single dish antennae and later, higher spatial resolution was achieved with radio interferometers. The study of the distribution of H I in samples of more than a few disk galaxies has been possible only since the advent of aperture synthesis measurements of the 21 cm line.

The H I observations are taken in a number of frequency channels, each frequency corresponds to one velocity, separated according to the velocity resolution available for the observation, and within a range of velocities. The velocity estimated from each pointing in the radio data, can be combined to estimate velocity maps. The extraction of kinematic data from the raw observations of moderately inclined systems has often been discussed. The basics are summarized in van der Kruit & Allen (1978), Bosma (1981), Wevers et al. (1986), and Begeman (1987). The results are a radial distribution of H I surface brightness, a rotation curve, and a radial distribution of velocity dispersion; from these one can, in principle, make maps of residuals compared to these azimuthal averages.

The kinematical analysis of external galaxies in the LG involves estimation of spider diagrams, position-velocity diagrams and rotation curves. Spider diagrams are basically the isovelocity contours, from which we can assess the first approximation of kinematical parameters like the PA of LON, and possibilities of structural anomalies like warps. The position velocity diagram is the variation of velocity with respect to a spatial coordinate (e.g., RA, x, ρ). It can be used to understand the sense of rotation and presence of anomalies like counter-rotating components. The rotation curves are the radial variation of velocities taking in to account the orientation of the disk of the galaxy. The rotation curves infer the dynamical mass of the galaxy and hence the details of its gravitational potential. Observations of spiral galaxies in the H I have not been consistent with the simple picture of a flat, self gravitating gaseous disk in circular, differential rotation. A

typical derived rotation curve does not show a Keplerian behaviour at large distances from the center, instead, it stays almost constant up to a large radii. Moreover, isovelocity and surface intensity diagrams often indicate that a large scale disturbance dominates the kinematics of gas, especially in the outer regions of the galaxy (Christodoulou et al. 1988).

Toomre & Toomre (1972) elegantly demonstrated that the tails and bridges emanating from many peculiar galaxies may arise kinematically from dynamically cold disk material torn off from the outer regions of galaxies experiencing strong gravitational interactions. H I mapping studies are particularly well suited to such studies, as the tidally ejected disk material is usually rich in neutral hydrogen and can be traced to very large distances from the merging systems (e.g., van der Hulst 1979, Simkin et al. 1987, Appleton et al. 1981, Appleton et al. 1987, Yun et al. 1994). Once mapped, the tidal kinematics can be used either alone to disentangle the approximate spin geometry of the encounter (Stockton 1974b, Stockton 1974a, Mihos et al. 1993, Hibbard & van Gorkom 1996, Mihos & Bothun 1997) or in concert with detailed numerical models to constrain the full encounter geometry (e.g., Combes 1978, Combes et al. 1988, Yun 1992, Yun et al. 1997, Hibbard & Mihos 1995, Gardiner & Noguchi 1996).

Since Gunn & Gott (1972) introduced the concept of ram pressure stripping, which can affect galaxies moving inside an intra cluster medium, this mechanism has been invoked to explain different observational phenomenons like the H I deficiency of spiral galaxies in clusters (Chamaraux et al. 1980, Giovanelli & Haynes 1985). Interactions between galaxies are common and are an important factor in determining their physical properties such as position along the Hubble sequence and star formation rate. There are many possible galaxy interaction mechanisms, including merging, ram pressure stripping, gas compression, gravitational interaction and cluster tides. The relative importance of these mechanisms is often not clear, as their strength depends on poorly known parameters such as the density, extent and nature of the massive dark halos that surround galaxies. A nearby example of a galaxy interaction where the mechanism is controversial is that between our own Galaxy and two of its neighbours - the Large and Small Magellanic Clouds.

1.8.2   Kinematical Structure of the Magellanic System

The kinematics of the Magellanic System in a very broad way comprise the topics like the orbital history of the system and proper motion estimates, origin, formation and evolution of the Magellanic complexes, the MS, MB and LA, the binarity of the L&SMC
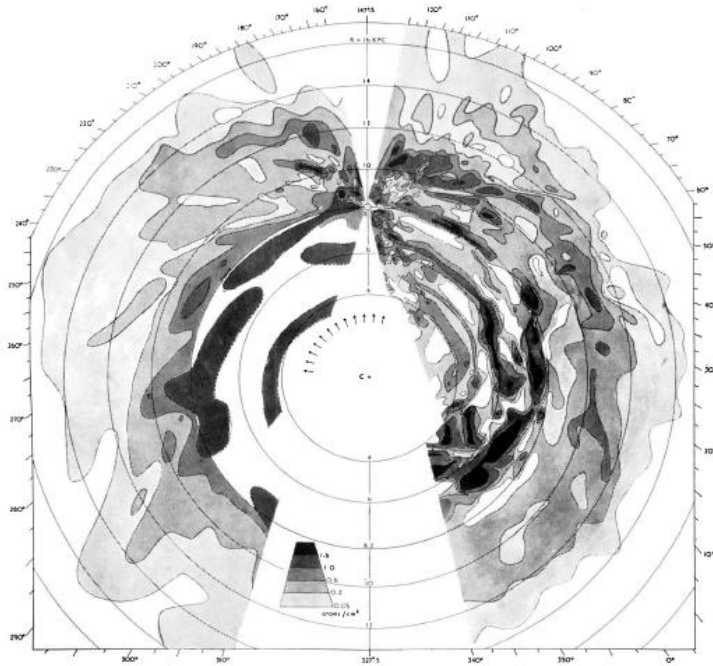
Fɪɢ. 4.—*Distribution of neutral hydrogen in the Galactic System. The maximum densities in the z-direction are projected on the galactic plane, and contours are drawn through the points.*

Figure 1.5: The distribution of H ɪ in the plane of the MW as inferred from early 21 cm observations. The region unmapped towards the Galactic center and anti-center is seen as an empty cone (Oort et al. 1958).

and their association with the MW, the peculiarities in the kinematical structure of the L&SMC and the presence of the kinematic anomalies like counter-rotating components, comparison of kinematics derived using stellar and gaseous tracers etc. There are numerous studies in this direction, using both theoretical and observational techniques. The theoretical studies involve the numerical simulations which trace the past orbits and evolutionary history of the Magellanic System by assuming suitable initial conditions and reproduce its current location and properties. The observational methods involve direct measurement of velocities using various tracers and analyse the results. Both these aspects are equally important and complimentary to each other, and eventually probe to the unresolved puzzles in the tidal or hydrodynamical interactions involved.

1.8.3 Gas Kinematics of the Clouds

As we discussed in previous sections the MCs are unique in nature with their proximity and being exceptionally gas rich. The Clouds are rather enveloped in H ɪ and connected to various H ɪ streams and arms which are collectively known as Magellanic

Complexes. Essentially the LG dwarfs within 270 kpc of their host galaxy (MW or M 31) are practically devoid of H I ($< 10^5$ ⊙; Grcevich & Putman 2009). Due to the above mentioned two reasons the MCs are ideal to analyse the gas dynamical effects in a great detail. Further the geometry and location of the Clouds are favourable to study their internal kinematical distribution since both the L&SMC are not edge on, and they are located rather away from the disk of the Galaxy. But the kinematics of these galaxies are extremely complex and continuously modified by their mutual interaction and interaction with the Galaxy. LMC is known to have a gas disk less extended (by a factor of ~ 3) compared to its stellar disk (Nidever 2013). This is attributed to the interaction with the hot gaseous halo of the MW. There are counter-rotating kinematical components detected in the LMC (Subramaniam & Prabhu 2005, Olsen et al. 2011, Diaz & Bekki 2012). While the SMC's stellar disk is been tidally disrupted, but it still possess an intact rotating H I disk which is severely disturbed by its close encounters with the LMC and tidal/hydrodynamical interactions with the Galaxy. Further the stellar and gas kinematics of the L&SMC show discrepancy which complicates the analysis of their gravitational potentials. Another equally interesting regime is the formation and evolution of the H I complexes including the MB, MS and LA. There are various studies which attributes their origin to tidal/hydrodynamical interactions or a combination of both. There are equally relevant and contradictory results tracing their origin to the LMC or SMC or both. The understanding of the gas accretion/outflows in the Clouds are only preliminary.

The gas distribution undergoes the kinematics or follows the velocity distribution according to the laws of fluid dynamics. It is viable to both gravitational and hydrodynamical interactions and hence may bear the signature of both these interactions. Hence mapping the gas disk and analysing its velocity distribution in detail may lead to important implications of the recent/ongoing interaction of the Clouds. The gas distribution, even though it is structured with filaments and holes, is rather continuous and uniform compared to the stellar distribution, and hence more apt for estimating the velocity maps.

The proper motion measurement bears an inevitable and rather significant role in the analysis of the kinematics of a galaxy. The line of sight velocity field what we observe will have a component of the transverse motion of the center of mass of the galaxy. It will also have components of the systemic velocity and precession/nutation motions of the disk of the galaxy, apart from the internal rotational motion. The effect of precession/nutation on the disk kinematics of a galaxy is only recently realised (van der Marel et al. 2002). Since the current proper motion measures are significantly different from the previous estimates it is demanded that the H I kinematics of the L&SMC are to be revisited. Also

the currently available all sky survey data sets like GASS, make it possible to analyse the disk kinematics to the largest radial extent ever done for the Clouds. The enhanced kinematical and spatial resolution of the data sets currently available enable us to peep in to the treasures of the valuable information it holds.

Therefore the Clouds, which are the only pair of interacting galaxies, resolvable to individual stars form ideal test beds to analyse various aspects of galactic/extra galactic astronomy. Apart from their proximity they are favourable in observational aspects due to their location with respect to the MW. As pointed out by Staveley-Smith et al. (1998) unlike Sagittarius dwarf the Clouds lie in a direction unobstructed by extinction and confusion from the MW. Another property which make them observationally favourable is that both the L&SMC are not edge on. To summarise, the MCs are unique in their nature and forms bench marks for various studies. In our study we analysed the two different aspects of the RSFH and H I kinematics of the Clouds, making use of the advanced data sets, and applying the new proper motion estimates. Our effort aims to understand the interaction and evolutionary history of the LMC-SMC-MW system.

1.9 Aim and Motivation of the Thesis Study

The high precision proper motion estimates of the MCs demands the revisit of the understanding of their SFH and a re-estimation of their kinematical analysis. It also restricts the interaction of the Clouds with the Galaxy to a very recent past of a few hundred Myr. Recent interactions between the LMC and the SMC and their tidal/hydrodynamical interactions with the MW can be understood by studying their recent star formation history. This thesis study aims to detect any directional or propagating star formation in the Clouds in the last 500 Myr, and analyse the results in the light of the recent proper motion estimates. Another aspect of this thesis study is to re-estimate the gas kinematics of the disks of the L&SMC in detail, using H I as tracer, taking in to account the two new proper motion estimates. The gas kinematics is expected to bear the signatures of the on going LMC-SMC-MW interaction. To summarise the study aims a better understanding of the very recent and on going interactions, both tidal and hydrodynamical, of the LMC-SMC-MW system, and the possible impacts of this interactions in the star formation episodes, structure and gas kinematics of the Clouds.

1.10   Overview of the Thesis

- **Chapter 1** : The history of the Clouds and the Magellanic Complexes are discussed and the previous studies are briefed. The two aspects of this thesis study, the RSFH and gas kinematics are introduced. The motivation and aim of the thesis study is presented in the light of the high precession proper motion measurements.

- **Chapter 2**: The optical and radio data sets used for the estimation of the RSFH and kinematics are discussed in detail. Various methods we apply in this thesis study are briefed.

- **Chapter 3**: The analysis of the RSFH of the LMC is presented considering the impacts of the recent proper motion measurements. Extinction maps are estimated. The Last Star Formation Event (LSFE) maps are studied in the plane of the LMC. The comparison with young clusters and H I clouds are presented. The various implications of the results are discussed, taking into account the tidal interaction with the MW and the hydrodynamical interaction with the Galactic halo.

- **Chapter 4**: The analysis of the RSFH of the SMC is presented considering the impacts of the recent proper motion measurements. Extinction maps and LSFE maps are estimated. The comparison with young clusters and H I column density distribution are presented. The effect of the MW-LMC gravitational interaction on the SMC SFH is discussed, by visualising the SMC, LMC and MW in a single plane.

- **Chapter 5**: The H I kinematics of the LMC is revisited, applying corrections for the recent proper motion estimates and the precession/nutation motion of the disk. The mean H I disk of the LMC is estimated and its kinematical structural parameters are derived. The kinematical outliers are identified and classified. Two models are proposed to explain the outliers. The possibilities and details of on going accretion and outflows and their connection to the H I features like the LA, MS and MB are analysed.

- **Chapter 6**: The nutation of the SMC disk is estimated using H I as tracer. The H I kinematics of the SMC is revisited, applying corrections for the recent proper motion estimates and the precession/nutation motion of the disk. The mean H I disk of the SMC is estimated and its kinematical structural parameters are derived. The

rotation curve of the SMC is estimated and the flat part is detected. The kinematical outliers are identified and classified. The tidal effect of the LMC and the MW on the SMC gas distribution and the tumbling of the SMC disk on its gas kinematics is discussed.

- **Chapter 7**: The summary and conclusions of this thesis work are presented in this chapter. The results and findings in the two aspects of the SFH and gas kinematics are compared and possible contrasts and unifications are discussed. The planned future projects are presented.

CHAPTER 2

DATA & METHODOLOGY

2.1 Data

The evolutionary as well as interaction history of the Magellanic Clouds (MCs) can be decoded from their star formation history (SFH) and kinematical properties independently. In our study we analyse these two aspects. The SFH is estimated using the optical photometric data. For estimating the kinematic properties we utilized the H I radial velocity data. The details of the data sets are given below.

2.1.1 Optical Data

For the estimation of SFH we make use of two publicly available photometric survey data sets that cover large area of the MCs. These are the catalogues produced by the Optical Gravitational Lensing Experiment (OGLE III, Udalski et al. 2008a, Udalski et al. 2008b) and the Magellanic Cloud Photometric Survey (MCPS, Zaritsky et al. 2002, Zaritsky et al. 2004). OGLE III has the advantage of better spatial resolution while MCPS covers a wider area. For uniformity, we use the photometric data in V and I passbands from both the catalogues. The details of the data sets are given below.

Optical Gravitational Lensing Experiment Survey

The OGLE project bears the main goal of searching for the dark matter with microlensing phenomena. The MCs and the Galactic Bulge are observed as part of the study since they provide large number of back ground stars for micro lensing. This long term experiment has completed three phases. OGLE I started in 1992 with the Galactic Bulge

as the first target. The second phase OGLE II observed the Galactic Bulge as well as both the L&SMC. But it covered only the central regions including the bar. OGLE III, the third phase of the OGLE project, started on June 12, 2001 was a significant extension of the OGLE survey. Much larger detector system made it possible to cover practically entire area of the L&SMC and large fraction of the Galactic Bulge. Since these regions of the sky are extremely interesting from the astrophysical point of view, OGLE maps have been widely used by astronomers for many astrophysical applications. The seven year survey provided mean calibrated photometry in V & I band filters. The fourth and on going phase OGLE IV recently published photometric images which cover the Magellanic Bridge (MB) region along with the Clouds and an extended area in the Galactic Bulge and Disk. OGLE I is observed using the 1 m Swope telescope, while the succeeding phases are observed using 1.3 m Warsaw telescope, both belong to the Las Campanas Observatory, Chile. As an out come of the second and third phases of the project the large photometric data base of the MCs are published. The OGLE III photometric catalogue is utilized for our study.

OGLE III images of the LMC used for construction of the OGLE III photometric maps of the galaxy were collected between July 2001 and March 2008 and cover seven observing seasons of the LMC. Similarly the SMC observations were taken between June 2001 and January 2008. Observations were carried out with 1.3 m Warsaw telescope equipped with the eight chip mosaic camera (Udalski 2003). One full mosaic image covers approximately $35' \times 35'$ on the sky with the scale of $0.''26$/pixel. Since the majority of observed fields have high stellar density, observations were conducted only in good seeing and transparency conditions. The median seeing of the V and I band OGLE III datasets is equal to $1''.2$. For the LMC the total observed area is 40 square degrees, covering 116 LMC regions, each of which covers an area of $35' \times 35'$. The catalogue consists of calibrated photometry in V and I passbands of about 35 million stars. Each of the 116 regions are observed using eight chips each with an area of $8.'87 \times 17.'74$.

The OGLE III maps of the SMC constitute a significant extension to the OGLE II maps as they cover much larger area and contain many more objects. The catalogue consists of V and I photometry of 6.5 million stars from 41 fields, covering an area of 14 square deg in the sky.

Magellanic Cloud Photometric Survey

The Magellanic Cloud Photometric Survey (MCPS) is a broadband photometric survey of the MCs. It was conducted using the Las Campanas Swope telescope (1 m) and
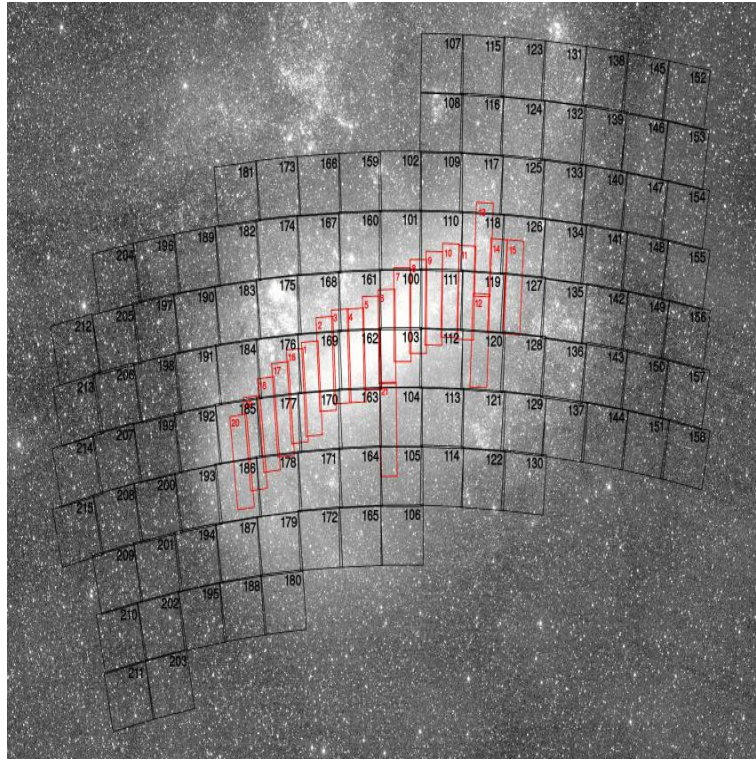
Figure 2.1: OGLE III fields in the LMC (black squares: 100 - 215) over plotted on the image obtained by the ASAS all sky survey. Red strips (1 - 21) mark OGLE II fields. (Udalski et al. 2008a)

the Great Circle Camera (Zaritsky, Shectman, & Bredthauer 1996) with a 2K CCD. The 5 year survey started in 1995 provides photometry of virtually all stars in the L&SMC, brighter than 21 magnitude in V band. Drift-scan images are provided for both the Clouds in the Johnson U, B, and V and the Gunn I bands. The pixel scale is 0.″7/pixel and the typical seeing is 1.″5. The data are reduced using a pipeline that uses DAOPHOT II (Stetson 1987) and IRAF.

The MCPS spans a total area of 64 square deg ($8.°5 \times 7.°5$ with the longer direction corresponding to the eastwest (EW) axis) in the LMC. It contains about 24 million objects. The survey presents photometric as well as extinction maps in U, B, V, and I passbands.

The MCPS survey consists of UBVI photometry of the central 18 square deg of the SMC ($4.°5 \times 4°$ where the longer direction is along the northsouth (NS) axis) covering 5 million stars.

As one could see the resolution of the OGLE III data set is around 3 times that of MCPS. Hence OGLE III catalogue makes a better choice for analysing the finer details of the features studied. But the data coverage of MCPS is 1.5 times that of OGLE III for
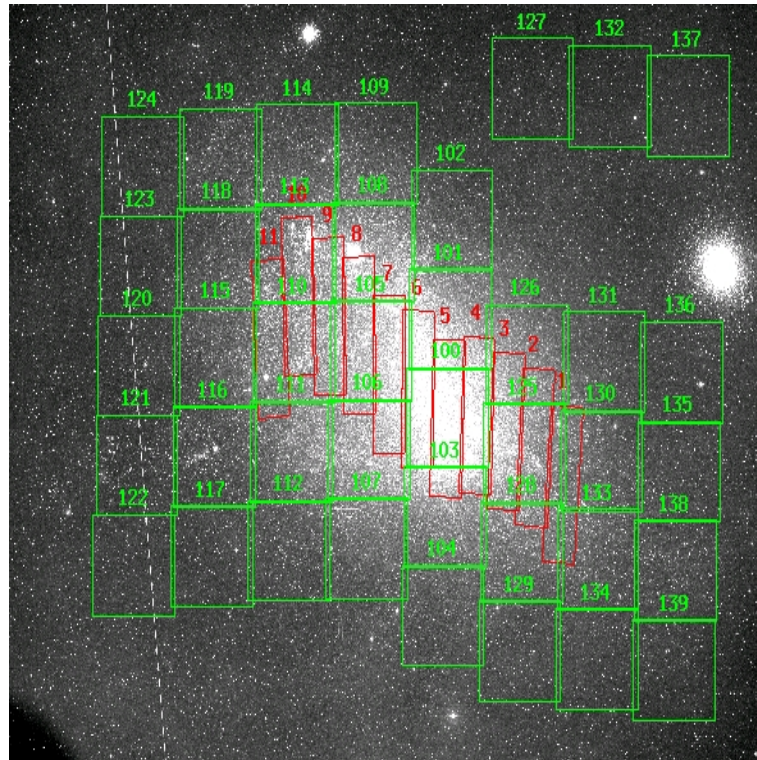
Figure 2.2: OGLE III fields in the SMC (green squares: 100 - 140) over plotted on the image obtained by the ASAS all sky survey. Red strips (1 - 11) mark OGLE II fields. (Udalski et al. 2008b)

the LMC, and nearly 1.3 times for the SMC. For analysing global features, especially in the northern parts of the disk, MCPS catalogue is suitable.

2.1.2   Radio Data

To estimate the mean H I disk of the MCs we used the combined H I velocity data, observed with the Australian Telescope Compact Array (ATCA) and the Parkes telescope (Stanimirovic et al. 1999, Kim et al. 2003). To analyse the velocity distribution of the H I beyond the L&SMC disks, including the MB region we utilized two all sky survey data sets - Parkes Galactic All Sky Survey (GASS) and the Leiden Argentine Bonn Survey (LAB). The details of these data sets are described below.

ATCA+Parkes Data

It is a high-resolution H I survey of the MCs, combining ATCA observations with the relatively newer observations made with the multibeam receiver on the Parkes telescope.
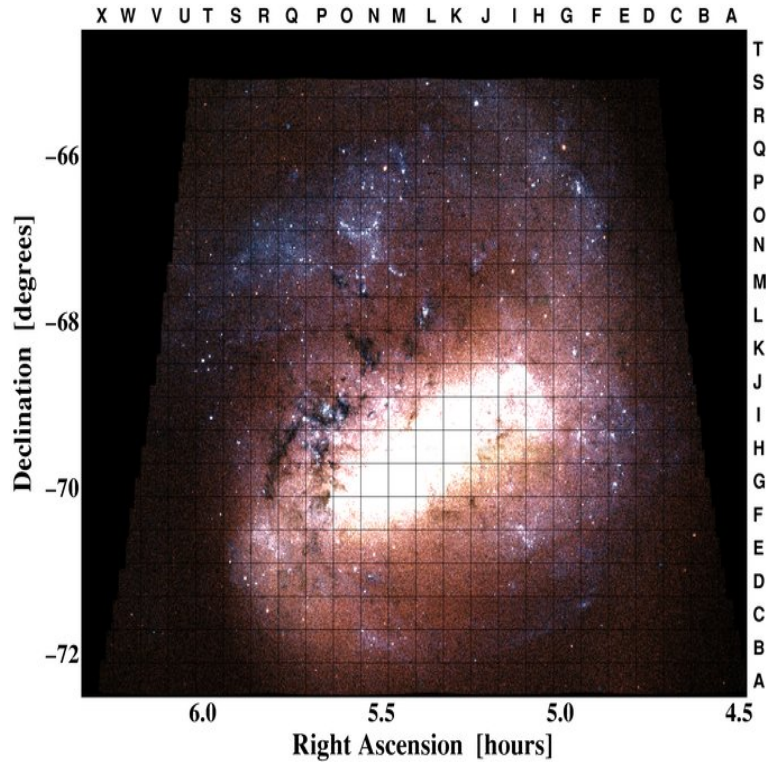
Figure 2.3: Stellar flux density map derived from MCPS UBVI photometry of the LMC. The MCPS region is divided into $24' \times 24'$ cells. (Zaritsky et al. 2004)

A combination of aperture synthesis and single-dish data is done in order to provide a data cube containing structure over the full range of spatial frequencies on the sky. For e.g.. the ATCA images, on their own, may not provide reliable H I masses for objects extended over more than $10'$ - $20'$, as the minimum ATCA baseline for these observations was 30 m. Similarly, Parkes H I images have a resolution of $14'$ - $16'$, depending on the details of the gridding of the data, and are therefore not useful for examining structures smaller than $25'$. Hence the ATCA and Parkes surveys provide comparable area coverage and velocity resolution but they compliments each other in spatial resolution.

The LMC was observed in four different configurations of ATCA in the years 1994 - 1996 (Kim et al. 1998). The combined configuration has 40 independent base lines, ranging from 30 to 750 m with a baseline increment of 15.3 m. The ATCA has been used in mosaic mode to survey a region of $10°$ - $12°$ covering the LMC, at an angular resolution of $1'$, corresponding to a spatial resolution of 15 pc in the LMC. The observing band was centered on 1.419 GHz, corresponding to a central heliocentric velocity of 297 km s^{-1} with a coverage of -33 to $+627$ km s^{-1}, at a velocity resolution of 1.65 km s^{-1}. The LMC was divided in to 12 regions, each one containing 112 pointing centers. The data were
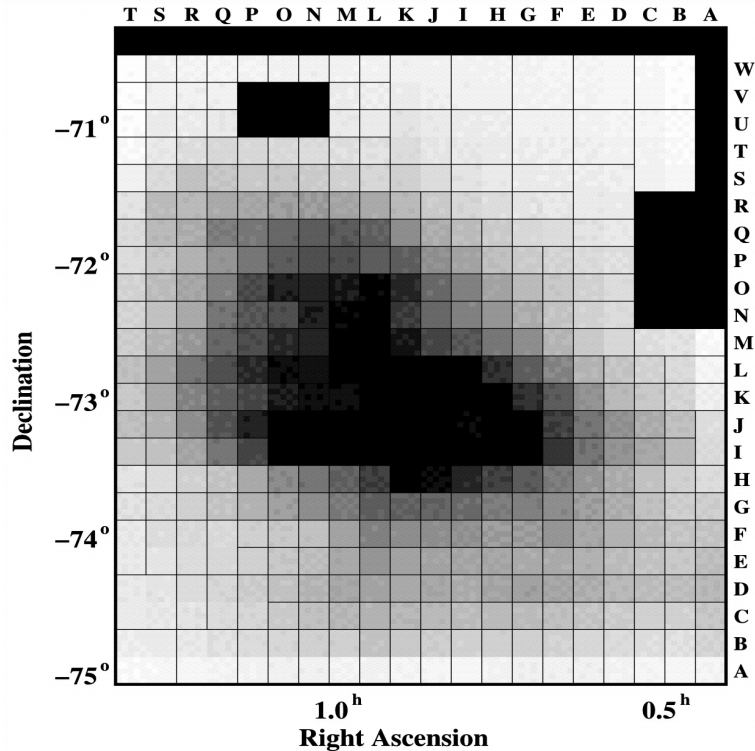
Figure 2.4: The division of the SMC MCPS catalogue into 351 subregions. The gray-scale image shows the number of stars present in the MCPS catalogue from each subregion (where white means zero stars, and black means approximately 30,000 stars). The primary division imposes a uniform 20 × 23 grid of subregions, each approximately 12′ × 12′ in extent. Where the density of stars is very low, adjacent grid cells are combined into larger subregions. Some regions are masked where foreground contamination (due to Galactic globular clusters along the line of sight) is significant. The large masked region on the west edge (regions AN through CR) is due to 47 Tucanae; the smaller masked region near the north edge is due to NGC 362.

edited, calibrated and mosaicked using MIRIAD data reduction package. The pixel size is 20″ and the final size of the LMC cube is $11.°1 \times 12.°4$. The H I emission in the LMC is detected mainly in the range V_{hel} = 190 - 387 km s^{-1}.

The 64 m Parkes telescope is part of the Australia Telescope, a National Facility managed by CSIRO. The Parkes multibeam H I survey (Staveley-Smith et al. 2003) which is sensitive to spatial structure in the range 200 pc to 10 kpc, complements the ATCA survey, which is sensitive to structure in the range 15 - 500 pc. Observations were taken with the inner 7 beams of the Parkes 21 cm multibeam receiver (Staveley-Smith et al. 1996) in 1998. The telescope scanned across the LMC in orthogonal great circles aligned approximately EW and NS. The area covered was 13 × 14 square degree in RA and
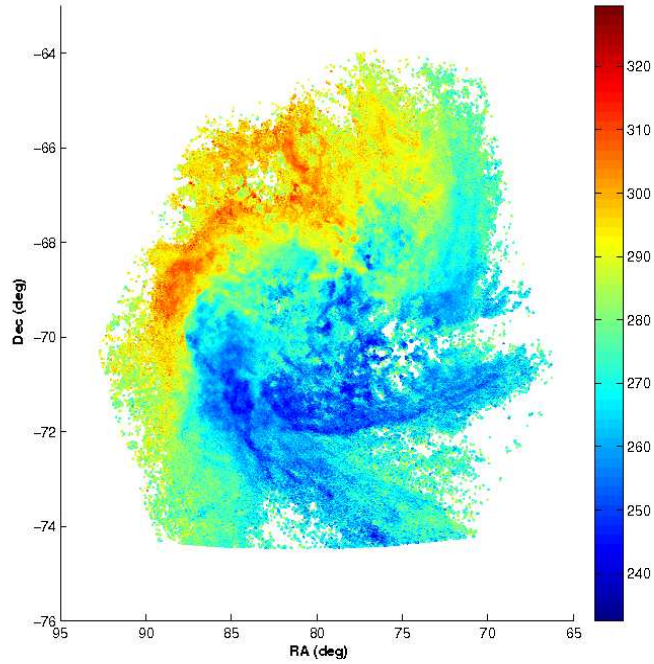
Figure 2.5: The velocity map of the combined data set of ATCA and Parkes surveys of the LMC. The colour coding is according to the intensity weighed mean velocity in km s^{-1}

Dec, respectively, and centred on RA = 05^h 20^m, Dec = $-68°$ $44'$ (J2000). The central observing frequency was switched between 1417.5 and 1421.5 MHz, every 5 s. The velocity spacing of the multibeam data is 0.82 km s^{-1}, but the final cube was Hanning-smoothed to a resolution of 1.6 km s^{-1}. The useful velocity range in the final cube (i.e. after excluding frequency side lobes of the LMC and the Galaxy, and band-edge effects) is -66 to 430 km s^{-1}.

The ATCA observations of the SMC were taken over 8 days in the year 1992, using ATCA's 375 m configuration. This gives an angular resolution of 1.6′, which is 28 pc in the SMC. This configuration has 10 base lines which are all even multiples (2, 4, 6, 8, 12, 14, 16, 18, 22 and 30) of the basic ATCA 15.3 m increment. The central observing frequency was 1420 MHz. The band width of 4 MHz (844 km s^{-1}) was divided in to 1024 channels resulting a channel spacing of 0.82 km s^{-1}. The boxcar averaged data covers a heliocentric velocity range of 88 - 216 km s^{-1} with a spacing of 1.6 km s^{-1}. The mean system temperature was 40 K. The survey covers an area of 4.°5 × 4.°5 with center at RA

45
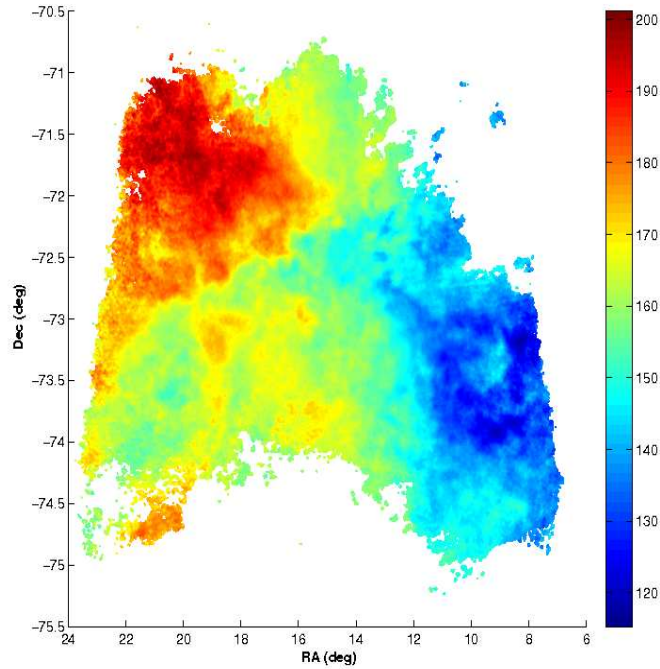
Figure 2.6: The velocity map of the combined data set of ATCA and Parkes surveys of the SMC. The colour coding is according to the intensity weighed mean velocity in km s^{-1}

01^h 01^m, Dec $-72°56^m$ (J2000). It encompasses the main body of H I in the SMC, above a column density of 10^{21} cm^{-2}, and extends well outside the optical bar of the SMC. Initial reductions of the data is done with AIPS and the mosaicking is done in the MIRIAD system.

Observations of the SMC were made with the Parkes telescope in 1996. A single-beam, cooled, 21 cm receiver was used to observe a total of 1540 pointings centred on RA 01^h 01^m , Dec $-72°56^m$ (J2000) and covering a total area of 4.°5 × 4.°5 (which matches the ATCA coverage). This gives a channel spacing of 0.82 km s^{-1}, though consecutive channels were later averaged to give a channel spacing of 1.65 km s^{-1} to match the ATCA data.

The two sets of observations were then combined by Stanimirovic et al. (1999), resulting in the final H I data cube with angular resolution of 98$''$, velocity resolution of 1.65 km s^{-1}, and 1 σ brightness temperature sensitivity of 1.3 K to the full range of spatial scales between 30 pc and 4 kpc. The sky covered with these observations is RA 00^{h}30^m to 01^{h}30^m and Dec $-71°$ to $-75°$ (J2000.0), over a velocity range of 90 - 215 km s^{-1}.

Leiden Argentine Bonn Survey

The Leiden Argentine Bonn (LAB) Survey of Galactic H I (Kalberla et al. 2005) is intended to be a general resource useful to a wide range of studies of the physical and structural characteristics of the Galactic interstellar environment. The LAB Survey presents the observations of 21 cm emission from Galactic H I over the entire sky. It merges the Leiden/Dwingeloo Survey (LDS: Hartmann & Burton 1997, Atlas of Galactic H I) of the sky north of $\delta = -30°$ with the Instituto Argentino de Radioastronoma Survey (IAR: Arnal et al. 2000 and Bajaja et al. 2005) of the sky south of $\delta = -25°$. The angular resolution of the combined material is $\sim 36'$. The velocity observations with respect to the Local Standard of Rest (LSR) spans the interval -450 km s^{-1} to $+400$ km s^{-1} , at a resolution of 1.3 km s^{-1}.

The Dwingeloo is a single-dish radio telescope with a diameter of 25 m. It is no longer in operation in an official capacity. Since August 2009 it is officially a Dutch industrial heritage monument. The telescope was owned by ASTRON, the Netherlands Institute for Radio Astronomy. But currently the C.A. Muller Radio Astronomy Station foundation (CAMRAS) restored the telescope and use it for programs like EME (moon bounce) which allows people on different parts of Earth to communicate via the Moon. In this technique, radio wave signals which are aimed at the Moon by one location and bounce off the Moon's surface, are detected by an antenna at a different location on Earth. The telescope possess an alt-az mount, with a Dec range $>-30°$. It covers a velocity range of -450 km s^{-1} to $+400$ km s^{-1}. The velocity resolution is 1.25 km s^{-1} and the channel separation is 1.03 km s^{-1}. The rms noise is ~0.09 K and the system temperature is 35 K.

The Villa Elisa telescope which is used for IAR survey bears an antenna diameter of 30 m. It belongs to the Argentine Institute of Radio Astronomy. It has an equatorial mount with a Dec range $<-25°$. It bears a system temperature of 35 K and rms noise $\sim$ 0.07 K. The velocity coverage is -450 km s^{-1} to $+400$ km s^{-1} and velocity resolution is 1.27 km s^{-1}. The channel separation is 1.05 km s^{-1}.

The coverage of the LAB data set is shown in an Aitoff projection in figure 2.7. One can see the MCs, connected by the Bridge, visible as red spots, in the lower right quadrant.

Parkes Galactic All Sky Survey

The Parkes Galactic All Sky Survey (GASS) is a survey of H I emission in the MW for the entire sky south of $\delta = +1°$ using the thirteen beam 20 cm multibeam receiver on the Parkes Radio Telescope. GASS covers all MW velocities between LSR -400 km
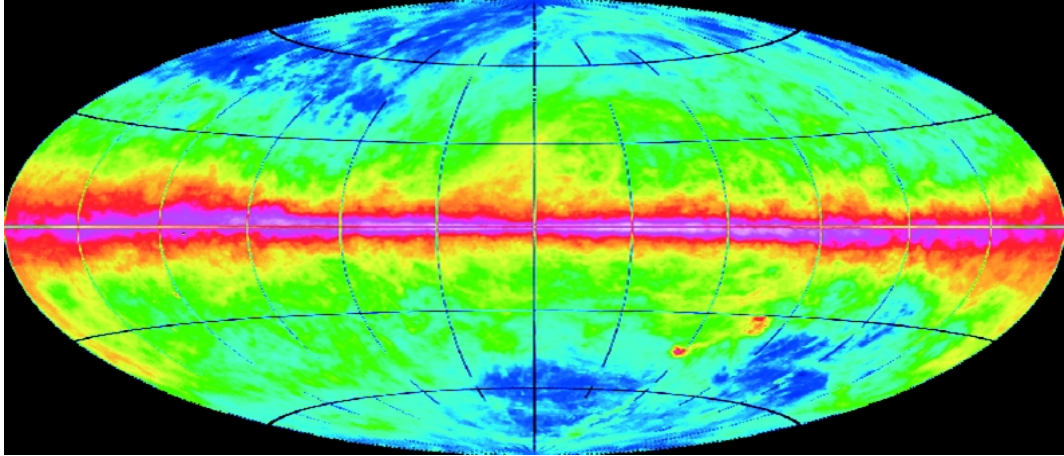
Figure 2.7: H I emission integrated over the velocity range $-400 < v < +400$ km s^{-1} in the LAB dataset, shown in an Aitoff projection. The Galactic center is in the middle. The integrated emission ($0 < N_H < 2 \times 10^{22}$ cm^{-2}, logarithmic scale) yields column densities under the assumption of optical transparency; this assumption may be violated at latitudes within about 10° of the Galactic equator. (Kalberla et al. 2005)

s^{-1} and +500 km s^{-1}. GASS is known to be the most sensitive fully sampled survey of Galactic H I currently available for the Southern sky. Survey goals include a better understanding of the interaction of the MW disk and halo and the nature of high and intermediate velocity clouds. The first data release of GASS (McClure-Griffiths et al. 2009) provides spectra and velocity integrated maps with a 16′ angular resolution, 1.0 km s^{-1} spectral resolution and an rms sensitivity of 57 mK. The second data release presented by Kalberla et al. (2010) is free from instrumental effects. It is corrected for stray radiation by convolving the all sky response of the Parkes antenna with the brightness temperature distribution from the LAB all sky survey, with major contributions from the 30 m dish of the IAR in the southern sky. Remaining instrumental baselines are corrected using the LAB data for a first guess of emission free baseline regions. Radio frequency interference is removed by median filtering. We used the stray radiation corrected second data release. GASS data set has 1137 velocity frames from which the velocity frames for the L&SMC and the MB are selected. For the LMC we have selected an area of 20° × 20° and for the SMC 12° × 12°. The spatial resolution is 4′.8 and the velocity resolution is of the order of 0.8 km s^{-1}.
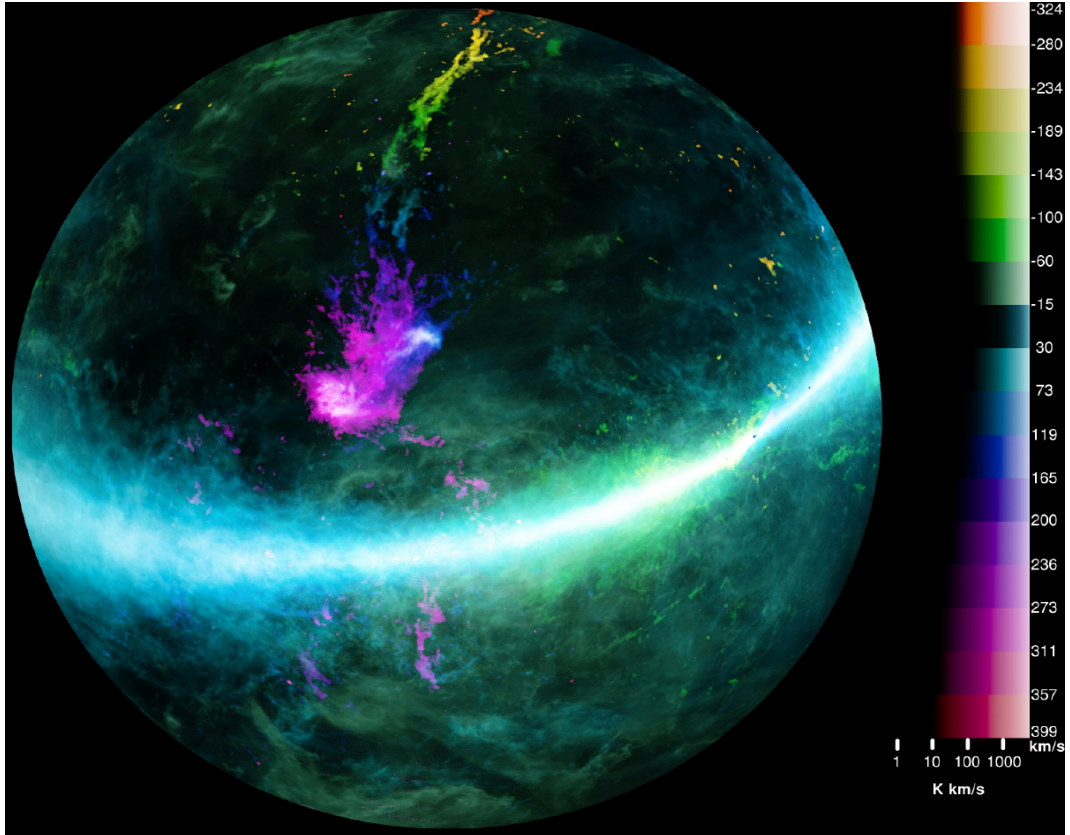
Figure 2.8: The entire GASS data set shown in a ZEA projection centered on the south celestial pole with 0^h RA at the top and with RA increasing counter-clockwise. The colours correspond to integrations over velocity chunks of ~ 40 km s^{-1} as indicated by the bar on the right of the image. The intensity of each colour corresponds to the brightness temperature integrated over the 40 km s^{-1} velocity chunk, and is scaled logarithmically as shown by the horizontal extent of the colour bar. Credit: S. Janowiecki

2.2 Methods

The various methods applied in the analysis of the star formation history and gas kinematics, comprising the coordinate conversions, the corrections applied to line of sight velocity, technique of deprojection on to the disk of a galaxy and the procedure to estimate the precession/nutation of the disk are discussed in the following sections.

2.2.1 Coordinate conversion

The equatorial coordinates (α, δ) are converted to Cartesian coordinates in kpc in a projected plane with respect to the L/SMC center (van der Marel & Cioni 2001). The

conversion equations are as follows.

$$x(\alpha, \delta) = D_0 \sin\rho \cos\phi \qquad (2.1)$$

$$y(\alpha, \delta) = D_0 \sin\rho \sin\phi \qquad (2.2)$$

Where D_0 is the distance to the center of the galaxy (α_0, δ_0). The quantities ρ & ϕ are the angular coordinates of a point defined by the coordinates (α, δ) in the celestial sphere, where ρ is the angular distance between the points (α, δ) and (α_0, δ_0) which is defined to be the center of the LMC, and ϕ is the PA of the point (α, δ) with respect to (α_0, δ_0). By convention, ϕ is measured counter-clockwise starting from the axis that runs in the direction of decreasing α, at constant declination δ_0. ρ & ϕ can be determined by combining the cosine and sine rules of spherical trigonometry (Smart & Green 1977) as described below,

$$\cos\rho = \cos\delta \cos\delta_0 \cos(\alpha - \alpha_0) + \sin\delta \sin\delta_0 \qquad (2.3)$$

$$\sin\rho \cos\phi = -\cos\delta \sin(\alpha - \alpha_0) \qquad (2.4)$$

$$\sin\rho \sin\phi = \sin\delta \cos\delta_0 - \cos\delta \sin\delta_0 \cos(\alpha - \alpha_0) \qquad (2.5)$$

For the LAB data set the spatial coordinates are converted from galactic to equatorial system using the conversion equations below,

$$\delta = sin^{-1}(\cos b \cos 27.4 \sin(l - 33) + \sin b \sin 27.4) \qquad (2.6)$$

$$\alpha = tan^{-1} \frac{\cos b \cos(l - 33)}{\sin b \cos 27.4 - \cos b \sin 27.4 \sin(l - 33)} + 192.25 \qquad (2.7)$$

where l and b are in degrees and v_{lsr} in km s^{-1}. x, y and z are the three coordinates of the fits file. The equatorial coordinates α and δ are calculated in degrees (Theory from 'Practical Astronomy With Your Calculator' By Peter Duffett-Smith) which are further converted to projected Cartesian coordinates in kpc using equations 2.1 and 2.2.

2.2.2 Deprojection onto the plane of a galaxy

The technique of analysing the data after deprojecting it on to the plane of a galaxy is introduced by van der Marel & Cioni (2001) for the LMC. In order to use this technique, we need to know the viewing angles i and θ of the plane of the galaxy. The LMC plane is inclined with respect to the sky plane by an angle i (the face-on view corresponds to i = 0) and the PA of the LON (measured counter-clockwise from the north) is θ. The near

side of the LMC plane lies at $\theta_{near} = \theta - 90$ and the far side $\theta_{far} = \theta + 90$.
Correction for the PA of LON and i can be applied if we know the mean distance D_0 to
the LMC center, using the conversion equations

$$x' = \frac{D_0 cos(\phi - \theta_{far}) sin\rho cos i}{cos i cos\rho - sin i sin\rho sin(\phi - \theta_{far})},$$ (2.8)

$$y' = \frac{D_0 sin(\phi - \theta_{far}) sin\rho}{cos i cos\rho - sin i sin\rho sin(\phi - \theta_{far})}.$$ (2.9)

It is useful in practice however not to use the coordinates in the LMC disk plane, but a
new system, in which the LON lie at the same angle in the (x″, y″) plane of the LMC, as
in the projected (x,y) plane of the sky. It is obtained by rotating (x′,y′) by an angle θ_{far}

$$x'' = x'cos\theta_{far} - y'sin\theta_{far},$$ (2.10)

$$y'' = x'sin\theta_{far} + y'cos\theta_{far}.$$ (2.11)

2.2.3 Heliocentric correction for velocity

The velocity values from the radio data set of LAB/GASS survey are with respect to
the LSR (v_{lsr}). This must be converted to helio centric frame, if we have to compare with
our studies on ATCA/Parkes data. The space velocity of the Sun with respect to the LSR
is 18.044 km s^{-1} (Schönrich et al. 2010). The observed line of sight velocity v_{los} in the
heliocentric frame is given by,

$$v_{los} = v_{lsr} - v_{solar}$$ (2.12)

where v_{solar} is the component of Sun's velocity towards the L/SMC, which is calculated
as follows,

$$v_{solar} = v_\odot (cos\, b \cos b_\odot \cos(l - l_\odot) + \sin b \sin b_\odot)$$ (2.13)

where $v_\odot$ is the sun's space velocity and $l_\odot, b_\odot$ represents the direction of its motion with
respect to the LSR.

2.2.4 Correction for Transverse Motion

The observed line of sight velocity of a galaxy is required to be corrected for the
three dimensional space motion, precession and nutation of the system. For the L&SMC

we used the recent proper motion estimates by Piatek et al. (2008) and Kallivayalil et al. (2013). The line of sight velocity field of a system at a point with an angular distance ρ from the center and PA ϕ (measured counter clock wise from north) is given by equation 24 of van der Marel et al. (2002),

$$v_{los}(\rho,\phi) = v_{sys}\cos\rho + v_t\sin\rho\cos(\phi-\theta_t) + D_0(di/dt)\sin\rho\sin(\phi-\theta) - sV(R)f\sin i\cos(\phi-\theta)$$
(2.14)

In the above equation v_{sys} is the systemic velocity, v_t is the transverse velocity, and θ_t is the PA of the transverse velocity vector in the sky. The first term corresponds to the systemic motion and the second term corresponds to the transverse motion of the center of mass of the galaxy. i is the angle of inclination of the plane of the galaxy and θ is the PA of kinematic LON. D_0 is the distance to the galaxy. The third term on the right hand side represents the precession and nutation of the galaxy. The last term represents the internal rotational motion of the galaxy with $V(R)$ as in plane rotational velocity. The quantity s is called the spin sign of rotation and f is a function of ρ, ϕ, θ and i. Simplifying the above relation and rearranging, we get the velocity field of the galaxy as,

$$v_{mod}(\rho,\phi) = v_{los}(\rho,\phi) - v_{sys}\cos\rho - v_t\sin\rho\cos(\phi-\theta_t) - D_0(di/dt)\sin\rho\sin(\phi-\theta) \quad (2.15)$$

2.2.5 Estimation of di/dt

The LMC is the first galaxy for which the quantity di/dt, which is an indicator of precession/nutation motion of the disk is uniquely determined. Weinberg (2000) and van der Marel et al. (2002) interpreted the observed di/dt as induced by tidal torques from the MW. The line of sight velocity field of a system at a point with an angular distance ρ from the center and PA ϕ (measured counter clock wise from north) is given by equation 31 of van der Marel et al. (2002),

$$v_{los}(\rho,\phi) = v_{sys}\cos\rho + \omega_{ts}\sin\rho\sin(\phi-\theta) + [v_{tc}\sin\rho\sin(\phi-\theta) - sV(R)f\sin i]\cos(\phi-\theta)$$
(2.16)

In the above equation v_{sys} is the systemic velocity, v_{tc} is the component of transverse velocity. (There is a spin sign 's' included as derived from equation 24 of van der Marel et al. (2002). The value of 's' could be ±1, and van der Marel et al. (2002) consider it to

be +1 in their equation 31.)

$$v_{tc} = v_t \cos(\theta_t - \theta), \ v_{ts} = v_t \sin(\theta_t - \theta) \tag{2.17}$$

The proper motion values μ_W & μ_N, (Piatek et al. 2008 and Kallivayalil et al. 2013) are converted to linear velocities, v_x & v_y using equation 28 of van der Marel et al. (2002),

$$v_x = D_0 \mu_W, \ v_y = D_0 \mu_N \tag{2.18}$$

We estimated the transverse velocity v_t as the resultant of v_x & v_y and also estimated its direction θ_t. ω_{ts} is defined as follows.

$$\omega_{ts} = v_{ts} + D_0(di/dt) \tag{2.19}$$

where,

$$v_{ts} = D_0 \mu_s \tag{2.20}$$

and

$$\mu_s = -\mu_W \cos\theta - \mu_N \sin\theta \tag{2.21}$$

The function f is defined as,

$$f = \frac{\cos i \cos \rho - \sin i \sin \rho \sin(\phi - \theta)}{[\cos^2 i \cos^2(\phi - \theta) + \sin^2(\phi - \theta)]^{1/2}} \tag{2.22}$$

$V(R)$ is defined as,

$$V(R) = 2V_0 \frac{R^\eta}{R^\eta + R_0^\eta} \tag{2.23}$$

where R is defined as the in-plane radius,

$$R = \frac{D_0 \sin \rho}{f} \tag{2.24}$$

Here the line of sight velocity field is fitted for seven free parameters using equation 2.16. The parameters are, v_{sys}, ω_{ts}, θ, v_{tc}, R_0, η, and V_0. From the estimated ω_{ts} value, using equations 2.19, 2.20 and 2.21 the value of di/dt is estimated. The value of i is given as an input parameter for fitting. For non-linear curve fitting, the function 'MPFIT' using Levenberg-Marquardt technique of IDL is used.

CHAPTER 3

RECENT STAR FORMATION HISTORY OF THE LARGE MAGELLANIC CLOUD*

3.1 Introduction

The Large and Small Magellanic Clouds form the nearest interacting binary galaxies, moving in the gravitational potential of the Galaxy. Their proximity make them unique and help to resolve individual stars. The Clouds are gas rich, and have active on going star formation. They are the test beds to understand the star formation in low metallicity environments. The star formation episodes of the Clouds are influenced by the LMC - SMC - MW interaction. The estimation of star formation history (SFH) is proven to be a useful tool to decode the evolutionary history of the Clouds. Also a detailed analysis of the star formation episodes can reveal the details of mutual interaction of the Clouds and also their interaction with the MW.

As we discussed in chapter 1, the new high precision proper motion estimates redefined the understanding of the SFH of the Clouds. Almost all the previous studies were based on the belief that the Clouds are long term satellites to the MW. The star formation episodes and the 'quiescent epoch' (an interval devoid of star formation) were attributed to the multiple perigalactic passage of the Clouds. But according to the new transverse velocity estimates, the Clouds are too fast to be bound to the MW and they are passing near our Galaxy for the first time. So the Clouds can interact with the MW only in the recent past and the SFH estimates need to be revisited. In this study, we estimate the distribution of recent star formation events in the LMC, which can eventually throw light to its recent interaction with the MW and the SMC.

---

*Results of this chapter are published in Indu, G., Subramaniam, A., 2011, A&A, 535, A115

The recent star formation history (RSFH) has been studied by various authors using star clusters as well as the field star population. Glatt et al. (2010) studied the SFH of the LMC based on star clusters with age <1 Gyr. They found that the cluster formation peaks at 125 Myr and 800 Myr. The comparison of both cluster formation and star formation is also done to find the correlation between the two processes (Holtzman et al. 1999, Subramaniam 2004). Harris & Zaritsky (2009) (hear after H&Z09) reconstructed the SFH of the LMC and concluded that field and cluster star formation modes are tightly coupled. They found a quiescent epoch from 12 to 5 Gyr ago and star formation peaks at 2 Gyr, 500 Myr, 100 Myr, and 12 Myr. The study of the spatial distribution of cluster as well as star formation are also equally interesting. A study of the distribution of the bar cluster population in the LMC (Bica et al. 1992) has shown that clusters younger than 200 Myr are not homogeneously distributed throughout the bar. In particular, a strong star formation event at 100 Myr was detected in the eastern part of the bar. Using MACHO Cepheids as tracers, Alcock et al. (1999) found that the star formation in the LMC has propagated from southeast (SE) to northwest(NW), along the bar, in the last 100 Myr. Though some studies have found that there is evidence of propagating star formation, the details are not clear. Study of a larger area using homogeneous data is required to obtain the details of any propagating star formation.

The most common method used to constrain the SFH involves a quantitative comparison of observed colour magnitude diagrams (CMD) with synthetic CMDs constructed using theoretical isochrones according to an adopted IMF and input model SFH. H&Z09 performed such a study for the LMC using the MCPS data, where they modelled the complete SFH of the LMC. They used just five time steps to represent the RSFH (6.3 Myr, 12.5 Myr, 25 Myr, 50 Myr, and 100 Myr), with a an interval equal to 0.3 in log(age). The gaps between the steps are large and these large gaps in the RSFH provide insufficient time resolution to identify and study any propagating star formation. If one aims to study the RSFH with a time resolution of 5-10 Myr for ages younger than 100 Myr, then it is more efficient to model only the young stars and not the entire range of stars in a given region. Since large numbers of stars are required in the CMD of a region to model the full range of age, the area required is also large and the spatial resolution is consequently low. To achieve a higher spatial as well as temporal resolution, we adopt a different method. In this method, we estimated the age of the last star formation event (LSFE) in a given region, by identifying the turn-off of the main sequence in the CMD of the corresponding region. The turn-off identified from the luminosity function (LF) of the main sequence represents the LSFE experienced by the region. The reddening in the direction of this

region is also estimated from the turn-off. The spatial map of age of the LSFE is used to help us identify any propagating star formation. We also produce a map of the average reddening in regions studied in the LMC. The spatial and temporal resolutions achieved using this method are both higher than those obtained using the traditional method, as only a small range in age is studied. For the same reason, this method does not assume any age-metallicity relation.

3.2 Data

For the estimation of SFH we make use of two publicly available photometric catalogues produced by the Optical Gravitational Lensing Experiment (OGLE III, Udalski et al. 2008a, Udalski et al. 2008b) and the Magellanic Cloud Photometric Survey (MCPS, Zaritsky et al. 2002, Zaritsky et al. 2004). The OGLE III data is used for the first time in SFH analysis. The total observed area is 40 square degrees, covering 116 LMC regions, each of which covers an area of 35′ x 35′. The catalogue consists of calibrated photometry in V and I passbands of about 35 million stars. Each of the 116 regions are observed using eight chips each with an area of 8.′87 x 17.′74. In this statistical study, each of these were divided into subregions of three different areas. The division goes like 3473 subregions with area 4.′43 x 4.′43, 2291 subregions of area 4.′43 x 8.′87, and 1335 subregions of area 8.′87 x 8.′87. The different sizes for the subregions are chosen, to study how their area, effects the identified turn-off magnitude and thus the estimated age of the LSFE. The MCPS spans a total area of 64 square degrees, and contains about 24 million objects in the LMC. The survey presents photometric as well as extinction maps in U, B, V, and I passbands. In the case of the MCPS, 595 subregions have area in the range, 10.′5 x 30′, 1087 have 10.′5 x 15′, and 1942 have 5.′3 x 15′. For uniformity, we use the V and I photometric data from both the catalogues.

3.3 Methodology

3.3.1 Identifying the main sequence turn-off

We adopted the following method to identify the age of the LSFE from the CMDs. The observed region is divided into several smaller subregions to increase the spatial resolution. The area of the smallest subregion is decided based on the number of main sequence stars in the CMD, that is, it has a minimum of about 600 main sequence stars

in the LMC. For each subregion, (V−I) versus (vs) V CMD is constructed and the main sequence is identified as stars brighter than 21 mag and with a colour index less than 0.5 mag. The turn-off is identified from the main sequence by constructing a LF which involves binning in V magnitude with a bin size of 0.2 mag. The brightest bin in the LF is identified using a statistical cut-off of 2σ significance (minimum five stars in the brightest bin). The cut-off means that the tip of the main sequence should have at least five stars such that it has a variance of $\sqrt{(5)} = 2.2$. Thus, the number of stars identified as the tip of the main sequence is more than twice the variance. This cut-off is chosen to reduce the statistical fluctuation in identifying the main sequence turn-off. Thus, after computing the LF of the main sequence, the brightest bin that has five or more stars is identified as the tip of the main sequence. This condition also implies that, the age of the LSFE identified in a subregion will have a certain threshold star formation rate to form so many stars. On the other hand, star formation events with rates lower than this threshold will not be identified. The above condition would also minimise the chances of identifying blue supergiants as main sequence stars. Since the number of stars in the brightest bin depends on the area used, the age of the LSFE will also depend on the area of the bin considered. Thus we used three sizes to describe the area of the subregions, to map the age of the LSFE. The average V magnitude corresponding to the brightest bin with the required number of stars is taken as the tip of the main sequence. This is considered as the turn-off magnitude V_{to} of the youngest stellar population present in the region.

To convert V_{to} to age, it has to be corrected for extinction, which we estimated from the colour of the turn-off. This colour of the turn-off was in turn identified as the densest point on the main sequence, which appears as a peak in a colour distribution of the stars near the turn-off. In other words, the peak of the distribution of stars with respect to the (V−I) colour near the turn-off can be used to identify the colour of the main sequence. To estimate the peak (V−I) colour of the turn-off, a strip parallel to (V−I) axis with a width 0.5 magnitude is considered (given by V_{to} + 0.5 mag). This strip is binned in colour (with a bin size of 0.1 mag) to study the distribution of stars along the (V−I) colour. This distribution is found to have a unique peak and asymmetric wings. The (V−I) bin corresponding to the peak of the distribution is identified as the location of the main sequence. The average value of the bin corresponding to this peak was taken as the (V−I) colour of the main sequence turn-off. Since we consider the peak of the distribution and not the average, the colour estimated corresponds only to the main sequence stars. As the distribution is found to be asymmetric, the average is likely to be redder than the peak. Since we statistically trace the brightest part of the CMD in a region, this method is not

significantly affected by crowding or incompleteness of the data. The following section describes the method that we used to estimate the reddening and extinction.

3.3.2   Estimation of reddening and turn-off age

We estimated the reddening towards a subregion, from the colour of the turn-off identified from the CMD. The reddening is estimated as the difference between the estimated colour of the turn-off and the expected colour. Hence one needs to know the expected M_v and the $(V-I)_0$. Since we know the distance modulus (DM), by applying an average value of extinction to the observed apparent magnitude we can approximately estimate the M_v, given by

$$M_v = m_v - DM - A_v, \tag{3.1}$$

where m_v is the apparent magnitude. An initial extinction value is needed to calculate the M_v. To begin with, we assumed an extinction of $A_v = 0.55$ (Zaritsky et al. 2004), along with a DM of 18.5, for the LMC. This value of A_v is the average value of the extinction towards the LMC. M_v thus obtained is used to identify the approximate location of the turn-off and its expected colour $(V - I)_0$ from the isochrones of Marigo et al. (2008) for a metallicity of $Z = 0.008$. The difference between the expected colour and the observed colour of the turn-off is defined as the colour excess for a subregion

$$E(V - I) = (V - I) - (V - I)_0 \tag{3.2}$$

Then the actual value of A_v for each subregion is found using the formula (Nikolaev et al. 2004)

$$A_v = 2.48 E(V - I) \tag{3.3}$$

Thus the reddening, E(V−I), and extinction, A_v are estimated for the LMC subregions. The above equations are used to estimate the extinction towards each subregion. Using these estimated values of extinction, the actual magnitude M_v corresponding to the turn-off is estimated for all the subregions. Applying the calculated colour excess and extinction for each subregion, CMDs can be obtained with absolute magnitude, M_v, and dereddened colour, $(V-I)_0$. The CMDs of some sample regions are shown in figure 3.1. The left panel shows the CMD of an LMC subregion using MCPS and the right panel shows the CMD using OGLE III. The red dot on the main sequence shows the location of the identified turn-off. We show various cases here, where we can see broad/tight main sequence turn-offs. For example, we consider the region shown in the top right panel,

which corresponds to the location with mean RA = 79.8^o & Dec = −69.3^o. It covers an area of 4.43′ x 8.87′. The total number of stars is about 6090. The identified apparent turn-off magnitude is 16.5, and the colour index is −0.05. Applying the initial extinction value and DM as described above, the approximate location of the main sequence is identified to have an absolute magnitude of 16.5 − 18.5 − 0.55 = −2.55. The nearest absolute M_v value from the isochrone table is −2.54. The corresponding $(V − I)_0$ value is −0.287. Thus, the reddening towards this region is estimated as $E(V − I) = 0.237$ and a corresponding extinction, $A_v = 0.588$ mag. Correcting the turn-off m_v for extinction using these values, we estimate the main sequence turn-off at $M_v = −2.588$ mag. Converting this turn-off magnitude into an age with the estimated conversion relation, we get $log(age) = 7.41$.

The estimated turn-off M_v is used to estimate the age of the LSFE in each subregion. We estimated an age-M_v relation for the turn-off, using the isochrones of Marigo et al. (2008). The age-M_v relation is obtained for the LMC where the metallicity of the isochrones is chosen to be 0.008. The plots of the log (age) vs M_v is given in figure 3.2. The relation is found to be linear and we have derived a linear relation between the two by fitting a line to the data points. The turn-off ages for the sample regions, estimated using the above relation are also shown in figure 3.1. The identification of main sequence turn-off was found to be ambiguous for turn-offs fainter than 18.0 magnitude. Therefore, we have put a limiting apparent turn-off magnitude of 18.0, which will eventually lead to a higher cut-off for the age of the LSFE, around 120 Myr for the LMC. Therefore, subregions with turn-off magnitudes fainter than 18.0 magnitude are not considered and these locations will appear as gaps in the extinction and LSFE maps.

Since the number of stars in the CMD increases with the area of the subregion considered, the derived turn-off parameters, extinction, and the age of the LSFE will depend on the area considered. To determine the effect of area on the estimated parameters, we derived the extinction and the age of the LSFE for all the three sizes of subregions, in both the data sets and in both the galaxies.

3.4 Results

3.4.1 LMC: Extinction

For all the regions, the estimated colour excess E(V−I) and extinction A_v can be used to create an extinction map of the LMC. The extinction is estimated from the brightest main sequence stars in each region. Figure 3.3 shows the map estimated using the MCPS
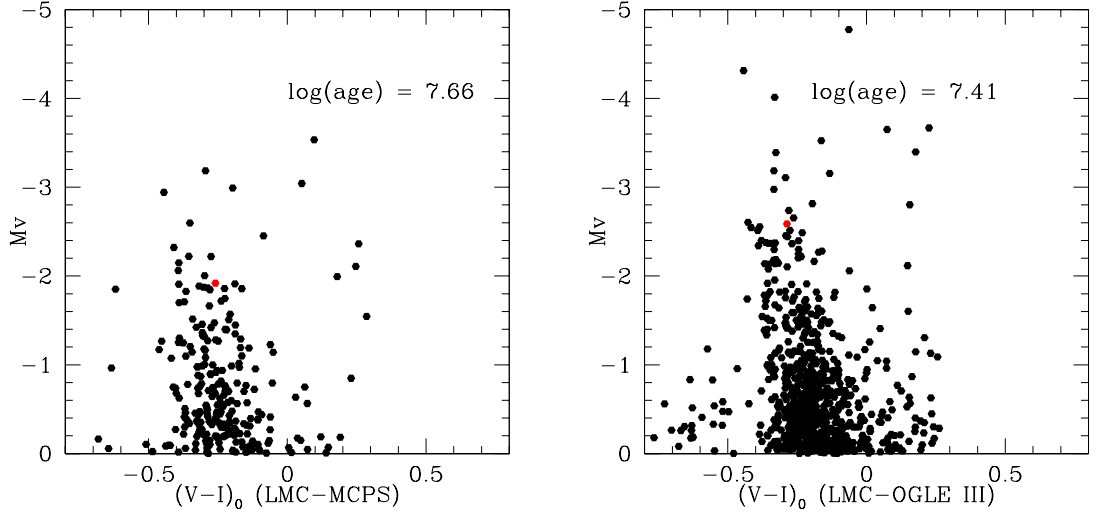
Figure 3.1: M_v vs $(V - I)_0$ CMDs for subregions in the LMC. The figure shows two regions, with left panel using MCPS data and the right using OGLE III data. The red dot marks the turn-off point, and the estimated turn-off age is also shown.

data, and figure 3.4 shows the map estimated using the OGLE III data. Each figure has three panels which show the extinction estimated using area bins as indicated in the figure. Since the estimated extinction would depend on the area used, the corresponding maps are used for the estimation of age of the LSFE.

The extinction map estimated from the MCPS data (figure 3.3) shows that the extinction varies within the range $A_V = 0.2$ - 2.0 mag. Relatively high extinction is seen in the bar region, with the eastern part having higher extinction. A few regions in the north eastern part are also found to have high extinction. These features are seen in all the three plots, which show extinction for different area bins. It can be seen that with the increase in area, the estimated extinction increases. The average value increases from about 0.4 to 0.6 mag, from the maps A to C. The extinction map presented in figure 3.4 is obtained from OGLE III data and has smaller area coverage and higher resolution. The extinction estimated here is also in the range $A_V = 0.2$ - 2.0 mag. These maps show that the bar region has the highest extinction, along with the 30 Doradus region. The northern star forming regions are not covered here. The eastern region is found to have high extinction and this region coincides with the location of massive H I clouds, extending out to the 30 Doradus star forming region. The map A shows that the extinction has a very clumpy distribution with pockets of lower extinction. We also note the increase in extinction with the increase in area in these maps. These maps will be useful for studies related to young stars, since the reddening in the LMC is known to depend on the population studied (Zaritsky et al.
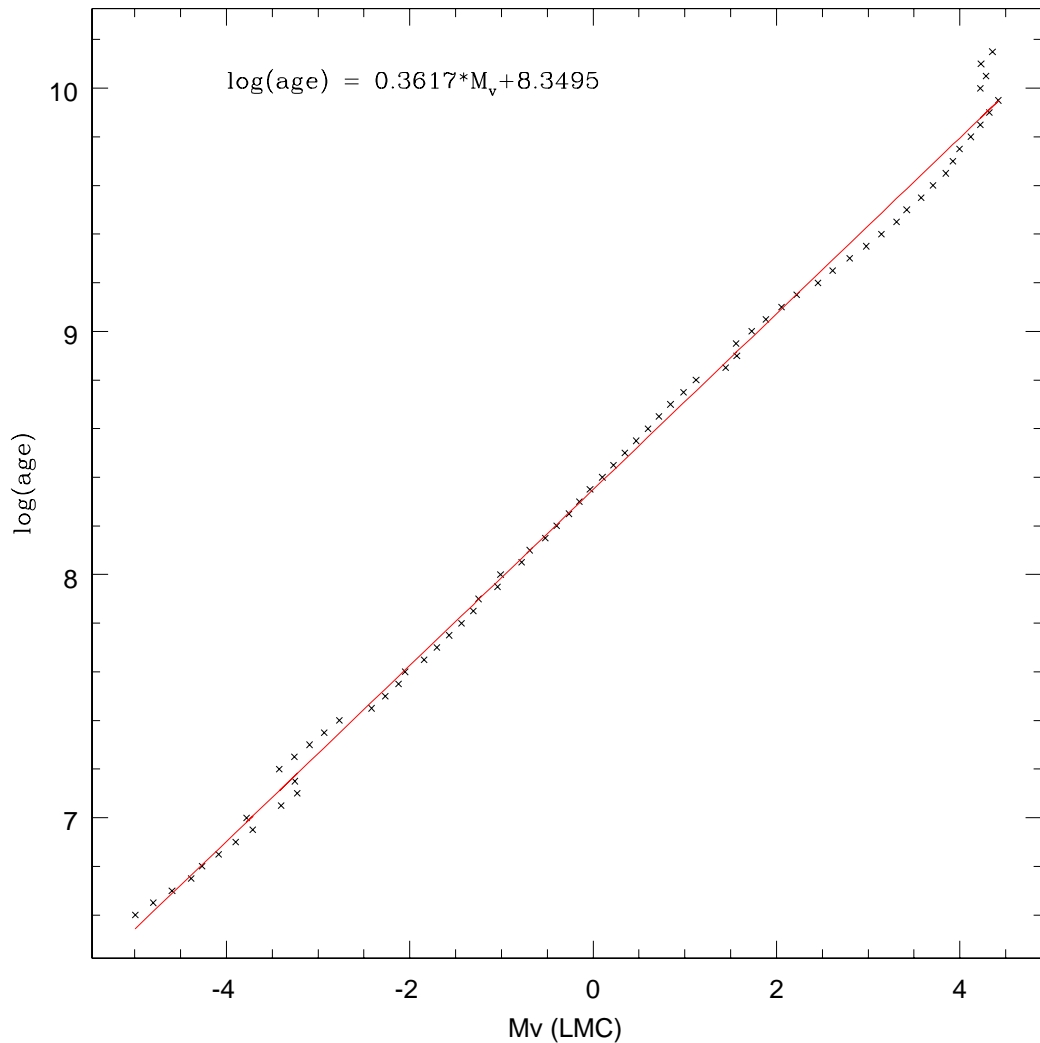
Figure 3.2: The log(age) vs M_v plot for the LMC. The turn-off M_v corresponding to various ages are inferred from Marigo et al. (2008) isochrones. The fitted line is shown in red.

2004).

Zaritsky et al. (2004) published a reddening map of the early-type stars in the LMC derived from the MCPS data using stars with effective temperature from 12000 to 45000K. They presented individual reddenings to stars and hence can be considered as a high resolution map. We compare the reddening distribution derived in this paper with that of Zaritsky et al. (2004). The histograms in figure 3.5 shows the distribution of our extinction values (shown as solid line) and the extinction map provided by Zaritsky et al. (2004)
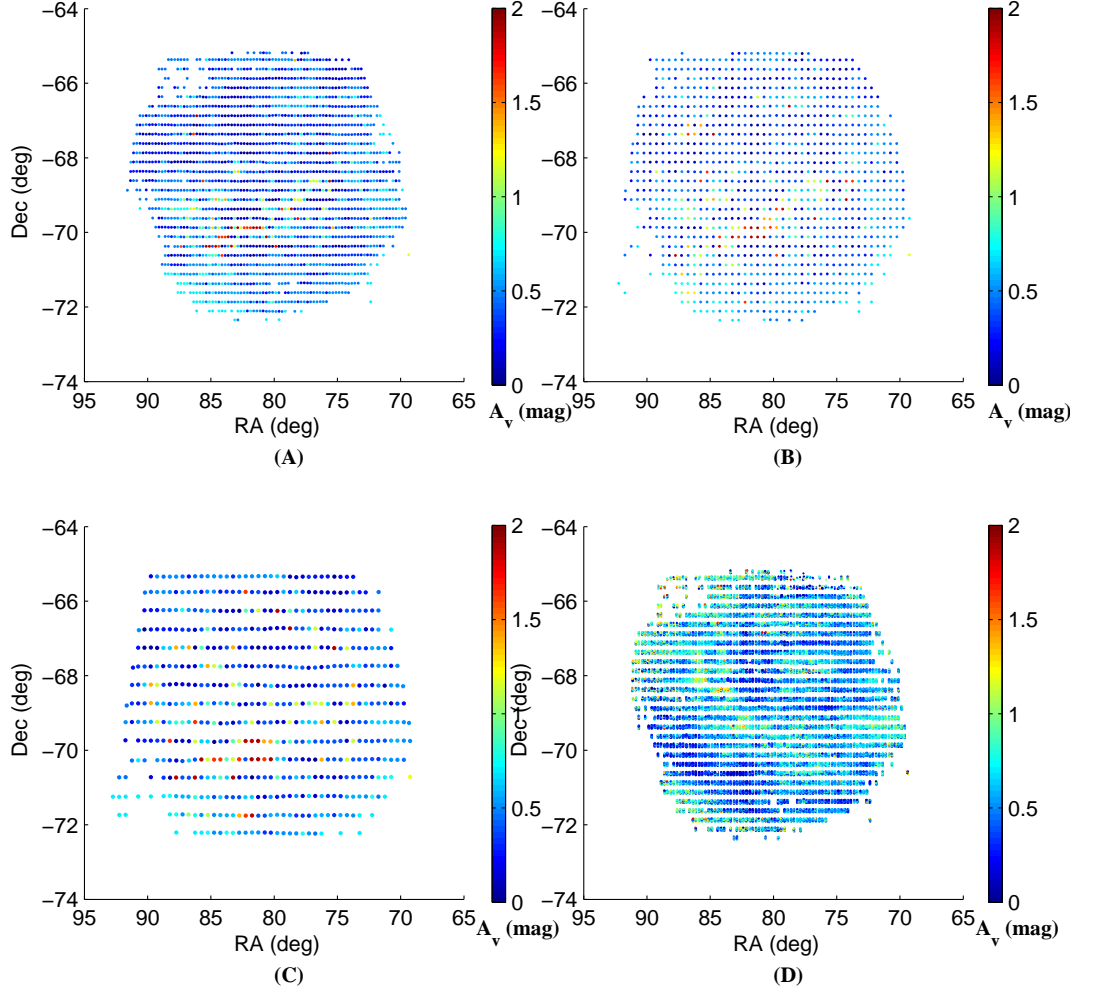
Figure 3.3: The extinction map of the LMC using MCPS data in the RA-Dec plane with three different area binning, A. 5.3 x 15 arcmin^2, B. 10.5 x 15 arcmin^2 & C. 10.5 x 30 arcmin^2. The bottom right panel is the extinction map of Zaritsky et al. (2004), where the regions used in our analysis are selected and shown. Colour coding is according to the A_v value, which varies from 0.2 to 2.0 as shown in the colour bar.

(shown as dashed line). We used the 10.5′ x 15′ area bin for comparison. The distributions are found to be more or less similar. The peaks of both the distributions coincide at $A_v = 0.5$ mag. The reddening estimated here in this study has more regions with less than the peak value. This may be because that we estimate extinction for stars located on the main sequence and ignore stars that are redder than the main sequence. Since we use a bin size of 0.2 mag in colour, the mean of this bin is taken as the colour of the main sequence

62
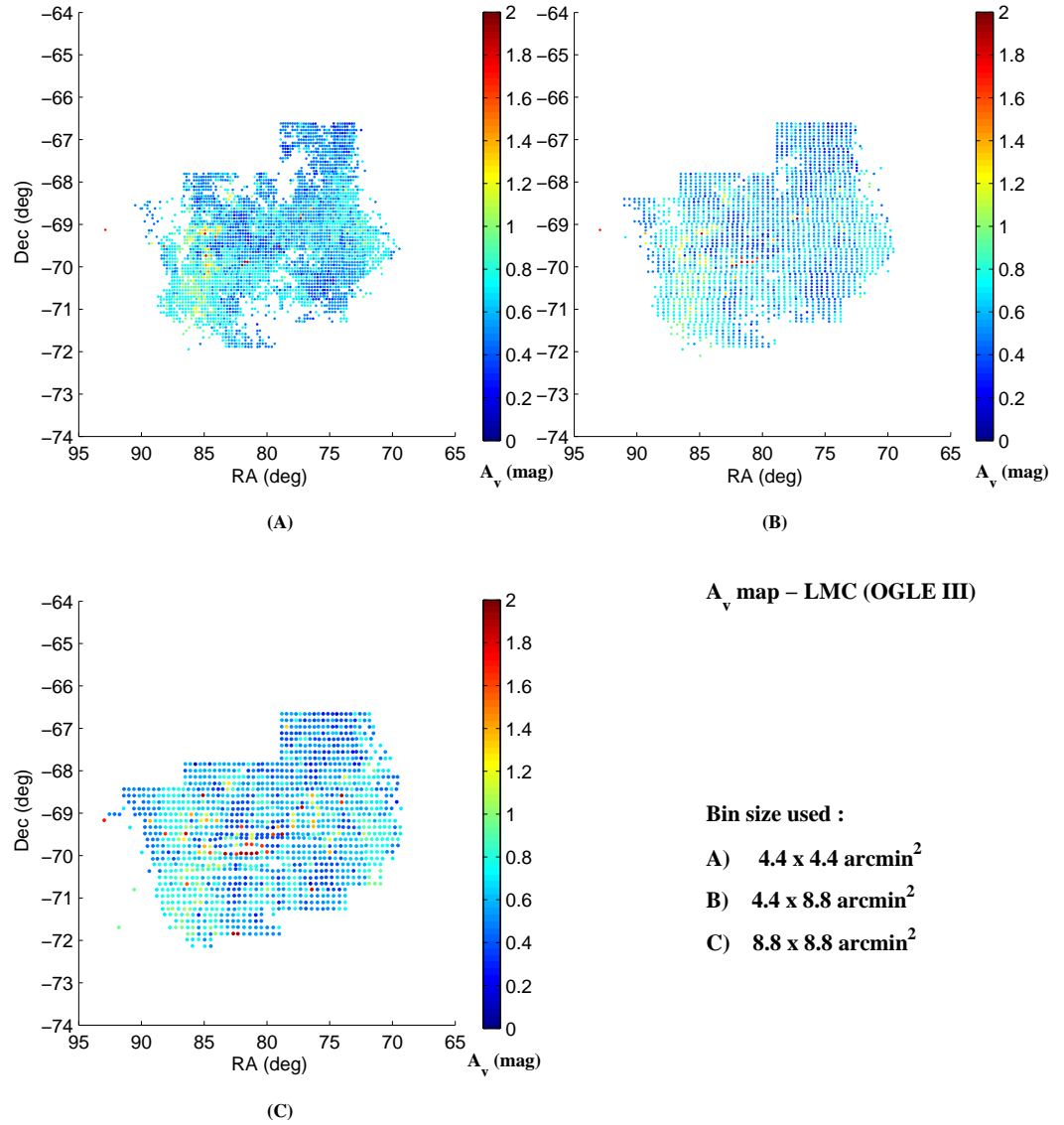
Figure 3.4: The extinction map of the LMC, similar to figure 3.3, using OGLE III data.

and hence could introduce a shift of ±0.1 mag in reddening. This would correspond to a shift of 0.25 in extinction. The variation one notices between the two distributions, as seen in figure 3.5, is of this order. This variation in the extinction measurement can introduce a shift in the estimated age which we account for estimating the error in age estimation (see Appendix A). In figure 3.3 D, we show the extinction map estimated by Zaritsky et al. (2004) for the regions analysed in this study. This map was obtained by
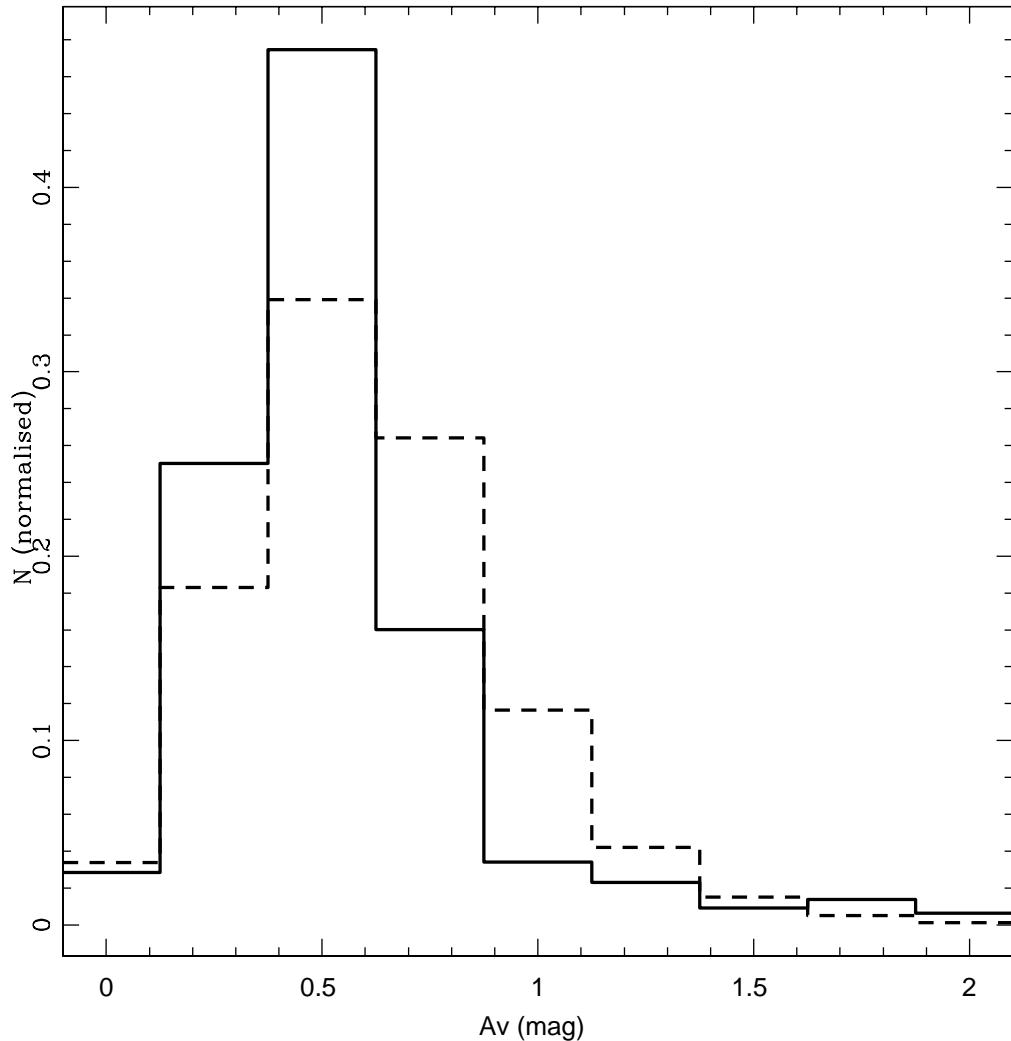
Figure 3.5: The estimated distribution of extinction in the LMC (shown as solid line) is compared with distribution obtained from the extinction map of hot stars provided by Zaritsky et al. (2004) (shown as dashed line, extracted from the fits image from the authors' website).

spatially correlating the Zaritsky et al. (2004) map with our sample of selected regions in the MCPS data. The map includes extinction estimates of all the stars present in a given region. This map can be compared with the MCPS extinction maps derived in this study (shown in figure 3.3a - 3.3c). The maps are more or less comparable. We do not detect isolated high extinction values, probably because we derive extinction values for regions and not individual stars.
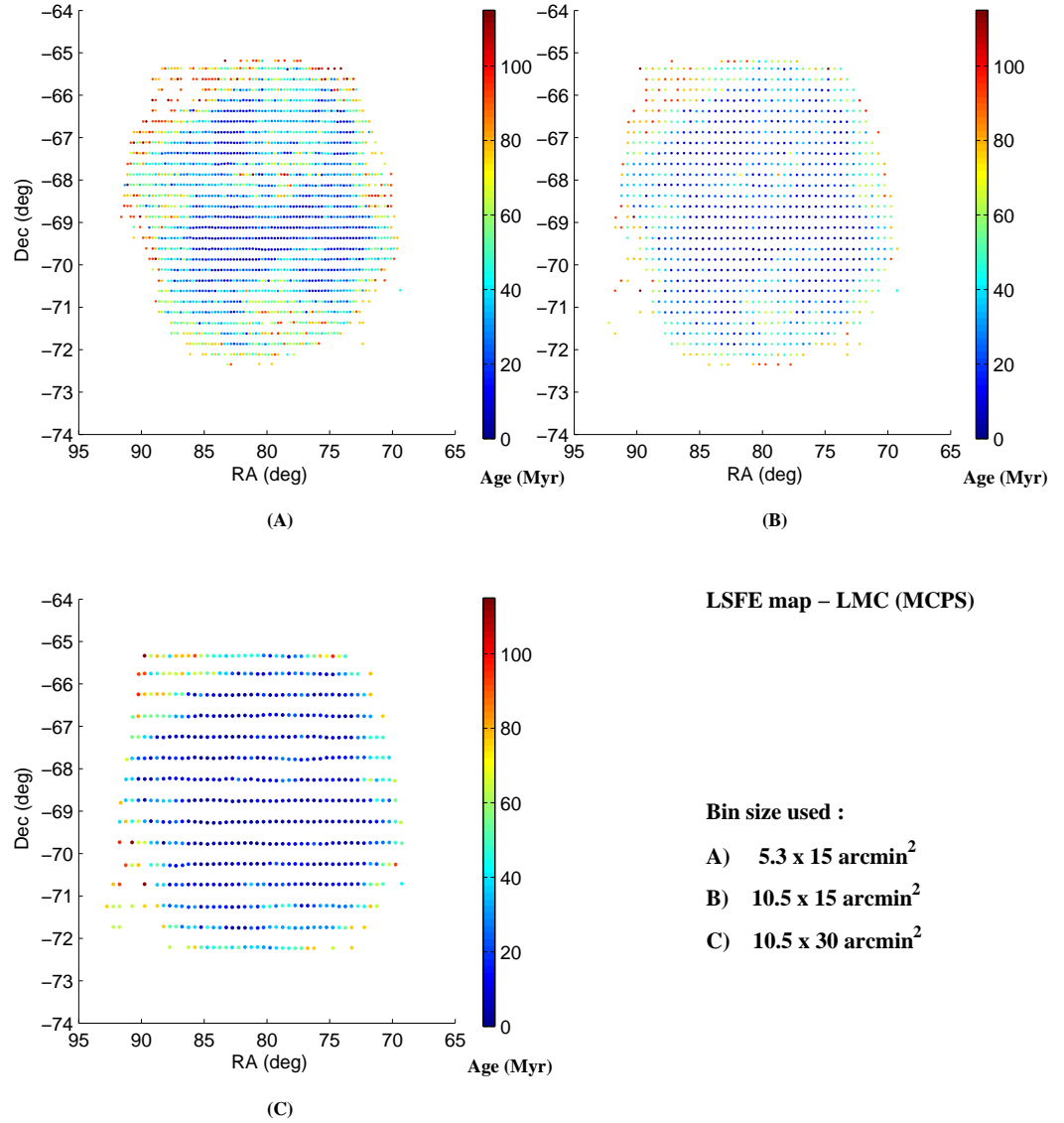
Figure 3.6: The LSFE map of the LMC using MCPS data, in the RA-Dec plane with three different area binning, as specified in the figure. Colour coding is according to the LSFE age as shown in the colour bar.

3.4.2 LMC: Distribution of age of the LSFE

We estimated the age of the LSFE across the LMC for subregions of three different sizes. The distribution of age of the LSFE can be used to study the quenching as well as the propagation of star formation in the central regions of the LMC. The maps of the age

65
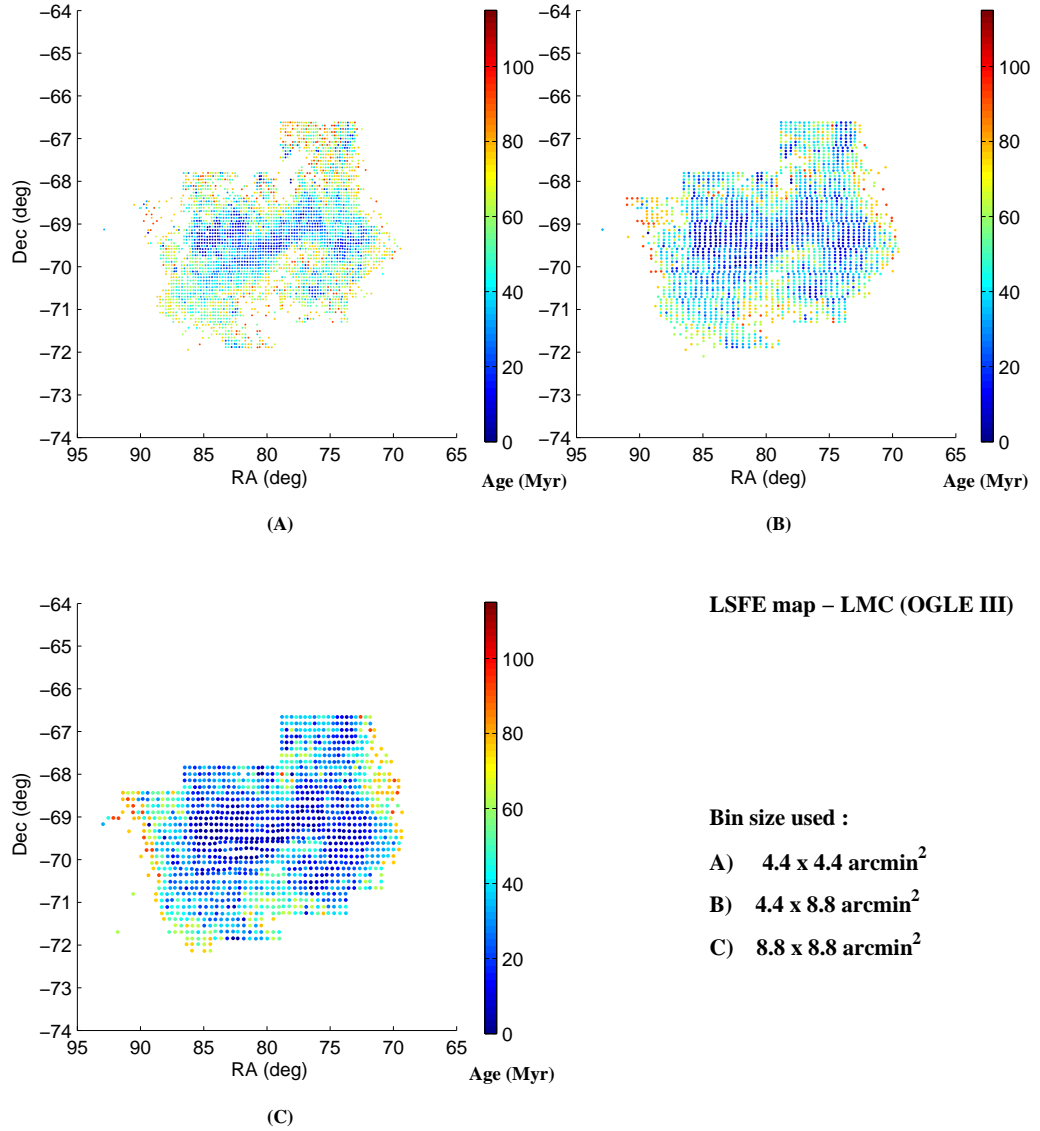
Figure 3.7: The LSFE map of the LMC, similar to figure 3.6, using OGLE III data.

of the LSFE derived from the MCPS and the OGLE III data are shown in figures 3.6 and
3.7, respectively.

Figure 3.6 shows that the age of the LSFE is within the range 0-120 Myr. The figure
shows maps for three different area bins as indicated. When we inspect the high resolution
map A, we can see that it is a clumpy distribution with many central pockets of very young
age, as suggested by the dark blue colour points. The youngest ages are found in the bar
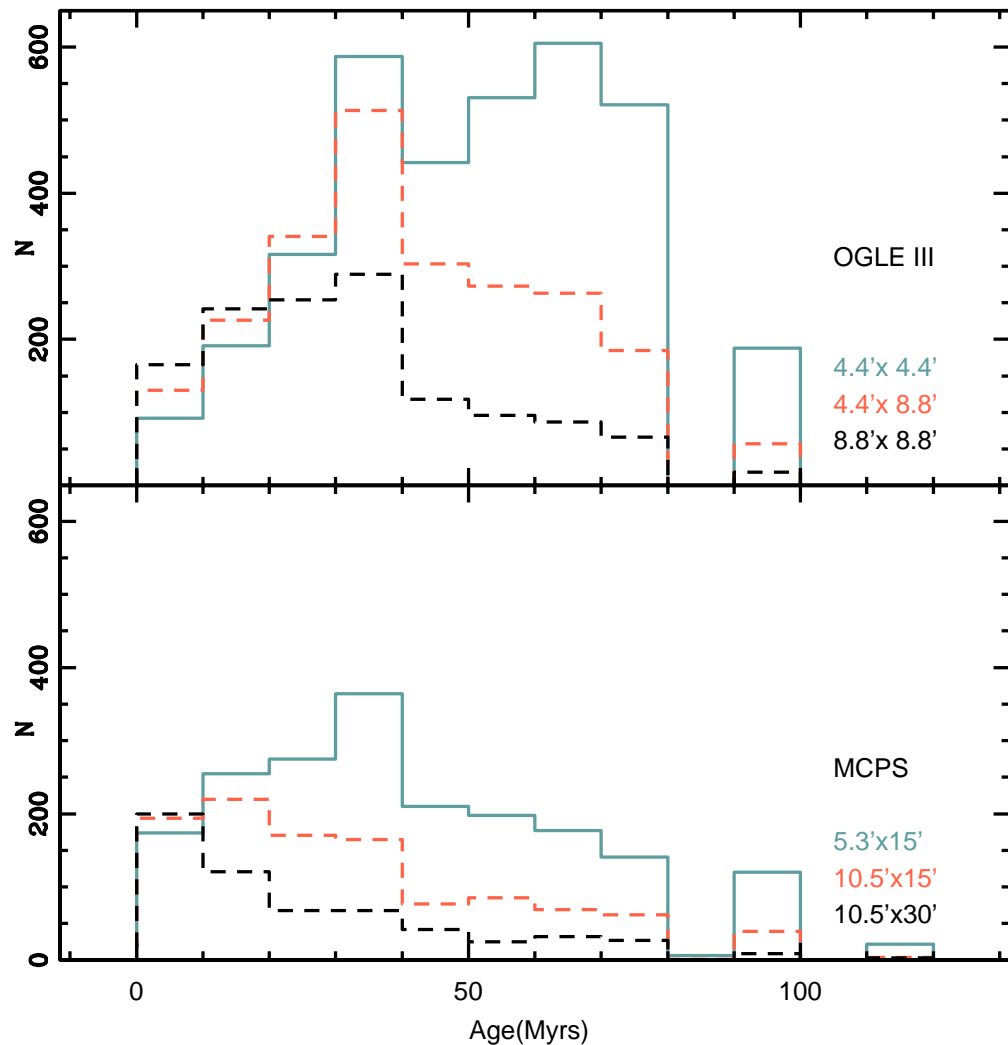
Figure 3.8: The statistical distribution of LSFE ages of the LMC. Upper panel shows OGLE III data and lower panel shows MCPS data, with the three colours corresponding to different area, as specified in the figure.

region, near the 30 Doradus and the northern regions. The locations are similar to the regions identified by H&Z09, such as the blue arm, constellation III, and 30 Doradus. These young pockets are surrounded by regions of older star formation. We can also see that the age of the LSFE is found to progressively increase as we go towards the outer regions. We also see a couple of small pockets of older star formation in the inner regions. The map also identifies the northwestern void. On the whole, the inner regions have ages of the range 0 - 40 Myr, whereas regions towards the periphery have ages in the range 60
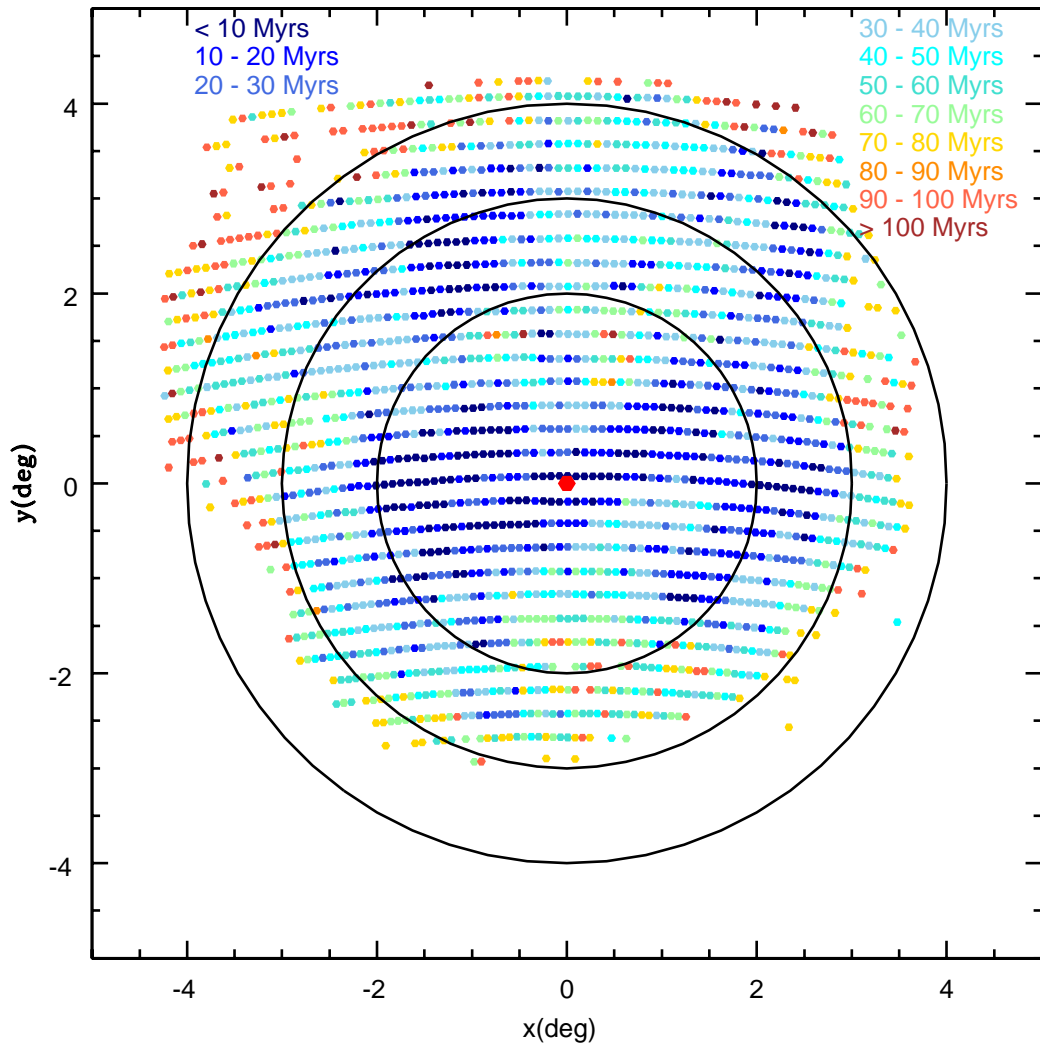
Figure 3.9: The LSFE map of the LMC (same as A in figure 3.6) in the projected x - y plane of the sky. Three concentric rings of radii 2°, 3°, and 4° are over plotted.The red dot at (0,0) is the optical center of the LMC.

- 100 Myr. The age map for larger area bins are shown in B and C. These maps identifies lesser details, when compared to the map A. The clumps seen in map A disappear in maps B and C. As mentioned earlier, the age limit of the technique is about 120 Myr and we did not consider regions that have an older turn-off. These regions are expected to appear as gaps in the map. It can be seen that these gaps do not appear in the inner regions, but do appear towards the periphery. In the case of map A, the outer regions are missing for the above reason. If we inspect maps B and C, we can see that more and more outer regions

are covered in these maps. This is because the outer regions have older turn-offs and their ages become younger when the area becomes larger. The point to be noted is that most of the regions in the inner 3° have experienced star formation in the last 100 Myr. Another result derived from these maps is that the age of the LSFE gets older with radius. The average age is around 20 Myr in the central regions, whereas it is about 80 Myr near the periphery. These values are found to be more or less similar for all the three area bins.

Figure 3.7 shows the age map of the LSFE as estimated from the OGLE III data. Map A has the highest spatial resolution and shows a clumpy distribution of ages. The central region, which includes the bar region and the 30 Doradus region, are found to have young ages. These sites have continued to form stars until quite recently. As we found in the MCPS map, we see that the star forming regions have shrunk to increasingly smaller pockets with time, where the star formation still continues. These pockets corresponds to the bar region and the 30 Doradus region. The spiral-type pattern one could see in the western side of the bar in figure 3.6, is found to break into smaller multiple regions with star formation. Since the OGLE III has lesser coverage of the north, we are unable to study the northern star forming regions. We see a gradual increase in the age of the LSFE towards the outer regions. The maps B and C are obtained with larger area bins and we can see that the details disappear in these plots. On the whole, we find that the central regions have an average age of the LSFE of ~ 20 Myr, whereas in the periphery the average age is about 80 Myr. This is similar to what was found in the MCPS maps. Since the OGLE III maps have the highest spatial resolution, we tried to identify any propagating star formation in the bar region. We do not detect any propagation along the bar. All along the bar, from the NW end to the SE end, we detect pockets of very young stars, as young as ≤ 10 Myr. These pockets are surrounded by slightly older stars (~ 20 Myr), as seen in map A. The medium resolution map, B also shows that young stars are distributed right across the bar suggesting the star formation has been active all along the bar in small pockets. Map A has missing regions towards the periphery which means that in these regions the age of the LSFE is older than 120 Myr. As for figure 3.6, maps B and C cover more of the outer regions, owing to their larger bin areas.

The maps obtained from both the data sets suggest that the inner regions have continued to form stars up to ≤ 10 Myr, whereas the outer regions stopped forming stars earlier (~ 80 Myr). This suggests that there has been an inward quenching of star formation. The outer regions are older with an age of about 80 Myr, implying that the star formation stopped at around this age. The younger ages of the LSFE for the inner regions suggest that the star formation has stopped relatively recently or is still continuing. The younger

LSFE regions located in the inner regions have a clumpy distribution which suggests that the star formation has broken up into smaller pockets. Around these pockets, one can see a gradation in the age with relatively older stars being located in the periphery. To summarise, the age maps suggest an outside-to-inside quenching of star formation in the inner 3° of the LMC, in the age range 80 - 1 Myr, with the inner regions experiencing star formation until very recently. Even though three maps correspond to three different area bins and hence the estimated age of the LSFE differ slightly, the above result is seen in all the maps, with varying details.

The statistical distribution of the age of the LSFE in the LMC is shown in figure 3.8. The histograms in three colours represent the distribution of ages derived with three different area bins as shown in the figure. In both the distributions obtained using OGLE III and MCPS (upper and lower panels in the figure), it is seen that as we go to higher and higher spatial resolution, the peaks of the distribution tends to shift towards older ages. This can be explained in terms of the number of stars present in a subregion of a particular area. As we create finer bins, the number of stars in the main sequence of the CMD becomes increasingly smaller, producing in turn an older main sequence turn-off. In the case of OGLE III, the age of the LSFE peaks at 60 - 70 Myr and 30 - 40 Myr, for small area bins. In the case of large area bins, the peak is found only at 30 - 40 Myr. The time at which the largest number of regions stopped forming stars (30 - 40 Myr) is similar for all the three area bins. Since OGLE III scans do not cover the northern star forming regions, the above distribution is applicable to the central regions, including the bar. Thus, we might conclude that most of the central regions stopped forming stars at about 30 - 40 Myr. All the area bins also show an isolated peak at 90 - 100 Myr. This peak is also found in the MCPS distribution for all the area bins. This peak may be similar to the 100 Myr star formation peak identified by H&Z09.

For the MCPS data, we see that the smallest area bin shows a peak at 30 - 40 Myr, whereas the largest area bin shows a peak at 0 - 10 Myr. We can clearly see the progressive shifting of the peak to younger ages with the increase in the area binned. The medium resolution map shows that the peak is in the range 0 - 40 Myr. Thus, our analysis of MCPS data which have a larger area coverage finds that the star formation stopped at 0 - 10 Myr for most of the regions. Thus, the influence of the northern regions is to make the peak shift to younger ages, suggesting that the star formation in the northern regions continued to younger ages, than in the central regions. Thus, we find a peak of star formation at 0 - 10 Myr, as for the 12 Myr star formation peak found by H&Z09, for the MCPS data. The peaks of star formation identified here coincide with those found by H&Z09, even though

the methods used are different. The above finding also suggests that the ages derived by this method are comparable to those derived by them.

Among the maps presented above, the OGLE III maps help us to understand the finer details of star formation in the central regions, because of the higher spatial resolution (with OGLE III we obtain the smallest area for subregions). The MCPS maps cover a larger area, in particular, for the northern regions. It can be seen that there are a number of star forming regions in the north of the LMC, but there are very few in the southern LMC. About the optical center at RA = $5^h 19^m 38^s$; Dec = -69°27"5.2' (J2000.0 de Vaucouleurs & Freeman 1972), one can discern a lopsidedness in the recent star formation towards the northern regions. That is, the quenching of star formation is asymmetric with respect to the center of the LMC. The quenching appears to have been more effective in the southern LMC, than in the northern part. To substantiate this finding, we plot the LSFE age map (the high resolution map (A) in figure 3.6) in the xy plane using the optical center to convert the RA-Dec to x-y coordinates (figure 3.9). We also show concentric circles with radii of 2°, 3°, and 4° with respect to the center. In the southern regions, it can be seen that older ages are contained within the inner circles, between radii 2° and 3°. In the northern regions, older star forming regions appear only in the outermost annulus and outside 4°. This map clearly shows the lopsidedness and the extension of the younger star forming regions to the north and the northeast (NE). The map also suggests that the southern regions are more or less symmetric with respect to the center. This result is consistent with the presence of star forming regions such as LMC1, LMC5, LMC4, and the Super Giant Shells (SGS) in the north, and 30 Doradus in the NE, whereas similar regions are not found in the southern LMC. The map presented above is in the sky plane and needs to be deprojected onto the LMC plane, to help enhance any lopsidedness. That is, in order to understand these features, one needs to study their location in the plane of the LMC and not in the sky plane. We describe this approach in the following section.

Deprojection of data onto the LMC plane

To study the lopsidedness of the age distribution, we need to deproject the data to obtain the distribution in the plane of the LMC. The LMC plane is inclined with respect to the sky plane by an angle i (the face-on view corresponds to $i = 0$) and the PA of the LON (measured counter-clockwise from the north) is θ. Here we use the new system x″ - y″ in which the LON lie at the same angle in the (x″, y″) plane of the LMC, as in the projected (x,y) plane of the sky. The method is described in detail in the section 2.2.2. The coordinates are in kpc, where 1° is equal to ~0.89 kpc at the distance of the LMC.
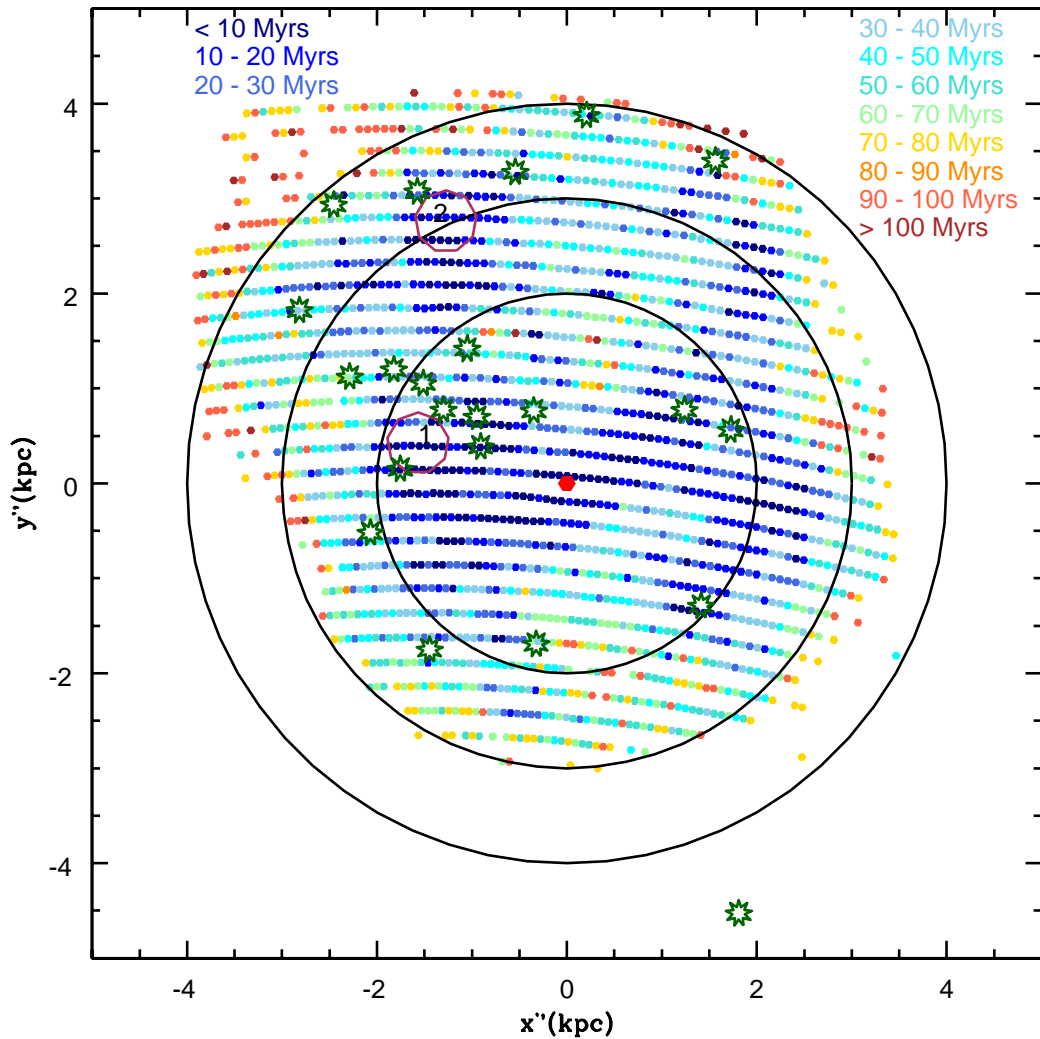
Figure 3.10: The LSFE map of the LMC which is similar to figure 3.9, in the deprojected x″ - y″ plane of the LMC, where concentric circles are drawn with radii 2 kpc, 3 kpc and 4 kpc centered on the optical center as in figure 3.9. The relevant features identified in the LMC plane are shown as hexagons. The numbering is decoded as 1. 30 Doradus, 2. Constellation III (Meaburn 1980), The dark green points are the H I SGS (Kim et al. 1999).

The deprojected MCPS map is shown in figure 3.10, where concentric circles of radii 2 kpc, 3 kpc and 4 kpc are also shown to compare the distribution with figure 3.9. This map also shows the lopsidedness, suggesting an extension in the north and northeastern directions. If we consider regions in which star formation stopped around 40 Myr or

younger, the location of such regions gives an impression that the star formation is being stretched in the northeast-southwest direction, with more such regions located in the NE, with respect to the LMC center. Thus, in the plane of the LMC, the recent star formation has a lopsidedness towards the north and NE, which was also detected less clearly in earlier maps. The direction in which the distribution appears to be stretched is in the direction of our Galaxy. van der Marel & Cioni (2001) found an elongation in the outer stellar distribution of the LMC disk, when viewed in the LMC plane. This elongation of the recent star forming regions is also in the similar direction. We compared this lopsidedness with the distribution of H I gas in the following section.

Comparison with H I clouds and star clusters

The results obtained above suggest that the recent star formation in the LMC has a lopsidedness in the north and NE direction. One would also then expect to see a similar lopsidedness in the distribution of the H I clouds in the LMC plane. We have plotted the H I clouds using the data from Kim et al. (2007) in the LMC plane in figure 3.11. The colour code used is according to the mass of the cloud, as indicated in the figure. Concentric circles at 2 kpc, 3 kpc, 4 kpc, and 5 kpc are also shown. The deprojected H I distribution is seen to be lopsided with respect to the center. Most of the clouds are located to the north of the center, with very few clouds in the south. The clouds are located within a radius of 3 kpc in the south, while their distributions extend outside a radius of 5 kpc in the north. The massive H I clouds are also preferentially populated in the north compared to the south. Thus, the distribution of the H I clouds show lopsidedness towards the north. The age maps and the H I distribution correlate well with each other and point to an extension of the LMC disk towards the north with respect to the optical center. On the other hand, the recent star formation also shows a NE extension. This might suggest that the star formation is more efficient in the north as well as the NE in converting gas to stars.

The spatial distribution of young clusters (age <120 Myr) in the LMC plane is shown in figure 3.12. The optical center is shown along with concentric rings at radii 2 kpc, 3 kpc, and 4 kpc. The cluster distribution is also found to be lopsided. The clusters in the age range 60 - 100 Myr are distributed out to 3 kpc in the south, whereas they can be seen out to 4 kpc and slightly beyond in the north. The clusters in the above age range show lopsidedness towards north. The distribution of clusters younger than 40 Myr is found to shrink within inner regions and are concentrated at the ends of the bar and in the northern regions. We can also see a large concentration of clusters in the NE. Thus
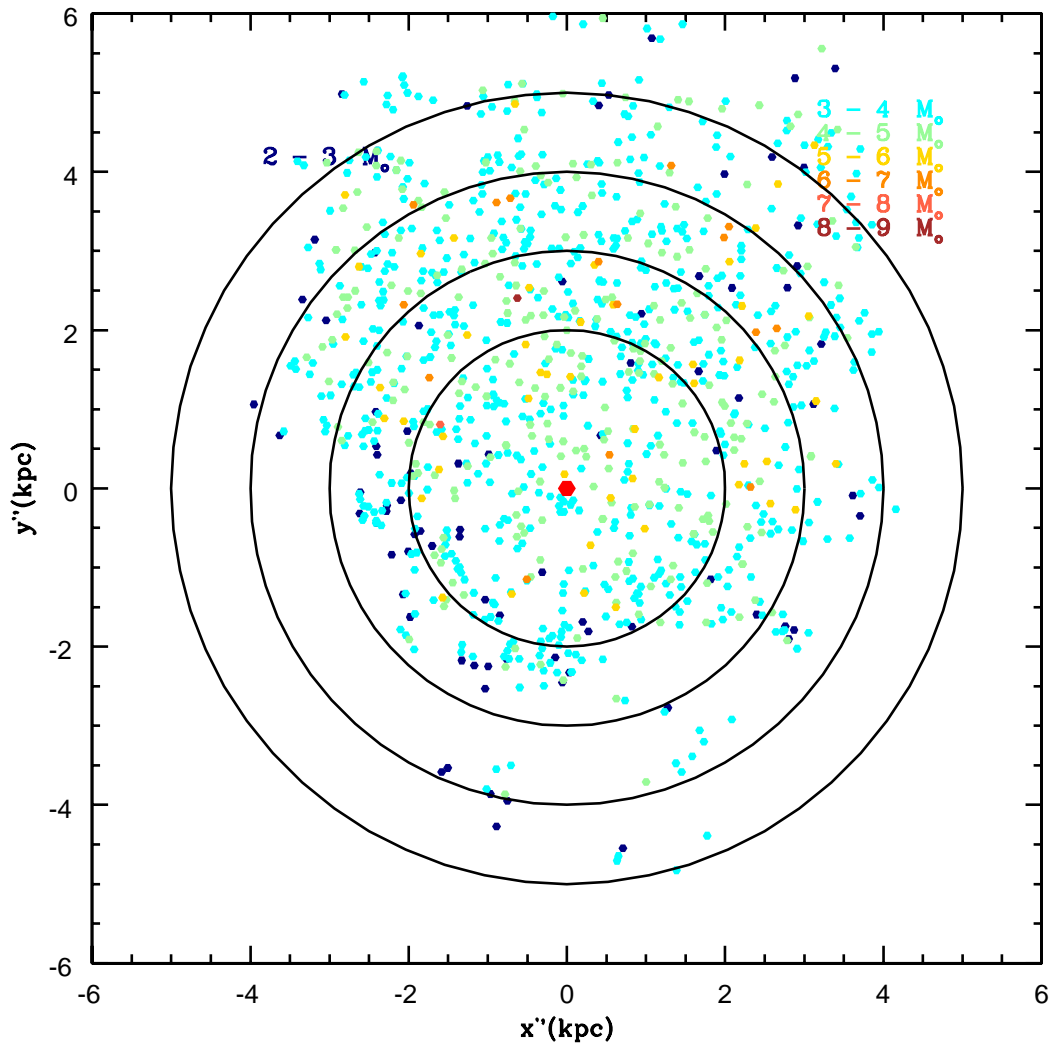
Figure 3.11: Map of H I clouds in the LMC plotted in x''-y'' plane. Colour coding is according to the mass in log scale, as specified in the figure. Data is from Kim et al. (2007). The LMC optical center is shown as a red point. Concentric rings are over plotted at radii 2 kpc, 3 kpc, 4 kpc, and 5 kpc.

the young (≤ 40 Myr) clusters seem to accumulate in the NE-north direction, except for a small group in the southwest (SW) of the bar, probably owing to the presence of the bar. We conclude that clusters in the age range 60 - 100 Myr show lopsidedness towards the north, whereas clusters younger than 40 Myr show lopsidedness towards north and NE. This might suggest that the NE enhancement in the star formation is likely to have happened in the last 40 Myr, whereas the northern enhancement has been visible for the
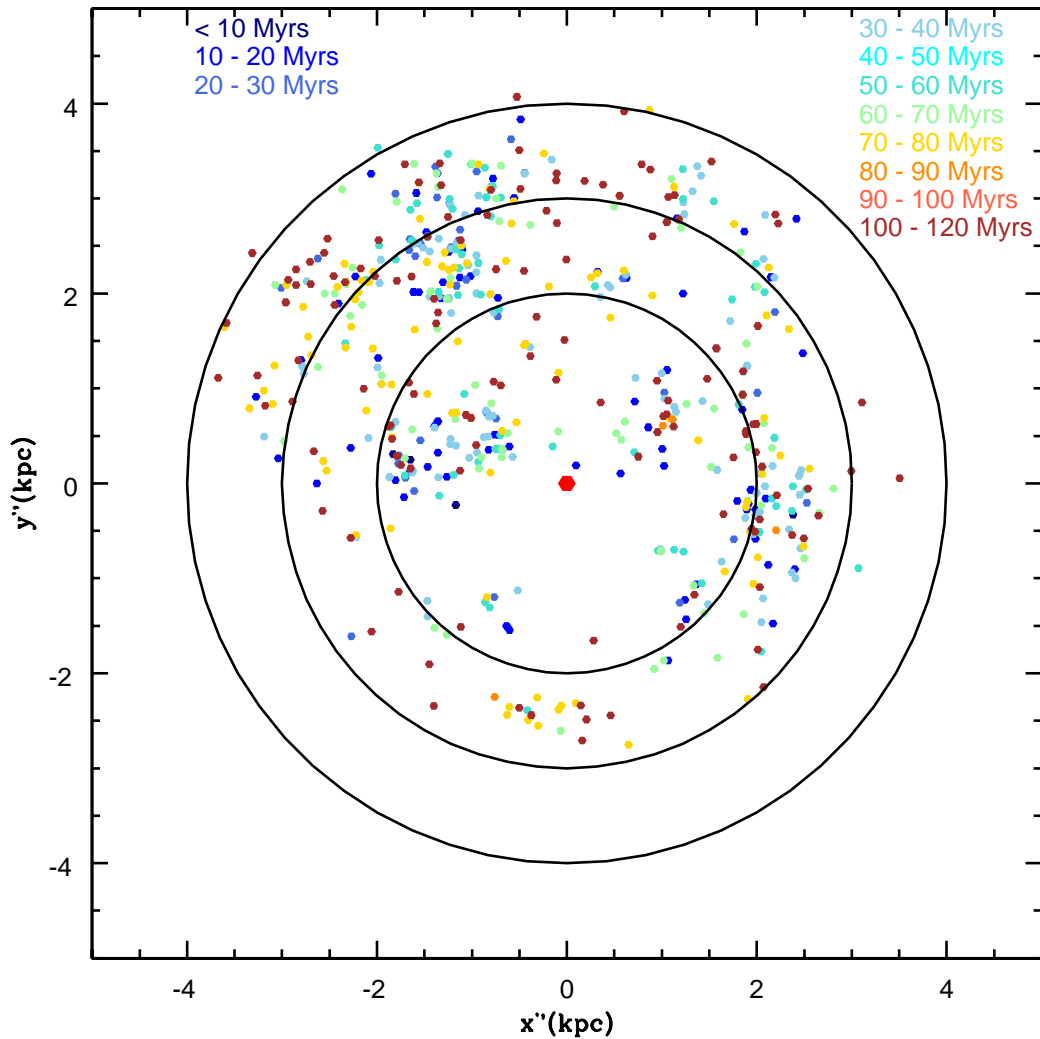
Figure 3.12: The spatial distribution of young clusters (< 120 Myr) from Glatt et al. (2010) is plotted in the deprojected plane of the LMC. Colour coding is according to cluster age as specified in the figure. The red dot is the optical center of the LMC. Concentric rings are drawn at radii 2 kpc, 3 kpc, and 4 kpc.

last 100 Myr.

To compare the ages of LSFE estimated here with the ages of clusters, we have plotted clusters in three age groups in figure 3.13. The LSFE age map only shows the age of the last star formation event and does not suggest anything about previous star formation episodes in the region. Therefore, while comparing with the cluster ages, we expect the ages of the youngest clusters in a given region to closely match the LSFE ages. In the

figure, clusters younger than 40 Myr are shown in the top-left panel. We see a good correlation between the locations of clusters and subregions in this age range such that clusters are located near subregions with similar ages. This also suggests that the ages estimated for the subregions are similar to the ages of the youngest clusters in the vicinity. We also note that there are some regions in the bar that have been forming stars until quite recently, but that there is no cluster formation in these regions. The plot on the top-right panel shows clusters in the range 40 - 70 Myr, and these clusters are distributed as for the younger clusters. We do not see any correlation as most of these clusters are located in regions that have continued to form stars and younger star clusters. In a few regions in the NW, east, and south, we see similar ages for cluster and the nearby subregions. The bottom-left panel shows the distribution of clusters in the age range 70 - 120 Myr. These clusters are distributed within a comparatively larger radius, than the young clusters. The ages of these clusters closely match the ages of the subregions in the outer regions of the map. Thus, we find that the age distribution of the LSFE closely agrees with the age distribution of the clusters. The cluster distribution also suggests the star forming regions have shrunk to smaller pockets in the inner LMC, in the last 100 Myr.

3.4.3   Shift in the center of the young stellar distribution

The LSFE age maps suggest that the young star forming regions are found to be lopsided to the north and NE. The distribution of young clusters as shown in figure 3.12 suggested that the clusters younger than about 40 Myr show a preferential location to the north and NE. The H I distribution suggests that most of the gas is located in the northern LMC disk. Thus, the center of recent star formation seems to have shifted to either the north or the NE, with respect to the optical center. To study this shift in the distribution of the young population as a function of age, we used the MCPS data. Since the number of clusters in a given age range is small, the estimation of the positions of the centroids was not done with clusters.

We used main sequence star counts to estimate the distribution of stars younger than a particular age using the MCPS data. In the main sequence, stars brighter than a cut-off magnitude are identified. These stars are younger than the age corresponding to the cut-off magnitude. The center of the distribution of these stars are estimated in the sky plane (RA vs Dec plane), as well as the LMC plane (x" vs y" plane). The age tagged with such a population is the age of the oldest population in the group, even though there are stars younger than this age in that group. Table 3.1 contains the age of the oldest population of the group, centers in RA & Dec, and x" & y", the number of stars considered for the
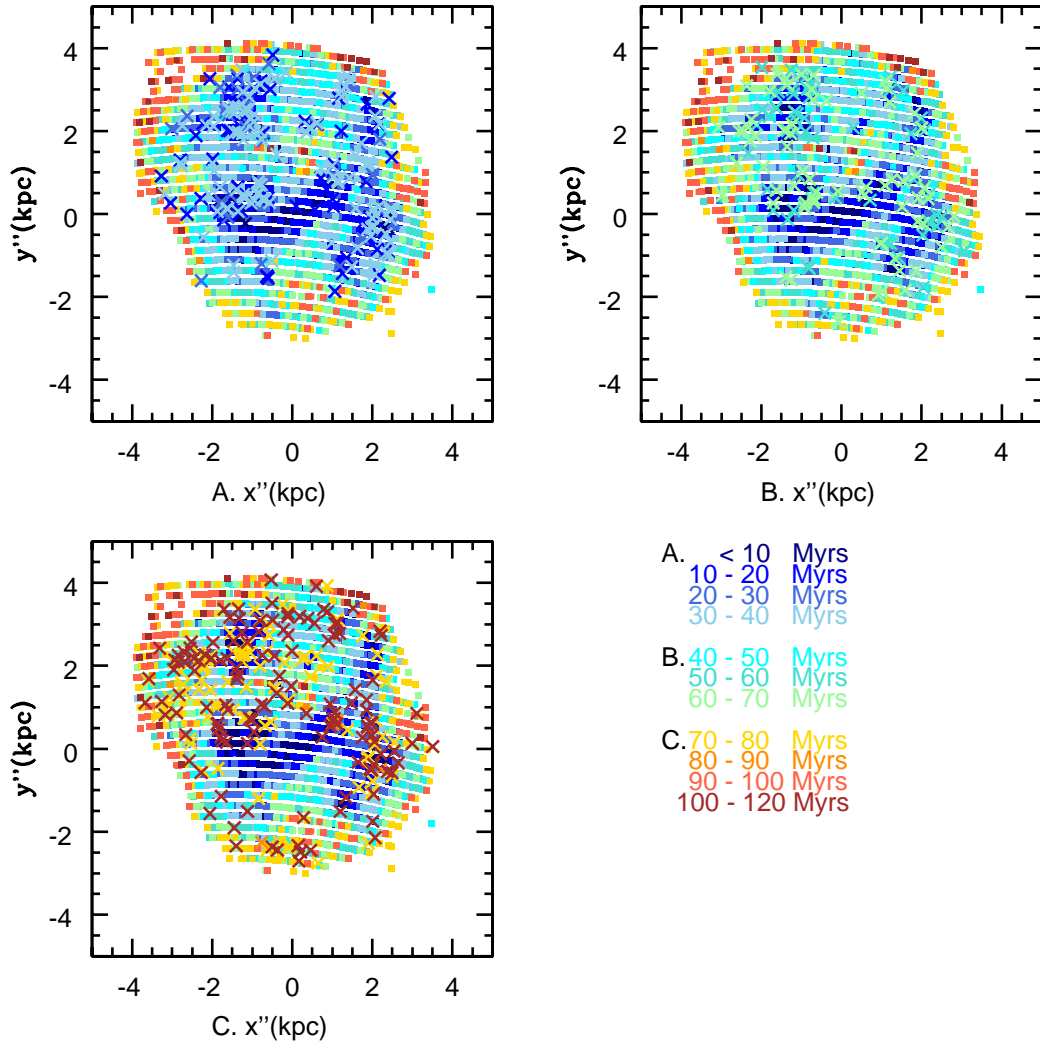
Figure 3.13: The age distribution of young clusters (from Glatt et al. 2010) are over plotted on the LSFE map of the LMC in the deprojected x''-y'' plane. Three different age groups are shown, top left, ≤ 40 Myr, top right, 40 - 70 Myr and bottom left, 70 - 120 Myr. Colour coding is according to the age as specified in the figure.

center estimation and the error in the values of the center. Both x'' & y'' are in kpc where 1° is equal to 0.89 kpc at the distance of the LMC. The centers of stellar population in the LMC plane, for various ages, are shown in figure 3.14. The optical center (OC) and the kinematic center of the gas (KC, taken from Kim et al. 1998) are also shown. The oldest population considered has an age of 500 Myr and the youngest is about 10 Myr. The center of the distribution does not shift in the interval 500 - 200 Myr, even though a small

Table 3.1: The centers of the stellar population in the LMC for various ages, using MCPS data.

Age (Myr)	RA(deg)	Dec (deg)	x'' (kpc)	$\sigma x''$	y'' (kpc)	$\sigma y''$	N#
8	80.5303	-68.5728	-0.2598	-0.0137	0.8000	0.0160	13327
18	80.4294	-68.6190	-0.2218	-0.0080	0.7584	0.0094	36536
40	80.3217	-68.7290	-0.1756	-0.0046	0.6505	0.0052	107243
60	80.3163	-68.8027	-0.1666	-0.0034	0.5780	0.0038	192619
93	80.3297	-68.8768	-0.1632	-0.0025	0.5051	0.0027	353207
214	80.3542	-68.9608	-0.1589	-0.0014	0.4184	0.0015	1141153
493	80.3146	-68.9201	-0.1451	-0.0009	0.4470	0.0010	3151134

shift towards the south can be noticed. The shift in 200 - 40 Myr is clearly visible along the y" axis, towards the north. We detect a shift of 7 pc/10 Myr towards the north during the interval 200 - 100 Myr, while an enhanced shift of 27 pc/10 Myr towards the north is detected in the 100 - 40 Myr age range. On the other hand, no significant shift is present along the x" axis (EW axis) in the above age range. For populations younger than 40 Myr, a shift along both the axes can be noticed suggesting that the center is progressively shifting in the NE direction. In the 40 - 10 Myr age range, a shift of 50 pc/10 Myr to the north and 28 pc/10 Myr to the east are detected. This analysis suggests that the northern lopsidedness in the stellar distribution started between 200 - 100 Myr. This can be compared to the appearance of the northern blue arm in the age range 160 - 100 Myr in the SFH by H&Z09, which could shift the center of the stellar distribution to the north. To summarise, we find that the center of the distribution of stars shifts northward in the age range 200 - 40 Myr, and that the center is found to shift in the NE direction for populations younger than 40 Myr. This correlates well with the age vs shift found in the cluster distribution. Thus, the stellar population as well as the cluster population has experienced a shift in the NE direction in the last 40 Myr only. H&Z09 also finds enhanced star formation in the northeastern regions for ages < 50 Myr, which can be inferred from their figure 3.8.

The line of interaction between the MW and the LMC is shown in figure 3.14. According to our convention, this line is at a PA of 26° (shown in black), whereas the direction given in van der Marel (2001) is 42° (shown in green). This is the direction towards the Galactic center. The direction of the velocity vector of the LMC is shown in red, at a PA of 72°. It can be seen that the direction of the shift of the center is almost in the direction towards the Galactic center. The LMC disk is known to be inclined such that the NE part is closer to the Galaxy. The lopsidedness in the star formation is in the same direction as the inclination. In addition, the LMC is moving past our Galaxy after its closest approach.
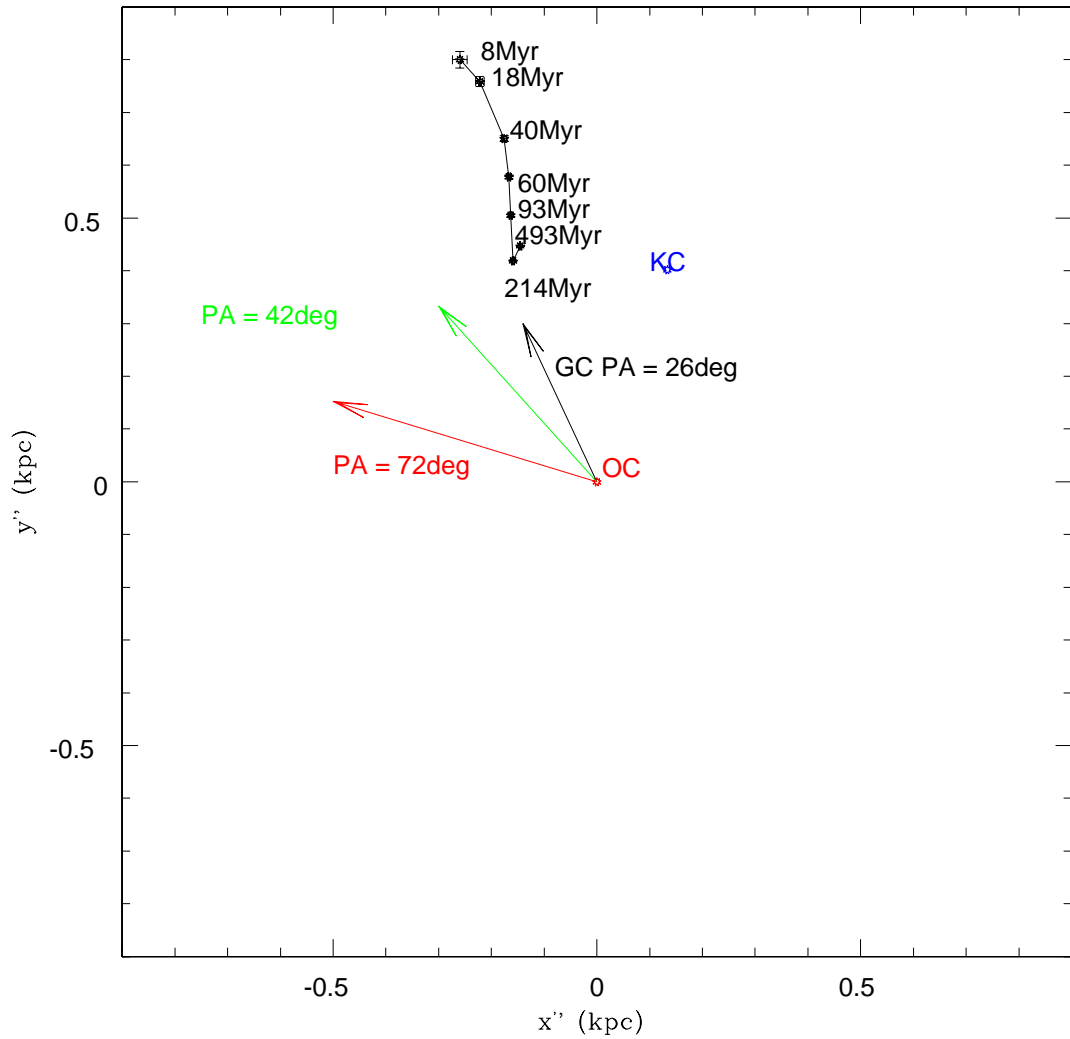
Figure 3.14: The centers of the stellar population in the LMC for various ages, is shown in the plane of the LMC, with error bars. The direction of the velocity vector of the LMC is shown in red at a PA of 72°, (calculated from the proper motion values provided by Piatek et al. 2008) and the line of interaction of the MW and the LMC according to our convention at a PA of 26°. The direction given in van der Marel (2001) is shown in green. KC is the H I kinematic center (Kim et al. 1998) shown in blue, and OC is the optical center of the LMC shown as a red point.

Thus, the lopsidedness in the stellar as well as the H I distribution to the north may be due to the gravitational attraction of our Galaxy on the gas of the LMC disk and the enhanced compression in the northern regions. The movement of the LMC could cause compression of the gas in the northeastern side resulting in enhanced star formation in the NE. The center shifts and the timescales derived in this section can be used to understand the details of the above two processes on the gas resulting in star formation. We discuss these aspects in detail in our discussion section.

Comparison with the SFH of Harris & Zaritsky (2009)

A complete SFH of the LMC was derived by H&Z09 using the multi-band photometry of the MCPS. They provided the star formation rate (SFR) in $M_\odot/Myr$, for particular age bins for different regions of the LMC. Our analysis identifies the LSFE in a region and estimates its age, which is quite different from the analysis of H&Z09. Hence, it is impossible to compare the two results quantitatively. On the other hand, we can compare our results with the RSFH as estimated by H&Z09. We compare our figure 3.9 with the 12.5 Myr and 6.3 panels of figure 8 in H&Z09. It can be seen that there is a very good correlation between the star forming regions identified in figure 8 and those in our figure 3.9. The shrinking of star formation to smaller regions is clearly seen if we compare their 12.5 Myr and 6.3 Myr panels. They find that the northern blue arm appears in the 160 - 100 Myr age range. We note that there has been a shift in the population to the north in the last 200 Myr. In addition, the enhanced star formation in the NE regions appear for ages younger than 50 Myr in H&Z09, whereas we find such an enhancement at 40 Myr. They identified peaks of star formation at 12.5 Myr and 100 Myr, which correlates well with the peaks of 0 - 10 Myr and 90 - 100 Myr identified by us. Thus, the ages of the LSFE estimated here correlates well with the RSFH derived by H&Z09.

3.5 Discussion

Recent high-precision proper motion estimates suggest that the LMC and the SMC are either on their first passage or on an eccentric long period (> 6 Gyr) orbit about the MW. This differs markedly from the canonical picture in which the Clouds travel on a quasi-periodic orbit about the MW (with a period of ~2 Gyr). Without a short-period orbit about the MW, the origin of the Magellanic Stream, a young (1 - 2 Gyr old) coherent stream of H I gas that trails the Clouds and spans 150° across the sky, can no longer be attributed to stripping by MW tides and/or ram pressure stripping by MW halo gas (taken

from Besla et al. 2010). In addition, the episodes of star formation found in the LMC have been traditionally attributed to its repeated interaction with the MW and the SMC. Since the SMC is less massive relative to the LMC, it is unlikely to have a significant impact on the LMC. In the first passage scenario, the LMC has probably had its closest approach about 200 Myr ago. This event is likely to have had a significant impact on both the Clouds, especially on the LMC.

In the plane of the LMC, we find that the present distribution of the H I gas is lopsided towards the north. The star formation in the last 40 Myr is lopsided towards both the north and NE. The center of the stellar population is found to have shifted to the north in the last 200 - 40 Myr, and towards the NE in the last 40 Myr. Similarly, H&Z09 found the appearance of the blue arm around 160 - 100 Myr ago and the northeastern enhancement for ages < 50 Myr. To understand the MW-LMC-SMC interaction, their locations are shown in the plane of the LMC, in figure 3.15. The direction of velocity vector of the LMC is at a PA 72° (shown in red). The location of the galactic center is shown according to our convention (PA = 26°)and that of van der Marel (2001) (PA = 42°, shown in green). The direction of motion of the LMC is in the same quadrant as the line connecting the LMC and the GC, which is the NE quadrant. The location of the SMC is such that the LMC lies in the line of interaction of the SMC and the MW. This line is also in the NE direction. It is quite possible that the recent star formation in the Clouds is due to the effect of the gravitational attraction of the MW on the H I gas within them.

We propose the following scenario to explain the lopsidedness in the LMC. We suggest that the H I gas in the LMC is shifted/pulled to the north by the perigalactic passage at about 200 Myr. The gas in the north is shocked/compressed to form stars starting from about 200 Myr, owing to the motion of the LMC in the MW halo. The efficiency in converting gas to stars seems to have increased in the 100 - 40 Myr age range. The direction of the center shift is more or less in the direction of the line connecting the LMC and the MW. At about 40 Myr, we detect the northeastern regions to have enhanced star formation, suggesting that there has been efficient compression/shocking in the NE. The LMC is moving away from the MW, after their closest approach. This could result in the NE becoming more compressed than the north, which is the direction of motion of the LMC. We do not detect any age difference or propagating star formation along the northern blue arm. The NE enhancement in star formation is probably due to the compression of gas by the motion of the LMC. A similar scenario of bow-shock induced star formation was proposed by de Boer et al. (1998). They suggested that the gas gets compressed in the east and then moves towards north with the LMC disk rotation. This implies that there

should be a gradient in the age along the northern region from the east, but such a gradient is not seen here. We suggest that this compression has been active only in the last 40 Myr and not before then.

Another result of this study is the detection of an outside-to-inside quenching of star formation within the last 100 Myr. We identify a peak in the star formation at 90 - 100 Myr, which was also identified by H&Z09. The peak of star formation found at 100 Myr is probably a global feature in the LMC, which is probably the effect of the perigalactic passage on the H I gas of the LMC. This star formation was present in most of the regions and the star formation then became restricted to the inner LMC. Thus, the star formation was quenched from the outside to the inside after the 100 Myr peak. In the central regions, there is an indication that most of the regions stopped forming stars in 30 - 40 Myr age range with only a few pockets continuing to form stars. On the other hand, the NE regions, SW end of the bar, and some northern regions continued to form stars until very recently, giving rise to the 0 - 10 Myr peak in star formation. The quenching of star formation was efficient in the southern LMC as most of the gas present was converted to stars and there is not much gas left. The star formation in the north and the NE continues owing to the presence of gas and the efficient compression produced by the motion of the LMC.

In summary, the recent star formation in the LMC has been dictated by the last perigalactic passage. The timescales and locations of star formation identified in this study are valuable to model the recent interactions between the Clouds and the MW. The lopsidedness of the H I distribution towards the north can provide constraints on the parameters governing the gravitational force of the Galaxy on the LMC, before, during, and after the perigalactic passage. The compression of gas in the northern regions during the perigalactic passage and the compression of gas in the last 40 Myr can also place constraints on the direction of motion of the LMC, as well as the effect of the Galactic halo on the H I gas. It will be interesting to generate these details in the LMC disk, using an SPH simulation.

The SMC, being less massive doesn't seem to have a significant role in the star formation episodes in the LMC. The details in this direction will be discussed in the following chapter by the estimation of RSFH of the SMC.
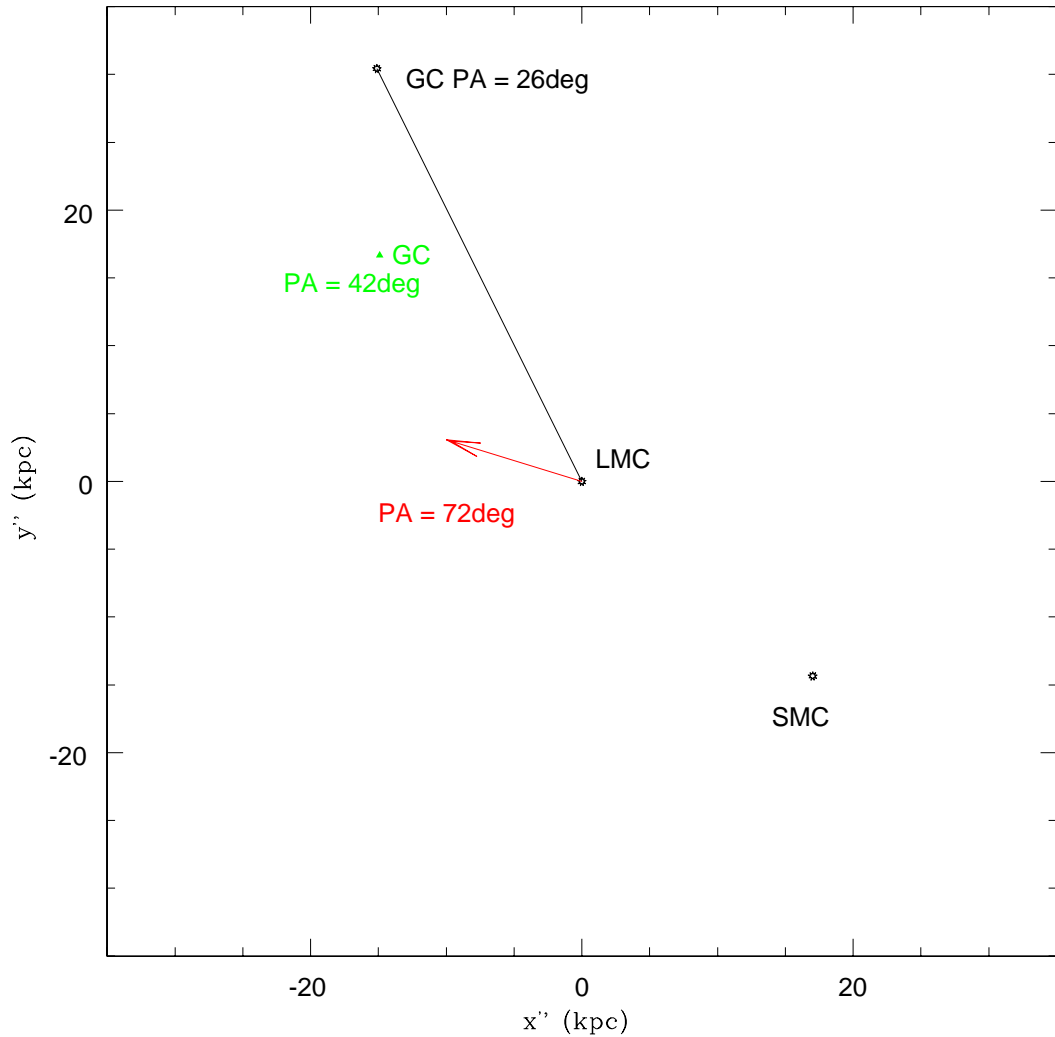
Figure 3.15: The locations of the MW, LMC, and the SMC are shown in the plane of the LMC, the direction of the velocity vector of the LMC is shown in red at a PA 72°, and the line of interaction of the MW and the LMC according to our convention is drawn at a PA of 26°. The Galactic center taken from van der Marel (2001) is shown in green at a PA 42°. The location of the SMC is such that the LMC lies in the line of interaction of the SMC and the MW.

3.6 Appendix A: Error analysis

In this study, we used a simple method of identifying the main sequence turn-off and converting into the age of the youngest star formation. The ages estimated by this

Table 3.2: The input parameters to the synthetic CMD and the estimated LSFE, A_v values in the LMC. The extinction applied for synthesising CMD is 0.55 magnitude.

log(age)	nstar#	Mass($M_\odot$)	LSFE log(age)	derived A_v
7.40	500	1124.5	7.88	0.7018
	1000	2361.3	7.90	0.4538
	1500	3670.9	7.49	0.5878
	2000	4980.1	7.34	0.5878
	2500	6258.8	7.41	0.5878
	3000	7546.2	7.41	0.5878
	3500	8824.9	7.41	0.5878
	4000	10133.7	7.41	0.5878

Table 3.3: The error in the derived ages estimated using synthesised data. The tabulated error holds for synthetic CMDs with minimum mass shown in column 3.

log(age)	error in log(age)	mass ($M_\odot$)
7.0	0.15	7550
7.10	0.15	4980
7.35	0.10	4274
7.40	0.09	3671
7.50	0.07	4986
7.60	0.06	3668
7.70	0.06	4280
7.75	0.04	3657
7.90	0.02	2367
8.00	0.03	2362

method, are in general, found to be comparable with the cluster ages and ages estimated by H&Z09. The ages estimated here are affected by the photometric errors, errors in the estimation of extinction, and the finite resolution in binning along the luminosity as well as the colour axes. We derived the error in the estimated values of extinction and LSFE age using two methods: (1) synthetic CMDs and (2) the propagation of errors. These are described below.

We synthesised CMDs with an IMF 2.35, in the mass range 0.6 - 20 M⊙, incorporating the observed (typical) photometric error and using the Marigo et al. (2008) isochrones for metallicities 0.008. Synthetic CMDs are created for turn-off ages in the range of 10 to 100 Myr. To quantify the sampling effects and errors in the derived turn-off age, we performed the same analysis on the synthesised data. For each population, we estimated the LSFE age and extinction. To understand the effect of sampling, the analysis was repeated by varying the total number of stars in a CMD. We applied an A_v of 0.55 mag to synthe-

sise the CMDs. The LSFE age and extinction estimated from the synthetic CMDs were compared with the input values to find the error. To incorporate the effects of sampling, the number of stars (or total mass) is also varied. Synthetic CMDs are created with a wide range in the number of stars (more as well as less than that found typically in the observed CMDs). As an example, the input parameters for the synthetic CMD and the estimated results for the LMC for a single age are tabulated in table 3.2. Columns 1, 2, and 3 are the log (age), the total number of stars and the total stellar mass in the synthetic CMD. The total stellar mass can be used to estimate the typical star formation rate, which is detected using this method (and the cut-off) as a function of age. The star formation rate can be estimated by dividing the total mass with the age range corresponding to the M_v and the bin size. Column 4 and 5 are the estimated LSFE log (age) and extinction. The analysis was performed for various age ranges and the results are tabulated in Table 3.3. The columns are (log) age, estimated error in age, and the minimum mass (and hence the number of stars) required to produce the synthetic CMD, with the tabulated parameter. This number is found to be in the range 1500 - 2000 and is smaller than the number of stars found in the observed CMDs above the limiting magnitude. The maximum error in the extinction is found to be within 2.48 times the bin size (0.1 mag) of the (V−I) colour. The error in log (age) is found to be in the range of 0.01 - 0.15. This error includes the error in the estimation of extinction and magnitude of the main sequence turn-off, the statistical error, and a typical photometric error. This method gives an estimate in the error as a function of the LSFE age.

The error in the estimated LSFE as a function of location is estimated using the second method. The error is calculated by means of the propagation of error method, starting with the photometric error in V & I bands, σV & $\sigma(V\text{-}I)$.

$$\sigma A_v = 2.48 \sqrt{\sigma(V - I)^2 + (V - I)^2_{bin}} \tag{3.4}$$

$$\sigma M_v = \sqrt{\sigma V^2 + V^2_{bin} + \sigma A^2_v} \tag{3.5}$$

$$\sigma age = constant \ \sigma M_v \tag{3.6}$$

where V_{bin} & $(V - I)_{bin}$ are half the bin sizes used for magnitude and colour binning, σM_v is the error in absolute magnitude, σA_v is the error in the estimated extinction and σage is the error in LSFE age on a logarithmic scale. The spatial plots of the errors are shown in figures 3.16 and 3.17, for both the data sets MCPS and OGLE III. The error in log(age) varies from 0.06 to 0.12. The error is found to be higher along the bar of the
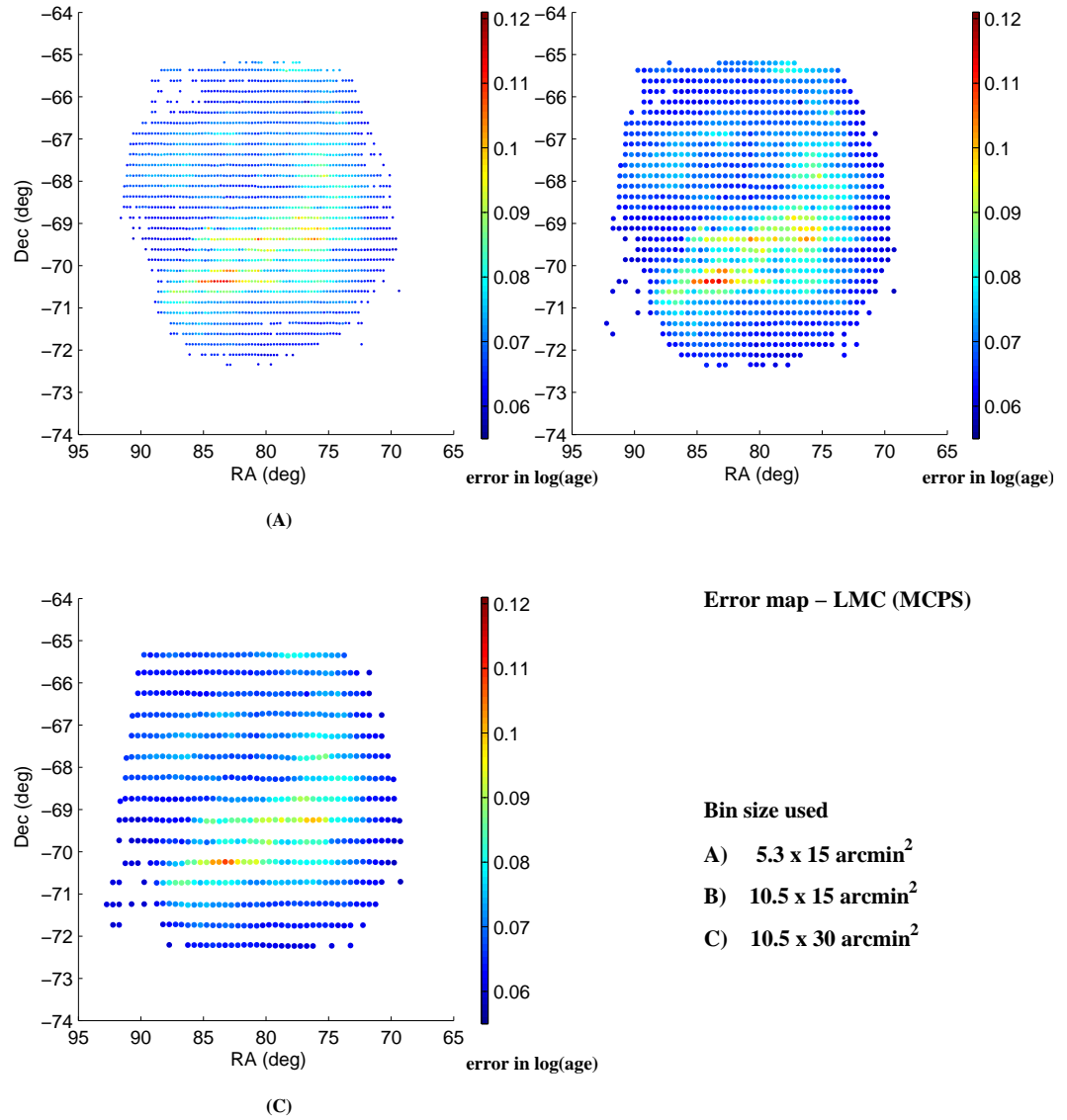
Figure 3.16: The error in estimated age for the LMC using MCPS data for all the three area bins as indicated in the figure. Colour coding is according to the error in log(age).

LMC. This is primarily the effect of photometric errors due to the crowding, as this is the densest regions in the LMC. The error in the LSFE age, as estimated by the above two methods are comparable. The first method is likely to estimate the true error and the second method is likely to overestimate the error. Both the methods are included to show the variation of error as a function of both age and location.
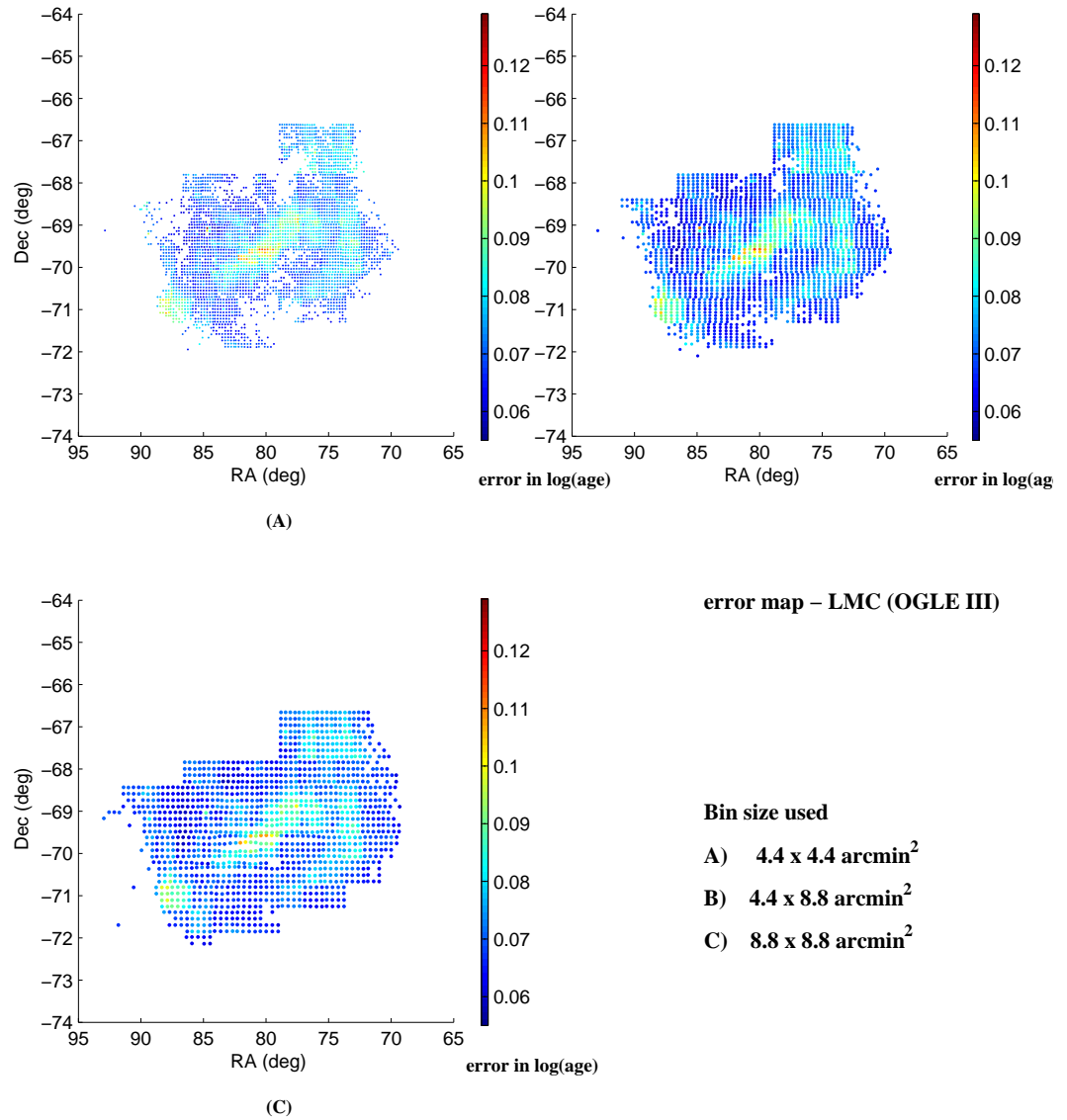
Figure 3.17: Error map for the LMC using OGLE III, similar to figure 3.16.

CHAPTER 4

RECENT STAR FORMATION HISTORY OF THE SMALL MAGELLANIC CLOUD*

4.1 Introduction

The Small Magellanic Cloud, the smaller companion of the LMC forms an equally attractive astronomical laboratory. As we discussed in the previous chapter, the era of new proper motion and the first passage scenario demands a revisit to the SFH of the SMC. Here we performed an analysis similar to what we have done for the LMC, to estimate the statistical distribution of the recent star formation events in the SMC.

Harris & Zaritsky (2004) studied the SFH of the SMC and found a quiescent epoch between 8.4 and 3 Gyr. They also found evidence of a continuous star formation from 3 Gyr to the present epoch with star formation peaks at 2-3 Gyr, 400 and 60 Myr. Noël et al. (2009) also studied the SFH of the SMC and found that the younger stars (200 - 500 Myr) have an asymmetric distribution with the appearance of the wing, while the older population (> 1 Gyr) is distributed similarly at all radii and all azimuths. In contrast to Harris & Zaritsky (2004), Noël et al. (2009) did not find any quiescent epoch at the intermediate ages. The star clusters in the LMC were studied and their derived age distribution compared with that in the SMC by Pietrzynski & Udalski (2000). Glatt et al. (2010) studied the SFH of both L&SMC based on star clusters with age <1 Gyr. They found that the cluster formation peaks at 160 Myr and 630 Myr for the SMC and 125 Myr and 800 Myr for the LMC. Thus, the studies completed so far have found that the age of the star formation peaks in the LMC and the SMC fall in the similar range, but the values do not coincide.

The method we applied here is the main sequence turn-off identification and statistically tracing the LSFE. The method as we discussed in chapter 3, bears the advantage of better spatial as well as temporal resolution, and it is free from age-metallicity degeneracy. An extinction map is also estimated for the SMC. The H I and young cluster distribution is compared with the distribution of LSFE. Also the propagation of young star forming events is analysed to reveal the interaction of the SMC with the LMC and the MW.

4.2 Data

We have used the OGLE III and MCPS photometric catalogues for this study. The OGLE III catalogue consists of V and I photometry of 6.5 million stars from 41 fields, covering an area of 14 square deg in the sky. For this study the area binning in the SMC was done as 911 subregions with area 4.′43 x 4.′43, 651 subregions of area 4.′43 x 8.′87, and 415 subregions of area 8.′87 x 8.′87. The MCPS survey consists of UBVI photometry of the central 18 square deg of the SMC covering 5 million stars. 162 subregions of area 10.′5 x 30′, 265 of 10.′5 x 15′, and 442 of 5.′3 x 15′ were made to estimate the age of the LSFE.

4.3 Methodology

The main sequence turn-off identification is done following the same procedure described in section 3.3.1. The statistical division to subregions is done such that each region in the SMC has a minimum of 250 stars in the main sequence. This threshold is less than half of that in the LMC, since the total number of the observed stars in the SMC is much less than that in the LMC. The bin sizes used to estimate the turn-off magnitude and colour are same for both the LMC and the SMC.

In the case of the SMC, to estimate the reddening a constant DM of 18.9 and an average extinction value of $A_v = 0.46$ mag (Zaritsky et al. 2002) are used. The expected value of the unreddened colour, $(V - I)_0$ is obtained from Marigo et al. (2008) isochrones for a metallicity of Z = 0.004. The equations 3.1, 3.2 and 3.3 are used to estimate the extinction towards each subregion. Using these estimated values of extinction, the actual magnitude M_v corresponding to the turn-off is estimated for all the subregions. The CMDs of some sample regions are shown in figure 4.1. The left panel shows the CMD of an SMC subregion using MCPS and the right panel shows the CMD using OGLE III.
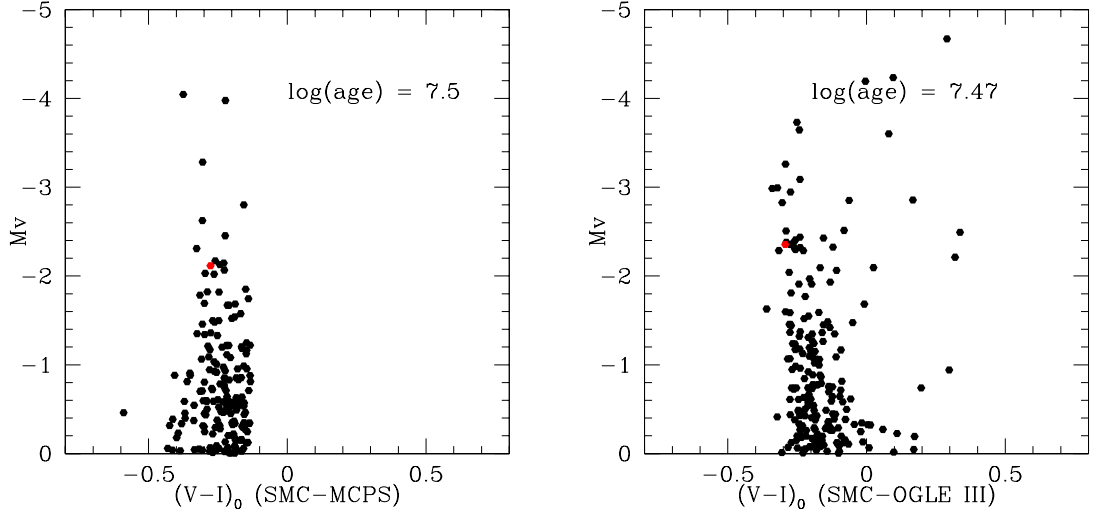
Figure 4.1: M_v vs $(V - I)_0$ CMDs for subregions in the SMC. The figure shows two regions, with left panel using MCPS data and the right using OGLE III data. The red dot marks the turn-off point, and the estimated turn-off age is also shown.

The estimated turn-off M_v is used to estimate the age of the LSFE in each subregion. We estimated an age-M_v relation for the turn-off, using the isochrones of Marigo et al. (2008) with metallicity 0.004. The plots of the log (age) vs M_v is given in figure 4.2. The relation is found to be linear and we have derived a linear relation between the two by fitting a line to the data points. The turn-off ages for the sample regions, estimated using the above relation are also shown in figure 4.1. As we discussed in section 3.3.2 the identification of main sequence turn-off was found to be ambiguous for turn-offs fainter than 18.0 magnitude. Therefore, subregions with turn-off magnitudes fainter than 18.0 magnitude are not considered and these locations will appear as gaps in the extinction and LSFE maps. Since we have put a limiting apparent turn-off magnitude of 18.0, it will eventually lead to a higher cut-off of around 100 Myr for the age of the LSFE.

4.4 Results

4.4.1 SMC: Extinction

The extinction towards the SMC is estimated using the MCPS and OGLE III data sets. As in the case of the LMC, we estimated the reddening $E(V-I)$ of the main sequence stars near the turn-off for each region. The extinction (A_V) maps estimated using the MCPS data are shown in figure 4.3 and those estimated from OGLE III are shown in figure
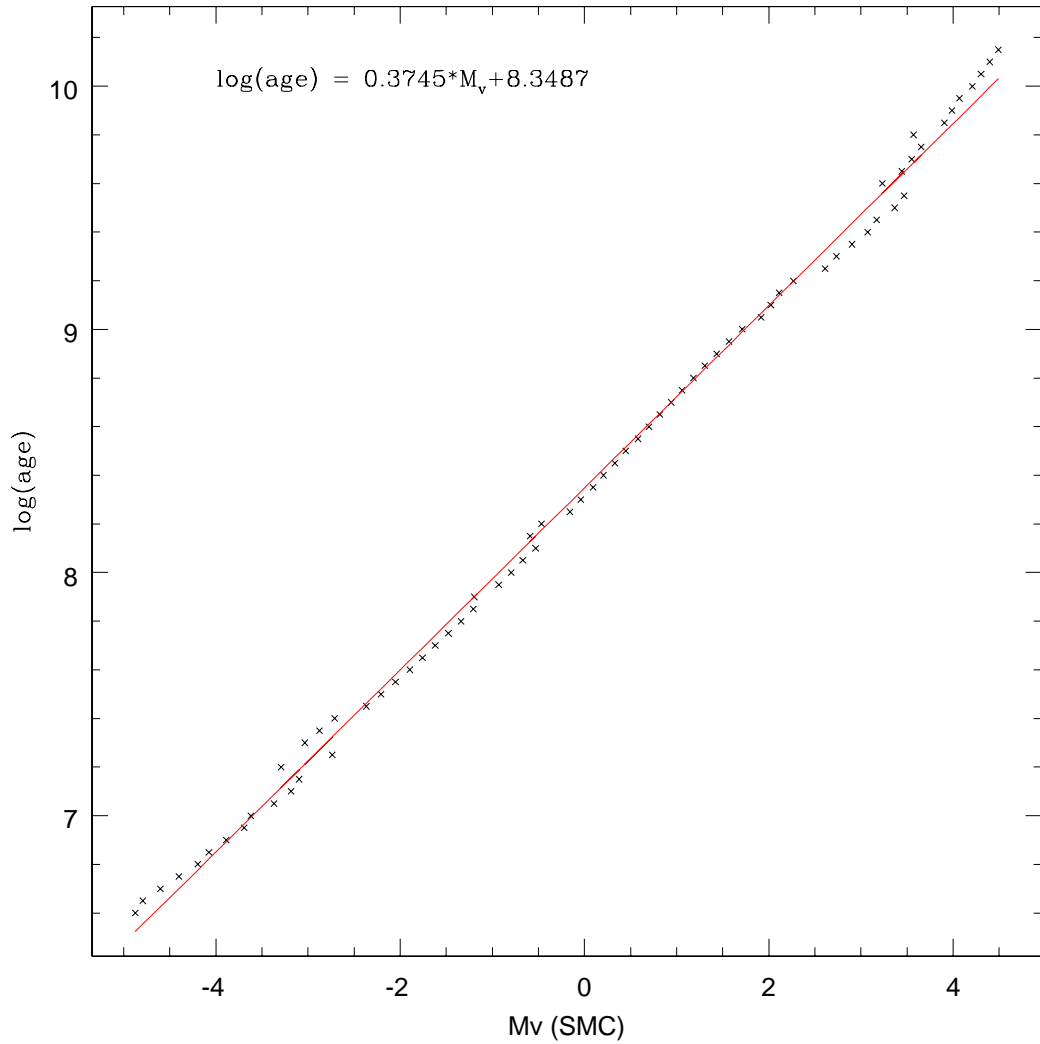
Figure 4.2: The log(age) vs M_v plots for the SMC. The turn-off M_v corresponding to various ages are inferred from Marigo et al. (2008) isochrones. The fitted line is shown in red.

4.4. The area used for three different bin sizes are mentioned in the figure. The maps are found to be similar with the extinction value in the range, 0.2 - 2.0 mag. The average extinction is found to be in the range 0.2 - 0.5 mag with central regions showing a higher value of extinction. The eastern wing also has regions with high extinction. Zaritsky et al. (2002) estimated the extinction across the SMC. We compared our estimation with their values in the form of a distribution, in figure 4.5. In general, both distributions closely match and both have a peak in the range, 0.2 - 0.4 mag. As for the LMC, we derive
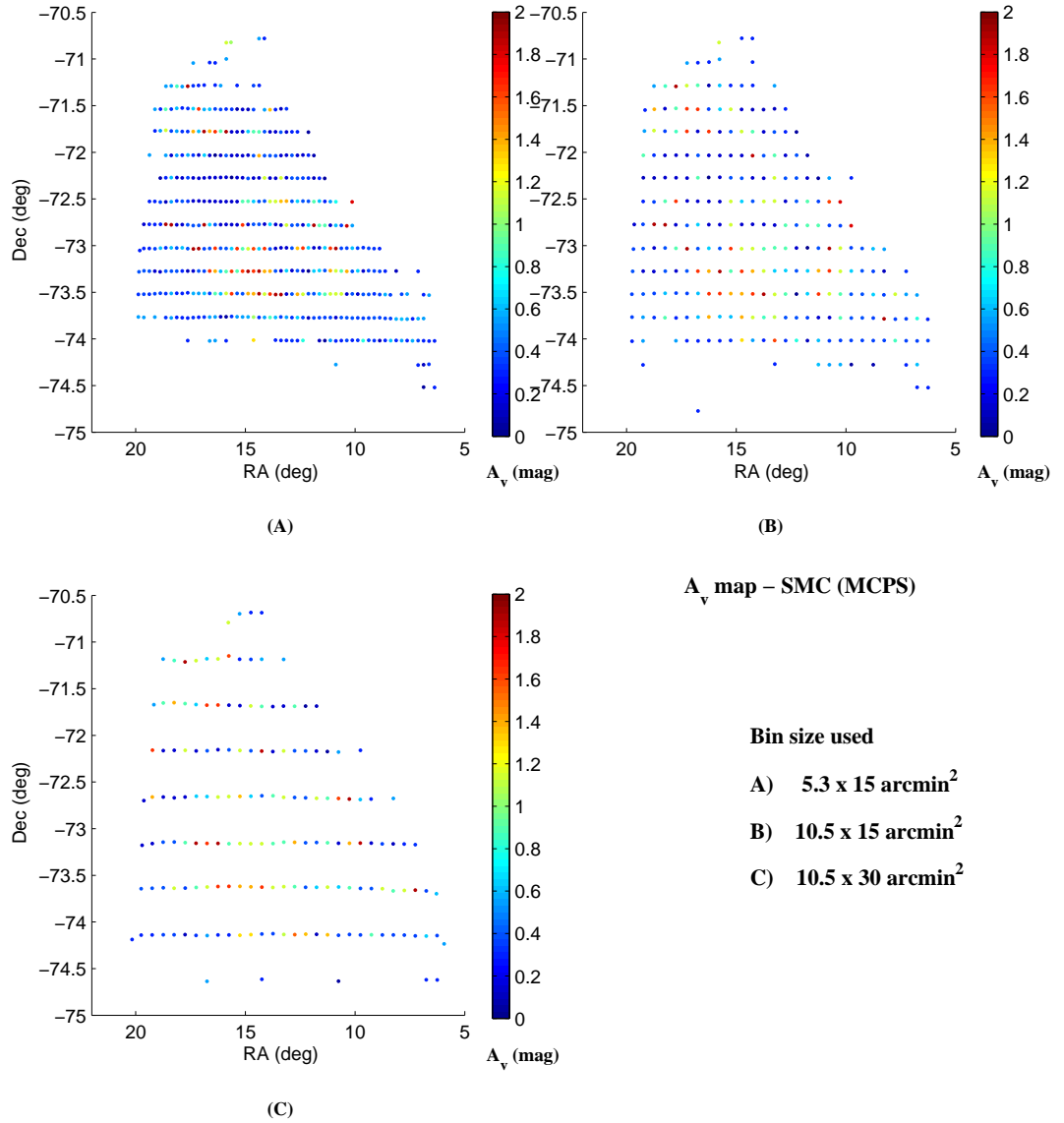
Figure 4.3: The extinction map of the SMC using MCPS data in the RA-Dec plane for three different area binning, as specified in the figure. Colour coding is based on the A_v value, which varies from 0.2 to 2.0 as shown in the colour bar.

lower extinction than Zaritsky et al. (2002), for the reasons mentioned in section 3.4.1. We do observe a mild inconsistency in the distribution for extinction values higher than 1.5 magnitude. Since the number of regions involved is small, it is unlikely to affect the results derived below.
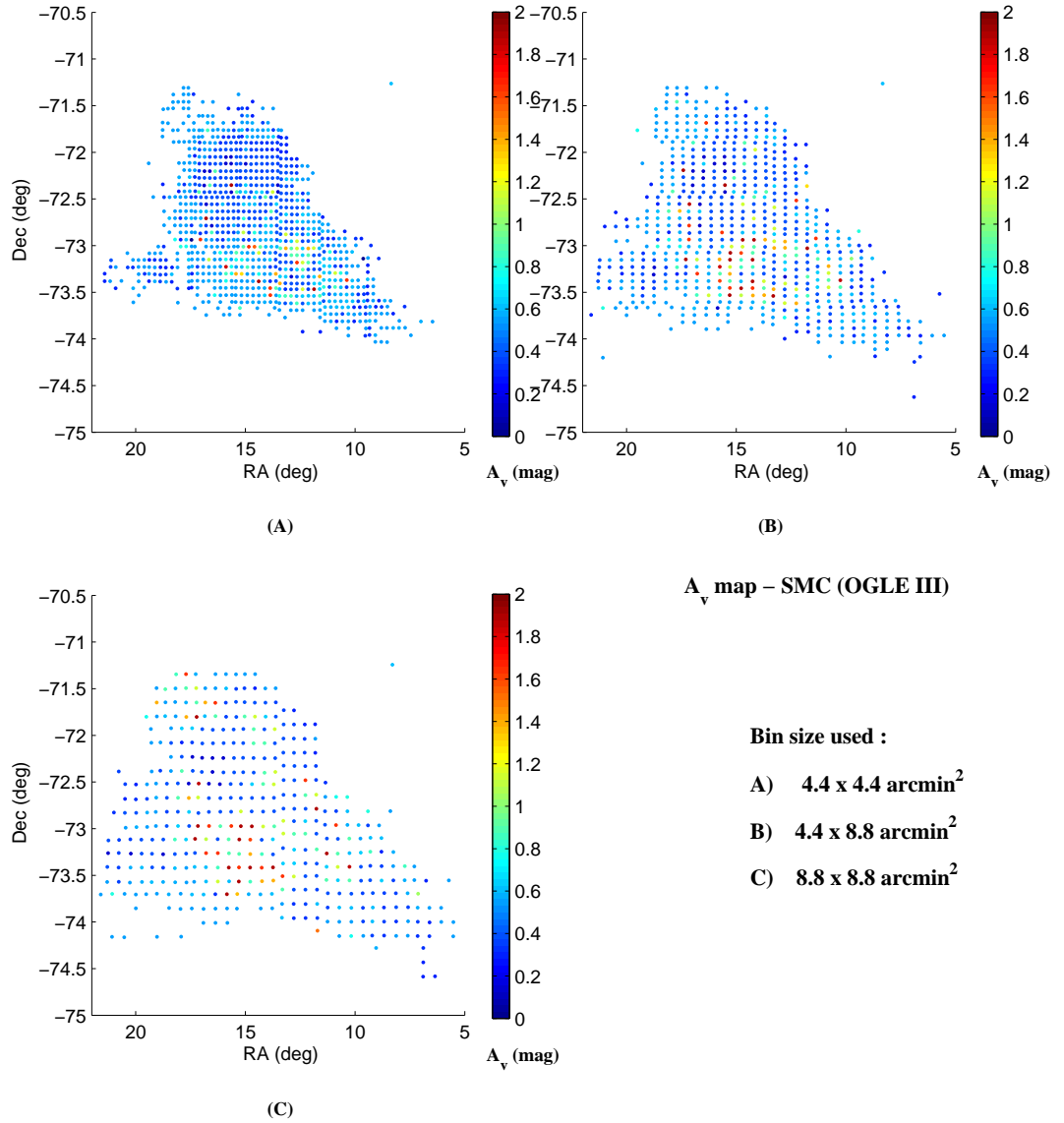
Figure 4.4: The SMC extinction map for three area bins, as in figure 4.3, using OGLE III data.

4.4.2 SMC: age map of the LSFE

We estimated the spatial distribution of age of the LSFE in RA vs Dec plane and presented the maps in figures 4.6 (MCPS) and 4.7 (OGLE III). We adopted three sizes of area (bin sizes as specified in the figure) to estimate the ages and to understand the
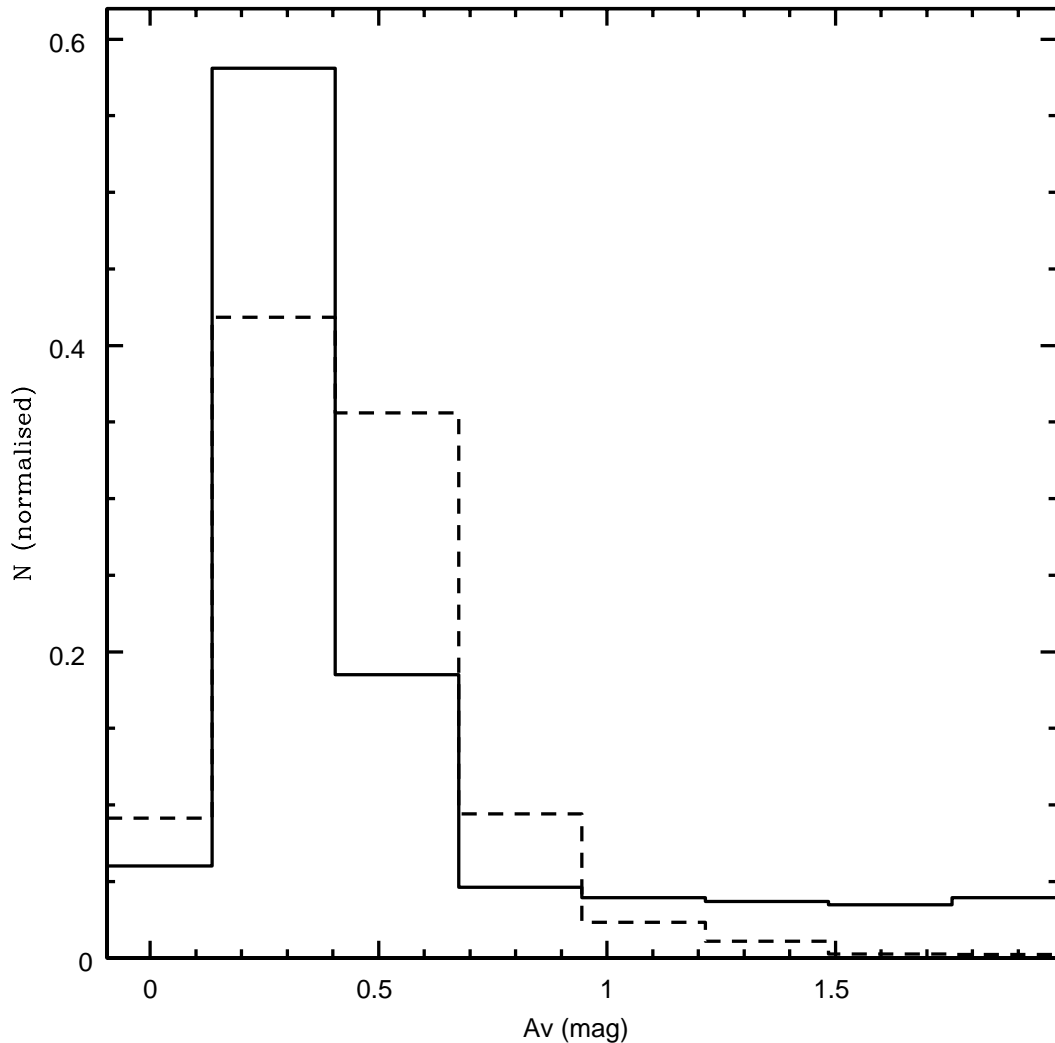
Figure 4.5: The estimated distribution of extinction in the SMC (shown as solid line) is compared with distribution obtained from the extinction map of hot stars provided by Zaritsky et al. (2002) (shown as dashed line, extracted from the fits image from the authors' website).

effect of the area on the estimated age. The MCPS maps show that the central region has experienced star formation until very recently (0 - 20 Myr). In the high resolution (smallest area size) map A, the outer regions appear to have older ages of about 60 - 80 Myr. This is not so clear in the map B, and in map C, we do not see any such increase in the age of the LSFE with radius. This clearly shows the effect of the area used in estimating the age of the LSFE. The OGLE III plots use smaller sizes of area (figure 4.7),
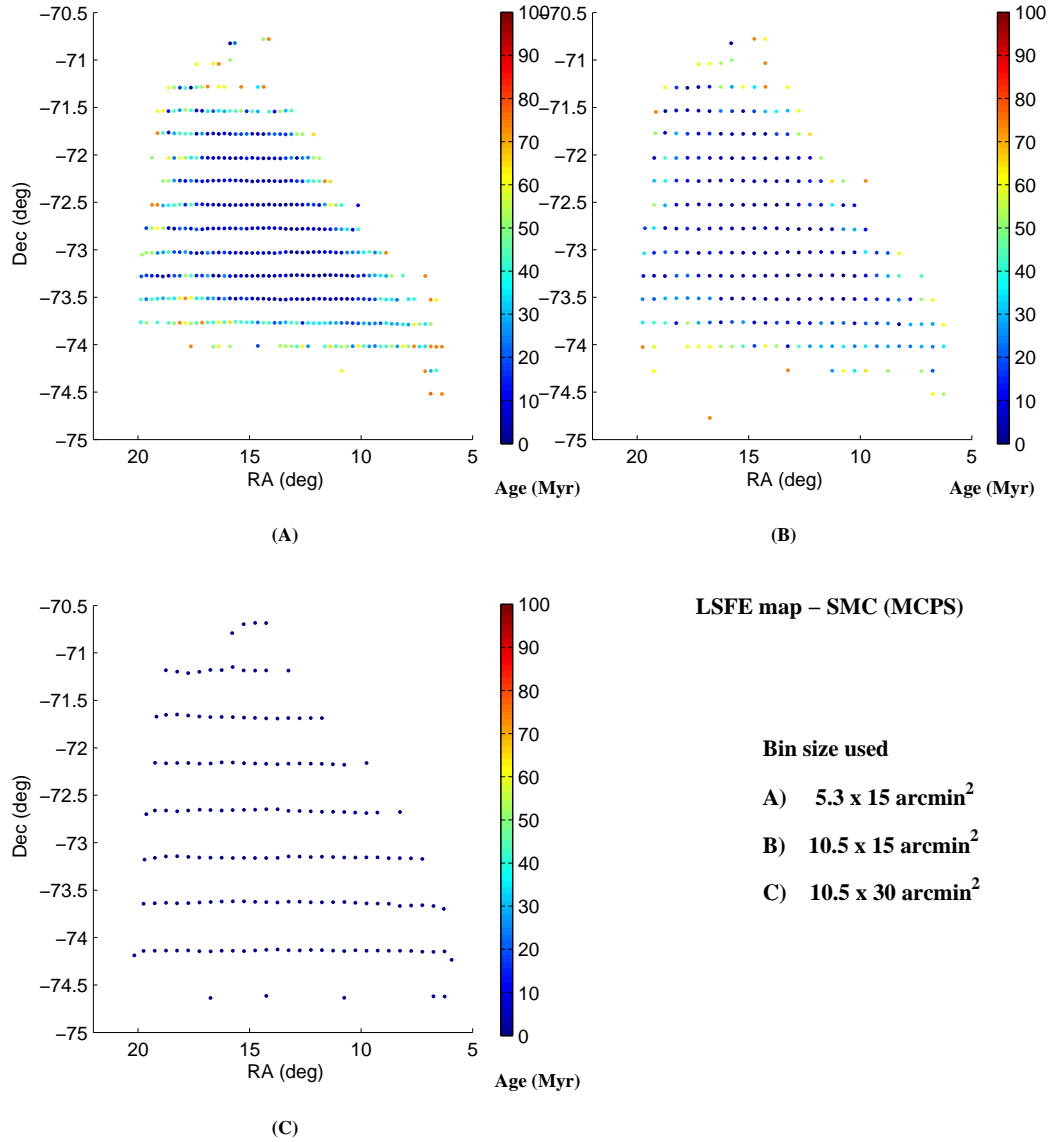
Figure 4.6: The LSFE map of the SMC using MCPS data in the RA - Dec plane with three different area binnings, as specified in the figure. Colour coding is based on the LSFE age as shown in the colour bar.

and the high resolution map A, shows that the inner region has a substructure with two clumps in the NE and SW direction. This substructure is similar in location to the two H I super giant shells, 304A and 37A (Stanimirovic et al. 1999). The map also suggests that the NE wing has more regions with recent star formation, than the southern clump,
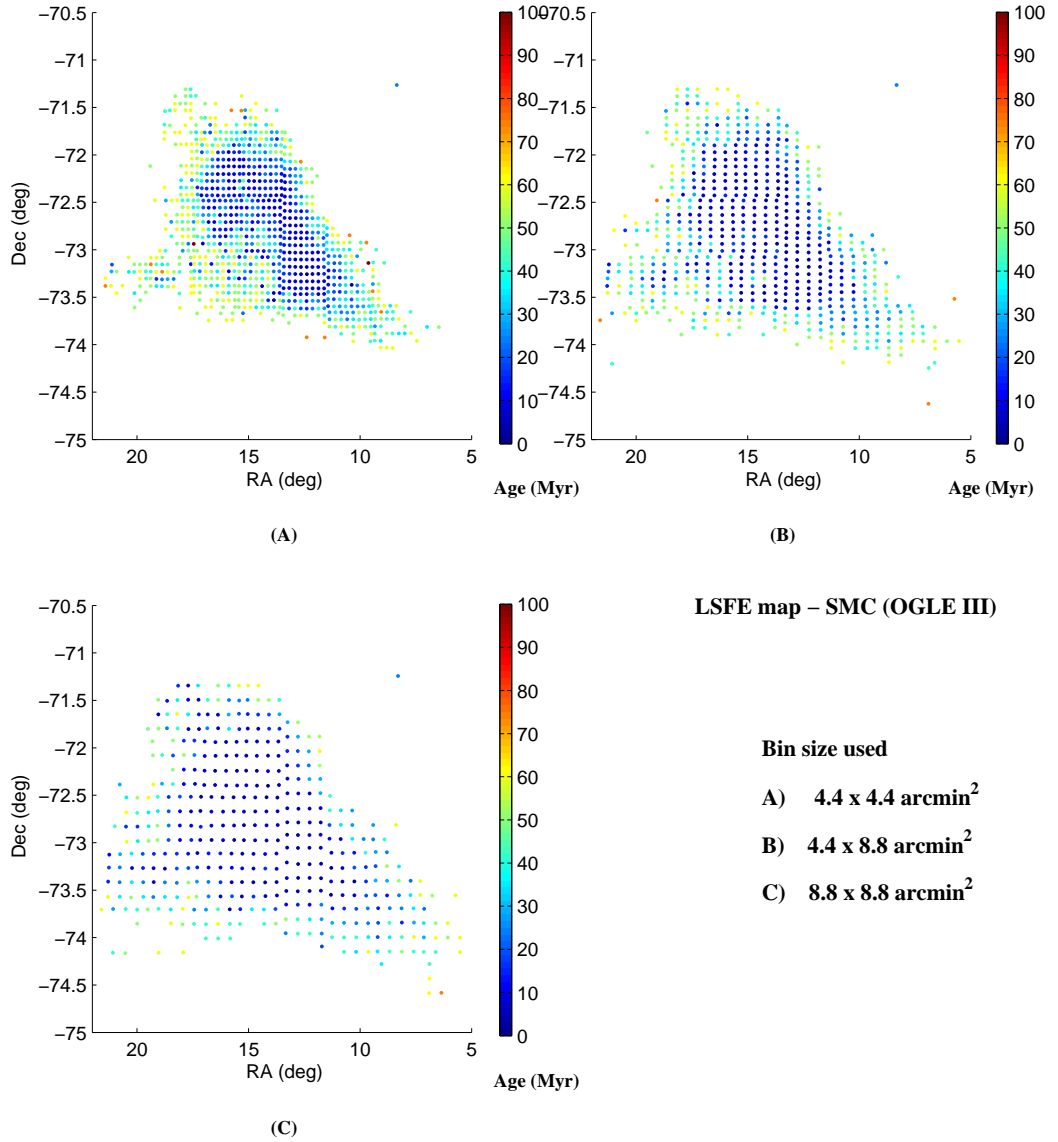
Figure 4.7: The LSFE map of the SMC similar to figure 4.6, using OGLE III data.

which is located near the center of the SMC. This structure disappears in the maps B and C. In all the OGLE III maps, we can find that the age of the LSFE in the central regions is in the age range 0 - 20 Myr, while the periphery shows an age of ∼ 60 Myr. Unlike in the LMC, we do not see a gradient in age, increasing outward from the center, even though the outer regions have older age. We also find that the missing regions caused by the limiting magnitude appear only in the periphery, suggesting that all the inner regions
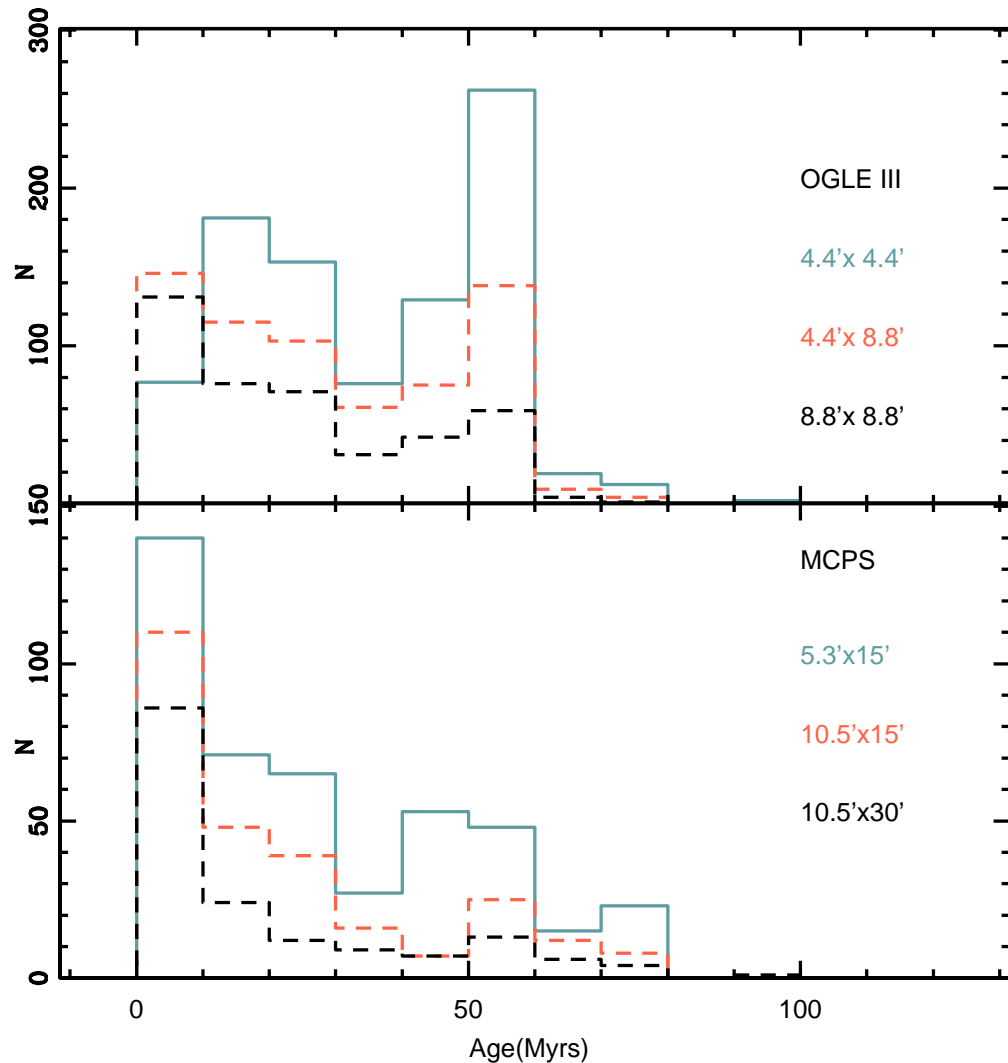
Figure 4.8: The statistical distribution of LSFE ages for the SMC. Upper panel shows OGLE III data and lower panel shows MCPS, with the three colours correspond to different area, as specified in the figure.

have experienced star formation in the last 100 Myr. The missing outer regions also suggest that the star formation stopped in the outer regions much earlier. As the area of the bin (maps B and C) increases, more regions get added to the periphery owing to the shift of the LSFE to younger ages. To summarise, we find that the star formation in the inner SMC is not very structured, in comparison with that in the LMC. We can identify the eastern wing in the map. Most of the inner regions have experienced star formation in the last 0 - 20 Myr. As for the LMC, we find marginal evidence of an outside-to-inside

97

quenching of star formation in the last 60 Myr.

The histogram of the age distribution of the LSFE is shown in figure 4.8. All three maps from the OGLE III (upper panel) identify a peak at 50 - 60 Myr. The younger peak shifts from 10 - 30 Myr in the highest resolution to 0 - 10 Myr in the low resolution maps. The shift to younger ages is found as the area considered increases. The distributions obtained from the MCPS map (lower panel) show a mild peak at 50 - 60 Myr in the two lowest resolutions, whereas the peak widens to 40 - 60 Myr at high resolution. All three resolutions show a peak at 0 - 10 Myr. In summary, we find that most of the regions in the SMC have experienced star formation until very recently, with one peak at 0 - 10 Myr and another at 50 - 60 Myr. The SFRs of the SMC are shown in figure 19 of H&Z09, which is derived from the SFH estimated in Harris & Zaritsky (2004). They identified a peak around 50 Myr and another around 10 Myr, which is in good agreement with our finding. Hence, the results derived here correlate well with the RSFH derived by Harris & Zaritsky (2004).

Comparison with the H I gas distribution and star clusters

We have plotted the H I column density distribution of Stanimirović et al. (2004) in figure 4.9. The H I has the highest column density in the southwestern part. The LSFE age map (corresponding to the high resolution map A in figure 4.7) is shown in the x-y plane in figure 4.10 for comparison. The NE and the SW substructures of the LSFE age map match well with the location of the H I. The LSFE map also identifies young star forming regions in the eastern part of the wing as well as in the NE part. Overall, the young star forming regions identified here coincide with the locations of H I with column densities higher than $7 - 8 \times 10^{21}$ atom cm^{-2}. We identify more regions with recent star formation in the NE substructure than the SW substructure, whereas relatively more/denser H I is found in the SW substructure. This suggests that the star formation is more efficient in converting gas to stars in the northeastern wing. This might also suggest an efficient gas compression in the NE, similar to the case of the LMC.

The ages of young star clusters given in Glatt et al. (2010) is over plotted on the LSFE maps in figure 4.11. As mentioned in section 3.4.2, while comparing with the cluster ages, we expect that the ages of the youngest clusters in a given region should match with the LSFE ages. The top-left panel shows clusters in the age range 0 - 40 Myr. In general, these clusters are found to be located near regions of recent star formation. Clusters in the age range 30 - 40 Myr located towards the outer regions, are also found near subregions with similar ages. Young clusters (0 - 30 Myr) are found to be located in the NE and SW
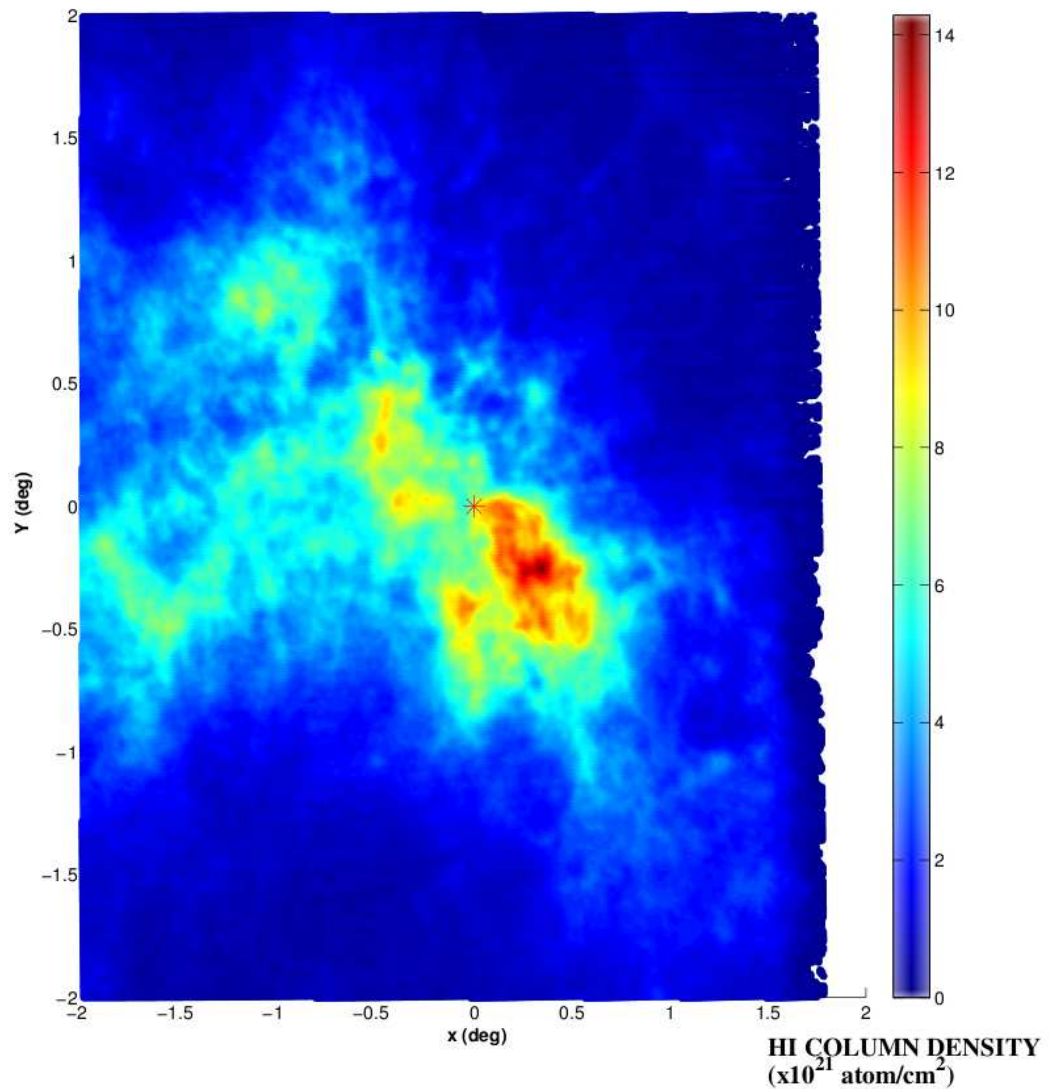
Figure 4.9: The H I column density distribution in the SMC is shown in the projected x-y plane of sky. Colour coding is according to H I column density as depicted in the colour bar. Data is taken from Stanimirović et al. (2004).

substructures and relatively higher number of clusters are found in the NE substructure. This suggests that the cluster formation is more efficient in the NE substructure. The top-right panel shows clusters in the age range 40 - 70 Myr. We note that older clusters near younger star forming regions imply that there have been older cluster forming episodes in these regions. Clusters in the age range 70 - 100 Myr are shown in the bottom-left panel.
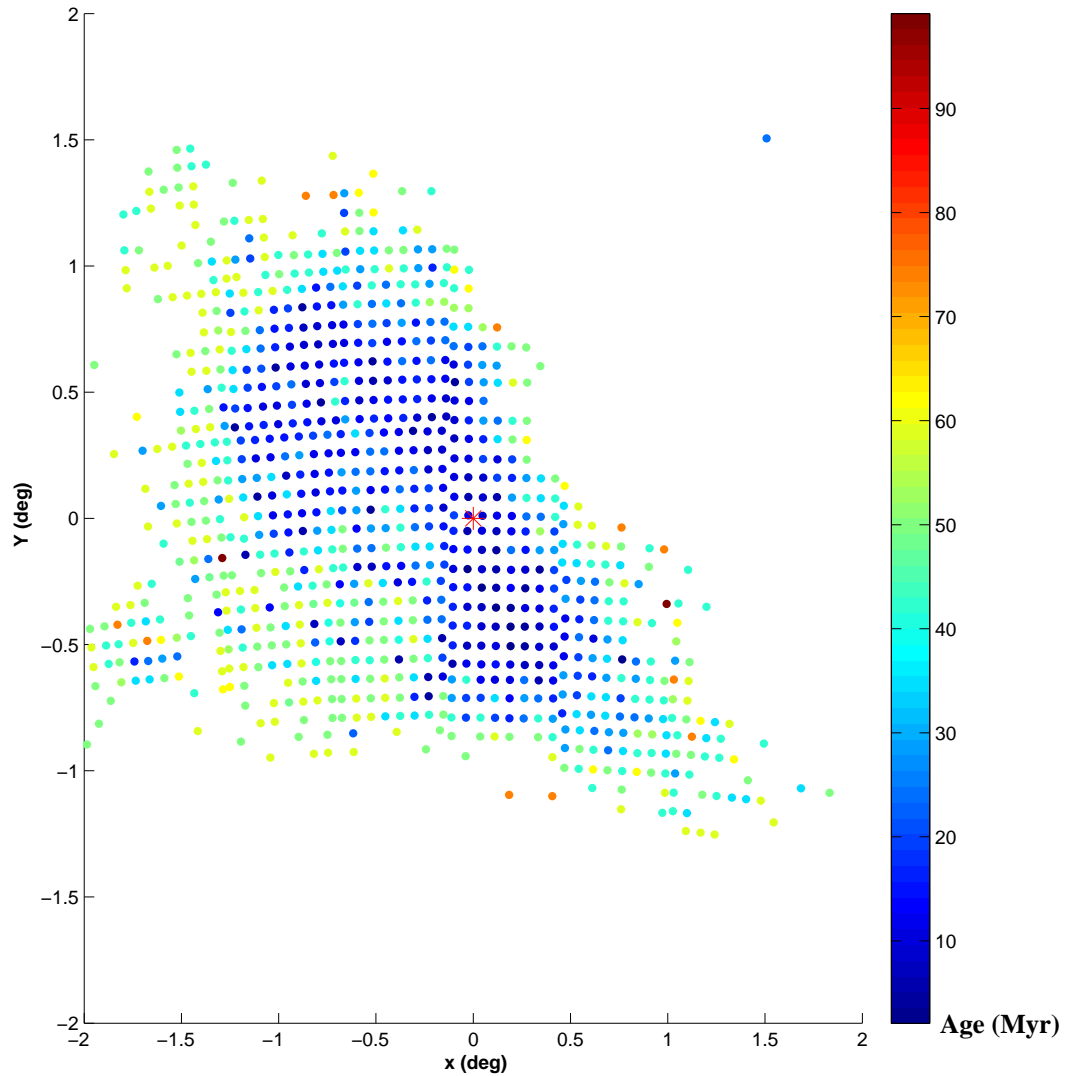
Figure 4.10: The LSFE map of the SMC is shown in the projected x - y plane of the sky, as in figure 4.7 A. The optical center is shown in red.

Since we do not see many regions with LSFE in this age range, no clear comparison is possible. The older clusters are found to occupy a relatively large radial extent compared to the younger clusters. This is indicative of an outside-to-inside quenching of star/cluster formation.
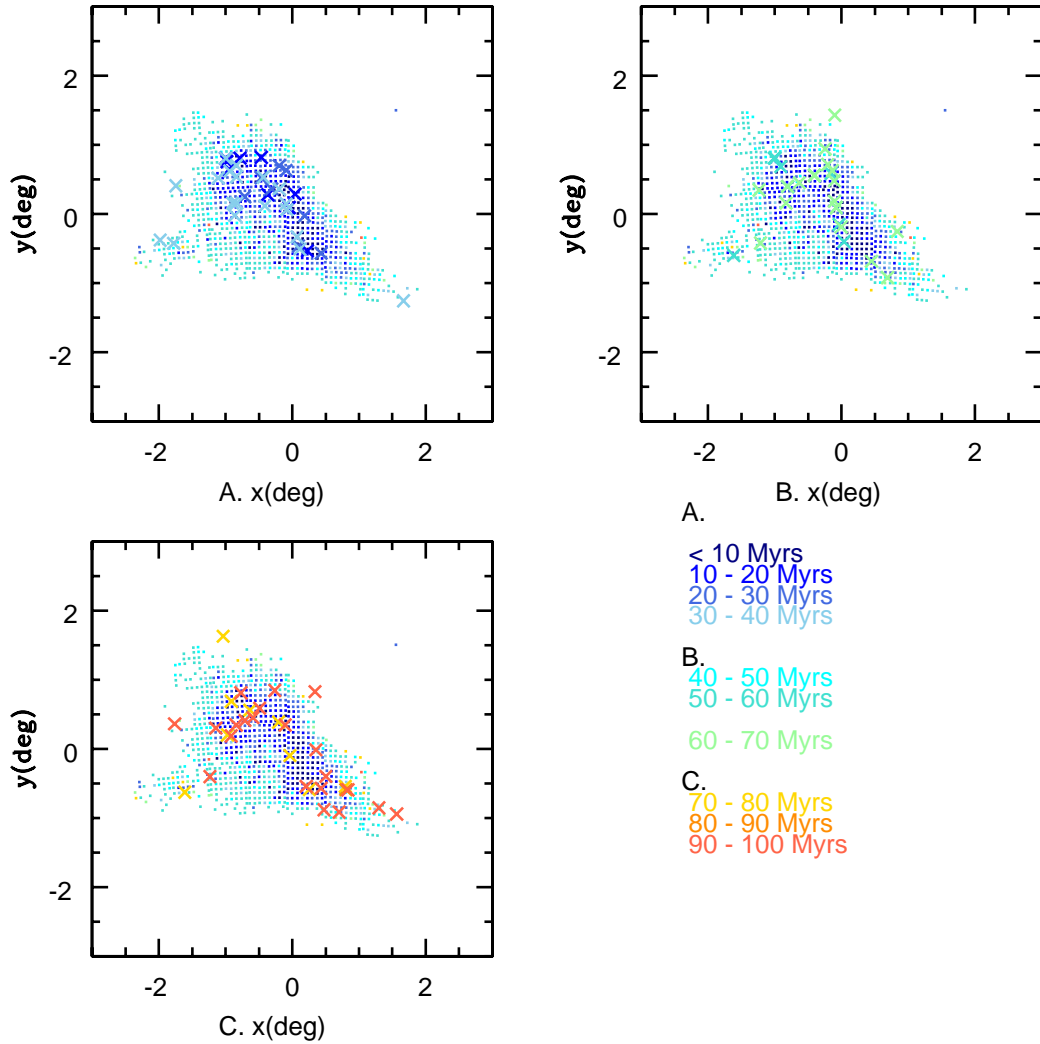
Figure 4.11: The age distribution of clusters as old as or younger than 100 Myr (Glatt et al. 2010) over plotted with the LSFE map (same as figure 4.10) in the projected x - y plane of the sky. Three different age groups are shown, top left ≤ 40 Myr, top right 40 - 70 Myr, and bottom left 70 - 100 Myr. Colour coding is according to the age as specified in the figure.

4.4.3 Shift in the center of the young stellar distribution in SMC

We used main sequence stars younger than various age cut-offs to study the shift of the centroids in the SMC. We used the OGLE III data for this purpose, taking into account its higher resolution and larger number of stars. Since the geometry of the SMC is not clearly understood, the center of the distribution of these stars are estimated both in

Table 4.1: The centers of the stellar populations in the SMC for various ages using OGLE III data.

Age (Myr)	RA(deg)	Dec (deg)	x (kpc)	σx	y (kpc)	σy	N#
6	14.2007	-72.7345	-0.3631	-0.0197	0.0445	0.0128	2430
14	14.3156	-72.7533	-0.3981	-0.0109	0.0472	0.0069	7968
33	14.2957	-72.7728	-0.3916	-0.0063	0.0334	0.0041	23377
79	14.1303	-72.8157	-0.3413	-0.0036	-0.0088	-0.0024	67919
188	14.0868	-72.8496	-0.3279	-0.0021	-0.0425	-0.0014	203383
445	13.9135	-72.9043	-0.2739	-0.0011	-0.0980	-0.0008	597714

RA-Dec and in the x-y coordinates (with respect to the optical center of the SMC). The optical center is taken as RA = $0^h 52^m 12.5^s$; Dec = -72°49"43' (J2000.0 de Vaucouleurs & Freeman 1972). The coordinates x & y are in kiloparsec where 1° corresponds to 1.04 kpc at the distance of the SMC. Table 4.1 contains the age of the oldest population of the group, centers in RA & Dec, and x & y, the number of stars considered for the center estimation, and the error in the values of the center. The oldest population considered is about 450 Myr and the youngest is about 5 Myr. The location of the centers, along with the ages and error bars, are shown in figure 4.12. We detect a shift in the center during the time interval 500 - 200 Myr in the NE direction. We estimate a shift of 2.1 pc/10 Myr along the x and 2.2 pc/10 Myr along the y directions. The shift then continues until 30 Myr in the same direction, with an enhanced rate of 4 pc/10 Myr along the x direction and 5 pc/10 Myr along the y direction in the 200 - 30 Myr age range. There is no significant center shift for ages younger than 30 Myr. We see a mild shift to the west in the range 14 - 6 Myr, but to within 2σ of the error, as can be seen from figure 4.12. The amount of shift in the center is far smaller than the shift we detected in the LMC. Thus, we detect a significant shift in the center of the population younger than 500 Myr in the NE direction. This is the direction towards the LMC. H&Z09 detected a coincident peak of enhanced star formation at 400 Myr in both the Clouds and they suggested that this may be caused by their mutual interaction. The above center shift during the interval 500 - 200 Myr may be due to this star formation episode and enhanced star formation in the northeastern region, as well as the appearance of the wing in this age range. We detect an enhanced center shift in the 200 - 30 Myr age range, this could be caused by the gravitational attraction of our Galaxy during the perigalactic passage.
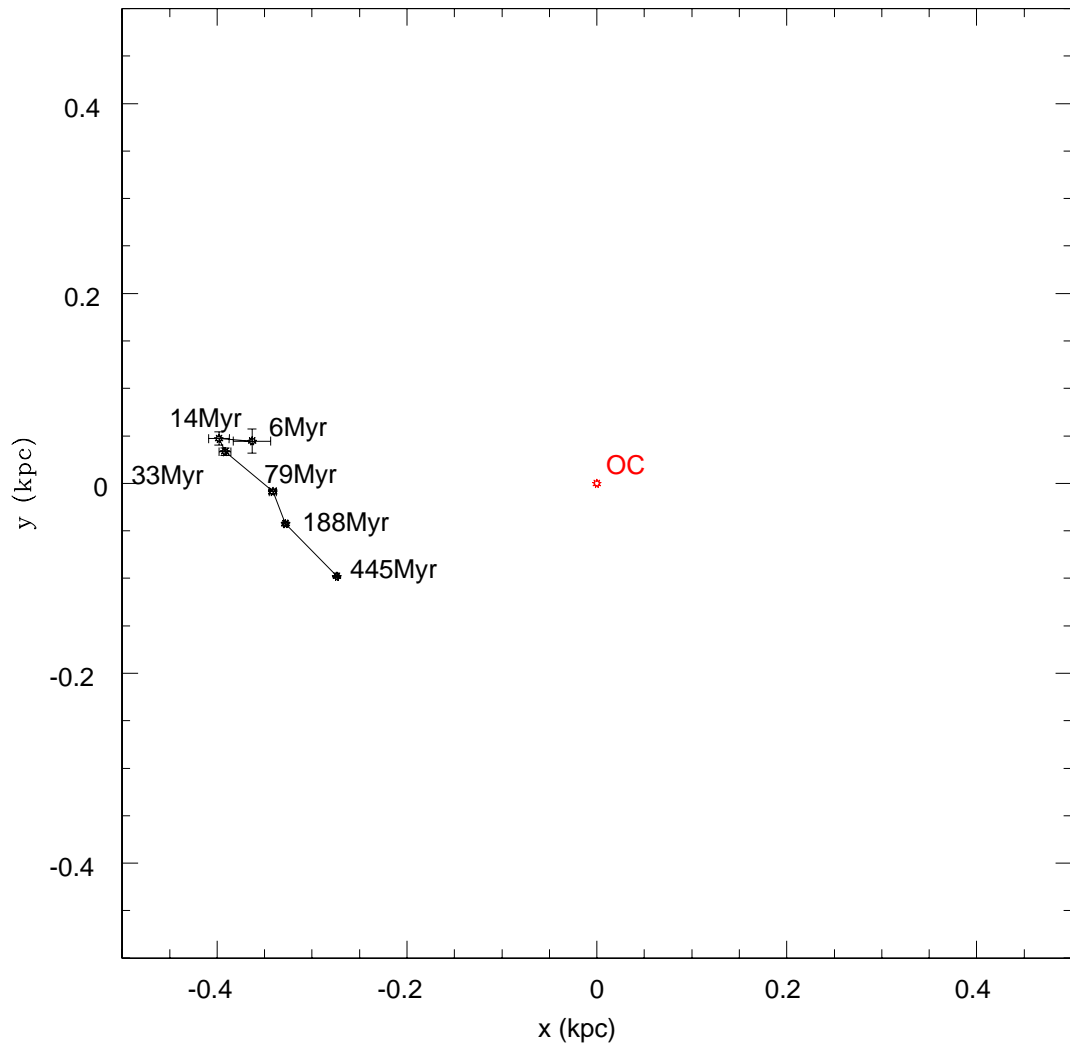
Figure 4.12: The figure depicts the locations of the center of the number density distribution of stars tagged with various upper age cut-offs in the projected sky plane for the SMC (table 4.1). The error bars are shown and the optical center is shown in red.

4.5 Discussion

The case of the SMC has been found to be different from the LMC. We have detected peaks of star formation at 0 - 10 Myr and at 50 - 60 Myr. The recent star formation is not found to be as structured as in the LMC. We have detected a shift in the center of the stellar population younger than 500 Myr. This might be due to the interaction of the SMC with the LMC about 400 Myr ago, as suggested by the coincident star formation

(H&Z09). We have detected an enhanced shift in the center of the population in the 200 - 40 Myr age range, which is similar to that found in the LMC. It can be inferred from figure 3.15 that the directions of the lines connecting the LMC and the Galaxy to the SMC, are similar. This means that the gravitational effect of the LMC and the Galaxy on the SMC will be in the similar direction. Thus, shift in the center of the stars in the 200 - 40 Myr age range may be a combined effect of the LMC as well as the perigalactic passage. In the SMC, we also see that the northeastern regions are active in star formation, relative to the south and the west. This may also be due to the effective compression of the H I gas in the northeastern regions of the SMC, owing in turn to the motion of the LMC-SMC system in the halo of the MW.

To summarise the recent star formation in the SMC is complicated because of the combined gravitational effect of the LMC and the Galaxy, especially with both of them located in the same direction. Thus, disentangling the effect on the SMC caused by its interaction with the LMC and the effect of the perigalactic passage may be difficult.

4.6   Appendix B: Error analysis

The error analysis is done with the same procedure mentioned in section 3.6. We derived the error in the estimated values of extinction and LSFE age using two methods: (1) synthetic CMDs and (2) the propagation of errors. We synthesised CMDs with an IMF 2.35, in the mass range 0.6 - 20 M⊙. The observed (typical) photometric error is incorporated. The Marigo et al. (2008) isochrones for metallicity 0.004 are used. Synthetic CMDs are created for turn-off ages in the range of 10 to 100 Myr. We performed the same analysis on the synthesised data. For each population, we estimated the LSFE age and extinction. To understand the effect of sampling, the analysis was repeated by varying the total number of stars in a CMD. We applied an A_v of 0.46 mag to synthesise the CMDs. The LSFE age and extinction estimated from the synthetic CMDs were compared with the input values to find the error. To incorporate the effects of sampling, the number of stars (or total mass) is also varied. Synthetic CMDs are created with a wide range in the number of stars (more as well as less than that found typically in the observed CMDs). The input parameters for the synthetic CMD and the estimated results for a single age are tabulated in table 4.2. Columns 1, 2, and 3 are the log (age), the total number of stars and the total stellar mass in the synthetic CMD. The total stellar mass can be used to estimate the typical star formation rate, which is detected using this method (and the cut-off) as a function of age. The star formation rate can be estimated by dividing the total mass with

Table 4.2: The input parameters to the synthetic CMD and the estimated LSFE, A_v values in the SMC. The extinction applied for synthesising CMD is 0.46 magnitude.

log(age)	nstar#	Mass($M_\odot$)	LSFE log(age)	derived A_v
7.50	500	1123.1	8.11	0.4290
	1000	2372.7	7.95	0.4712
	1500	3666.4	7.62	0.5332
	2000	4987.3	7.54	0.5630
	2500	6299.9	7.54	0.5630
	3000	7663.7	7.54	0.5630
	3500	8990.9	7.54	0.5630
	4000	10392.2	7.54	0.5630

the age range corresponding to the M_v and the bin size. Column 4 and 5 are the estimated LSFE log (age) and extinction. The analysis was performed for various age ranges and the results are tabulated in Table 4.3. The columns are (log) age, estimated error in age, and the minimum mass (and hence the number of stars) required to produce the synthetic CMD, with the tabulated parameter. This number is found to be in the range 1500 - 2000 and is smaller than the number of stars found in the observed CMDs above the limiting magnitude. The maximum error in the extinction is found to be within 2.48 times the bin size (0.1 mag) of the (V−I) colour. The error in log (age) is found to be in the range of 0.01 - 0.17. This error is a sum of the error in the estimation of extinction and magnitude of the main sequence turn-off, the statistical error, and a typical photometric error.

The error in the estimated LSFE as a function of location is estimated using the second method using equations 3.4, 3.5 and 3.6. The spatial plots of the errors are shown in figures 4.13 and 4.14, for both the data sets MCPS and OGLE III. The error in log(age) varies from 0.06 to 0.12 similar to that in the LMC. The error is found to be higher in the central regions of SMC. It is the the densest region in the SMC and it may be the effect of the photometric errors due to the crowding. We identify a larger error for the OGLE III data than for the MCPS data for the central regions of the SMC. The error in the LSFE age, as estimated by the above two methods are comparable.

Table 4.3: The error in the derived ages estimated using synthesised data. The tabulated error holds for synthetic CMDs with minimum mass shown in column 3.

log(age)	error in log(age)	mass ($M_\odot$)
7.0	0.15	6298
7.2	0.17	6310
7.3	0.15	4975
7.4	0.14	3680
7.5	0.12	3666
7.55	0.11	3669
7.65	0.12	3680
7.70	0.07	3669
7.80	0.07	2356
7.90	0.05	2375
8.00	0.02	2366
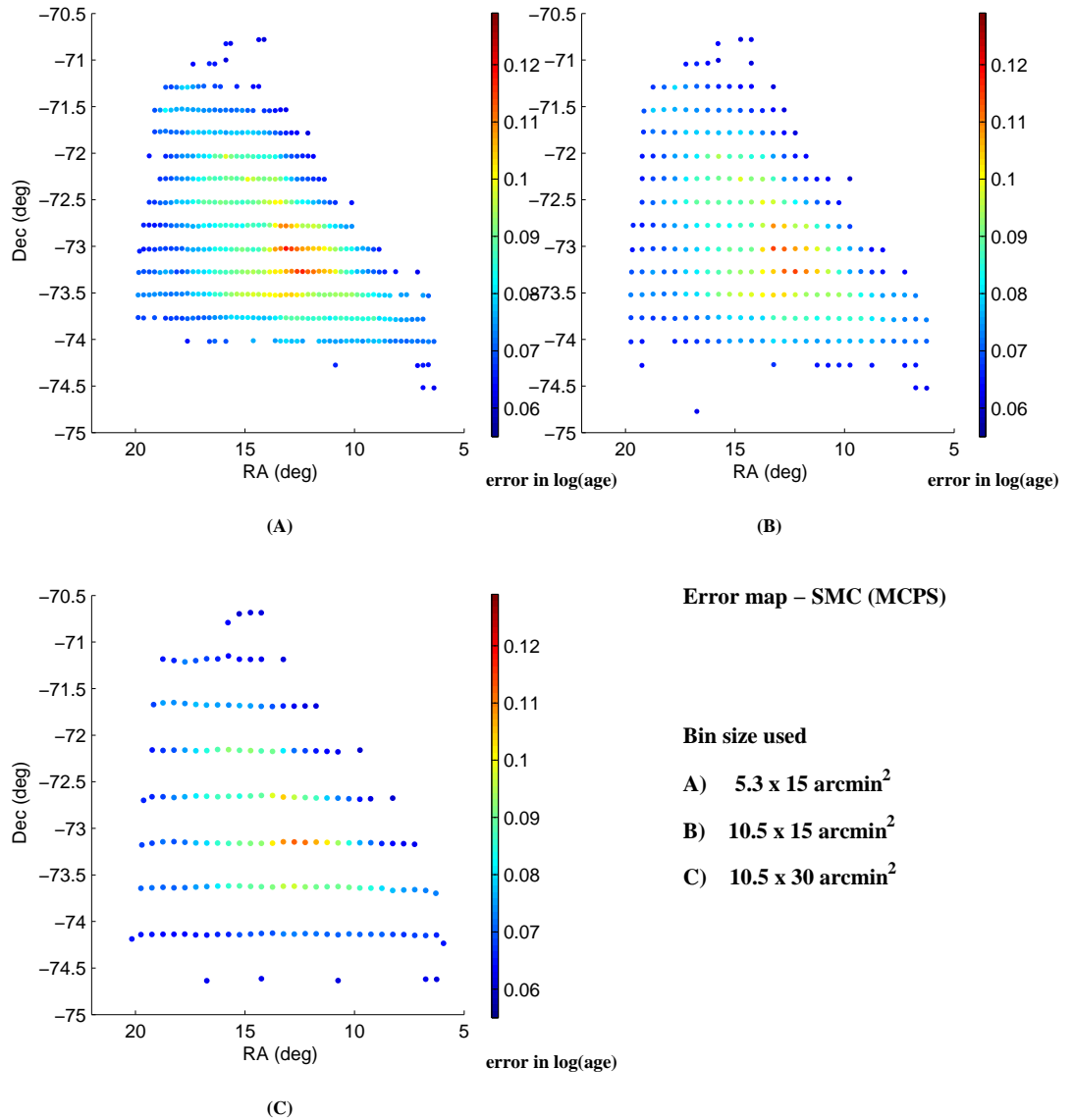
Figure 4.13: Error in age estimation shown as a map for the SMC using MCPS data for all the three area bins as indicated in the figure. Colour coding is according to the error in log(age).
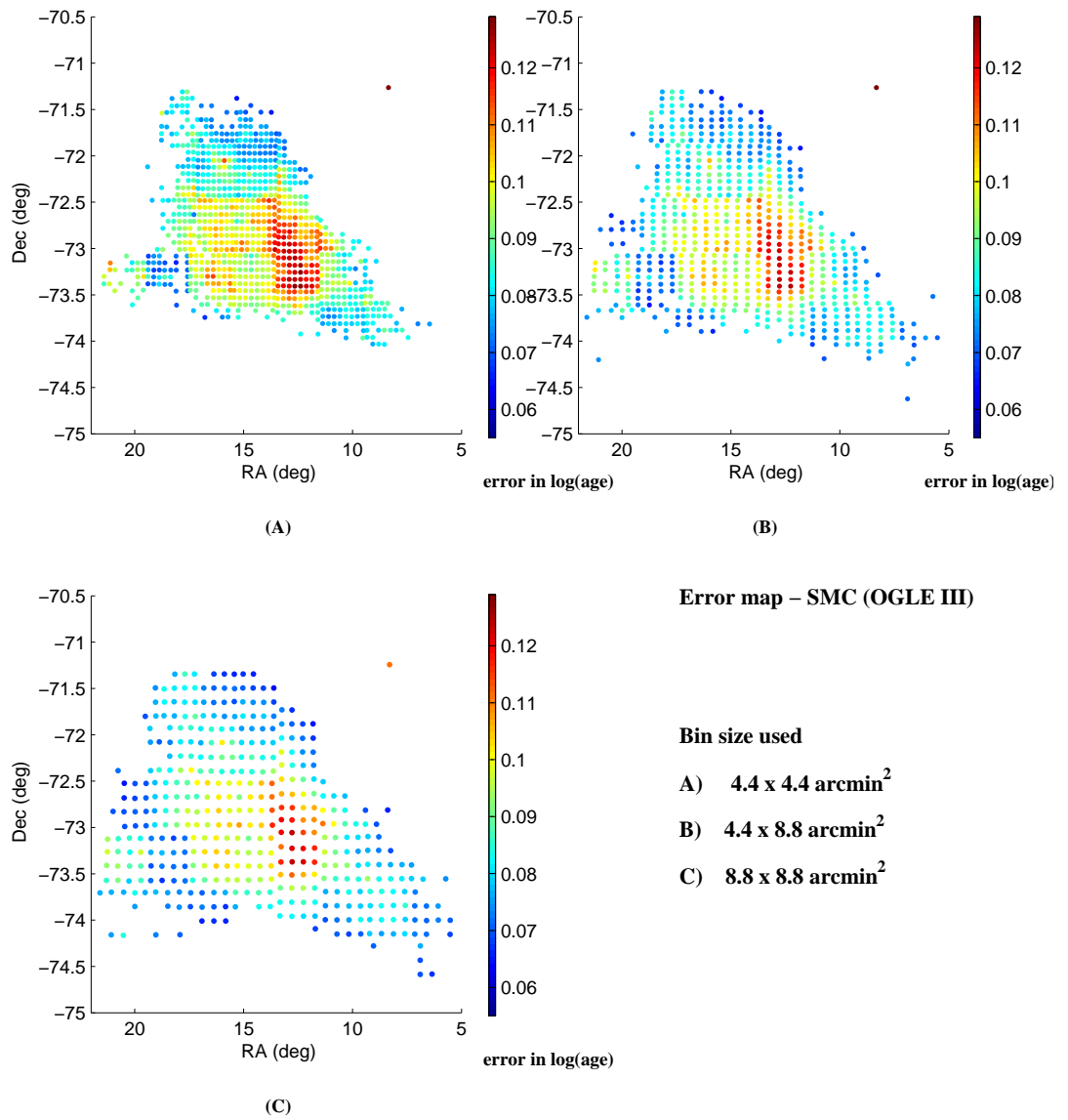
Figure 4.14: Error map for the SMC using OGLE III, similar to figure 4.13.

CHAPTER 5

H I KINEMATICS OF THE LARGE MAGELLANIC CLOUD*

5.1 Introduction

Our nearest neighbours, the MCs continue to be the two most studied objects in extra galactic astronomy. There are numerous studies using various tracers to understand the impact of the LMC-SMC-MW interactions. As we discussed in chapters 3 and 4 the RSFH analysis revealed valuable details of the LMC-SMC-MW interactions in the last 500 Myr. The star formation episodes in the LMC is found to be dictated by the peri-galactic passage as well as the hydrodynamical interaction with the hot gaseous halo of the MW. Similarly, the gas distribution in the LMC is expected to bear the signatures of its tidal interaction with the SMC and the Galaxy and also the hydrodynamical interaction with the Galactic halo. The gas distribution as well as the kinematics of the rotationally supported disk may be continuously modified or disturbed by the above mentioned tidal/hydrodynamical interactions. A detailed study in this direction can reveal details about the ongoing LMC-SMC-MW interactions.

To analyse the gas kinematics, we used the neutral atomic Hydrogen (H I) as tracer. The distribution of the H I in the LMC is dictated by filaments combined with shells and holes. The LMC is known to have a rotationally supported disk and its structural parameters as delineated by the gaseous as well as stellar distribution are estimated by various studies. The summarised viewing angles are, an inclination in the range $25° - 35°$ and the PA of LON in the range $120° - 160°$ (van der Marel et al. 2009, Subramanian & Subramaniam 2010) for the stellar distribution, estimated with kinematic and photo-

---

*Results of this chapter are submitted to A&A and it is under review.

metric analyses. Recent estimates for the stellar kinematic major axis are, 131°, using carbon stars, with $di/dt \sim 0.0$ (Olsen & Massey 2007) and $142° \pm 5°$, using red super giants, with $di/dt = -184°/Gyr$ (Olsen et al. 2011) both estimated with the new proper motion values of Piatek et al. (2008) and Kallivayalil et al. (2006b), where di/dt is the rate of change of inclination which is a measure of precession and nutation of the LMC disk. Recently, van der Marel & Kallivayalil (2014) estimated the parameters as inclination = $39°.6 \pm 4°.5$ and PA = $147°.4 \pm 10°.0$ by combining their average proper motion measurements for stars in 22 fields, with existing line of sight velocity measurements for 6790 individual stars. The kinematic major axis for the gaseous distribution, estimated using the old proper motion (Jones et al. 1994), without a di/dt correction is about 168° (Kim et al. 1998), which clearly indicates the discrepancy between the kinematic parameters estimated using gaseous and stellar tracers. Thus, a re-estimate of H I kinematics of the LMC disk using the recent proper motion estimates is necessary. It has been recently realised that including the precession and nutation of the disk can change the estimated kinematics. Various features in the gas, which are connected to the MB, SMC and the LA have been found, but their formation and the details of the gas flow in these features are not clearly understood. Staveley-Smith et al. (2003) identified various arm like H I filaments (Arm E, B, S & W) in the H I distribution of the LMC. Kinematically different components in the gas and stars have been identified by various studies (Olsen et al. 2011, Casetti-Dinescu et al. 2012) and the reasons for the formation of these outliers are only suggestive. Olsen et al. (2011) found a kinematically distinct population of stars which are possibly counter-rotating and accreted from the SMC. These stars, around 5% of their total sample are associated with Arm E & B. Hence Olsen et al. (2011) proposed that Arm B and E may be signatures of gas accretion. He also suggested a possibility that arms could be counter-rotating. But if there is gas accretion present in the LMC, details on the possible direction of accretion, locations of accretion in the disk, etc are not known. Using N body simulations Diaz & Bekki (2012) predicted that, as a result of close encounters with the LMC, substantial fraction of the SMC gas is stripped and engulfed by the LMC. Nidever et al. (2008) found that a part of Arm B is connected to the MS. They also connected the LA feature with the arm E physically. They suggested that the LA and the stream connected to the MS originate from the H I over density region near 30 Doradus and gas leaves the LMC through both these streams. Thus, it is not quite clear whether there is gas infall or gas expulsion through these arms. We have performed a detailed analysis using H I data in an attempt to address the above issues.

The recent proper motion estimates of Piatek et al. 2008, Kallivayalil et al. 2006b,

Kallivayalil et al. 2006a and Kallivayalil et al. 2013 are very different from the older values and the estimation of the H I velocity field in the outer disk is affected by this change. Hence it is necessary to compute the H I velocity field in the LMC using the new proper motion values. In this study we computed the kinematic PA and the circular velocity curve using the data of Kim et al. (2003), after correcting for the transverse motion using the new proper motion estimates. The unresolved puzzles are the presence and origin of kinematical differences between stellar and gaseous distributions and the identification of the location, amplitude and origin of the non equilibrium features and their kinematics.

It is obvious that the structure, kinematics and the star formation history of the LMC is modified by its interaction with the MW and the SMC, even according to the first passage scenario. van der Marel (2001) found that the LMC is elongated in the general direction of the Galactic center and is elongated perpendicular to the MS and the velocity vector of the LMC center of mass. He suggested that the elongation of the LMC has been induced by the tidal force of the MW. According to the predictions of the N body simulations by Weinberg (2000), the MW tidal torques can cause the precession and nutation of the LMC disk plane. Mastropietro et al. (2005) claimed the combined effect of gravity and ram pressure can account for the majority of the LMC's kinematical and morphological features. According to them, the tidal forces exerted by the gravitational potential of the Galaxy elongates the LMC disk, forcing a bar and create a strong warp and diffuse stellar halo. The star formation in the central disk is dominated by the LMC bar. By applying new proper motion, Mastropietro (2009) found that the effect of tidal forces on the vertical stellar structure of the LMC are marginal and the tidal stripping is almost effectless. Subramaniam & Subramanian (2009) and Bekki & Chiba (2007) suggested that the off centered bar of the LMC could be resulted from the collision with the SMC.

Mastropietro et al. (2009) analysed the effect of the ram pressure on the gas distribution and star formation in the LMC. They found a compression of the gas in the leading edge. They also found enhanced star formation activities in the leading border and eastern part of the disk (where the 30 Dor and most of the SGS are located) in last 30 Myr. The study by Indu & Subramaniam (2011) on the RSFH of the L&SMC shows that the recent star formation in both the Clouds is dictated by the perigalactic passage. In the first passage scenario, the LMC has probably had its closest approach about 200 Myr ago. This event is likely to have had a significant impact on both the Clouds, especially on the LMC. There is an enhanced star formation detected in the northern regions of the LMC disk around 200 Myrs ago and in the north eastern part of the disk in the last 40

Myr. This was explained as a combined effect of the gravitational/tidal interaction of the Galaxy and the effect of ram pressure due to the motion of the LMC in the Galactic halo towards NE.

van der Marel (2001) calculated that the tidal force from the MW on the LMC is 17 times larger than that from the SMC. He suggested that the tidal effect of the SMC on the LMC is negligible compared with that of the MW. Besla et al. (2012) illustrated that the observed irregular morphology and internal kinematics of the Magellanic System (in gas and stars) are naturally explained by interactions between the LMC and the SMC, rather than gravitational interactions with the Galaxy. They also demonstrated that the off center, warped stellar bar of the LMC and its one armed spiral, can be naturally explained by a recent direct collision with its lower mass companion, the SMC. A stellar counterpart of the H I MB that was tidally stripped from the SMC ~200 Myr ago during a close encounter with the LMC, is discovered recently by Nidever et al. (2013b).

In this study we identified the mean H I disk of the LMC and presented the kinematical properties of the H I disk, and hence kinematic outliers are identified. We studied the kinematics of the LMC to an extended region of about three to four times the area of the ATCA/Parkes data, which also includes the MB. We utilized the GASS and LAB all-sky survey data sets for this purpose. We used two recently published values of proper motion, in order to compare their effect on the estimation of the kinematic properties. We also demonstrate the effect of precession and nutation (caused by the MW tidal torques) on the estimated kinematic parameters as a function of radius.

5.2   Data

We make use of three different H I velocity data sets for the analysis. They are the combined data set of ATCA/Parkes, the GASS and the LAB data sets. The ATCA/Parkes data cover only the disk of the LMC and have the highest spatial resolution to study the LMC kinematics in detail. The other two are all sky survey data, which are ideal for analysing the kinematics to a larger spatial extent. In this study we used the published H I velocity data of the LMC from Kim et al. (2003) observed with ATCA and Parkes telescope. The spatial resolution of the combined data set is $1'$ and its velocity resolution is 1.65 km s^{-1}. The area covered is around $13° \times 14°$. We used the stray radiation corrected second data release of GASS (The Parkes Galactic all sky survey data, McClure-Griffiths et al. 2009 and Kalberla et al. 2010). The spatial resolution is $4'.8$ and the velocity resolution is of the order of 0.8 km s^{-1}. GASS data set has 1137 velocity frames

from which the velocity frames for the LMC and the MB are selected. For GASS we have an area coverage of $20° \times 20°$. We also analysed the LAB data (Leiden Argentine Bonn Survey, Kalberla et al. 2005). LAB has a velocity resolution of 1.3 km s^{-1} and a spatial resolution of $36'$. LAB data is available as velocity cubes with 891 velocity frames. We have selected the frames with the LMC and the MB. We selected a region with the LMC and the MB with an area coverage of around $24° \times 24°$.

It is important to note that, we have used the first moment map or the intensity weighted mean velocity map of all the three data sets for the analysis. Since we use the mean velocity for each pixel, the data is free from the multi peak velocity profiles. According to Kim et al. (1998) even though such a map is an imperfect way to analyse complex structure, it represents the best estimate of the mean velocity field which can be derived from the data set. Hence our analysis may only bring out coherent kinematic features which leave a major signature in the mean field. The method is insensitive to features with very less/insignificant contribution to the H I flux. Here we utilized the extensive sky coverage of the GASS and LAB surveys to trace the H I features in and around the LMC and the MB. The estimated intensity weighted mean velocity maps using GASS and LAB data sets compliments each other in spatial resolution.

5.3 Methodology

5.3.1 Transverse Motion Correction

The observed line of sight velocity is required to be corrected for the three dimensional space motion, precession and nutation of the system as described in section 2.2.4. The corrected velocity v_{mod} is estimated using equation 2.15. For the LMC we used the recent proper motion estimates by Piatek et al. (2008) and Kallivayalil et al. (2013). We keep the effect of inclination and do not do a deprojection. We used the H I kinematical center, $\alpha_0 = 5^h 17.6^m$, $\delta_0 = -69°02'$ and $v_{sys} = 279$ km s^{-1} estimated by Kim et al. (1998). According to van der Marel & Cioni (2001) the choice of center can be arbitrary to some extent since it does not effect the modelling significantly. Here we have used the di/dt values $-184° \pm 80°/Gyr$ (Olsen et al. 2011) and $-103° \pm 61°/Gyr$ (van der Marel et al. 2002) and compared the estimates. We used the value of θ to be $138°$, our initial estimate. The proper motion values μ_W & μ_N, (Piatek et al. 2008 and Kallivayalil et al. 2013) are converted to linear velocities, v_x & v_y using equation 28 of van der Marel et al. (2002). We estimated the transverse velocity v_t as the resultant of v_x & v_y and also estimated its direction θ_t. The values are tabulated in Table 5.1 with first row using values of Piatek

Table 5.1: Transverse velocity estimates using two proper motion measurements.

μ_W(mas/year)	μ_N(mas/year)	v_x(km s^{-1})	v_y(km s^{-1})	v_t(km s^{-1})	θ_t
$-1.96 \pm 0.04^{\dagger}$	$0.440 \pm 0.04^{\dagger}$	-462.6	103.8	474.1 ± 9.4	$77°.4 \pm 1^o.2$
$-1.91 \pm 0.02^{\ddagger}$	$0.229 \pm 0.047^{\ddagger}$	-450.8	54.0	454.0 ± 4.9	$83°.2 \pm 1^o.4$

†Piatek et al. (2008) ‡Kallivayalil et al. (2013)

et al. (2008) and the second row using Kallivayalil et al. (2013). van der Marel et al. (2002) using the mean of the proper motion estimates available till then, quote the values of v_x & v_y to be -399 km s^{-1} and 80 km s^{-1} respectively. Their estimate of v_t is 406 km s^{-1} and θ_t is 78°.7.

The map of the line of sight velocity corrected for systemic, transverse, precession and nutation motion, v_{mod}, estimated using ATCA/Parkes data is shown in figure 5.1. (We used $di/dt = -184°/Gyr$, and $v_t = 474.1$ km s^{-1}.) The equatorial coordinates (α, δ) are converted to Cartesian coordinates in kpc in a projected plane with respect to the LMC center (van der Marel & Cioni 2001) as described in section 2.2.1. This scheme is followed to estimate all the maps in this chapter. While analysing ATCA data for the first time, Kim et al. (1998) did the transverse motion correction of the observed velocity field with the proper motion estimates of Jones et al. (1994) with a transverse velocity 286 km s^{-1}. Further the analysis is done with an approximation of $di/dt = 0$, not accounting for the precession and nutation of the disk. The precession and nutation plays an inevitable role in kinematical study because it contributes a velocity gradient perpendicular to the PA of LON. Figure 3 of Kim et al. (1998) shows the velocity map. The PA of kinematic major axis can be identified as almost vertical in the northsouth (NS) direction with an average value of 168°. One can see vividly the difference in the velocity distribution and the rotational shift in the PA of the apparent kinematic major axis in figure 5.1, which is corrected for transverse motion with the new proper motion estimates and also corrected for the precession and nutation of the LMC disk, as described above. Thus, there is an apparent change in the kinematic major axis of the H I disk, and hence there is a requirement to re-estimate the parameters of the H I disk, such as the PA and peak velocity as a function of radius. We performed this task and the details are discussed in the following sections.

5.3.2 Annular Ring Analysis

To identify the mean H I disk of the LMC and reveal its kinematical properties, we used the following method. The line of sight velocity field corrected for transverse,
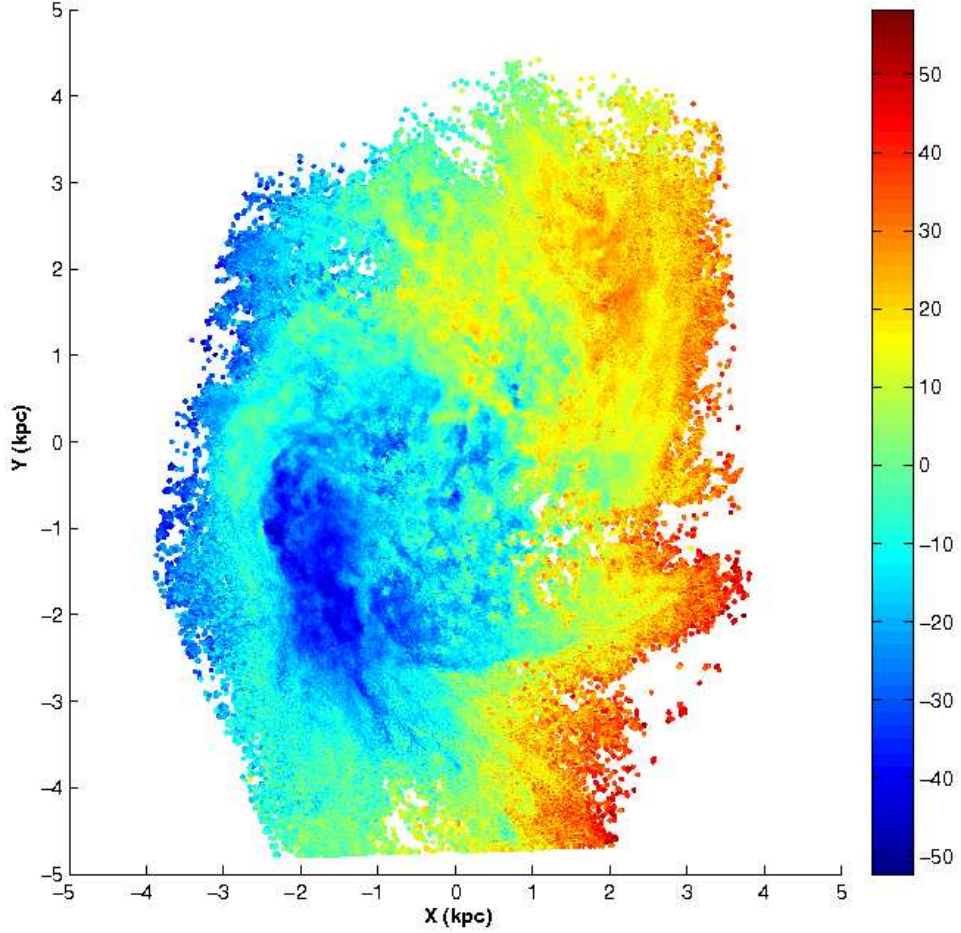
Figure 5.1: The LMC H I intensity weighted mean velocity map using ATCA/Parkes data, after correcting for transverse, systemic, precession and nutation motions. Colour coding is according to the variation in v_{mod} in km s^{-1}.

systemic, precession and nutation motions is estimated as mentioned above. The disk of the LMC is divided in to annular rings of width $0°.2$ according to the available spatial resolution of the data set. In each annular ring, we fitted a sine curve to the velocity field, the PA of maxima of which will be the PA of the kinematic major axis. We used the following equation,

$$v_{fit}(\rho, \phi) = v \, \sin(\phi - \phi_0) + \delta v_{sys} \qquad (5.1)$$

where v represents the amplitude of the sine curve which is expected to increase as a function of radius. ϕ is the PA measured from north towards east. ϕ_0 is the zero point of

the sine curve (the point where $v_{fit} = \delta v_{sys}$). The PA of kinematic major axis is derived as $\phi_0 \pm 90°$. We estimated the parameters for 29 annular rings covering a radius of 5°.7 of the LMC. Figure 5.2 demonstrates the fitted sine curves for annular rings at mean radii of 0°.1, 0°.9, 1°.9, 2°.9, 3°.9 & 4°.9. From the first fit, we removed points which deviate from the model by ≥ 12 km s^{-1}, (the choice of this cut-off is explained in section 5.4) and fit was repeated to make a refined model. The green points are the removed outliers, and only the black points are used for the refit. The refit thus excludes all possible outliers and the estimated parameters are likely to be as close as possible to the true disk parameters. One can see the amplitude of the sine curve increases with increasing radius. It can be seen that in the panel 'f' for 4°.9 radius the data points are sparse. This happens in the outer most 7 annular rings from a radius of 4°.5 to 5°.7. After a radius of 4°.3, the azimuthal variation of velocity along annular rings does not give a continuous sine curve due to inadequacy of data coverage.

Panel 'a' of figure 5.3 shows the variation of the estimated PA as a function of radius with and without the precession and nutation correction. The curves for two different estimates of di/dt and v_t are shown. The overall effect is that as the magnitude of di/dt increases the estimated PA decreases. The variation of PA across the radius is only mild, except in the central region. The mean values of PA estimated for different radial extents are tabulated in Table 5.2. The first row gives the estimate for the whole radius range till 5°.1 after which the fit error is more than $\sim 11\%$. The second row gives the estimated PA values omitting the central 0°.5 since the central region shows a twist in the PA with values $> 180°$. One can notice that the PA values decrease after a radius of 4°. Hence omitting the values after 4° the mean PA is tabulated in third row. The mean values of PA tabulated in the fourth and fifth columns are estimated with different v_t values, but same di/dt. It can be seen that there is no significant change in the value of mean PA. The last column gives the calculated standard deviation for the PA estimates in the fourth column. (The standard deviation estimates for the corresponding PA estimates in other columns are found to be comparable with these values.) Previous estimates for the stellar kinematic major axis are, 131°, using carbon stars, with $di/dt \sim 0.0$ (Olsen & Massey 2007) and $142° \pm 5°$, using red super giants, with $di/dt -184°/Gyr$ (Olsen et al. 2011) both estimated with the new proper motion. These values are comparable to the kinematic major axis of the H I disk within the estimated errors. Hence, our results suggest that the kinematic major axis of gaseous and stellar components of the LMC are similar. The panel 'b' of figure 5.3 shows the radial variation of circular velocity inferred from annular ring analysis. The solid curves shown are not the conventional rotation curves since we

116
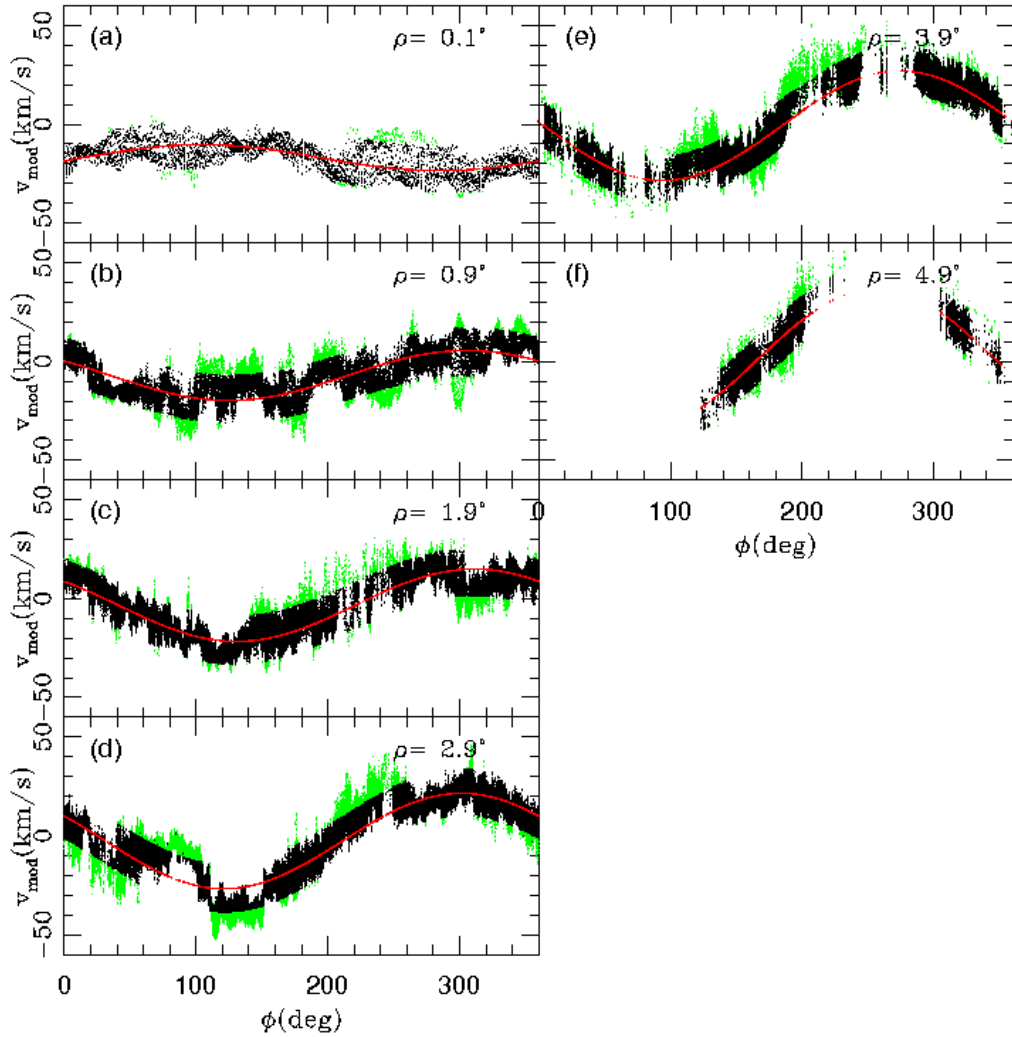
Figure 5.2: The azimuthal variation of v_{mod} and the fitted sine curves for annular rings. Panel (a) at mean radii of $0°.1$, (b) $0°.9$, (c) $1°.9$, (d) $2°.9$, (e) $3°.9$, & (f) $4°.9$. The green points are the removed outliers, and only the black points are used for the refit or first iteration.

have not performed inclination correction and are the velocity distributions including the effect of inclination. The velocity varies almost linearly till a radius of $2°.9$ and then shows a dip and again rises. Also one can notice that the velocity increases directly with the magnitude of di/dt. Both the panels 'a' and 'b' of Figure 5.3 also demonstrate that the kinematic parameters of the H I disk estimated using the proper motion values of Piatek et al. (2008) and Kallivayalil et al. (2013) remain the same within errors. Hence for further

Table 5.2: The PA estimated for various radial extents using different v_t, di/dt values. The last column is the estimated standard deviation in PA. The di/dt values are given $/Gyr$.

$\rho(°)$	$MeanPA(°)$ $v_t = 474.1$ km s^{-1} $di/dt = 0.0°$	$MeanPA(°)$ $v_t = 474.1$ km s^{-1} $di/dt = -103°$	$MeanPA(°)$ $v_t = 474.1$ km s^{-1} $di/dt = -184°$	$MeanPA(°)$ $v_t = 454$ km s^{-1} $di/dt = -184°$	$PA_{SD}(°)$
0.0 - 5.1	140	131	125	130	45
0.5 - 5.1	132	121	115	120	28
0.5 - 4.0	143	133	126	131	23

analysis, we used the proper motion estimates of Piatek et al. (2008). This also helps to compare the estimated values with the stellar kinematical parameters estimated by Olsen et al. (2011). The bold curve in orange shows the resultant curve from the refined model (after the first iteration, removing the outliers) the parameters estimated from which are used for further analysis.

Subramanian & Subramaniam (2013) in their Table 1 provided a summary of orientation measurements of the LMC disk plane. The table lists out the estimated inclination and PA values in literature till date using various tracers. For adopting an inclination we estimated the weighted average of inclination values in the table. The deprojected rotation curve as estimated, applying this weighted average, $i \sim 25°$, is shown as a dotted curve in figure 5.3 panel 'b'. The value of v_{rot} shows a decline after $2°.9$ radius at 57 km s^{-1}. At $4°.3$ the v_{rot} is $\sim 70 kms^{-1}$ after which the fitted data seem to be sparse. We are unable to trace the flat part of the rotation curve with the coverage of ATCA/Parkes data. The deprojected rotation curve estimated by Kim et al. (1998) using H I shows a sudden decline at a radius of $2°.8$ and v_{rot} of 63 km s^{-1}. Kim et al. (1998) attributes this decline to non-circular motions due to various reasons like interaction with the SMC and the MW, presence of bar etc. Olsen et al. (2011) estimated the rotation curve using 738 red super giants with a maximum value of v_{rot} 87 ± 5 km s^{-1} at a radius of $2°.8$, (and goes flat beyond that) which is said to be consistent with the H I rotation curve. Piatek et al. (2008) presented a rotation curve with amplitude 120 km s^{-1} at a radius of $4°.6$ using HST data and van der Marel et al. (2002) estimated 50 km s^{-1} at $4°.6$ using carbon stars. van der Marel & Kallivayalil (2014) estimated the rotation curve of the LMC (their figure 6). Their estimate of the velocity at similar radius is found to be consistent with our estimates. As mentioned earlier, we used the parameters estimated before doing the deprojection but after the first iteration (the bold orange curve in figure 5.3) for further analysis.
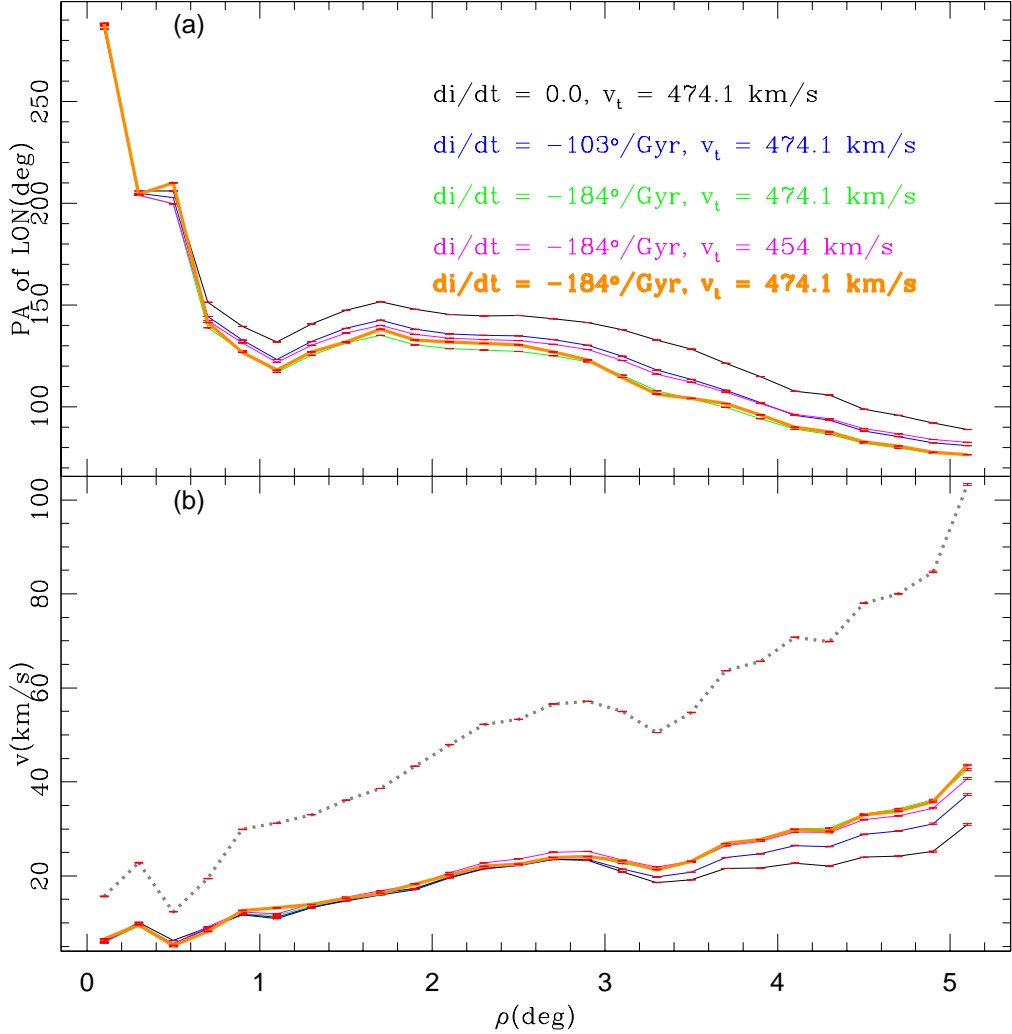
Figure 5.3: Panel (a) shows the variation of PA of LON as a function of radius. Panel (b) shows the radial variation of circular velocity. Five curves are shown for various v_t, di/dt values as mentioned in panel (a). The bold orange curve is from the first iteration after removing the outliers. The parameters corresponding to this curve is used for further analysis. The dotted curve in panel (b) is the deprojected rotation curve. The error bars are shown in red.

5.3.3 The mean H I disk

As mentioned above, we estimated the expected velocity distribution for the 29 annular rings. Combining the velocity distributions of these 29 annular rings we computed the velocity map of the mean H I disk of the LMC, shown in figure 5.4. We used $di/dt =$

$-184°/Gyr$, and $v_t = 474.1$ km s^{-1} to estimate figure 5.4. One can compare this velocity map of the mean H I disk of the LMC with the observed velocity map shown in figure 5.1. Our map estimated by the method of annular rings, beautifully reproduces almost all the features of the observed map, except the dark blue stream of points representing the high velocity gas moving towards us, located in the SE direction. We also expect outliers in the periphery of the western side of the disk with dark red points. We discuss the identification and analysis of these outliers in detail in the next section.

The mean H I disk of the LMC, as shown in figures 5.2 and 5.3, suggest that even the averaged mean disk, which we have estimated has complicated kinematics. The inner regions are found to have different PA, when compared to the outer regions. The kinematics in the inner $1°$ is quite different in terms of velocity as well as PA. This might suggest a strong internal perturbation, could be due to the presence of the bar. The kinematics of regions outside the bar region is found to be quite smooth. Between the radius of $1.°0$ and $2.°9$, the disk is found to have similar PA and the velocity is found to increase with radius. After $2.°9$ radius, the disk shows effects of perturbation as seen by a sudden kink in the velocity and a gradual decrement in PA. The outer perturbation seen in the disk kinematics may be caused by MW-LMC-SMC interactions.

What we have estimated in our analysis is the average of the mean H I velocity field of the LMC, obtained from the intensity weighted velocity map. This mean disk is thus devoid of all small deviations in H I velocity, but will have the signatures of large scale or global events. This disk is likely to show disturbance/effect of any external interaction either tidal or hydrodynamical, by the MW as well as the SMC with respect to the mean disk. The annular ring analysis suggested the presence of deviations from the mean disk and these might be due to the above disturbance. Thus, in the following sections, we present the outlier maps, estimated as regions which show the kinematical deviations from the average of the mean velocity distribution.

5.4   Residuals & Outliers

After estimating the mean H I disk of the LMC, our next motive is to find the distribution of kinematic outliers. A detailed analysis can bring out the properties of the outliers with respect to the bulk motion in the disk. To distinguish the kinematic outliers, we estimated the distribution of the velocity dispersion about the mean disk velocity statistically. To estimate the velocity dispersion, we binned the velocity data in the projected X-Y plane, to subregions of area $17' \times 17'$. The number of data points in the subregions
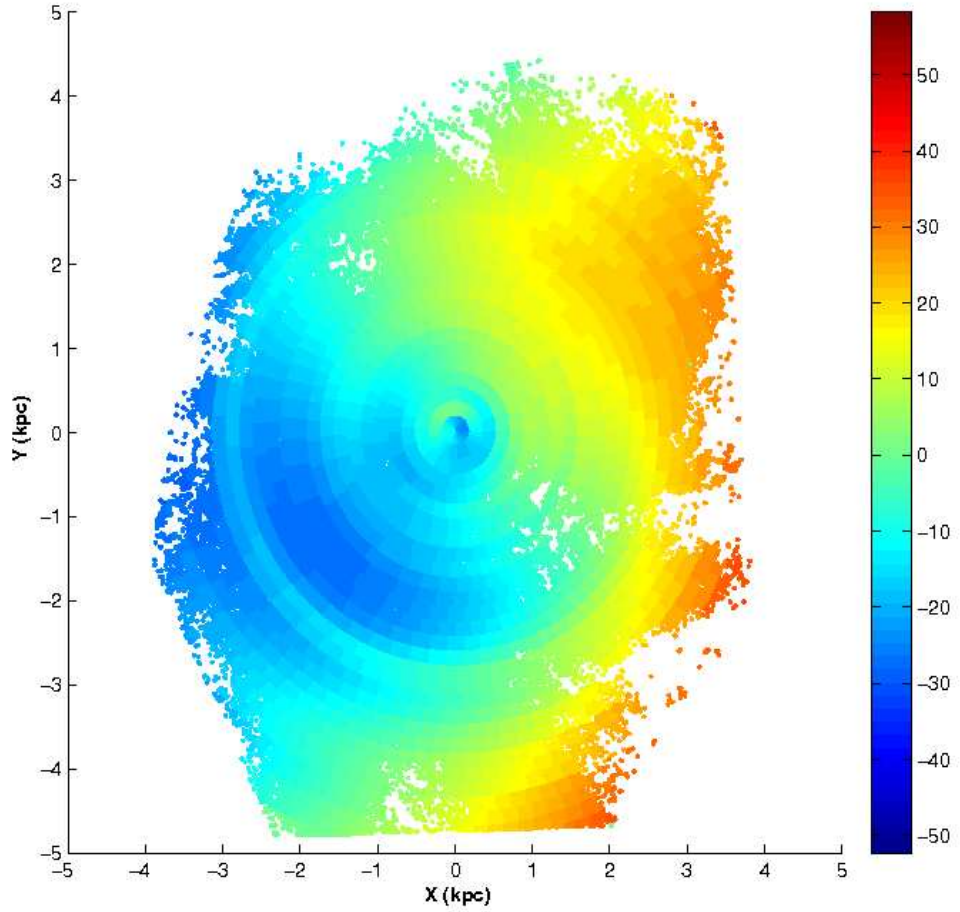
Figure 5.4: The estimated mean H I disk of the LMC. Colour coding is according to the variation in v_{fit} in km s^{-1}.

varied from 1 to 2500 and the maximum Poisson error in this estimation is 50. A statistical cut-off of 3σ is applied, so that the subregions with less than 150 data points are not considered for the analysis. For each selected subregion, the mean and standard deviation of the first moment velocity is found. The statistical distribution of the standard deviation (V_{SD}) is shown in figure 5.5, which shows a maximum value of about 13 km s^{-1} with an accuracy of 2 km s^{-1}. About 94.2 % of the data points are within a V_{SD} of 10 km s^{-1}. Therefore for further analysis the maximum value of V_{SD} is taken to be 12 km s^{-1}, including the bin width of 2 km s^{-1}. The dispersion distribution is found to be a narrow one as expected for a kinematically cold system and has a single peak at 6 km
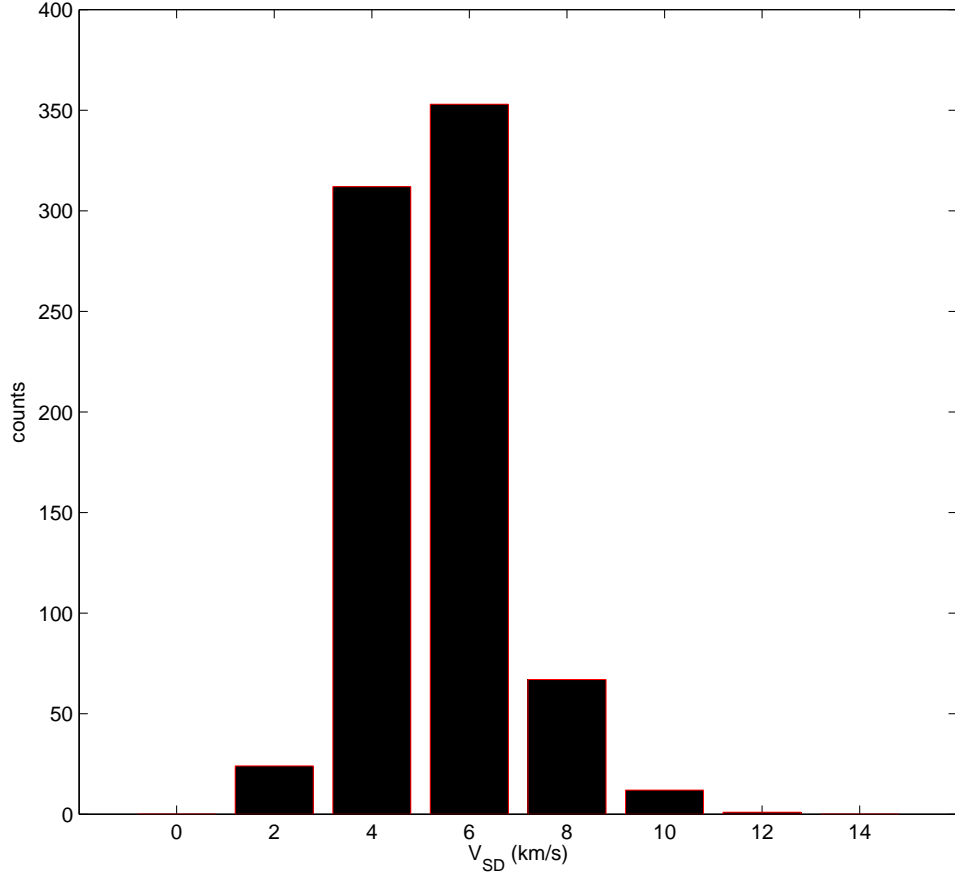
Figure 5.5: Statistical distribution of the standard deviation V_{SD} of the velocity field.

s^{-1}. Kim et al. (1999) estimated the velocity dispersion to be between 6.8 and 7.7 km s^{-1} and adopted a mean value of 7.3 km s^{-1} for the vertical velocity dispersion of the gas. Hence the two estimations of velocity dispersion match fairly well. In the V_{SD} map (figure 5.6), we could identify locations with higher value of V_{SD} around 12 km s^{-1} or more near the SEHO region, 30 Doradus and constellation III. Also there are regions with large deviation near the center and SW part of the center.

The residual velocity is estimated as the difference between v_{fit} & v_{mod}.

$$v_{res} = v_{mod} - v_{fit} \tag{5.2}$$

Data points which have $v_{res} > 12$ km s^{-1} (maximum value of V_{SD} + accuracy) are

122
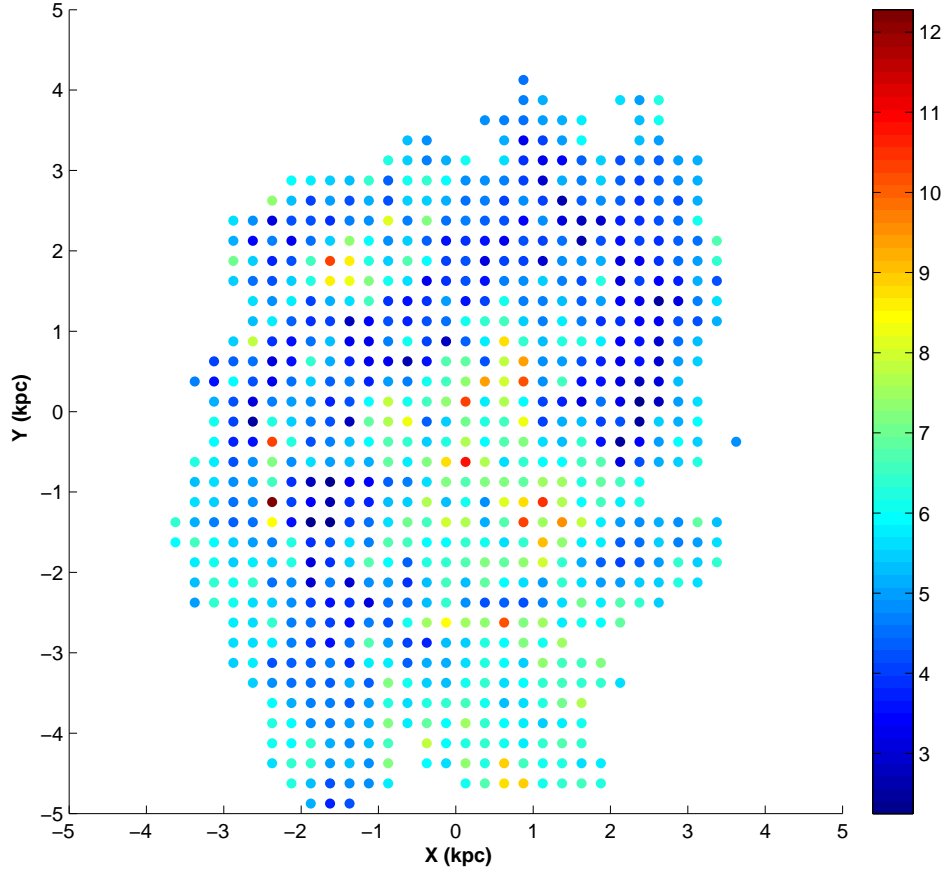
Figure 5.6: Map of the standard deviation V_{SD} of the velocity field.

defined as kinematic outliers. In the total set of H I data points 12.1% are identified as outliers using the above criterion. The fact that about 88% of the data points are within the estimated disk suggests that the estimated disk is indeed close to the true disk of the LMC and the deviating points are a minority. These kinematic outliers can be classified widely into two categories, type 1 outliers, where the observed velocity v_{mod} shows an opposite sense of rotation compared to the expected v_{fit} and the type 2 outliers wherever the v_{mod} and v_{fit} rotate in the same sense. The type 1 outliers will be counter-rotating only if these outliers are located in the plane of the LMC disk. The type 2 outliers can be further classified into faster and slower components. In other words, if the $v_{mod} > v_{fit}$ by 12 km s^{-1} or more, and if both v_{mod} & v_{fit} bear same sign, then we define it to be a faster type 2. In the same way if $v_{mod} < v_{fit}$ by 12 km s^{-1} or more and both have same sense of

rotation, then we identify it as a slower type 2. If the magnitude of the $v_{res} > 12$ km s^{-1} and if v_{mod} and v_{fit} bear opposite signs then the location is identified to belong to type 1 outlier. With an inclination of around 25° and with the NE part of the disk towards us, the mean disk of the LMC is found to have a clock-wise rotation. Also, the present model is valid only upto a radius of 4°, hence the differentiation of an outlier to be of particular type is possible only within this radius. The locations with such type 1 and type 2 data points are identified and addressed in detail in the following sections.

5.4.1 Type 1 kinematic outliers

We found around 2.7% of the total data sample to be type 1 outliers. Map of the type 1 kinematic outliers is shown in figure 5.7. In the eastern side of the disk, the type 1 gas forms an arm like feature (the pale green stream of points extended vertically from north to south, marked as E in figure 5.7), very similar in location to Arm E (Staveley-Smith et al. 2003). Olsen et al. (2011) also traced their counter-rotating stellar component to be similar in location to Arm E and concluded that Arm E may not be coming out of the LMC, but probably falling in. We also find that Arm E is part of the type 1 component in the LMC, which has a velocity very close to the systemic velocity. If we examine figure 5.7, the same component is found to continue to the north and NW. The data points here have velocity around -10km s^{-1}, whereas the disk rotation velocity is about 25 km s^{-1}. It is tempting to extend the Arm E up to the NW. Another feature of interest is the component near the southern end of Arm E at X=+0.5, Y=−4.5 having velocity around 10 km s^{-1} towards us (the light blue points). This feature is at a radius of about 5° and we cannot classify them reliably.

There are a few more specific locations in figure 5.7 which attract our attention where we found regions which are spatially concentrated but cover a large range in velocity. One such location is around X=+0.8, Y=+0.6, where we see a concentration of dark blue points surrounded by light blue points. If we trace the same location in the V_{SD} map (figure 5.6), it shows a relatively high standard deviation in velocity. A similar location can be found near constellation III (the small black dot at X=−1.5 and Y=+2 in figure 5.7). The location of SGS as well as Giant Shells (GS) (from Kim et al. 1999) are shown in figure 5.7. Only a few SGS and some GS are located along the blue/green points distributed between the above two locations. In general, the locations of SGS as well as GS are not coincident with the type 1 outliers.

Figure 5.7: Map of the kinematic outliers identified as type 1. Colour coding is according to the variation in v_{mod} in km s^{-1}. The big black dot represents the location of 30 Doradus and the small dot is constellation III. The locations of H I SGS are shown as stars and the locations of H I GS are shown as diamonds (from Kim et al. 1999). The possible location of arm E is marked.

5.4.2 Slower type 2 kinematic outliers

If we consider the kinematic outliers which rotate in the same sense as the mean disk rotation of the LMC, type 2, then there are two components in this class, one with apparent faster rotation, faster type 2, and the other with apparent slower rotation, slower type 2. Figure 5.8 shows the map of slower type 2 outliers. This component which constitutes 3.9% of the H I data, has velocities in the range −14 to +16 km s^{-1}. The statistical

distribution is a narrow one with a single peak at around -6 km s^{-1} which constitutes around 12000 points. The slower type 2 component is accumulated mostly in the SE of the LMC disk. The light blue stream of points located vertically in the NS direction, in the SE part of the disk, closely resembles the location of Arm E marked as E, in figure 5.8). As its location is coincident with the location of the type 1 gas (arm E), it is possible that the slower type 2 and the type 1 are connected. In figure 5.8, we also notice that the presence of slower type 2 in the central as well as in the NW regions. As the southern most point is outside the radius of $4°$, we cannot reliably classify them.

5.4.3 Faster type 2 kinematic outliers

The velocity map of the faster outlier component, which is nearly 5.5% of the total H I data, has v_{mod} ranging from -50 to $+60$ km s^{-1} as shown in figure 5.9. This component does not cover this whole velocity range. The statistical distribution is not continuous and has prominent peaks at around -32 to -30 km s^{-1}, at -40 km s^{-1} which constitute around 5000 and 6500 data points respectively and smaller peaks at ±20 km s^{-1}, which constitutes around 3000 points each. We found a stream of H I gas identified as faster type 2 (the dark blue stream of points in the SE direction, marked in figure 5.9 as B), coincident with Arm B (Staveley-Smith et al. 2003). As shown in Staveley-Smith et al. (2003), Arm B is pointed towards the MB/SMC. Arm B is found to disappear near the 30 Doradus region (close to X=-1.5 and Y=0), shown as big black dot. At this location, one can also see one section of the structure like digit 8, as seen in figure 1 of Staveley-Smith et al. (2003). Also, the Arm B splits up into three parts near the central LMC. If arm B is connected to the MB, then this might suggest a connection of gas from the LMC disk to the MB/SMC. van Loon et al. (2013) suggested a possibility of 30 Dor region accreting cool gas.

We also notice another less prominent arm like structure resembling Arm B, but found in the eastern part of Arm B. This is a newly identified structure and we call it the 'Outer Arm' (marked in figure 5.9). The newly identified Outer Arm seems to be located to the east of Arm B and moves in through the outer part of the LMC disk. This stream can be traced from X=-2 and Y=-4.5 up to X=-3, Y=$+1$, close to the location of the SGS in the NE. At this point, the stream gets spread and we see a large area occupied by this component (a pool of blue points). This is also the region which is expected to get compressed due to the motion of the LMC in the halo of the MW (at the PA $\theta_t \sim 80°$). At this point, some part of the gas gets spread to larger area, loses velocity and falls/moves to the inner part of the LMC disk. We also notice the presence of a few SGS coincident
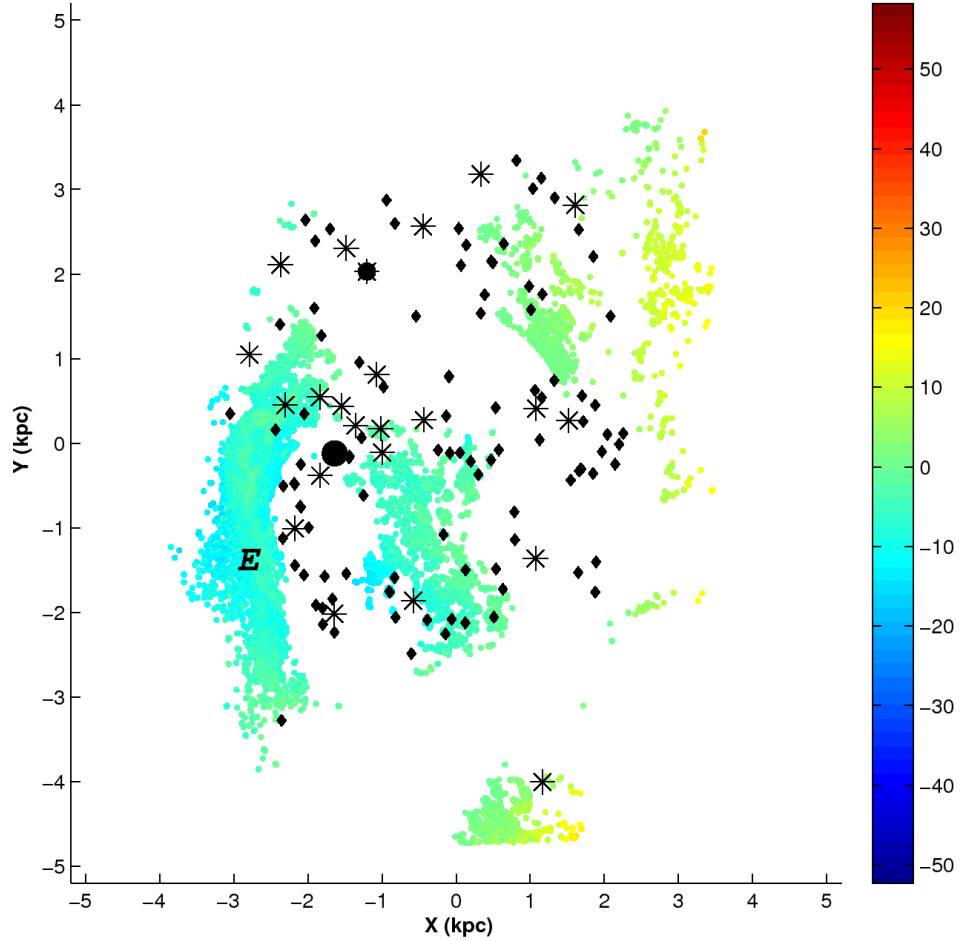
Figure 5.8: Map of the slower type 2 kinematic outliers. Colour coding is according to the variation in v_{mod} in km s^{-1}. The big black dot represents the location of 30 Doradus and the small dot is constellation III. The locations of H I SGS are shown as stars and the locations of H I GS are shown as diamonds (from Kim et al. 1999). The possible location of arm E is marked.

with this location. On the other hand, a stream can be traced to continue beyond this pool of blue points, towards the north. We can notice that this stream changes velocity as it moves towards the west. This change over from the blue points to the red points suggests a change in the direction of motion. That is, the gas which was moving towards us, now starts moving away from us, similar to a change over across the minor axis of a rotating disk. Near the SGS in the NW side of the disk (at X=+2, Y=+3), the stream

splits into two, one falls towards the inner part of the disk probably after losing velocity and the other stream continues in the outer radius. The inner stream is found to be similar to Arm W as identified by Staveley-Smith et al. (2003) (marked as W in figure 5.9). This stream then can be traced upto the SW corner, where it joins the large area occupied by the high velocity gas. Beyond this point, considerable spread in the velocity as well as the location of the stream can be noticed, suggestive of the gas getting dispersed. The locations of many of the SGS fall in the path of the identified outliers, suggesting that this gas could be interacting with the gas in the disk resulting in vigorous star formation and the creation of such shells. At the location of the shells, a part of the outer stream is found to move towards the inner LMC, may be due to loss of velocity. These outliers appear to have almost completed one rotation of the LMC. We detect high velocity (red) points in the SW/south of the LMC disk and these are suggestive of gas moving away from us. There is a possibility that this gas could leave the LMC disk if the velocity is high enough to overcome the gravitational force of the LMC. The direction of this possible outflow is diagonally opposite to the direction of movement of the LMC.

According to Mastropietro et al. (2009) the current orientation of the LMC disk with respect to its orbit is nearly edge on, whereas its orientation according to Besla et al. (2007), is $-30°$. Also the motion of the LMC in the Galactic halo is analogous to a wedge moving super sonically with the vertex facing upstream. As soon as the satellite moves in the surrounding medium, the external gas density develops a peak centered at a PA of the direction of its movement. (In the case of the LMC disk this PA is $\sim 80°$ as the average of θ_t values from table 5.1.) The disk particles localized in regions of maximum ram pressure get compressed and move on to inner orbits while their circular velocity increases consequently. This may be the reason for the origin of high velocity gas, which moves along with the disk. The NE region is expected to be compressed due to LMC's motion. The high velocity streams which we identify in the west, including Arm W, might have caused by the above mentioned effect. Also, in the diagonally opposite end south/SW there will be gas stripped away due to ram pressure. The high velocity red points which looks like an outflow can be part of the ram pressure stripping. We also identify a faint feature, similar to the Arm S (Staveley-Smith et al. 2003) at X=0, Y=-2.5, (marked as S in figure 5.9) located to the south of the high velocity gas (pool of red points) near the SW side. The shape and curvature of Arm S is very different and it does not appear to be connected to any other feature. As this arm appears immediately to the south of the large velocity gas, there is a possibility that the gas in this arm is likely to be coming from the interaction of the high velocity gas with the disk, as part of the gas
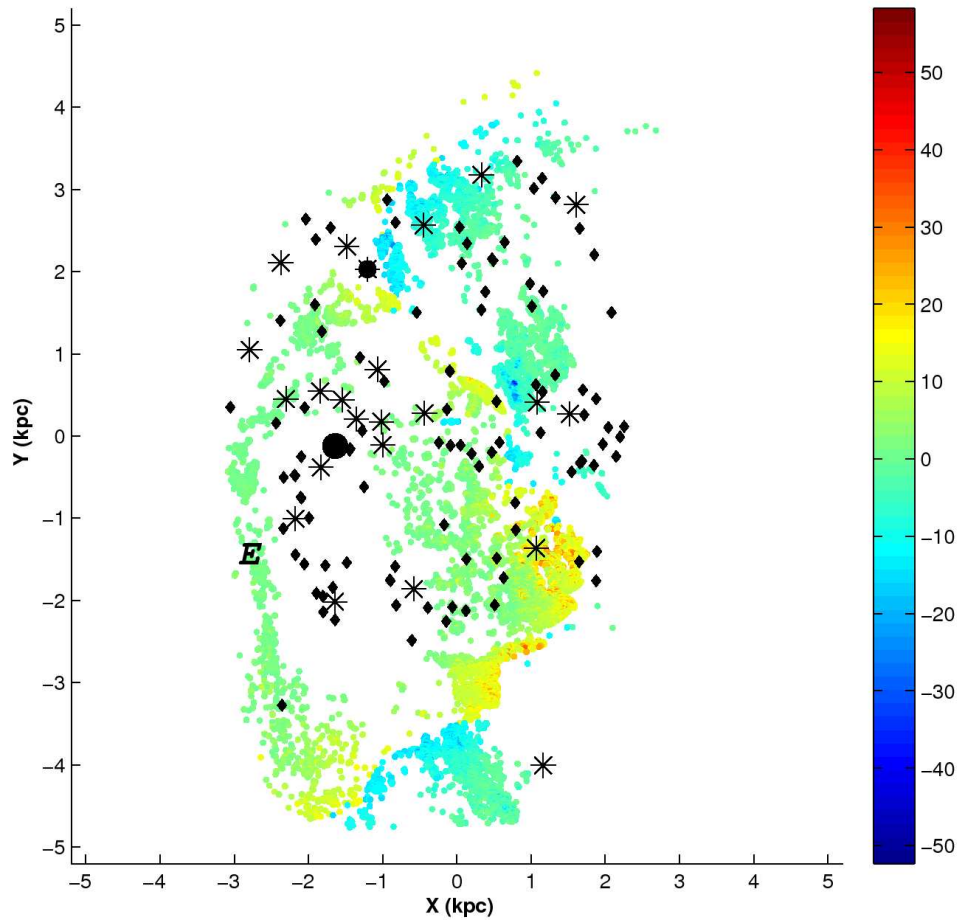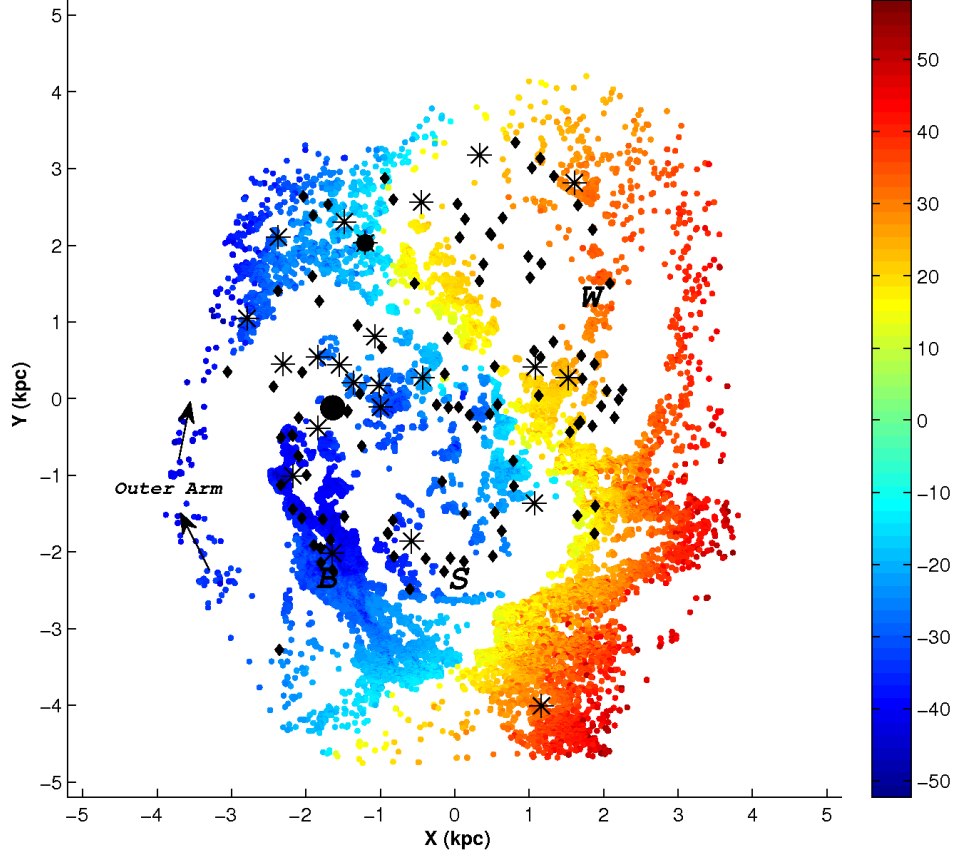
Figure 5.9: Map of the faster type 2 kinematic outliers. Colour coding is according to the variation in v_{mod} in km s^{-1}. The big black dot represents the location of 30 Doradus and the small dot is constellation III. The locations of H I SGS are shown as stars and the locations of H I GS are shown as diamonds (from Kim et al. 1999). The Outer Arm, is marked along with arms B, W & S.

spiralling into the inner LMC due to loss of angular momentum. This is similar to the features seen in the NE side and Arm W. Hence we speculate that the Arm S could be a feature which takes the gas in the outer LMC to the inner LMC. In summary, the arms S and W could arise due to the gas compression in the NE direction caused by the motion of the LMC.

We thus identified and located three types of H I kinematic outliers in the H I gas present in the LMC disk. The type 1 and the slow type 2 are mostly located in the SE region, which are identified as part of Arm E. The arm E is known to connect to the

LA. Arm B, Arm W and Arm S are detected as fast type 2 outliers and we also identify an eastern arm called Outer Arm. We need to understand the possible origin of these outliers. As suggested by Mastropietro et al. (2009), the faster outliers and the arms may be due to the effect of LMC motion in the MW halo. Also, the arm B and the Outer Arm point to MB/SMC. In order to connect these features outside the region observed by ATCA/Parkes, we have made use of two data sets which cover a larger area. These are described below.

5.5 LAB & GASS Data Analysis

ATCA/Parkes data does not cover the outer regions of the LMC and hence we are unable to trace various features to the outer disk of the LMC. In order to study their extensions, we have analysed the LAB as well as GASS data sets. We estimated the intensity weighted mean velocity map for both the LAB & GASS data sets. The intensity weighted average of the v_{los} is calculated for each pixel. These first moment maps provide the best estimate of the mean velocity field of the LMC extractable from the data sets. We corrected the line of sight velocity field for systemic, transverse, precession and nutation motions of the LMC to get the distribution of v_{mod}. As the ATCA/Parkes data cover the LMC H I disk to a significant radial extent, the kinematic parameters of the mean disk estimated using ATCA/Parkes data is used to analyse the LAB/GASS data set as well. The annular ring analysis is not performed with the LAB/GASS data set due to the lesser spatial resolution compared to ATCA/Parkes data. For LAB data, the mean of the parameters v, δv_{sys} and ϕ_0 for each $0°.6$ annular rings are taken, while for GASS data, the parameters are used without averaging since the spatial resolution of GASS is at least six times that of LAB. Using these parameters, the expected velocity distribution of the H I disk is estimated. The v_{res} values are estimated as the difference between v_{mod} & v_{fit} using equation 5.2. In order to identify the kinematically distinct features, points which have $v_{res} > 12$ km s^{-1} are defined as outliers for both LAB & GASS data. The outliers are classified in the same way as done previously. As the estimated mean disk using ATCA/Parkes data is spatially restricted within a radius of $\sim 5°$ within the LMC, we assumed the disk to be flat beyond this radius. So it is ambiguous to classify the outliers beyond this radius.

5.5.1 The mean H I disk and the distribution of outliers

Figure 5.10 shows the intensity weighted mean velocity map of the LMC using GASS data, after applying the corrections mentioned earlier. Such a map using GASS data is generated for the first time. This is a spectacular H I map of the LMC which covers a large area, thus including the MB. The features seen in the data are not affected by any assumptions on the LMC disk, just the line of sight velocity field is corrected for systemic, transverse, precession and nutation motions of the LMC. Thus the details identified in the outer regions of the LMC disk as well the MB are true features. In the inner regions upto a radius of 4-5°, the features seen are very similar to figure 5.1. Outside this radius, we can see that the GASS data goes quite farther, particularly in the south and SW direction. The most prominent feature is the MB, which is connected to the LMC disk and its large extent. This figure brings out the details of the connection between the LMC disk and the MB. We also notice the large width of the MB apart from its radial extent. These extensions will help us to connect various features identified using the ATCA/Parkes data. The main features which can be noticed are the red points towards the west and SW end and the extension of Arm B feature to the MB/SMC (a1 and b in figure 5.10). We also notice a plume of blue points near the NW edge (c in figure 5.10) as well as in the east (d in figure 5.10). The high velocity red points in the west and SW (a1 in figure 5.10) are suggestive of gas moving away from the LMC.The main feature in the SW is the MB which in turn is connected to the SMC. If we proceed radially inward through the SW feature (a2 in figure 5.10), we could notice that the velocity changes from red to blue, suggesting a change from high positive velocity to negative velocity. As this feature is part of the MB, this suggests that gas in the inner part of the MB has velocity opposite to the outer part. We now identify the kinematic outliers in the GASS data as shown in figure 5.11. We did not provide separate plots for the three types of outliers, but we separately discuss various outliers below. In figure 5.11, we are able to trace all the previously identified outliers using ATCA/Parkes, in the inner region, though the details of the features are missing due to poorer resolution. This figure is ideal to connect the inner features to the outer regions, which was absent in the ATCA/Parkes data. Most importantly, the Arm B is found to be connected to MB, whereas we could only suggest that it was pointed towards MB using the ATCA/Parkes data. The gas pool seen in the MB is found to be connected to the LMC through arm B (blue points analogous to b in figure 5.10), and the end close to the SMC has high velocity. The velocity pattern is suggestive of the MB being sheared due to tidal and ram pressure effects. The gas closer to the LMC could fall into the LMC, whereas the other end is stripped due to ram pressure. We also

Figure 5.10: The intensity weighted mean velocity map using GASS data. Colour coding is according to the variation in v_{mod} in km s^{-1}. The alphabets marked are locations of (a1) high velocity gas in the west and SW of the LMC disk, (b) the extension of Arm B feature to the MB/SMC, (c) the plume of blue points near the NW edge and (d) the blue points in the south and SE of the LMC disk, (a2) and (a3) are locations of high velocity gas in the south and SW of the MB respectively.

notice an outflow of gas from the western side of the LMC disk, (red points analogous to a1 in figure 5.10) probably due to the same reason. The Arm E is clearly seen which has both the type 1 and slow type 2 components (green and yellow points respectively). Their superposition confirms their co-location and probably suggests common origin. The blue points located to the east of Arm E are part of the newly found Outer Arm, which is not
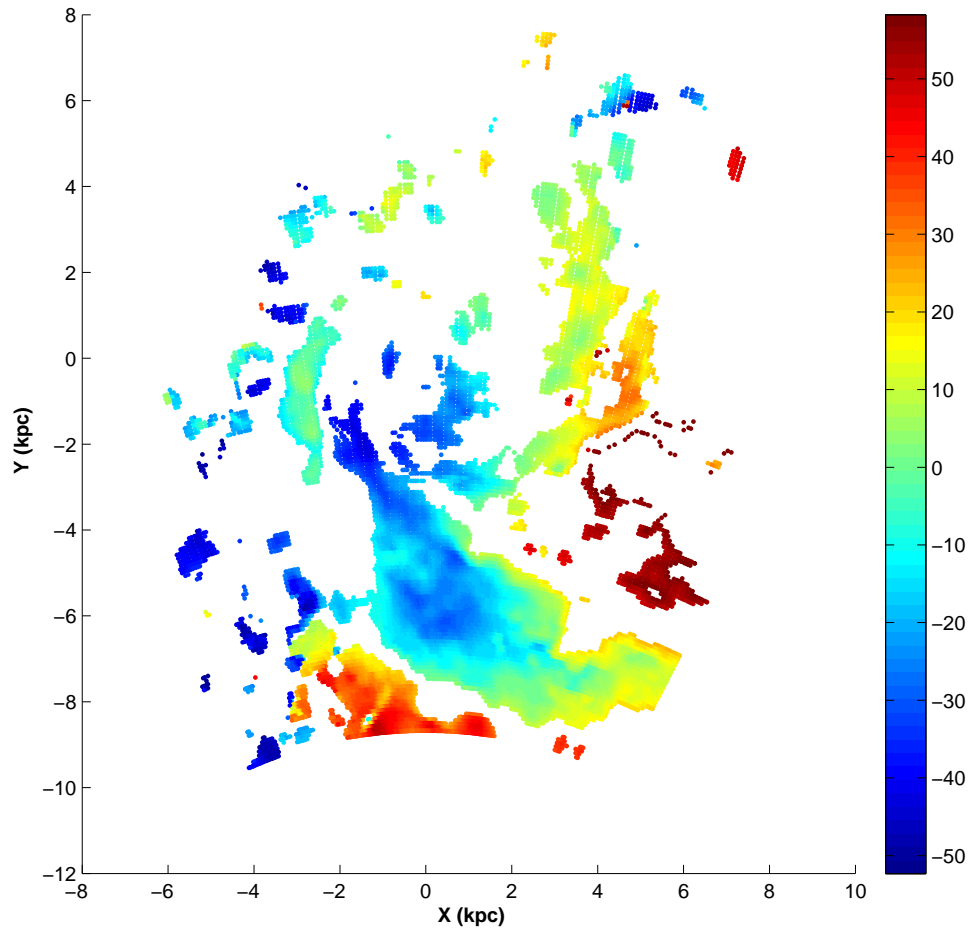
Figure 5.11: The outlier component map identified using GASS data. Colour coding is according to the variation in v_{mod} in km s^{-1}.

seen as a continuous stream. On the other hand, the blue points can be noticed at large radii in the east and SE regions. This stream is found to terminate at a similar location in the NE, as in figure 5.9. In the western side, we notice the arm W and a feature suggestive of arm S. We also notice a blue plume of points in the NW region (location analogous to c in figure 5.10), which is part of the type 1 feature. This feature is found to eventually connect to the arm E, as suggested in figure 5.7. This region is directed towards the MS, as shown in figure 1 of Staveley-Smith et al. (2003).

In Summary, GASS data analysis found to connect the arm B to the MB. Figures 5.10 and 5.11 suggest that the gas from the MB might be reaching the LMC through the arm

B. We also identify a possible connection between the type 1 arm E and a gas pool in the NW. The GASS data analysis also identifies possible outflows from the western side of the disk and the south and SW of the MB.

Figure 5.12 shows the intensity weighted mean velocity map of the LMC using LAB data, after applying all the above mentioned corrections. The map clearly makes an extension of velocity map using ATCA/Parkes (figure 5.1) to a larger radial extent of 6 to 14 kpc. The velocity gradient along the PA of LON of the disk is apparent. This map has almost all the features noticed in the GASS map (figure 5.10), but at a lower resolution. The extension of the southern part of the gas to the MB is clearly seen. The gas in the MB is found to have velocity similar to the gas velocity in arm B, closer to the disk and gradually increases away from it. The gas in the west and the SW region have high velocity with respect to the disk. To analyse the kinematically distinct features we estimated the outlier map shown in figure 5.13. The stream of blue points seen extended upto the MB supports the connection of MB to the LMC through arm B. It extents upto a radial distance of 9 kpc, after which the velocity changes. Only a part of the Outer Arm is found in this data. The arm E is clearly seen and again it is found to be connected to the plume of blue points in the NW (c in figure 5.10). The arm W can be noticed, but arm S is not clear. The red points denoting the outflow can be seen in the western part of the disk and south/SW of the Bridge. Thus, the LAB data supports the findings from the GASS data.

One feature which is noticed in figures 5.10 - 5.13 are the high velocity point at the southern extreme of the GASS and LAB data sets (a3 in figure 5.10). This high velocity gas which is at the eastern periphery of the highly extended MB, is suggesting of leaving the LMC. This could also be caused by the ram pressure due to the motion of the LMC. We are unable to connect this feature to the inner regions clearly, in figures 5.11 and 5.13, though the blue points identified in the eastern side appears to originate from this part of the MB.

Thus we find evidence for connection of LMC to the MB through arm B and possibly through the Outer Arm. If the gas in the MB falls in to the LMC disk, then accreted gas reaches the LMC to 30 Dor and the NE region.Various arms are identified with the fast outlier gas, such as arm B, arm W and arm S. These probably are created by the motion of LMC in the MW halo, forcing gas in the outer disk to move inward but with higher rotational velocity. We notice that the path of the fast outlier coincides with the locations of many of the SGS and GS. We also notice a likely connection between a pool of gas in the NW and the arm E, which is connected to the LA. We are not sure whether there is any gas infall from the NW, which creates this type 1 arm and the LA. The western
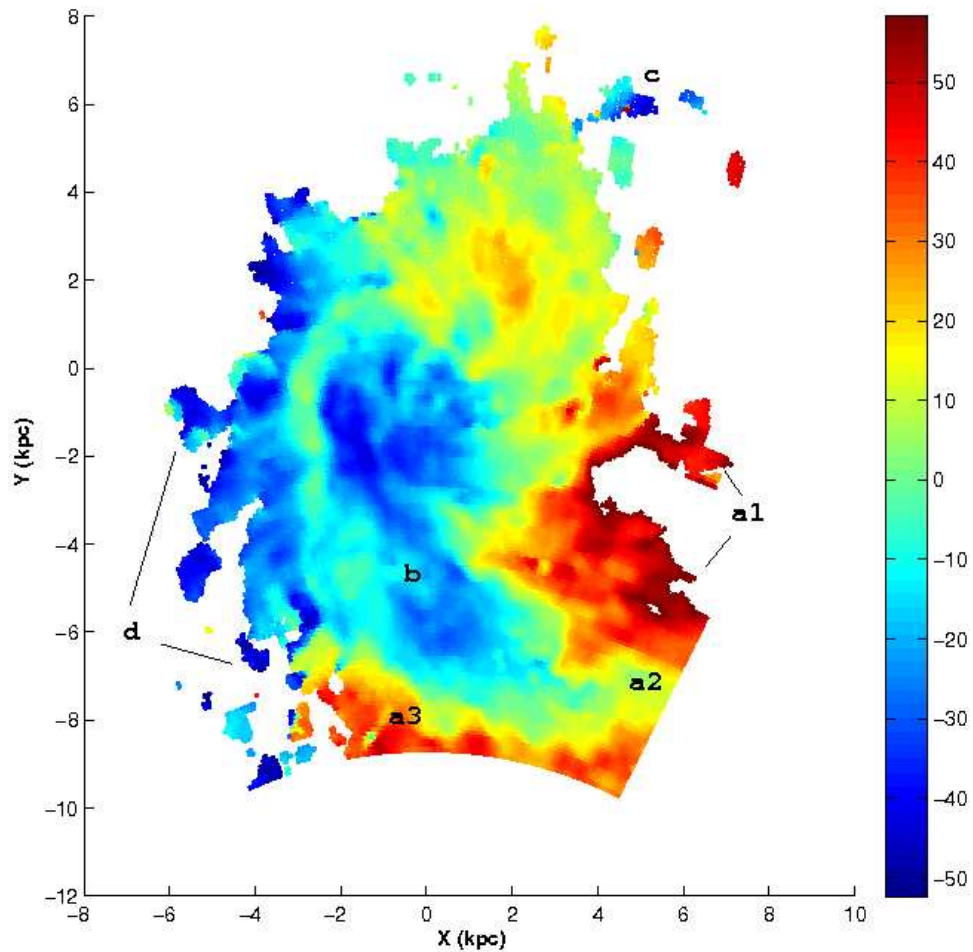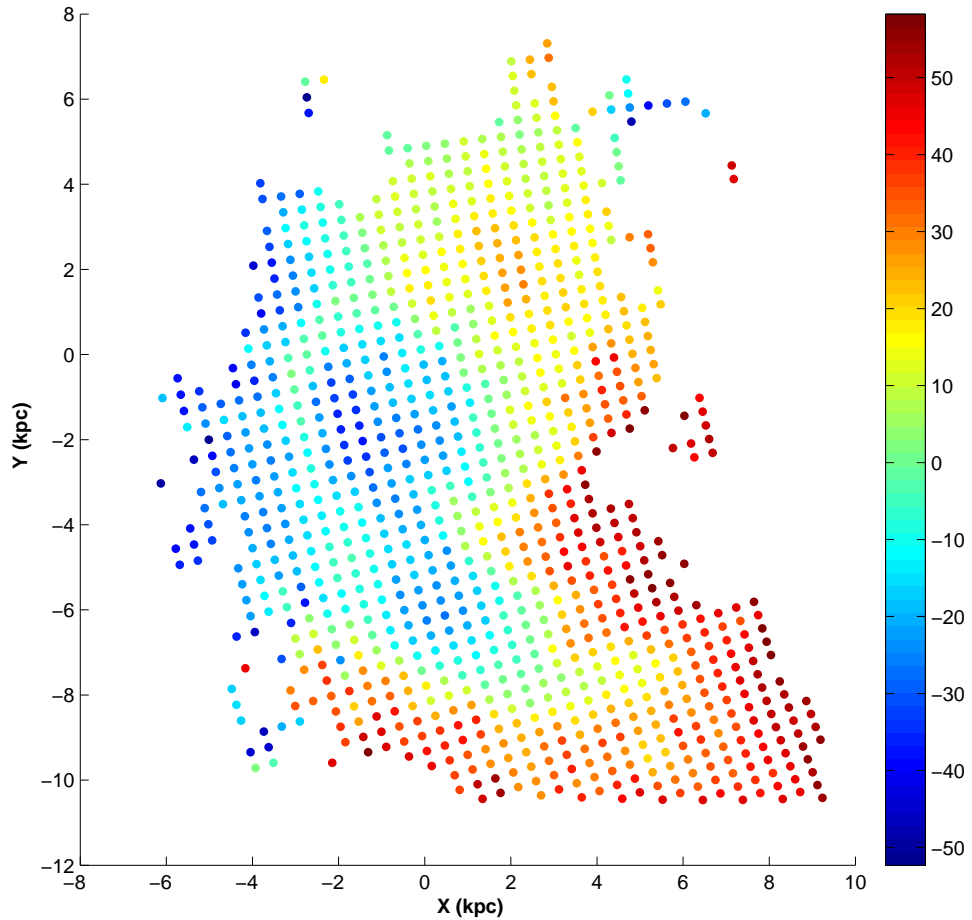
Figure 5.12: The intensity weighted mean velocity map using LAB data. Colour coding is according to the variation in v_{mod} in km s^{-1}.

and the south-western and southern part of the disk is likely to be losing gas due to ram pressure stripping. This gas flows out of the LMC and probably reaches the MS, as they move away from us. In order to address the above, we have come up with two possible scenarios of accretion from the SMC/MB as described below, which can create all the three kinematic outliers.
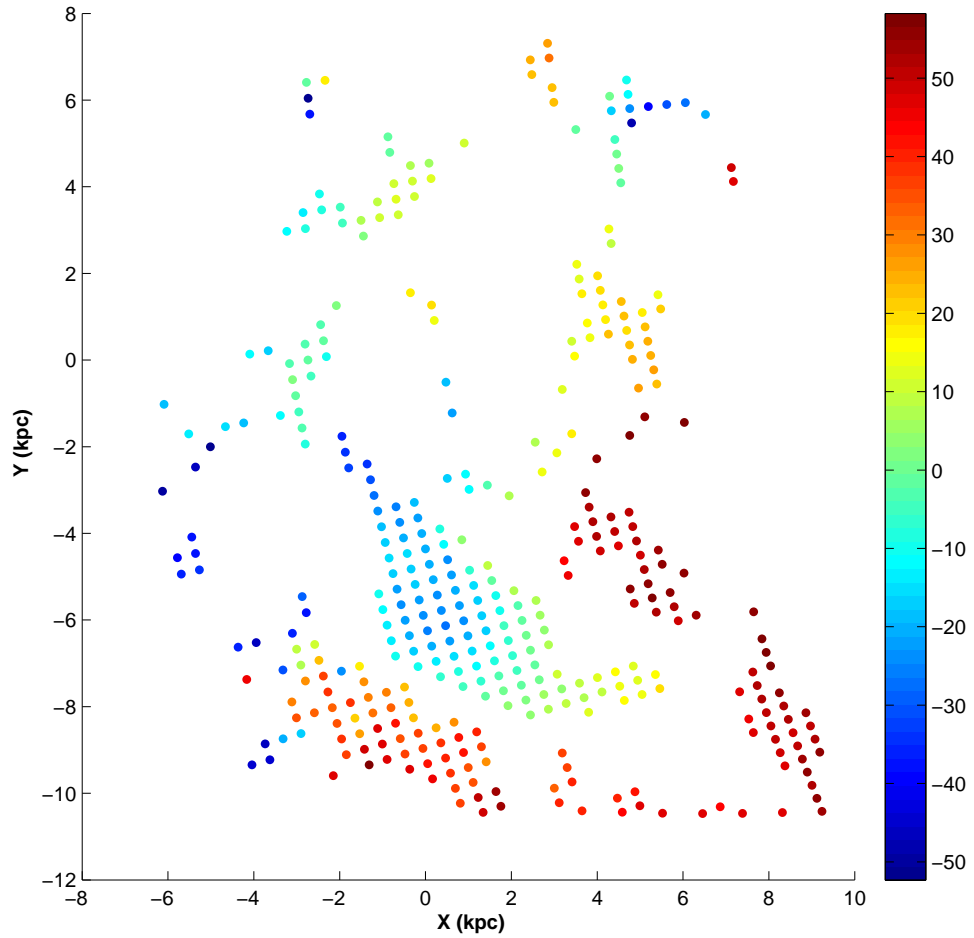
Figure 5.13: The outlier component map identified using LAB data. Colour coding is according to the variation in v_{mod} in km s^{-1}.

5.6 Origin of Outliers

In this section, we have put forward two scenarios to explain the possible origin and current distribution of all the three kinematic outliers. The scenarios could also explain some of the observed features in the LMC disk successfully.

5.6.1 Scenario I : Outlier Gas in the plane of the LMC disk

The above analysis suggests that gas in the LMC disk is connected presently to the MB. We identified two such streams only in the eastern side of the LMC. We know that

the SW side of the LMC is closest and well connected to the MB and hence the gas may also be connected to the LMC through the SW/western side of the LMC disk. The apparent velocity of the faster type 2 is suggestive of either the gas is in the LMC plane and moving faster than the disk (scenario I), or the gas is in a plane more inclined than the plane of the LMC disk (scenario II). Thus, if the gas was in the plane of the LMC, which is the basis for scenario I, the velocity faster than the disk and moving in the same sense as the disk, could suggest that the gas is moving in to the LMC from the MB. Thus, for a case of the gas being located in the plane of the LMC, there is a possibility that the gas from the MB is accreted by the LMC. A schematic of a possible gas flow into the LMC from the MB is shown in figure 5.14. The arrows indicate the direction in which the gas would fall from the MB. It can be seen that the velocity of the infalling gas in the eastern side has the same sense of rotation as the LMC disk. On the other hand, if it falls in the western side, the gas will have the velocity directed opposite to the direction of the LMC disk rotation. As the infalling gas sees only the gravitational potential of the LMC, and not the sense of rotation of the LMC disk, the gas is likely to move in either clockwise or counter clockwise direction at the point of infall. The velocity/the direction of the infalling gas will decide the radius of the curved path it takes. If the gas has low velocity, it is likely to move close to the center directly, without spiralling in. Based on the model I, we discuss whether we can produce all the kinematic components and explain their present distribution.

In this section we speculate on the possible outcome of gas infall through the MB. These assume that all the outlier gas are in the plane of the LMC. If there is an infall of gas close to the systemic velocity of the LMC, the gas would slowly move towards the center of the LMC without spiralling in. If we see the distribution of the slow type 2 component, we see a distribution of gas connected from SW towards the center. Hence we can explain this feature as due to accretion of low velocity gas from the MB. If the infalling gas has velocity higher than the systemic velocity and moves in counter clockwise sense, it will move towards north. While moving towards the north, it can get slowed down due to interaction with the disk gas moving in the opposite direction. Gas which is slowed down will move towards the center in a path with lesser radius, which should be similar to what is seen in figure 5.8 and we do see a very similar distribution in figure 5.7. Gas which retains higher velocity would move towards the north in a relatively outer orbit. We are not able to detect such a stream in figure 5.7. On the other hand, we do see some blue dots near the two western SGS (at about X=+1 and Y=0), these are probably gas falling in like the upper most arrow shown in figure 5.14. These infall points are also seen in

the channel maps of (Staveley-Smith et al. 2003) for velocities around 215 km s^{-1}. We also notice a large chunk of blue points in the NW, near (X=6, Y=6), in both GASS and LAB data (marked as c in figure 5.10), which suggests connection to arm E. The large H I density close to these two SGSs and the far NW point could be produced by the infalling gas in the velocity range −20 to −30 km s^{-1}. The H I distribution in the eastern part (Arm E) identified as type 1 outlier can be produced by the faster component of this infalling gas. The gas as it moves would get slowed down further and eventually will have velocity similar to the systemic velocity. This is probably what we see along Arm E, where the type 1 gas has velocity very close to zero, or systemic velocity. Once the velocity of the gas approaches zero velocity, then it can get dragged by the disk, which can produce the slow type 2 component. This explains the presence of gas in the eastern side as shown in figure 5.7 as well as 5.8. Extension of this feature is dependent on the velocity of the gas accreted from the MB/SMC and the eventual slow down due to interaction with the gas in the disk. Thus, gas with sufficiently high velocity located in the arm E would leave the LMC, whereas the low velocity gas would fall back into the LMC.

Subramaniam & Prabhu (2005) first suggested the presence of counter-rotating stars and gas in the LMC. Recently, Olsen et al. (2011) identified that this counter-rotating stellar population is accreted from the SMC. Thus, along with the gas, the accretion event could be bringing stars as well, from the MB. There could also be kinematically similar stellar component in the inner LMC. Thus, in our model I, gas with velocity ranging from systemic velocity upto −50km s^{-1} with respect to the LMC disk falling into the west/SW disk of the LMC from the MB can explain not only the type 1 as well as the slow co-rotating kinematic outliers, but also the production of the LA.

According to model I, the gas falling from the eastern side will have the same sense of rotation as the LMC disk. Once again, the path taken by the gas will depend on its velocity/direction of motion with respect to the LMC disk. The gas with lower velocity will take an inner curved/circular path and the gas with higher velocity is likely to take a relatively outer path. The gas falling in to the LMC experience pressure due to the motion of the LMC in the MW halo. The gas coming in from the MB, might get pushed in, creating the arms B and the Outer Arm. In the GASS and LAB data, we do see diffuse gas towards the east of the Outer Arm. Such gas will try to go around the LMC, like the Outer Arm, but may reach the north side of the disk due to the LMC motion. Thus, gas with systemic velocity and up to about −50 km s^{-1} with respect to the disk accreted in the eastern side gives rise to the fast co-rotating kinematic outlier, comprising of Arm B, the Outer Arm and the diffuse gas around the LMC disk.

In this model, it is assumed that all the outliers are located in the disk of the LMC or very close to it and the gas falls into the plane of the disk. This coplanarity or near-coplanarity of all outliers is the main assumption of this model, such that the gas is falling into the LMC from the SMC, through the MB, and almost in the plane of the LMC. The assumption is based on the fact that the inclined disk of the LMC and the line connecting the centers of the L&SMC makes a small angle $\sim 5°$ (figure 5.15). Since this angle is small, it is reasonable to assume that the infalling gas is in the plane of the disk. On the other hand, this model could allow mild offsets for the plane of the outliers and hence the accreted component.

5.6.2 Scenario II : Outlier Gas in planes shifted from the disk

Another scenario to explain the outliers is when gas is present in different planes with respect to the LMC disk. The gas can appear to be type 1 if it actually belongs to another plane which is inclined in the opposite sense as the LMC plane. Similarly, the faster type 2 component appears to be faster with respect to the LMC disk, if the gas is located in a plane with higher inclination. Also, the slow type 2 component appears to be so, if the gas is located in an almost face-on plane. In this model II, the outliers are modelled to be located in three different planes with respect to the LMC disk. In order to derive the parameters of these three planes, one would ideally like to perform a complete fitting of the outlier component. But this does not converge to estimate the parameters due to less spatial coverage of data points. Hence we tried to estimate the parameters of the plane which closely reproduces the velocity features of the outliers. The estimated planes are shown in figure 5.15. We identify that there is a nearly face-on plane, shown in figure 5.15 as disk C (with $i = 0.0$ to $-3°.0$), where the type 1 gas is located. The type 1 Arm E would then belong to a plane which is inclined $28°$ away from the plane of the LMC. The slower type 2 kinematic component has velocity very close to the systemic velocity and hence should be almost face on with $i \sim 4°$. Thus, the type 1 gas as well as the slower type 2 component are nearly face on, but their planes are significantly deviant from the LMC disk. This scenario also supports the suggestion that the slow type 2 and type 1 outliers are connected. In a similar estimate done by Olsen et al. (2011) with RSGs, the type 1 outlier component was estimated to belong to a plane $54°$ away from the plane of the LMC, that is, with an inclination of $i = -19°$. We see a difference in the planes of type 1 gas and stars. If gas and stars were accreted in the same event, then the type 1 gas could get disturbed due to collisions with the disk and hence could slow down, reducing the inclination of the plane.
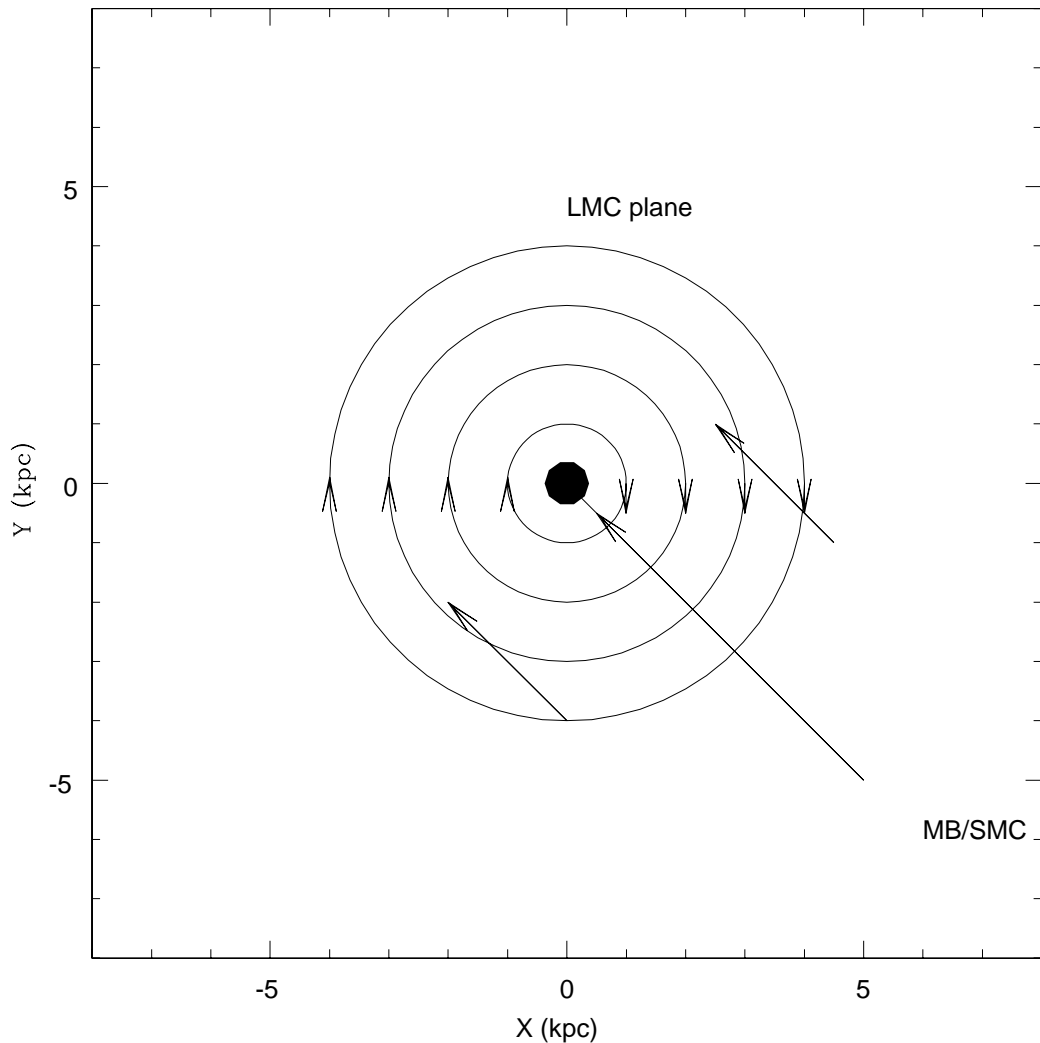
Figure 5.14: Model I : A schematic of the LMC plane with infalling gas. The sense of rotation of the LMC disk and the direction of the accreting gas from the MB/SMC are shown. The figure is in the plane of the LMC and the gas is expected to fall into the LMC from behind in a grazing angle.

In the case of Arm B, the likely inclination is found to be about 40°, which is 15° higher than the plane of the LMC. This is shown as disk F in figure 5.15. So Arm B can be a type 2 component with expected in-plane velocity, but appears faster due to its different inclination. Thus, the analysis supports the possibility of outliers belonging to planes with significantly different inclination. A close look at figure 5.15 shows that these different planes can cause significant changes in the structural parameters of the

140

LMC disk. On the other hand, scenario II demands that the gas from the SMC through the MB has to get fanned out to a very large angle of about 43°, as shown in the figure. The demanded expansion of the stream is also asymmetric with respect to the line joining the L&SMC. That is, more deviation is required to create the disk C, when compared to create the disk F. It is not clear whether such a large deviation in the direction of gas motion can be created in the MB. On the other hand, we notice a large extent of the MB in figures 5.10 and 5.12, suggesting that the MB is indeed extended.

Thus we have put forward two scenarios to explain the kinematic outliers present in the gas. Both scenarios explain most of the observed features in the LMC disk. Scenario I predicts the maximum range of velocity assuming all the gas to be in-plane and the scenario II predicts the maximum inclination possible to explain the observed velocity. It is quite possible that the real situation is a combination of the above two scenarios. That is, the gas could be located in disks with lesser inclination and moving with faster/slower velocity. This would then require a smaller angle for the spread of gas in the stream as well. More detailed study is needed to get these finer details.

5.7   Results and Discussion

We identified the mean H I disk of the LMC after correcting the observed velocity field for the transverse motion of the LMC using the recent proper motion measurements by (Piatek et al. 2008 and Kallivayalil et al. 2013). Corrections are applied for the precession and nutation motion of the LMC disk as well. The data used for the analysis are the intensity weighted velocity maps from three data sets. The estimated mean H I velocity distribution using ring analysis after removing the outliers, successfully reproduces the observed velocity field. The value of PA of kinematic major axis we derived from gas kinematics, $126° \pm 23°$ is comparable with the value estimated from the stellar kinematics ($142° \pm 5°$). Therefore, the discrepancy between gas and stellar kinematics in the LMC disk is effectively removed. The mean H I disk estimated using the above mentioned two proper motion values were found to be similar. The effect of precession and nutation of the disk on the estimation of PA and circular velocity is also analysed. We traced the kinematically distinct features present in the LMC. Most of the H I gas in the LMC ($\sim 87.9\%$ of the data points) is located in the disk and follow the disk kinematics, which gives the confidence that the estimated mean disk is close to the true disk of the LMC. The mean H I disk shows signs of disturbance within the central $1°.0$, might be due to the presence
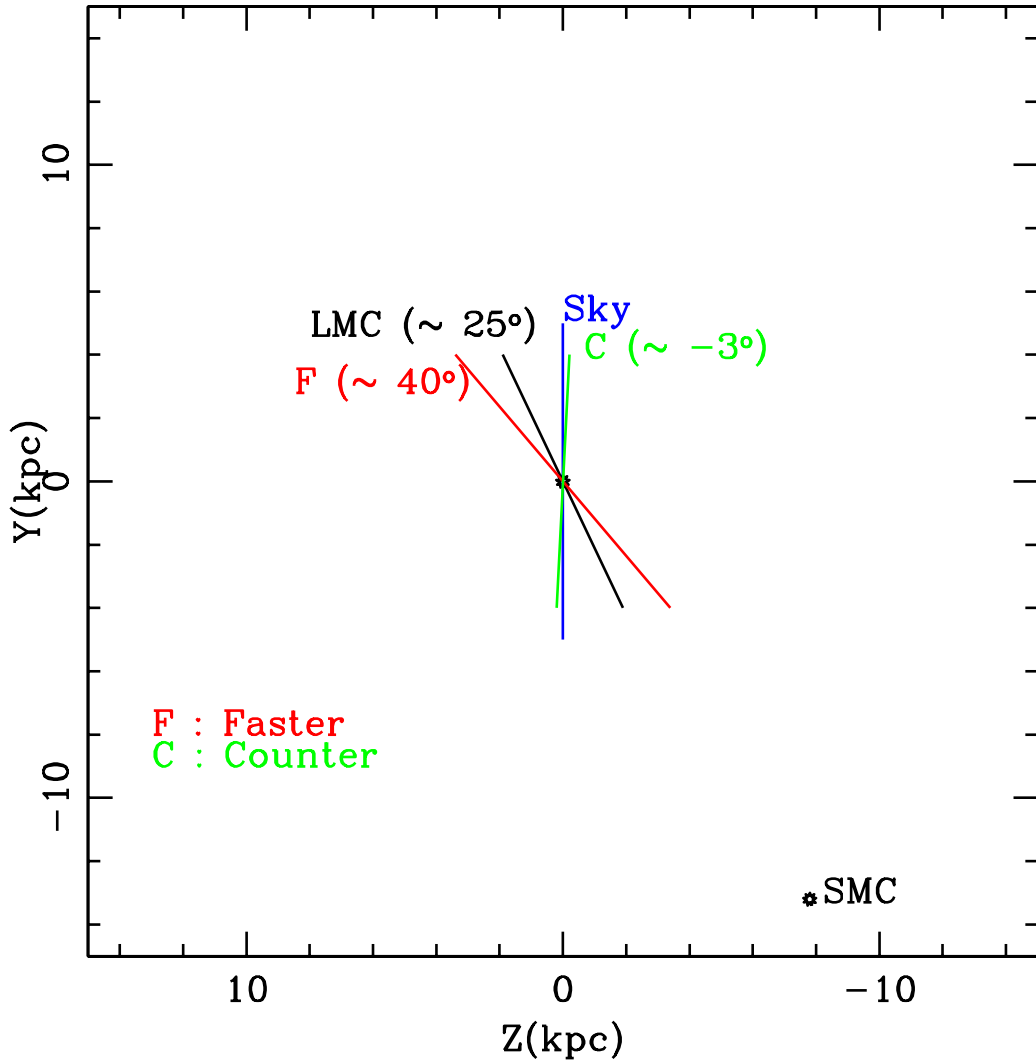
Figure 5.15: Model II : A schematic of the edge-on view of the LMC plane and the estimated planes of gas outliers. The plane of the sky and the position of the center of the SMC are also shown. The angular deviations of each of the planes from the sky plane i.e. the inclinations are marked. F corresponds to the plane of the faster type 2 outlier and C corresponds to the type 1 outlier.

of the bar. The disk region between 1.°0 - 2.°9 is found to be relatively undisturbed. Disk outside 2.°9 is found to be disturbed, likely to be due to the motion of the LMC in the MW halo and related ram pressure stripping.

We detect 12.1% of the data points as kinematic outliers. We identify 2.7% of the total data to be type 1, and 3.9% to be slow type 2. Significant part of these two components

are identified with Arm E. 5.5% of the total sample is found to belong to faster type 2. We identified the well known Arm S, Arm W, Arm B and a new stream, Outer Arm, as part of this faster type 2 outlier component. We find evidence for the connection of the LMC to the MB through arm B. There could be on going gas accretion to the LMC from the MB through Arm B, if the outlier gas is in plane with the LMC. We also identify outflows from the west of the LMC as well as the SW and southern part of the MB, possibly due to ram pressure stripping.

According to the two scenarios we have proposed, the gas in the arm B, arm W and the newly proposed Outer Arm move faster and/or inclined to the disk. According to Mastropietro et al. (2009), the gas in the outer part of the disk can move to the inner LMC due to the motion of the LMC in the MW halo. The Outer Arm, probably formed by a similar mechanism in the outer disk, can be traced up to the NE star forming regions, where vigorous star formation and SGS are noticed. The NE region is expected to be compressed due to motion of the LMC and the compressed gas could move to inner regions with higher velocity, which forms the arm W and probably arm S. Hence these arms could be created due to motion of the LMC in the MW halo and the resultant inward motion of the gas.

The Arm B and the Arm E are the most debated H I features in connection with gas infall/outflow from the LMC. We find that the arm B is connected to the MB and could be an infall feature if it is in plane. The connection of LA with Arm E as well as the other connected features like the LAI, LAII etc, which are closer to us make us believe that the Arm E feature is probably in front of the LMC disk. We find that the arm E has two kinematically distinct components, a slow type 2 component and a type 1 component. The co-location of these two components leads us to suggest that they belong to the same arm E and that both the outliers have similar origin. The scenario II suggests that this gas is in an almost face-on plane, which brings the Arm E in front of the LMC disk in the SE regions. Accordingly, we propose that the gas is likely to leave the LMC through arm E, if it has sufficient velocity. Otherwise, the gas will fall back into the LMC. Due to the motion of the LMC in the MW halo, the accreted type 1 gas can also be brought to the inner radii with faster velocity. This probably can create the arm E to extend to LAI, LAII etc. In the rotation curve, shown in figure 5.3 panel 'b', we notice a kink at a radius of $\sim 3.°0$. This kink could be produced by the presence of the slower type 2/type 1 H I gas present in the Arm E, which is also located at a similar radius. Diaz & Bekki (2012) had found an accreted component in the LMC, which looks like a polar ring. They attribute

that this is due to the earlier interaction of the LMC with the SMC at 1.92 Gyr ago and forms a feature resembling a polar ring about 0.68 Gyr ago. The almost face on feature of the type 1 and slow type 2 outliers appear to have similar orbit and could be the relic of such an interaction. If this is true, then gas in these outliers originated in the SMC.

The motion of LMC through the MW halo is expected to create ram pressure stripping of gas from the LMC disk. This is probably what we notice from the western, southern and southwestern part of the disk. A similar stream of gas was detected by Nidever et al. (2008) emerging from a location close to the southern SGS and was traced out of the LMC into the MS. This was also traced in the ATCA/Parkes data (figure 12, Nidever et al. 2008). We propose that these outflows are in general caused by ram pressure stripping, suggested by the distribution of high velocity along the periphery of the MB. We also detect a few outflows in the western side, probably reaching the MS, due to ram pressure stripping. Hence we find that the gas present in the MB is partially accreted by the LMC, whereas, some of the gas becomes part of the outflow in to the MS. The infall due to accretion as well as the outflow due to ram pressure stripping are controlled by the motion of the LMC through the MW halo. We noticed that the rotation curve in figure 5.3, shows a rising trend even at large radii. We note that the majority of the faster outliers traced in this analysis are located outside 3.°0 radius. This rising trend in the rotation curve could also be caused by the effect proposed by Mastropietro et al. (2009), which could make the gas move faster. Thus, the rising rotation curve may just be an effect due to the motion of the LMC in the MW halo.

The fact that the gas might have completed a minimum of one rotation can be used to estimate the starting time of infall as well as the related features. We estimated the velocity of gas in this stream corrected for the inclination of the disk is ~ 100 km s^{-1} at a distance of 4 kpc from the LMC center. Assuming a circular orbit, time taken to make a complete rotation in the plane of the LMC is ~ 245 Myr. Hence accretion should have started atleast 245 Myr ago. This timescale suggests that this accretion event may have started as a result of the last interaction between the LMC and the SMC. The effect of ram pressure stripping could also have reached the maximum after the perigalacticon passage at around 200 Myr ago.

Nidever et al. (2008) presented a case of two outflows from the LMC similar to the scenario proposed here. They suggested that the outflows were connected to the SEHO region and are caused by star formation. The outflows suggested here are similar, but are different as explained below. We identify that the eastern outflow, through the Arm E, is located in front of the LMC and not connected to the LMC disk or the star forming

regions. Hence, this outflow is unlikely to be driven by star formation. Infact, we do not detect any SGS shell in the location of Arm E. In the case of the western outflow, figures 5.10-5.13 clearly show that the outflow starts in the outer part of the MB, whereas the inner part of MB clearly shows gas with velocity similar to arm B. The SEHO region is connected to the Arm B by a similar velocity feature (blue points) only. Outflows are detected from the southern part of the MB, as well as the west of the LMC disk. These outflows are likely to be due to ram pressure stripping.

The most important observation from our analysis is that the MB is being stripped. The gas closer to the LMC disk is either falling in or at velocity similar to arm B, while the gas located further away is stripped and pushed away from the LMC. The large velocity gradient observed in the MB as a function of the distance from the LMC is suggestive of its stripping. Hence evidence of outflow is observed from the MB. It will be valuable to estimate what fraction of gas gets actually accreted into the LMC, if there is an infall and what fraction gets ejected out. This study shows that this nearest pair of interacting galaxies is ideal to understand the nuances of interactions and their effect on the gas distribution. As these details are not available in far away interacting pairs, this is an ideal test bed to understand the possible ways of infall/outflow.

5.8 Conclusions

1. The proper motion correction has a significant role in estimating the kinematics of the LMC H I disk. The precession and nutation correction bears a small but inevitable effect on the estimation of kinematic parameters. Both the recent proper motion estimates (Piatek et al. 2008 and Kallivayalil et al. 2013) were found to produce similar disk parameters, for a given value of di/dt.

2. Applying the recent proper motion estimates to the ATCA/Parkes data, the PA of kinematic major axis of the H I disk of the LMC ($126° \pm 23°$) is found to be consistent with that of the stellar distribution ($142° \pm 5°$, Olsen et al. 2011).

3. The mean H I disk shows signs of disturbance within the central $1°.0$ degree, might be due to the presence of the bar. The disk region between $1.°0 - 2.°9$ is found to be undisturbed. Disk outside $2.°9$ is found to be disturbed, likely to be due to the motion of the LMC in the MW halo and the related ram pressure effects.

4. Arm E is identified with type 1 as well as slow type 2 outliers. We identified the well known Arm S, Arm W, Arm B and a new stream, Outer Arm, as part of the

faster type 2 outlier component.

5. The intensity weighted H I velocity maps using GASS and LAB data clearly show the extension of the LMC disk to the MB, as well as the large extent of the MB. The kinematic analysis also find a velocity gradient in the MB.

6. We proposed two models to explain the presence of kinematic outliers. A model with gas in three different planes seems to explain most of the features found in the LMC, when compared to an in-plane accretion model.

7. The faster type 2 outliers could have formed in the last 245 Myr, based on the argument that these outliers have completed atleast one full rotation around the LMC. This is in tune with the time scale of the last LMC-SMC-MW interaction.

8. We find that the MB is being stripped. The gas closer to the LMC disk have relatively less velocity and the gas located further away have higher velocity, with evidence of outflow. The various arms identified in the LMC could be caused by the motion of the LMC in the MW halo. Thus this nearest pair of interacting galaxies is a gold mine to understand the nuances of interactions and their effect on gas.

CHAPTER 6

H I KINEMATICS OF THE SMALL MAGELLANIC CLOUD

6.1 Introduction

The Small Magellanic Cloud (SMC), the smaller companion of the Large Magellanic Cloud (LMC) is a gas rich galaxy with active on going star formation. The gas distribution in the SMC is being effected by its interaction with both the LMC and the Galaxy, continuously. The signatures of these interactions can be traced by analysing the kinematic properties of the gas distribution of the SMC. The structure of the SMC is rather complex compared to the LMC structure. The SMC is known to be a two component system where the old and intermediate age stars constitute a spheroidal/ellipsoidal component while the young stars and gas are distributed in a disk. There are previous studies to derive the disk parameters using the young stars, Cepheids and gaseous tracers. But the estimates of disk parameters using stellar and gaseous tracers showed a significant discrepancy. The various spatial coverages of the data sets is considered to be the reason for this discrepancy. In this study we performed a detailed analysis of the H I disk of the SMC. We evaluated the nutation of the SMC H I disk for the first time. The structural parameters of the SMC is re-estimated in the light of the recent proper motion estimates. We used all sky survey data sets to analyse the entire gaseous disk of the SMC, while previous studies used data sets of limited area coverage.

6.2   Data

To analyse the H I kinematics of the SMC we used the combined data set of ATCA and Parkes telescopes (Stanimirović et al. 2004). The data set has an angular resolution of 98″ and a velocity resolution of 1.65 km s^{-1}. It covers a velocity range of 90 - 215 km s^{-1}. To analyse the kinematics to a larger extent we used the all sky survey data set GASS (The Parkes Galactic all sky survey data, McClure-Griffiths et al. 2009 and Kalberla et al. 2010). The spatial resolution is 4′.8 and the velocity resolution is of the order of 0.8 km s^{-1}. GASS data set has 1137 velocity frames from which the velocity frames for the SMC are selected, with an area coverage of $12° \times 12°$. We estimated the intensity weighted mean velocity maps for the ATCA/Parkes as well as GASS data sets for the SMC. For this purpose the intensity weighted average of the v_{los} is calculated for each pixel. These first moment maps provide the best estimate of the mean velocity field of the SMC extractable from the data sets. These maps are used for the analysis in this Chapter.

6.3   Methodology

6.3.1   Determination of precession/nutation

The LMC is the first galaxy for which the quantity di/dt, which is an indicator of precession/nutation motion of the disk is uniquely determined (van der Marel et al. 2002). Weinberg (2000) interpreted the di/dt as induced by tidal torques from the MW. Here we determined the di/dt value for the SMC disk. The basic theory and equations are mentioned in Chapter 2, Section 2.2.5. Here the line of sight velocity field (the intensity weighted mean velocity field) is fitted for seven free parameters using equation 2.16. The parameters are, v_{sys}, ω_{ts}, θ, v_{tc}, R_0, η, and V_0. From the estimated ω_{ts} value, using equations 2.19, 2.20 and 2.21 the value of di/dt is estimated. The value of i is taken to be 40° from Stanimirović et al. (2004) and given as an input parameter for fitting. For non-linear curve fitting, the function 'MPFIT' using Levenberg-Marquardt technique of IDL is used.

di/dt estimated using ATCA/Parkes data

The estimates of di/dt using ATCA/Parkes data set, and the corresponding proper motion values are given in Table 6.1. We did the estimation using two proper motion esti-

Table 6.1: di/dt estimates using two proper motion measurements.

μ_W(mas/year)	μ_N(mas/year)	v_t(km s^{-1})	θ_t(°)	di/dt(°$/Gyr$)	θ(°)
$-0.754 \pm 0.06^{\dagger}$	$-1.252 \pm 0.06^{\dagger}$	428.2 ± 17.6	148.9	-452 ± 25	$67.1 \pm 2'.4$
$-0.772 \pm 0.06^{\ddagger}$	$-1.117 \pm 0.06^{\ddagger}$	397.9 ± 17.6	$145{\cdot}4$	-416 ± 19	$67.1 \pm 2'.4$

†*Piatek et al. (2008)* ‡*Kallivayalil et al. (2013)*

mates from Piatek et al. (2008) and Kallivayalil et al. (2013) given as the first and second row of Table 6.1 respectively.

Further we performed a first iteration in the fitting procedure to estimate di/dt, using the Kallivayalil et al. (2013) proper motions. Data points varying from the model by 9 km s^{-1} (the choice of this cut-off is discussed in another section of this chapter) are excluded and the di/dt is estimated again. The modified value is found to be -414°/Gyr. This is not significantly different from our first estimate, and lies within the estimated error.

Effect of sense of rotation

To analyse the effect of sense of rotation in the estimation of di/dt, in the equation 2.16, the quantity 's', the spin sign, is considered to be -1. For the analysis of the LMC disk, which is known to have a clock wise rotation van der Marel et al. (2002) used a value $+1$. Since the sense of rotation of the SMC is opposite to that of the LMC, we chose $s = -1$. Therefore the equation becomes,

$$v_{los}(\rho, \phi) = v_{sys}\cos\rho + \omega_{ts}\sin\rho\sin(\phi-\theta) + [v_{tc}\sin\rho\sin(\phi-\theta) + V(R)f\sin i]\cos(\phi-\theta) \quad (6.1)$$

Fitting the above equation with the same procedure as explained above, the estimated di/dt is -412°/Gyr. (This estimation is using proper motion values of Kallivayalil et al. 2013.) This value comes well within the estimated error of di/dt value. Therefore we concluded the sense of rotation doesn't effect the di/dt estimation significantly. The estimated value of the PA of LON (θ) is found to be 67°.1 $\pm$ $2'$.4, for both the proper motion values.

di/dt **estimation using GASS data**

Since the disk of the SMC is only covered to a radius of ~3° by the ATCA/Parkes data, we used the GASS data set for the estimation of di/dt. The GASS could cover the SMC disk up to a radius of ~9°. The estimated di/dt value is -404°/Gyr. This estimation

is done using proper motion values of Kallivayalil et al. (2013). Again this value is within the estimated error of di/dt value estimated using ATCA/Parkes.

6.3.2   Correction to observed velocity field

The observed line of sight velocity is required to be corrected for the three dimensional space motion, precession and nutation of the system. For the SMC, we used the recent proper motion estimates by Piatek et al. (2008) and Kallivayalil et al. (2013) to estimate both v_t and di/dt. The equations and the theory related to the correction to the line of sight velocity field is mentioned in Chapter 2, Section 2.2.4. We used the H I kinematical center, $\alpha_0 = 1^h5^m$, $\delta_0 = -72°25'$ and $v_{sys} = 160\,\mathrm{km\,s^{-1}}$ from Stanimirović et al. (2004). Here we have used the two different di/dt values $-452° \pm 25°/Gyr$ and $-416° \pm 19°/Gyr$ and the corresponding v_t and θ_t from Table 6.1 and compared the estimates. We used the value of $\theta = 40°$ from Stanimirović et al. (2004).

The map of the line of sight velocity corrected for systemic, transverse, precession and nutation motion, v_{mod}, is shown in figure 6.1. (We used $di/dt = -416°/Gyr$, and $v_t = 397.9$ km s^{-1} to estimate this map.) The equatorial coordinates (α, δ) are converted to Cartesian coordinates in kpc in a projected plane with respect to the SMC center (van der Marel & Cioni 2001). This scheme is followed to estimate all the maps in (X,Y) coordinates in this chapter. Stanimirović et al. (2004) used the proper motion estimates from Gardiner et al. (1994) to analyse the SMC H I kinematics. The contribution from the di/dt are not accounted. Comparing our map with the figure 3 of Stanimirović et al. (2004), it is found that the role of proper motion as well as precession/nutation of the disk in estimating the internal kinematics of the SMC is not as apparent as in the case of the LMC. The lesser angular extent of the SMC compared to the LMC may be a possible reason. From figure 6.1 the apparent PA of LON lies in the first quadrant as predicted by Stanimirović et al. (2004), the precise estimates are given in the following section.

6.3.3   Annular ring analysis and mean H I disk

To identify the mean H I disk of the SMC and estimate the kinematic parameters we followed the procedure of annular rings (Chapter 5, Section 5.3.2). The width of annular rings is taken to be 0°.2. For each annular ring the azimuthal variation of velocity is fitted with a sine curve and the parameters are estimated and tabulated. After a mean radius of 1°.7 data seems to be slightly sparse and the sine curve is not fully populated by the data points. After 2°.3 radius, we are able to fit only half of the sine curve and after
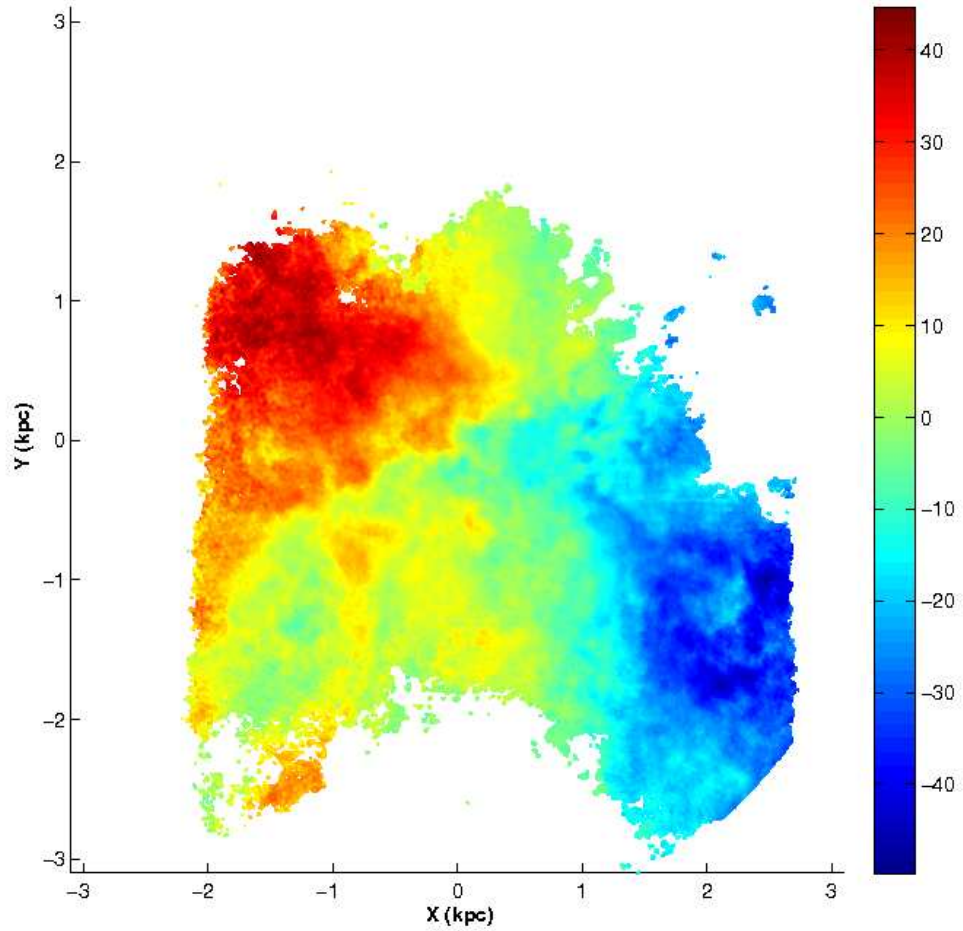
Figure 6.1: The SMC H I first moment velocity map using ATCA/Parkes data after correcting for transverse, systemic, precession and nutation motions. Colour coding is according to the variation in v_{mod} in km s^{-1}.

$3°.2$ we do not get enough data points for fitting. The analysis is done for the central 16 annular rings within a radius of $3°.2$ after which the fit error becomes larger than 10%. The sinusoidal variations of v_{mod} and the fitted sine curves for four annular rings are shown in figure 6.2, panels a, b, c & d. We performed a model refit or first iteration after removing the residuals which vary from the original fit by 9 km s^{-1} or more. (This cut-off is estimated statistically as we discussed in Chapter 5, Section 5.4; it is also discussed in Section 6.4). The green points in figure 6.2 are the removed outliers, and only the black points are used for the refit. The PA of LON and the circular velocity are estimated for

each annular ring and plotted in figure 6.4 in panels a and b. After a radius of 2.5° the sine curve is sparsely populated as we see in panel d of figure 6.2. Also the PA of LON and circular velocity flips to higher values, which may be erroneous. Due to the above mentioned reasons the analysis is restricted to be within a radius of 2°.5. The curves in magenta depicts the variation of PA of LON and circular velocity when a di/dt correction is not applied. Further, curves for two sets of proper motion measurements and di/dt estimates are shown. One could see the di/dt correction elevates the mean PA by on an average of 20°. But the curves with two proper motions, are found to be similar. The bold orange curve is the resultant estimate from the first iteration shown in both the panels. The parameters corresponding to this curve is used for the further analysis. One can see the curves run with the same trend within the considered radius range. The curve without a di/dt correction seems to have lesser value of PA of LON. The mean PA of LON within a radius of 2°.5 is found to be 69°±20°. The value is consistent with the estimates in Table 6.1 within the estimated error. From the estimates of kinematic parameters of 16 annular rings the mean H I field of the SMC is estimated and shown in figure 6.5. One can compare this map with the v_{mod} map in figure 6.1 to appreciate the reproduction of observed features.

6.3.4 Annular ring analysis using GASS data

Since the ATCA/Parkes data cover the SMC disk only up to a radius of ~3°, while the GASS covers ~5.5°, we did the annular ring analysis to estimate the mean disk parameters using GASS data. The width of the annular rings is chosen to be 0°.5, according to the spatial resolution of the data set. There are 11 annular rings fitted with sine curves. The azimuthal variation of v_{mod} for 8 annular rings are shown in figure 6.3 in panels a to h. From panel b to h one could see the variation which is not covered in the ATCA/Parkes data set as shown in figure 6.2. The parameters estimated are shown as radial variation of v and PA of LON in figure 6.3, as bold dark green curve in panels a and b. The PA of LON varies almost constantly with radius up to an extent of ~5°.25. Also in the central 2° the curve is more or less consistent with that from ATCA/Parkes data. The estimated mean PA is 67°.2 ± 9°.2 including the full radial extend. A summary of the PA estimates of the SMC is tabulated in Table 6.2. Our estimate of PA is slightly deviant from that estimated by Stanimirović et al. (2004), but lies in the same quadrant. Hence we once again find that the H I disk of the SMC is differently oriented, when compared to the stellar disk.

The circular velocity curve varies linearly till a radius of 3.75° and then becomes flat. The maximum deprojected velocity will be of the order of 64 km s^{-1}, assuming
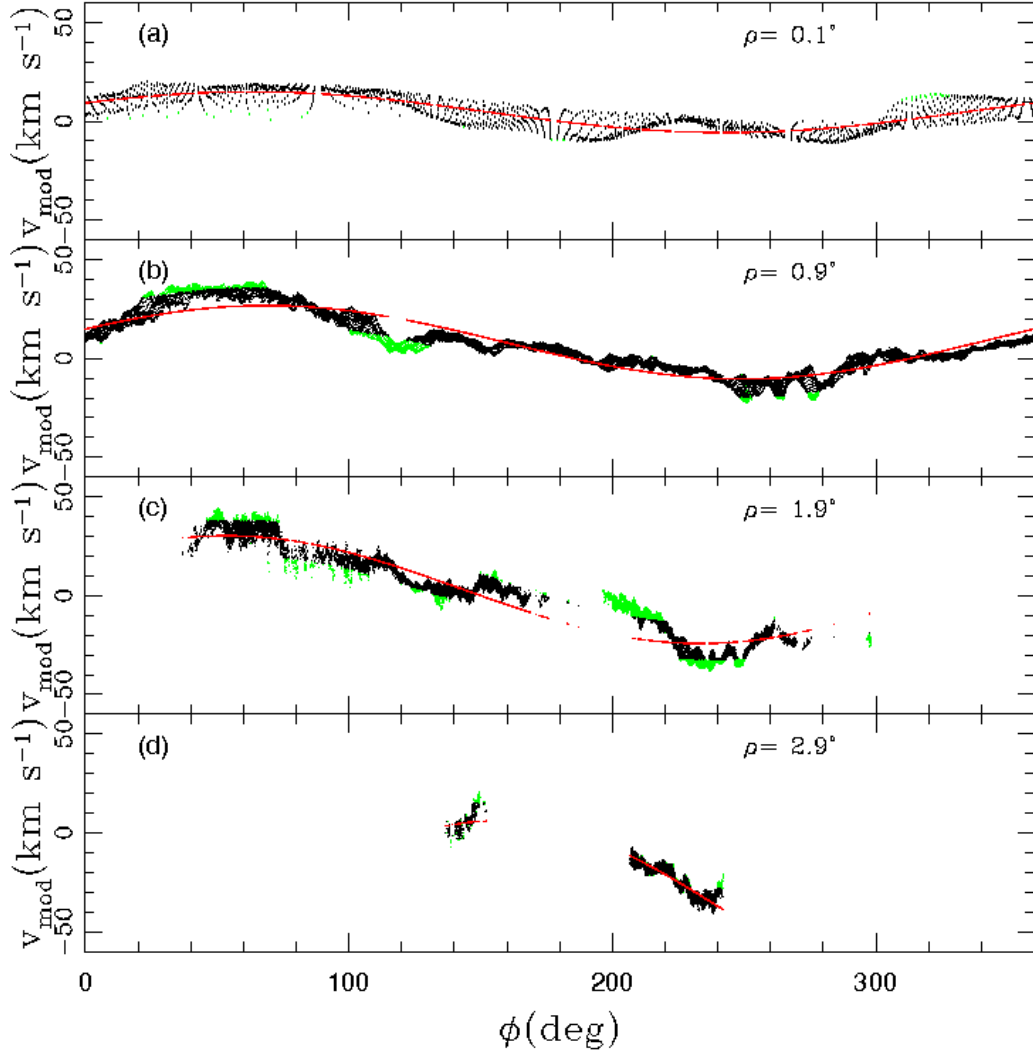
Figure 6.2: The azimuthal variation of v_{mod} and the fitted sine curves for annular rings. Panel (a) at mean radii of 0°.1, (b) 0°.9, (c) 1°.9, (d) 2°.9. The green points are the removed outliers, and only the black points are used for the refit or first iteration.

an inclination of 40° from Stanimirović et al. (2004). (The corresponding velocity in figure 6.4, panel b is 41 km s^{-1}.) van der Marel et al. (2009) mentioned that detailed velocity field fits using equation (2.1) (our equation 2.14) have not been attempted for the SMC. Stanimirović et al. (2004) found that the H I rotation curve in the SMC rises almost linearly to 60 km s^{1} at the outermost data point ($\sim$ 3.5 kpc), with no signs of flattening. In this study, we have detected the flat part of the rotation curve with a turn-over radius of 4.1 kpc, up to a mean radius of 5.7 kpc. The flat part of the rotation curve has a velocity
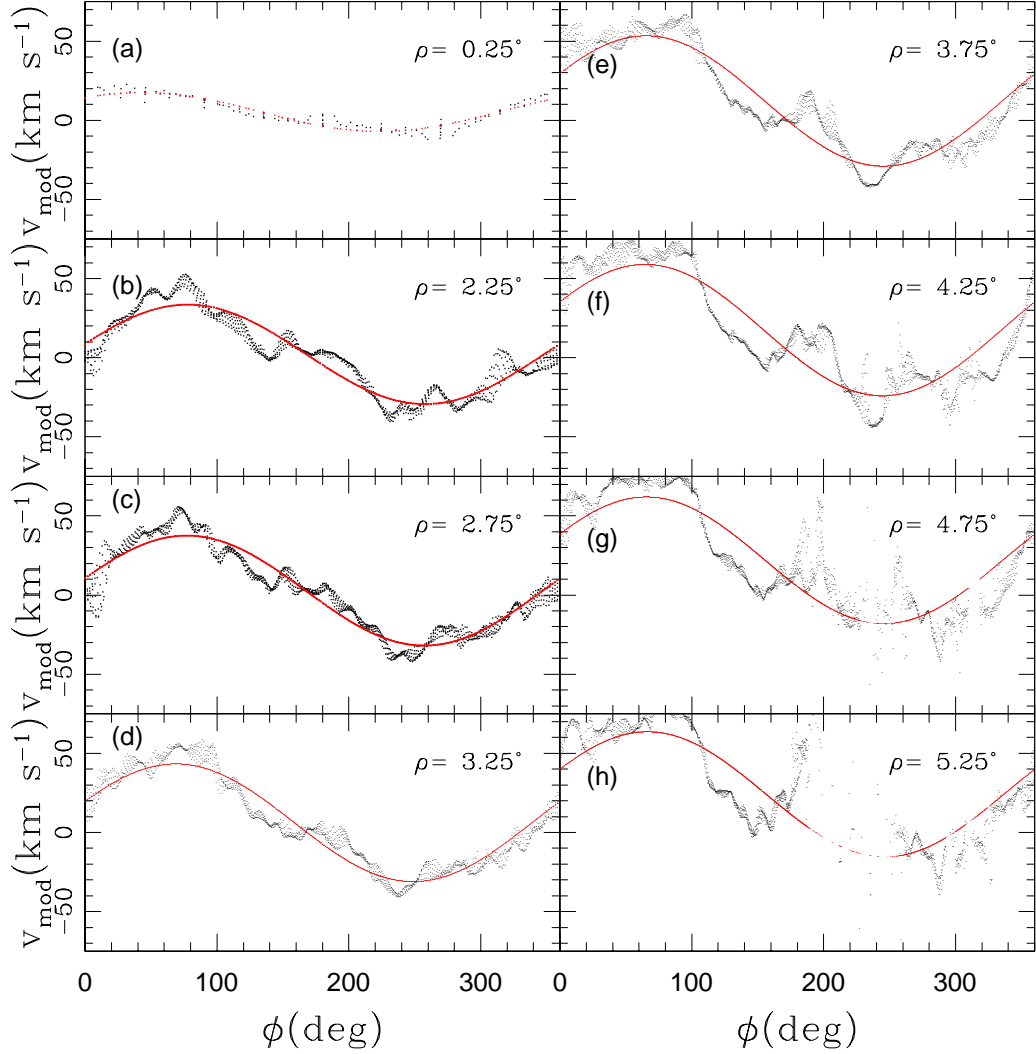
Figure 6.3: The azimuthal variation of v_{mod} and the fitted sine curves for annular rings using GASS data. Panel (a) at mean radii of $0°.25$, (b) $2°.25$, (c) $2°.75$, (d) $3°.25$, (e) $3°.75$, (f) $4°.25$, (g) $4°.75$, (h) $5°.25$.

of 64 km s^{-1}.

6.3.5 The dynamical mass of the SMC

The dynamical mass inferred from the H I rotation curve was estimated by Stanimirović et al. (2004) as 2.4×10^9 $M_\odot$ for the SMC. This is within a radius of ~3 kpc. They also suggest that a dark matter halo is not needed to explain the dynamics of the

154
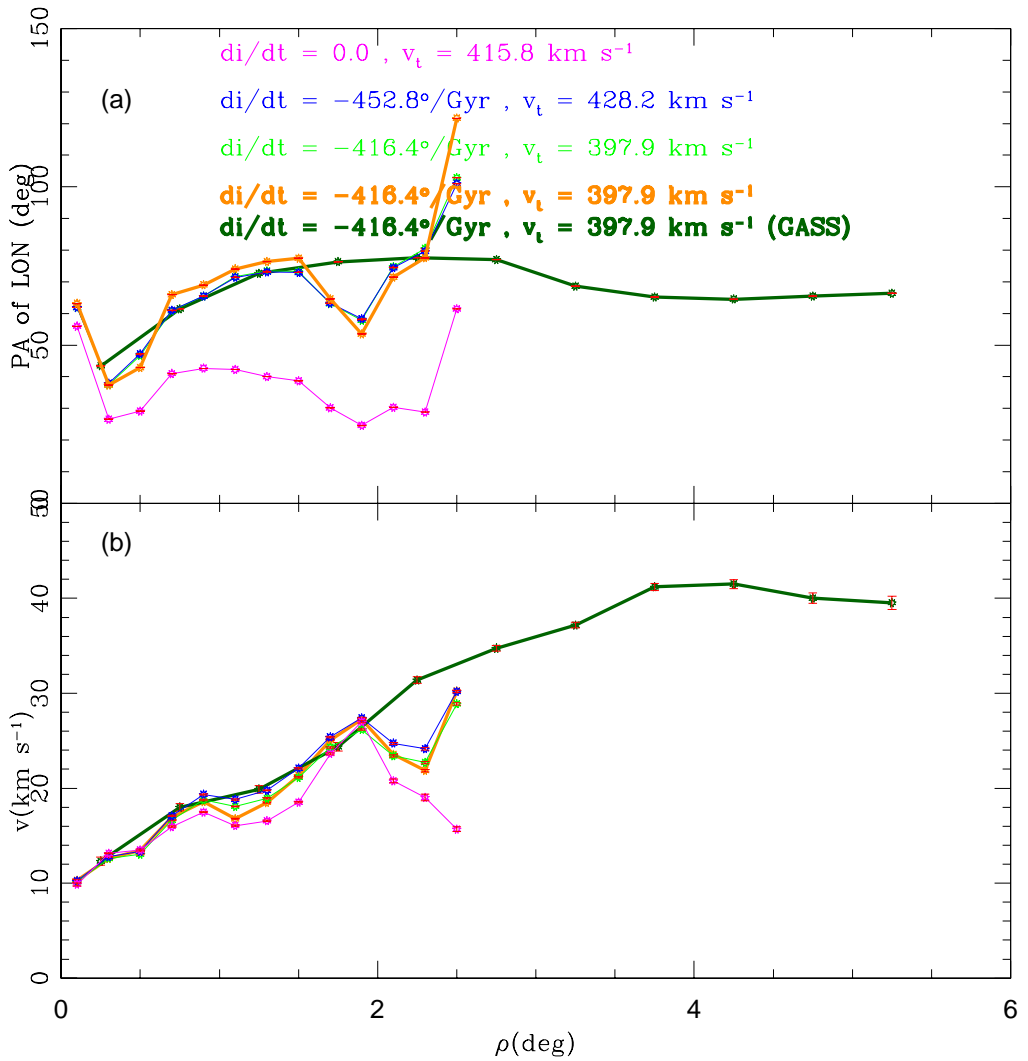
Figure 6.4: Panel (a) shows the variation of PA of LON as a function of radius. Panel (b) shows the radial variation of circular velocity. Various curves are shown for various $v_t, di/dt$ values. The error bars are shown in red. The bold green curve is using the GASS data and the other 4 curves are using ATCA/Parkes data. The bold orange curve estimated using ATCA/Parkes data is the resultant of first iteration.

SMC. But in contrast to this, quoting the same dynamical mass, van der Marel et al. (2009) concluded the combined mass of the visible material in the SMC is insufficient to explain the dynamically inferred mass, and the SMC must be embedded in a dark halo. The total stellar mass of the SMC is $\sim 3.1 \times 10^8 \ M_\odot$ and the mass of the neutral gas is $5.6 \times 10^8 \ M_\odot$ (van der Marel et al. 2009). From the rotation curve we estimated with the

Table 6.2: The PA estimated using various tracers for the SMC.

	Mean PA	tracer	Approx. radial extent
Caldwell & Coulson (1986)	148°±10°	Cepheids(< 100 Myr)	3°.9
Groenewegen (2000)	148°±7°	Cepheids in the bar region	1°.3
Evans & Howarth (2008)	126°±4°	OBA stars	3°.5
Subramanian & Subramaniam (2014)	142°.8±4°.9	Cepheids	2°.0
Stanimirović et al. (2004)	40°	H I (ATCA/Parkes)	3°.2
Our value	68°.9±19°.6	H I (ATCA/Parkes)	2°.5
Our value	67°.2±9°.2	H I (GASS)	5°.5
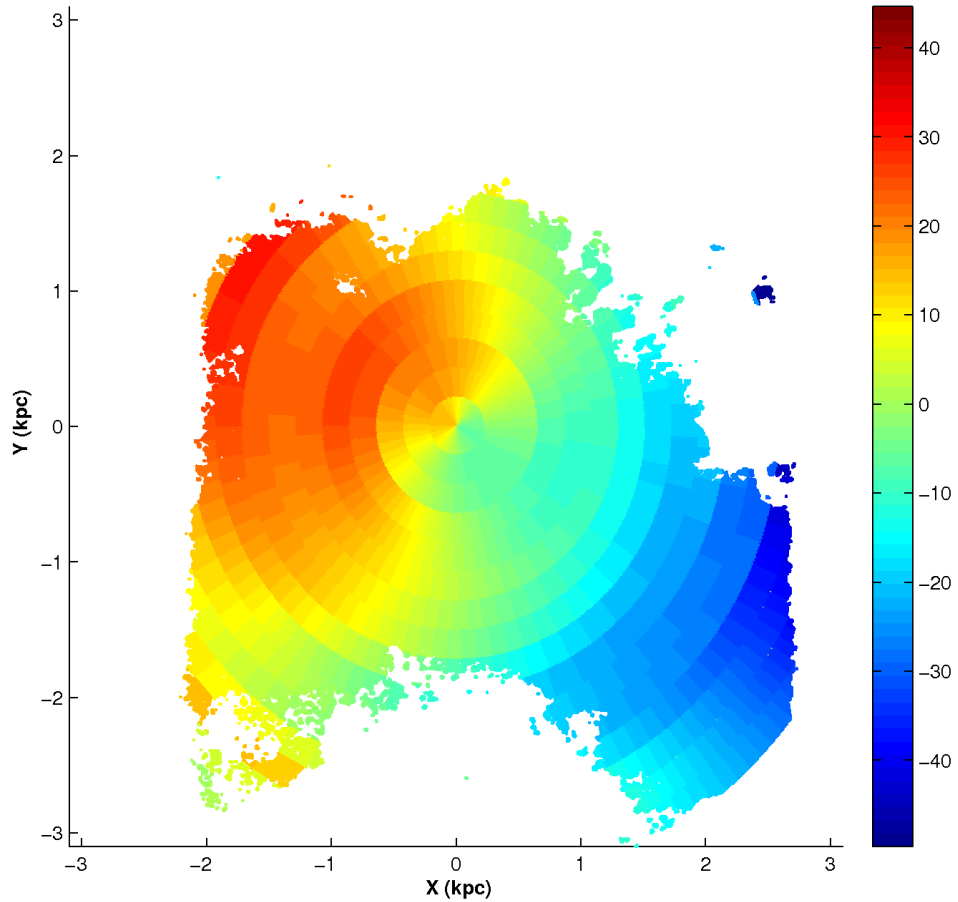
Figure 6.5: The estimated mean H I disk of the SMC using ATCA/Parkes data. Colour coding is according to the variation in v_{fit} in km s^{-1}.

GASS data, the outermost data point is at ~5.7 kpc. The mass inferred within this radius is 5.4×10^9 $M_\odot$. Therefore in our study the estimated dynamical mass is more than twice the previous estimate and it supports the possibility of the presence of a dark matter halo in the SMC. Further, unlike the rotation curve of Stanimirović et al. (2004) we detected the flat part of the SMC rotation curve, which is a clear indicator of the presence of a dark halo component.

6.4 Velocity dispersion V_{SD} and Outliers

To distinguish the disk velocity component from the kinematical outliers, a statistical cut-off in residual velocity v_{res} is needed to be fixed. For this purpose, the standard deviation in velocity V_{SD} is estimated for the SMC disk using subregions of area $14' \times 14'$. We used ATCA/Parkes data set for this analysis. The number of data points per subregion varies up to 786 and the estimated Poisson error is 28. A cut-off of 3σ is applied and subregions with number of data points < 84 are not considered for the analysis. The map of V_{SD} is shown in figure 6.7. The V_{SD} values are found to vary up to ~ 8 kms^{-1}. Stanimirović et al. (2004) gives a velocity dispersion map in their figure 4. The values vary from 6 - 37 km s^{-1} which are not consistent with our values, since the two maps are estimated using two different techniques. Their map is from the observed velocity dispersion for each pointings or pixels, and our estimates are by statistical methods by averaging the velocity within an area which may end up in lesser value for V_{SD}. But we could compare the maps qualitatively. The locations of the SGS, 304 A near the center and 37 A (at X = +2.5, Y = −1) show high dispersion of 6 - 7 km s^{-1}. The SGS 494 A (at X = −1.5, Y = −2) shows a slightly higher dispersion compared to the surrounding disk of the order of 4 - 5 km s^{-1}. Other than these locations the NE end of the disk shows high dispersion. The region with lowest dispersion identified by Stanimirović et al. (2004) is found at X = +0.5, Y = +1.5 with dark blue points. The statistical distribution of V_{SD} is shown in figure 6.6. The distribution is found to be narrower than the LMC V_{SD} distribution (Chapter 5, figure 5.5). A single peak at 3 km s^{-1} is found with number of data points around 100. The cut-off for v_{res} is determined as 9 km s^{-1} (maximum value of V_{SD} + tolerance). Hence locations with $v_{res} > 9$ km s^{-1} are identified as kinematic outliers. 81.8 % of the data points are found to be within the mean disk. The same classification scheme applied for outliers in the LMC, in Chapter 5 is applied. The type 1 outliers, are identified where the observed velocity v_{mod} shows an opposite sense of rotation compared to the expected velocity v_{fit} and the type 2 outliers are wherever the v_{mod} and v_{fit} rotate
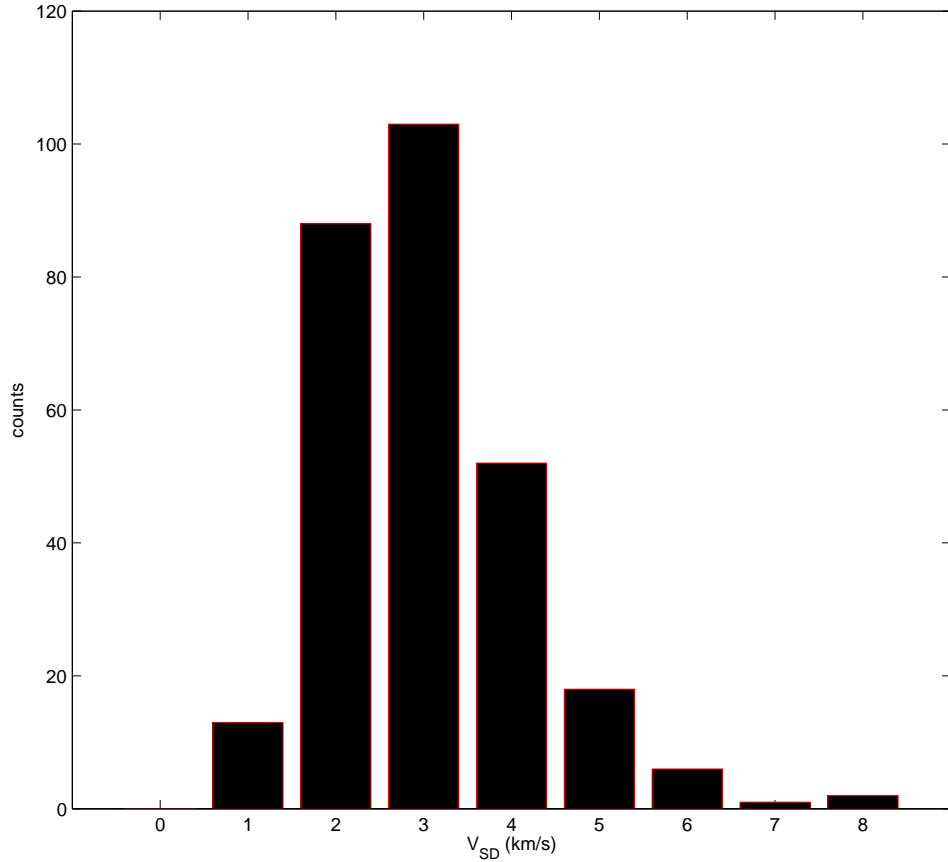
Figure 6.6: Statistical distribution of the standard deviation V_{SD} of the velocity field estimated using ATCA/Parkes data.

in the same sense. The type 2 outliers can be further classified into faster and slower components. In other words, if the $v_{mod} > v_{fit}$ by 9 km s^{-1} or more, and if both v_{mod} & v_{fit} bear same sign, then we define it to be a faster type 2 kinematic outlier. In the same way if $v_{mod} < v_{fit}$ by 9 km s^{-1} or more and both have same sense of rotation, then we identify it as a slower type 2 component. If the magnitude of the $v_{res} > 9$ km s^{-1} and if v_{mod} and v_{fit} bear opposite signs then the location is identified to be type 1. The type 1 and the slow type 2 components are found to be scattered in the observed region and they do not show any trend. As the area covered by the ATCA/Parkes data is only the central region, we discuss these features when we derive the outliers using GASS data. We discuss only the faster type 2 outliers here.
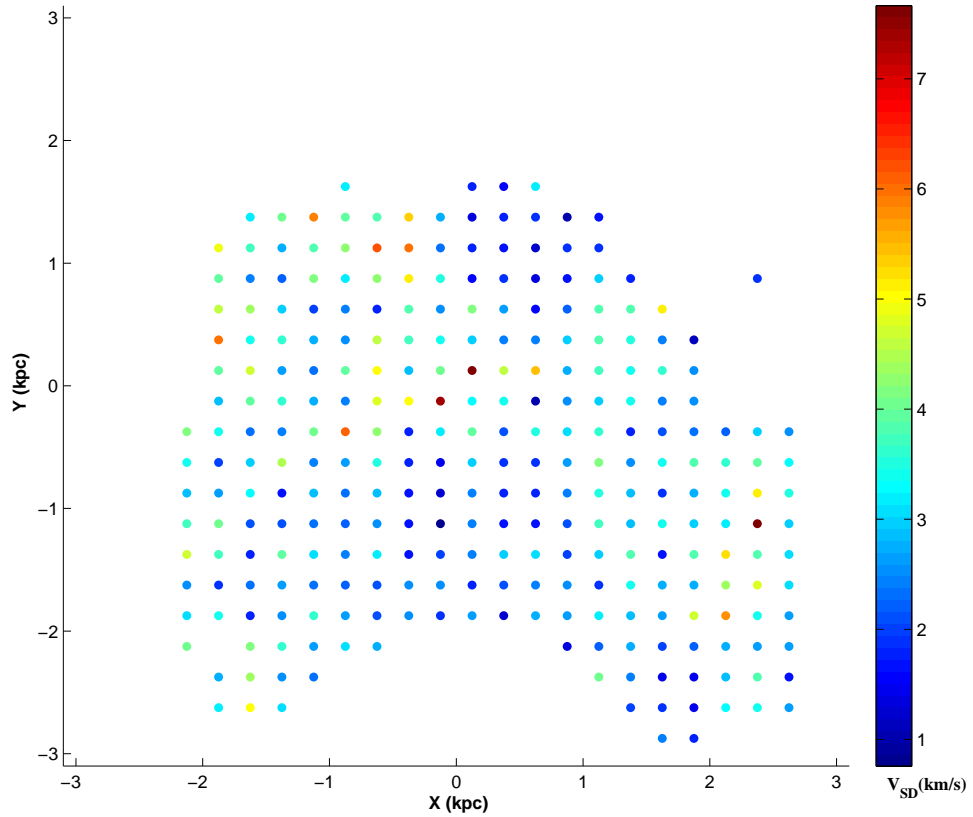
Figure 6.7: Map of the standard deviation V_{SD} of the velocity field estimated using ATCA/Parkes data.

6.4.1 Faster type 2 outliers

Out of the total no. of data points, 7.6% are found to be faster type 2 outliers with an apparent faster velocity than the mean disk velocity at the location. The statistical distribution of these outliers has peaks at $+25$ km s^{-1} with 4750 data points, and at -25 km s^{-1} with 2500 data points. The map with locations of faster outliers is shown in figure 6.8. There points are found to be located parallel to the PA of LON, in the NE-SW direction marked as 'a' and 'b'. The points in the NE are located as grouped together, whereas those in the SW are stretched over a distance. We are not sure about the reason for these features. One possibility for deviation along the PA, could be attributed to rather fast rate of change of inclination of the disk. We estimated a rather large negative value for the rate of change of inclination, which suggests that the inclination of the SMC is decreasing

159
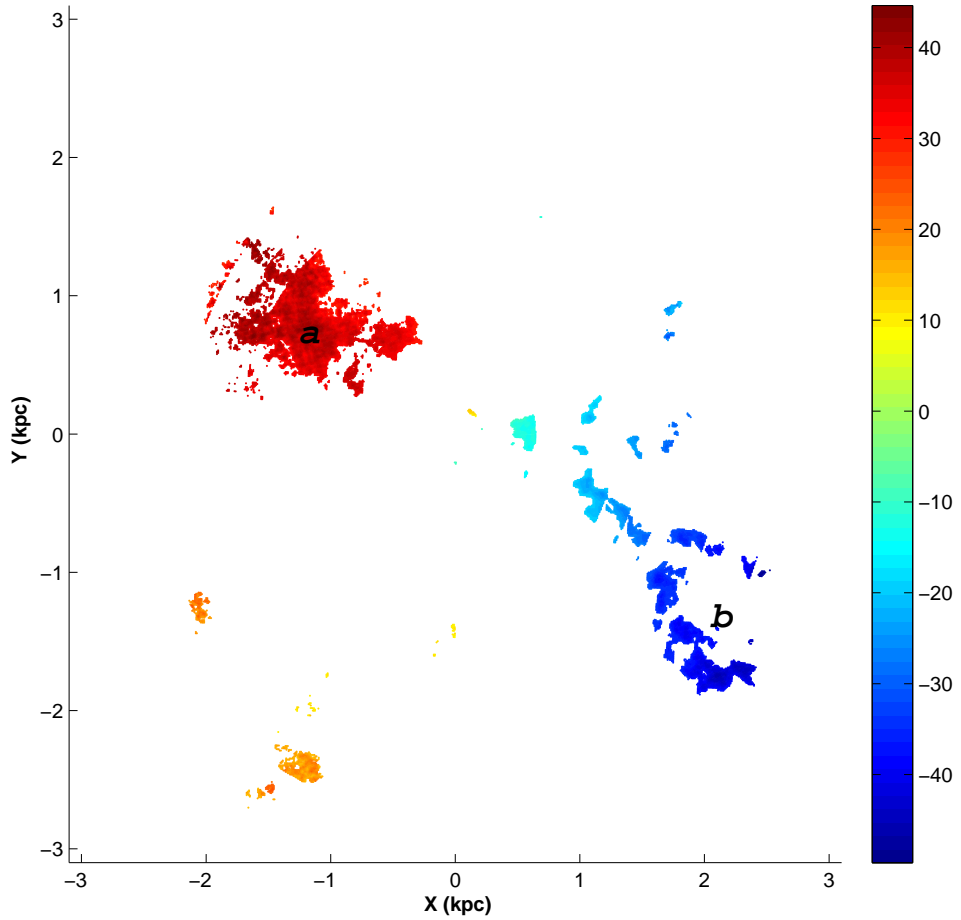
Figure 6.8: Map of the faster type 2 kinematic outliers estimated using ATCA/Parkes data. Colour coding is according to the variation in v_{mod} in km s^{-1}.

over time. Assuming the current inclination of the SMC disk to be 40° Stanimirović et al. (2004), to create an outlier at the location 'a' in figure 6.8, which differ from the mean disk by ~10 km s^{-1}, the inclination of the disk must be ~ 61°. With the estimated di/dt value, a time span of ~ 50 Myr can leave behind such a foot print. Hence we suggest the possibility that this may be the left over feature of the highly inclined disk of the SMC 50 Myr ago.

6.5 The mean H I disk and outliers using GASS data

ATCA/Parkes data does not cover the whole disk of the SMC. To study the mean disk and outlier features at large radial extends, we analysed the GASS data set. The line of sight velocity map corrected for systemic, transverse, precession and nutation motions of the SMC, using GASS data is given in figure 6.9. (We used $di/dt = -416°/Gyr$, and $v_t =$ 397.9 km s^{-1} to estimate this map.) The range in velocity is -100.2 km s^{-1} to $+118.9$ km s^{-1}. The map covers an area of around 3 times larger than the ATCA/Parkes map (figure 6.1). As discussed in section 6.3.4, from the 11 annular rings the parameters v, δv_{sys} and ϕ_0 are estimated. Using these parameters the mean H I disk of the SMC is estimated and shown in figure 6.10. The v_{res} values are estimated as the difference between v_{mod} & v_{fit} using equation 5.2 as we did previously. In order to identify the kinematically distinct features, points which have $v_{res} > 9$ km s^{-1} are defined as outliers. The outliers are classified in the same way as in the case of ATCA/Parkes data set. As the annular ring fitting is spatially restricted within a radius of $\sim 5°.5$, we assumed the disk to be flat beyond this radius. So it is ambiguous to classify the outliers beyond this radius.

6.5.1 Faster type 2 outliers

The map of locations of faster type 2 outliers identified using GASS are shown in figure 6.11. These are locations where the H I is found to apparently move faster than the mean disk velocity at that location. The component which lies parallel to the PA of LON, in the NE-SW direction, which is identified using ATCA/Parkes can be identified in this map, marked as 'a' and 'b'. The lob like feature marked as 'a' and 'b' extent beyond what was seen in the ATCA/Parkes data. In the NE side, the feature 'a', is found to connected to the red pool of points. The red pool of points is suggestive of a bifurcation in the northern side. We need to explore whether one part of this feature is connected to the MS. Diaz & Bekki (2012) predicted the presence of a counter-bridge originating from the NE side of the SMC, from their simulations. It is also possible that the red points may be the suggested counter-bridge. If this is the case, then the origin of this feature is tidal and due to the interaction of the SMC with the LMC. We had earlier suggested that, the central features 'a' and 'b' may arise due to the large value of the rate of change of inclination and may be the result of the debris of the highly inclined SMC disk past ~50 Myr.

There is another component which shows up at X = 7 kpc and Y = 3 kpc, with high velocity blue points towards us. These large velocity points are similar to those found by
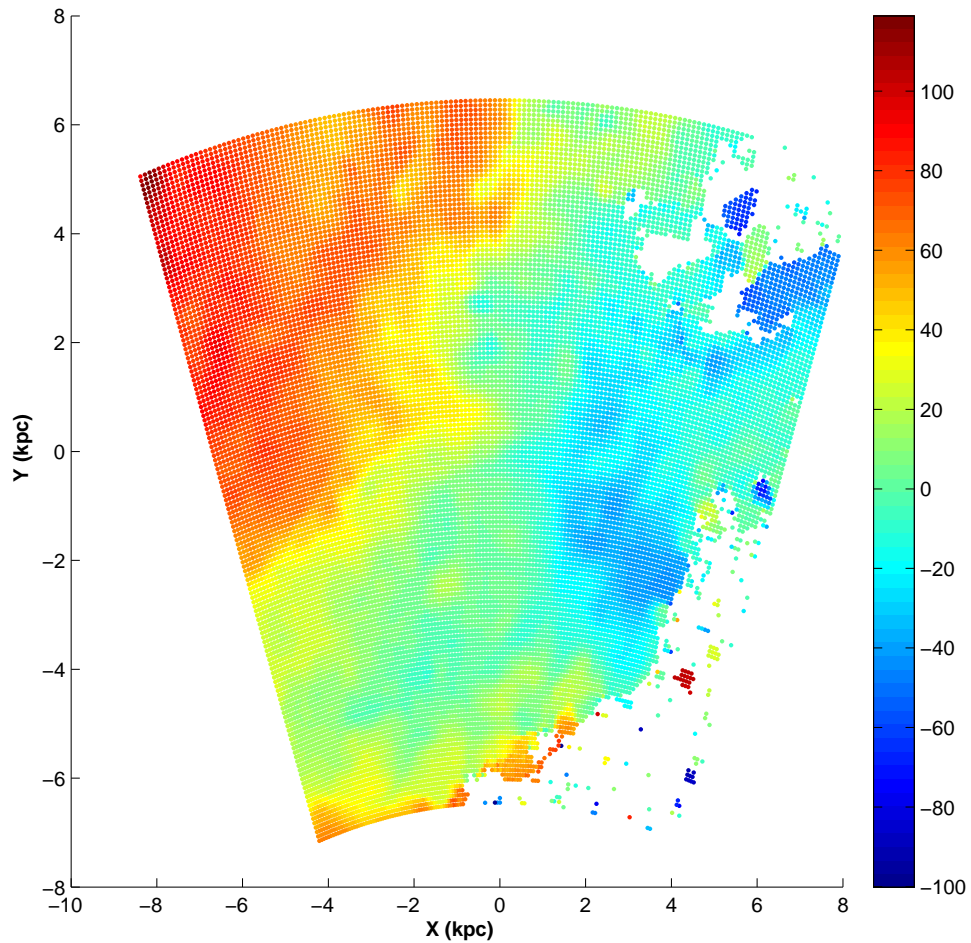
Figure 6.9: The intensity weighted mean velocity map using GASS data. Colour coding is according to the variation in v_{mod} in km s^{-1}.

Dobbie et al. (2014), in the radial velocity of red giants. Thus we confirm that there is a corresponding component in the H I also. The origin of this component is not clear but one possibility could be the tidal origin, as suggested by Diaz & Bekki (2012).

6.5.2 Slower type 2 outliers

The map of slower type 2 outliers are shown in figure 6.12. We identify a distinct feature, which spreads from the center towards the SE corner. It is a low velocity component with respect to the disk's bulk motion, with $v_{mod} \sim 10$ km s^{-1} to 40 km s^{-1} away from
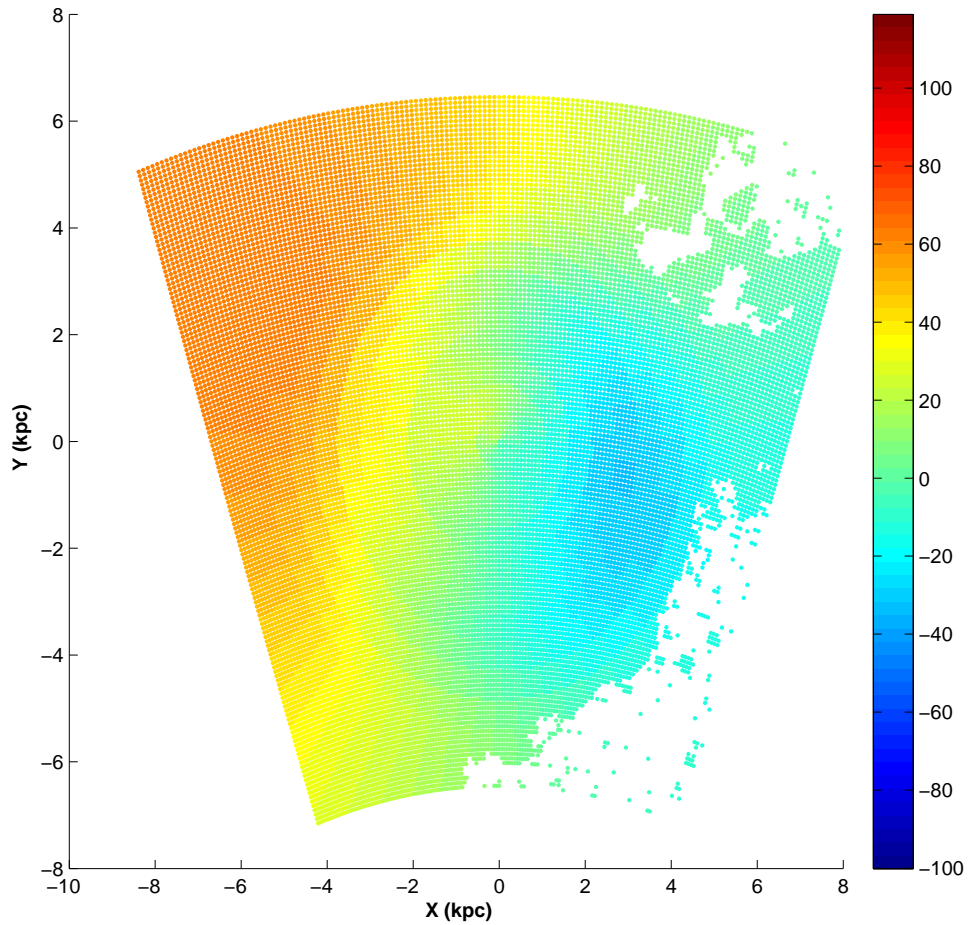
Figure 6.10: The estimated mean H I disk of the SMC estimated using GASS data. Colour coding is according to the variation in v_{fit} in km s^{-1}.

us. The velocity is also suggestive of increasing as a function of distance from the center of the SMC. Two arrows are shown in the figure which suggest the direction of the MB (black arrow) and the direction of motion of the SMC (red arrow). It can be noticed that the low velocity gas is located between these two arrows. As this is the direction towards the MB, this pool of gas may be connected to the MB. As we also notice a mild velocity gradient as a function of distance, this might be suggestive of the SMC gas feeding the MB. This is only suggestive and needs to be studied carefully for confirmation. We suggest that the feature we have identified here could be of tidal origin and may provide the link from the SMC to the MB. We also notice a few more slow components, including

Figure 6.11: The faster type 2 outlier component map identified using GASS data. Colour coding is according to the variation in v_{mod} in km s^{-1}. The two lob like features are marked as 'a' and 'b'

those in the NW, we are unable to comment on them and their origin.

6.5.3 Type 1 outliers

The map of the type 1 outliers are shown in figure 6.13. We identify a feature in the NW side, which is similar to the location of the feature identified in the fast component. We also note that the velocity range is also similar among these features. As these are located along the minor axis, where we expect the velocity to be close to the systemic
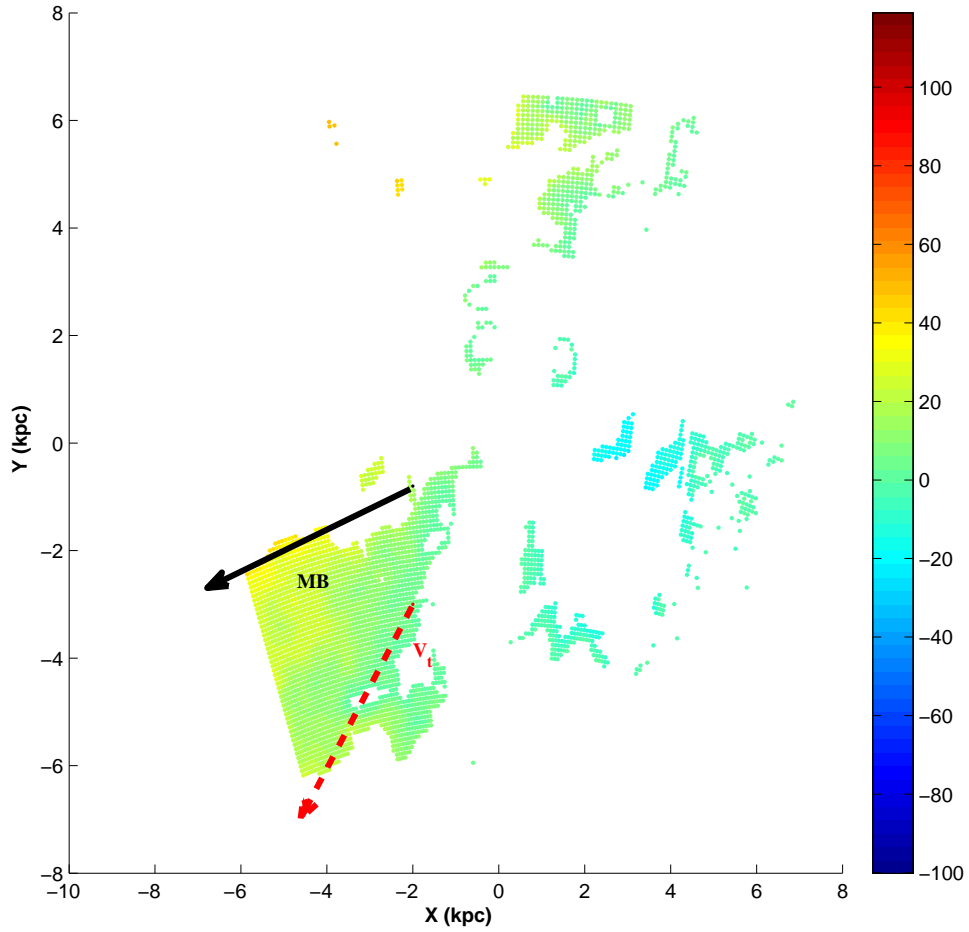
Figure 6.12: The slower type 2 outlier component map identified using GASS data. Colour coding is according to the variation in v_{mod} in km s^{-1}. The black arrow shows the direction towards the MB. The red dotted arrow shows the direction of the transverse motion of the SMC, v$_t$.

velocity. These may be related features and could be of tidal origin. We notice that this region has both fast and slow type 2 outliers, as well as type 1 outliers, suggesting that H I gas in this region has a large range in velocity and probably large dispersion. We also notice a component in the south of the SMC, which has higher velocity and suggestive of moving away from us. As this feature is close to the spatial limit of our data, its interpretation as having high velocity needs to be confirmed. Hence, we do not have enough information to discuss its nature as well as origin.
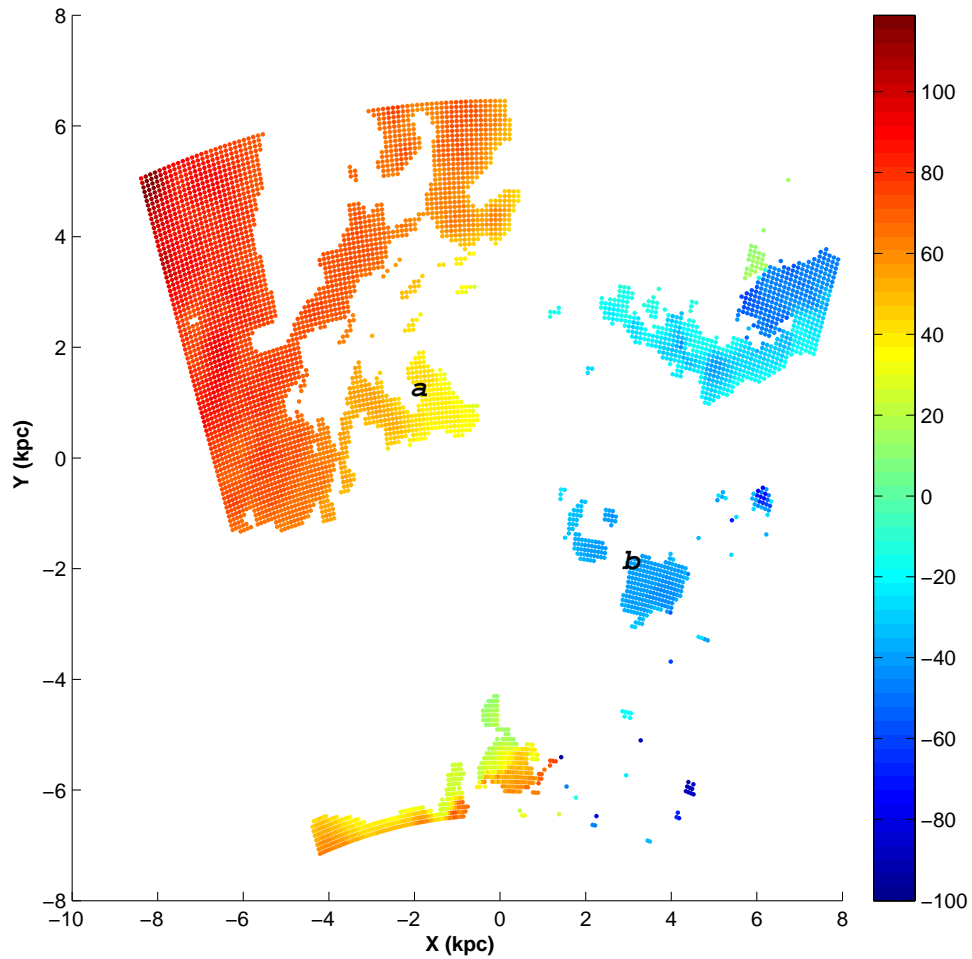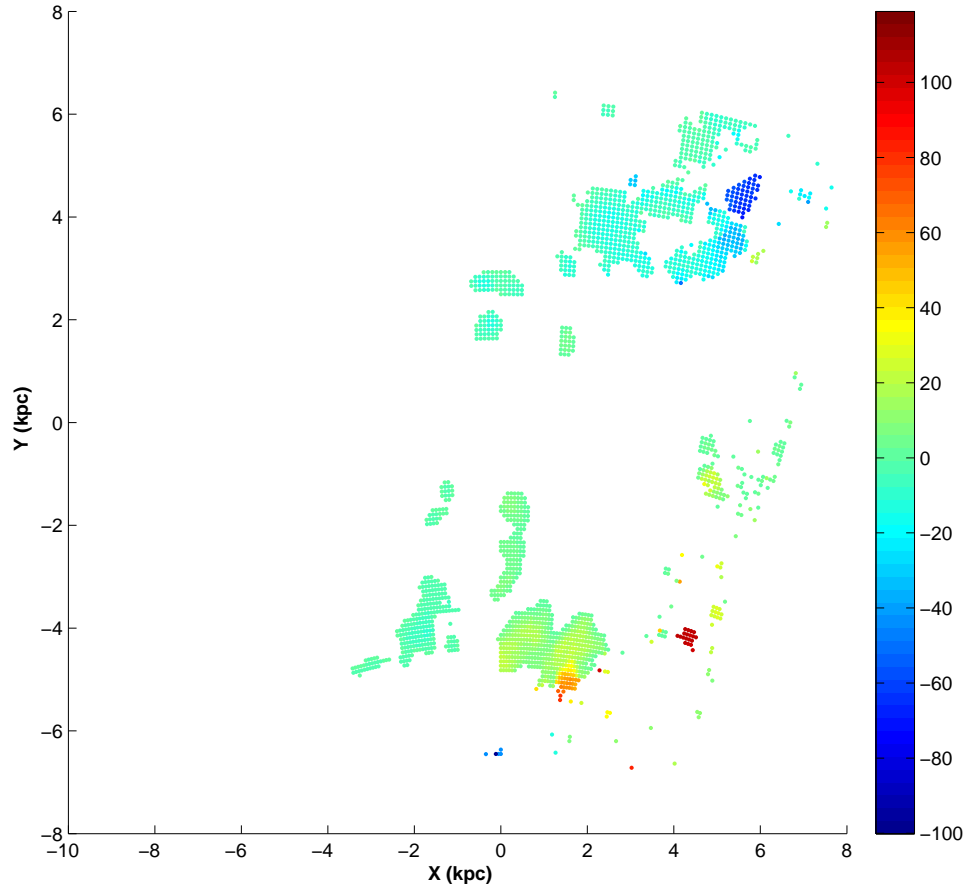
Figure 6.13: The type 1 outlier component map identified using GASS data. Colour coding is according to the variation in v_{mod} in km s^{-1}.

6.6 Discussion

In this study, we have analysed the H I data using two data sets. The ATCA/Parkes data cover only the inner 3 degree region, where the GASS data cover a wider region. We have derived the PA of LON of the H I disk over a large radial extent and is found to be fairly constant up to the outer radius studied here. This suggests that we do not find any evidence of internal kinematic perturbation within the SMC. This is in contrast to what was noticed in the LMC, where we notice evidence of internal perturbation in the inner LMC.

We estimate that the H I disk of the SMC has a large rate of change of inclination,

$di/dt = -416°/Gyr$. This suggests that the SMC disk has a large spin and it could be a result of the interaction with the LMC. As this is the first time this parameter is estimated, it will be good to understand the origin of such a large value. As this is the closest pair one can study in detail, this parameter needs to be understood in terms of simulations of interacting galaxies. Piatek & Prior (1995) have demonstrated the apparent spin on a dwarf spheroidal galaxy as a result of interaction with a large galaxy, using N-body simulations.

The rotation curve of the SMC is estimated for a largest radial extent so far. We have traced the flat part of the rotation curve and estimated the mass of the SMC which is twice that estimated before. The flat rotation curve confirms the presence of a dark halo for the SMC. The low mass galaxy like the SMC is thought to be dark matter dominated, but have not found any convincing evidence for its presence. Therefore, we have identified an evidence for the presence of dark matter in the SMC.

We have identified the presence of a few tidal features which appear as kinematic outliers. One of the interesting features identified is a feature which shows the probable connection of the SMC to the MB. This gas is found to be located along the direction of motion of the SMC and the direction towards the MB. If this is true, this stream of H I gas connects the SMC to the MB, which is a result of the recent interaction between the LMC and the SMC. We have identified H I features which are slow and fast type 2, as well as type 1 in the NW side of the disk. This feature thus has a large range in velocity over a large spatial area and probably originated by tidal forces. We identify a feature covering most of the NE region. This feature is also likely to be tidal in origin, but connects to the inner SMC. A detailed and accurate study of this region is necessary to study its connection with the MS and a possible identification with the counter-bridge. On the whole, these features have been identified for the first time due to large area covered by the GASS data.

6.7 Conclusions

1. The H I kinematics of the SMC is analysed in detail for the first time covering most of the gaseous disk of the SMC.

2. The new proper estimates (Kallivayalil et al. 2013) are applied for analysing the SMC kinematics for the first time.

3. The rotation curve of the SMC is estimated to a larger radial extent and the flat part

of the rotation curve is detected for the first time. The turn over radius is found to be 4.1 kpc and the deprojected rotational velocity is 64 km s^{-1}.

4. The nutation of the SMC disk is estimated for the first time. The SMC seems to undergo fast tumbling motion with a di/dt value $-416.39\pm19°$/Gyr.

5. The dynamical mass estimated within the outermost data point at 5.7 kpc is 5.4 x 10^9 $M_\odot$, which is more than twice of the previous estimate (Stanimirović et al. 2004). This could be an indicator of the presence of a dark matter halo in the SMC.

6. The PA of LON is estimated to be $67°.2\pm9°.2$, which is slightly larger than that estimated by (Stanimirović et al. 2004).

7. We have identified the presence of a few tidal features which appear as kinematic outliers. One of the interesting features identified is a feature which shows the probable connection of the SMC to the MB.

8. The inner SMC appears to be relatively unperturbed, whereas the outer region of the SMC shows a number of possible tidal features.

CHAPTER 7

SUMMARY & CONCLUSIONS

The Large and Small Magellanic Clouds, even after centuries of scientific explorations, continue to be equally fascinating and mysterious to astronomers. It was once believed, that they orbit our MW and may end up spiralling in to it. Now we believe that after coming close to the Galaxy they may move away, never to return. Nevertheless the current location of the Clouds at our door step, is a bliss, to learn various aspects of galaxy interactions and evolutions. The high precision new proper motion estimates and the first passage scenario restricts the LMC-SMC-MW interaction to a very recent past of a few 100 Myr. In this thesis study we analysed the two aspects - the recent star formation history and the gas kinematics of the Clouds - to reveal the details of the recent and on going interaction between the Clouds and the Clouds with the Galaxy. The results are summarised below.

7.1   Summary of Results

7.1.1   Recent Star Formation History of the MCs

1. The spatial and statistical distribution of extinction (A_v) are estimated for the L&SMC. The range of A_v is found to be 0.2 - 2.0 magnitude in both the Clouds. The average extinction is found to be around 0.5 in the LMC and 0.3 in the SMC. The extinction distribution match with the previous estimates of Zaritsky et al. (2004) and Zaritsky et al. (2002).

2. The maps of the last (significant) star formation event are estimated for the Clouds. The spatial distribution of the ages of this event shows that the star formation has shrunk to central regions in both the L&SMC in the last 100 Myr.

169

3. We detect peaks of star formation at 0 - 10 Myr and 90 - 100 Myr in the LMC and 0 - 10 Myr and 50 - 60 Myr in the SMC.

4. The age map of young star clusters of 100 Myr age range is found to be spatially as well as chronologically correlated with our maps of the last star formation event in both the Clouds.

5. The quenching of star formation in the LMC is found to be asymmetric with respect to the optical center such that most of the young star forming regions are located to the north and east of the LMC disk.

6. On deprojecting the data onto the LMC plane, the recent star formation appears to be stretched in the northeast direction.

7. The distribution of the massive H I clouds in the LMC plane are preferentially located in the north.

8. The stellar as well as cluster populations as young as 40 Myr, up to a few 100 Myr show lopsidedness towards north, while populations younger than 40 Myr are found to be relatively more in the northeast region, of the LMC disk.

9. The map of the last star formation event in the SMC shows two substructures one near the centre and one near the wing. These correlate well with the H I column density map, and comparable with the locations of H I super giant shells, 304A & 37A.

10. In the SMC, we detect a shift in the center of density distribution of younger population (200 - 30 Myr) towards northeast.

7.1.2   H I **Kinematics of the LMC**

1. We identified the mean H I disk of the LMC after correcting the observed velocity field for the transverse motion of the LMC using the recent proper motion measurements (Piatek et al. 2008 and Kallivayalil et al. 2013).

2. The mean H I disk estimated using the above mentioned two proper motion values were found to be similar, and well reproducing the observed features.

3. The effect of precession and nutation in the estimation of PA is found to be significant.

4. The value of PA of kinematic major axis estimated using ATCA/Parkes data (126° ± 23°) is found to be similar to the recent estimate of the PA using stellar tracers (142° ± 5°). Therefore, the discrepancy between gas and stellar kinematics in the LMC disk is effectively removed.

5. The mean H I disk is found to be disturbed within 1.°0 radius and beyond 2.°9 radius.

6. Most of the H I gas in the LMC (∼ 87.9% of the data points) is located in the disk. We detected 12.1% of the data points as kinematic outliers. These are classified as type 1 and type 2 outliers, with two sub classes in type 2.

7. Significant part of the type 1 as well as the slow type 2 H I gas are identified with Arm E.

8. We identified the well known Arm S, Arm W, Arm B and a new stream, Outer Arm, as part of the faster type 2 outlier component.

9. The GASS data analysis brings out the details of the Magellanic Bridge (MB) and its connection to the LMC disk. We find that the arm B is connected to the MB and the velocities might suggest a gas infall through arm B, if the arm B and the extension are in the plane of the LMC. On the other hand, these features may be in a plane with inclination larger than the LMC disk.

10. We detect outflows from the western disk of the LMC and the southwest and southern parts of the MB, likely to be due to ram pressure stripping.

11. We proposed two models to explain the gas connection with the MB/SMC. The model with gas located in three different planes in the LMC seems to explain the type 1 and type 2 features found in the LMC, when compared to an in-plane accretion model. In our in-plane model, the type 1 outliers become counter-rotating and type 2 outliers become co-rotating. Also, the in-plane model suggests accretion of material from the MB in to the LMC disk through arm B.

7.1.3   H I Kinematics of the SMC

1. The estimation of the nutation (di/dt) of the SMC disk is done for the first time, using the mean H I velocity field. The SMC seems to undergo fast tumbling motion with a di/dt value $-416.39 \pm 19°$/Gyr.

171

2. The sense of rotation doesn't seem to play a significant role in the estimation of nutation.

3. The H I kinematics of the SMC is analysed in detail for the first time covering almost the entire gaseous disk of the SMC, applying the high precision new proper motion estimates (Piatek et al. 2008 and Kallivayalil et al. 2013). The mean H I disk is estimated after correcting for the transverse, systemic, and nutation motion of the SMC disk. The estimated distribution successfully reproduces the observed velocity field of the SMC.

4. The rotation curve of the SMC is estimated up to a larger radial extend using GASS data and the flat part of the rotation curve is detected for the first time. The turn over radius is found to be 4.1 kpc and the deprojected rotational velocity is 64 km s^{-1}. The existence of the flat rotation curve possibly indicates the presence of a dark matter halo in the SMC.

5. The dynamical mass estimated within the outermost data point at 5.7 kpc is 5.4×10^9 $M_\odot$, which is more than twice of the previous estimate by Stanimirović et al. (2004).

6. The position angle of line of nodes is estimated to be $67°.2 \pm 9°.2$. This estimate is inconsistent with the PA estimates using stellar tracers (which lies in the southeast quadrant), as suggested by previous studies (Stanimirović et al. 2004).

7. Around 81.8% of the data points are within the mean disk, while 18.2% are found to be kinematical outliers (using ATCA/Parkes data).

8. The fast type 2 outliers (7.6% of the total data points) are found to be distributed along the line of nodes.

9. A distribution of the slow type 2 outliers is found to spread from the SMC center towards the southeast of the SMC disk, between the direction of the transverse velocity vector of the SMC and the direction towards the MB. The velocity along this feature mildly increases as a function of distance from the SMC center, and the feature probably connects SMC to the MB.

10. A location in the northwest of the SMC is identified where faster and slower type 2 and type 1 outliers are detected. We suggest that this feature could be due to tidal origin.

7.2 Conclusions

The main conclusions arrived in this study, in the two aspects of the recent star formation history and the H I kinematics are discussed in the following sections. The conclusions from both the aspects are compared and summarised in the last section.

7.2.1 Recent Star Formation History

- In this study, we have attempted to understand the interaction history of the LMC-SMC-MW system, with the aid of the estimation of the recent star formation history of the Clouds, in the last 500 Myr. In the last 200 Myr, our study suggests that there are changes in the recent star formation in these galaxies due to their mutual interaction as well as their interactions with the Galaxy.

- The lopsidedness of the H I clouds in the LMC towards north is suggestive of the tidal pull of the Galaxy on the LMC gas distribution. The extension of the young stellar as well as cluster distribution towards north restricts the time scale of this tidal interaction within the last 200 Myr, which is the estimated epoch of the closest approach.

- The clusters and stars younger than 40 Myr are lopsided towards northeast. This enhanced star formation in the northeast could be the result of the movement of the LMC in the hot Galactic halo at a PA of $\sim 80°$. The hydrodynamical compression exerted by the ionised halo on the tidally pulled LMC gas could be a possible reason for the enhanced star formation in the leading edge (northeast) of the LMC.

- In the LMC, we find a compression of gas in the northeast direction, due to the motion of the LMC in the Galactic halo and this is an important input to understand the density of the Galactic halo at the LMC distance. In the SMC, we see a combined effect of the tidal interaction of the LMC and the Galaxy, as both are located in the same direction.

7.2.2 H I Kinematics

- We find that the kinematic major axis of the gaseous disk of the LMC is found to be similar to the stellar disk, after incorporating the new proper motion values.

- The hydrodynamical interaction with Galactic halo strongly influence the gas distribution in the LMC disk, creating a faster gas components in leading edge, and

gas stripping in the opposite direction. Our study also suggests that the various arms identified in the LMC may be due to the hydrodynamical effect of the LMC's motion in the MW halo.

- The SMC gas disk is inconsistent with the stellar distribution as found by the previous studies. The tumbling motion of the SMC is found to be twice as fast as that in the LMC.

- By analysing the SMC H I kinematics we conclude that the tidal effect of the LMC is quite dominant on the SMC, rather than the hydrodynamic and tidal interaction of the Galaxy.

To summarise the conclusions, the gas distribution and the recent star formation in the LMC are dictated by its perigalactic passage. The tidal and ram pressure interactions with the Galaxy play equally significant roles. While there is a combined gravitational effect of the Galaxy and the LMC, on the recent star formation and gas distribution of the SMC. The gas kinematics of the SMC is found to be severely disturbed possibly by the tidal interactions with the LMC. The SMC gas distribution seems to have much more valuable information about the LMC-SMC interactions which demands a more detailed study in this direction.

7.3 Future Work

- The H I gas distribution in the Magellanic System holds the key to the details of the LMC-SMC-MW interaction and the unresolved problems of formation of the Magellanic Complexes. A detailed study of the brightness temperature and eventually the column density distribution of the H I gas can lead to a more quantitative analysis of the amount of H I involved in various features studied in this thesis. This will add value to the interpretations of the findings in this thesis study.

- The H I data in regions connecting the LMC, SMC, MB and MS are available from the GASS survey with relatively good velocity and spatial resolution. We plan to study features in the MB and MS using the data to study the gas kinematics in them.

- The kinematics of the young stellar populations in the SMC is to be performed with data sets of larger spatial coverage, to understand the details of the inconsistency exists between the stellar and gaseous kinematics.

REFERENCES

Alcock, C., Allsman, R. A., Alves, D. R., et al. 1999, AJ, 117, 920

Alves, D. R. 2004, ApJ, 601, L151

Appleton, P. N., Davies, R. D., & Stephenson, R. J. 1981, MNRAS, 195, 327

Appleton, P. N., Ghigo, F. D., van Gorkom, J. H., Schombert, J. M., & Struck-Marcell, C. 1987, Nature, 330, 140

Arnal, E. M., Bajaja, E., Larrarte, J. J., Morras, R., & Pöppel, W. G. L. 2000, A&AS, 142, 35

Arp, H. C. 1958, AJ, 63, 118

Bajaja, E., Arnal, E. M., Larrarte, J. J., et al. 2005, A&A, 440, 767

Bajaja, E., Cappa de Nicolau, C. E., Martin, M. C., et al. 1989, A&AS, 78, 345

Begeman, K. G. 1987, PhD thesis, , Kapteyn Institute, (1987)

Bekki, K. & Chiba, M. 2007, PASA, 24, 21

Bertelli, G., Mateo, M., Chiosi, C., & Bressan, A. 1992, ApJ, 388, 400

Besla, G., Kallivayalil, N., Hernquist, L., et al. 2007, ApJ, 668, 949

Besla, G., Kallivayalil, N., Hernquist, L., et al. 2010, ApJ, 721, L97

Besla, G., Kallivayalil, N., Hernquist, L., et al. 2012, MNRAS, 421, 2109

Bica, E., Claria, J. J., & Dottori, H. 1992, AJ, 103, 1859

Binney, J. & Merrifield, M. 1998, Galactic Astronomy, Princeton paperbacks (Princeton University Press)

Bosma, A. 1981, AJ, 86, 1791

Brüns, C., Kerp, J., Staveley-Smith, L., et al. 2005, A&A, 432, 45

Caldwell, J. A. R. & Coulson, I. M. 1986, MNRAS, 218, 223

175

Casetti-Dinescu, D. I., Vieira, K., Girard, T. M., & van Altena, W. F. 2012, ApJ, 753, 123

Chamaraux, P., Balkowski, C., & Gerard, E. 1980, A&A, 83, 38

Christodoulou, D. M., Tohline, J. E., & Steiman-Cameron, T. Y. 1988, AJ, 96, 1307

Cioni, M.-R. L., van der Marel, R. P., Loup, C., & Habing, H. J. 2000, A&A, 359, 601

Combes, F. 1978, A&A, 65, 47

Combes, F., Dupraz, C., Casoli, F., & Pagani, L. 1988, A&A, 203, L9

de Boer, K. S., Braun, J. M., Vallenari, A., & Mebold, U. 1998, A&A, 329, L49

de Vaucouleurs, G. & Freeman, K. C. 1972, Vistas in Astronomy, 14, 163

Diaz, J. D. & Bekki, K. 2012, ApJ, 750, 36

Dieter, N. H. 1965, AJ, 70, 552

Dobbie, P. D., Cole, A. A., Subramaniam, A., Keller, S., & Cannon, R. 2014, MNRAS, (submitted)

Dolphin, A. E., Walker, A. R., Hodge, P. W., et al. 2001, ApJ, 562, 303

Evans, C. J. & Howarth, I. D. 2008, MNRAS, 386, 826

Gardiner, L. T. & Noguchi, M. 1996, MNRAS, 278, 191

Gardiner, L. T., Sawa, T., & Fujimoto, M. 1994, MNRAS, 266, 567

Gibson, B. K., Giroux, M. L., Penton, S. V., et al. 2000, AJ, 120, 1830

Giovanelli, R. & Haynes, M. P. 1985, ApJ, 292, 404

Glatt, K., Grebel, E. K., & Koch, A. 2010, A&A, 517, A50

Grcevich, J. & Putman, M. E. 2009, ApJ, 696, 385

Groenewegen, M. A. T. 2000, A&A, 363, 901

Gunn, J. E. & Gott, III, J. R. 1972, ApJ, 176, 1

Harris, J. & Zaritsky, D. 2004, AJ, 127, 1531

Harris, J. & Zaritsky, D. 2009, AJ, 138, 1243

Hartmann, D. & Burton, W. B. 1997, Atlas of Galactic Neutral Hydrogen

Hibbard, J. E. & Mihos, J. C. 1995, AJ, 110, 140

Hibbard, J. E. & van Gorkom, J. H. 1996, AJ, 111, 655

Hindman, J. V. 1964, in IAU Symposium, Vol. 20, The Galaxy and the Magellanic Clouds, ed. F. J. Kerr, 255

Hindman, J. V., McGee, R. X., Carter, A. W. L., Holmes, E. C. J., & Beard, M. 1963, Australian Journal of Physics, 16, 552

Hodge, P. W. 1960, ApJ, 131, 351

Holtzman, J. A., Gallagher, III, J. S., Cole, A. A., et al. 1999, AJ, 118, 2262

Indu, G. & Subramaniam, A. 2011, A&A, 535, A115

Jones, B. F., Klemola, A. R., & Lin, D. N. C. 1994, AJ, 107, 1333

Kalberla, P. M. W., Burton, W. B., Hartmann, D., et al. 2005, A&A, 440, 775

Kalberla, P. M. W., McClure-Griffiths, N. M., Pisano, D. J., et al. 2010, A&A, 521, A17

Kallivayalil, N., van der Marel, R. P., & Alcock, C. 2006a, ApJ, 652, 1213

Kallivayalil, N., van der Marel, R. P., Alcock, C., et al. 2006b, ApJ, 638, 772

Kallivayalil, N., van der Marel, R. P., Besla, G., Anderson, J., & Alcock, C. 2013, ApJ, 764, 161

Kerr, F. J., Hindman, J. F., & Robinson, B. J. 1954, Australian Journal of Physics, 7, 297

Kim, S., Dopita, M. A., Staveley-Smith, L., & Bessell, M. S. 1999, AJ, 118, 2797

Kim, S., Rosolowsky, E., Lee, Y., et al. 2007, ApJS, 171, 419

Kim, S., Staveley-Smith, L., Dopita, M. A., et al. 1998, ApJ, 503, 674

Kim, S., Staveley-Smith, L., Dopita, M. A., et al. 2003, ApJS, 148, 473

Lindblad, B. 1927, MNRAS, 87, 553

Lu, L., Sargent, W. L. W., Savage, B. D., et al. 1998, AJ, 115, 162

Luks, T. & Rohlfs, K. 1992, A&A, 263, 41

Marigo, P., Girardi, L., Bressan, A., et al. 2008, A&A, 482, 883

Mastropietro, C. 2009, in IAU Symposium, Vol. 256, IAU Symposium, ed. J. T. Van Loon & J. M. Oliveira, 117–121

Mastropietro, C., Burkert, A., & Moore, B. 2009, MNRAS, 399, 2004

177

Mastropietro, C., Moore, B., Mayer, L., Wadsley, J., & Stadel, J. 2005, MNRAS, 363, 509

Mathewson, D. S., Cleary, M. N., & Murray, J. D. 1974, ApJ, 190, 291

Mathewson, D. S., Ford, V. L., Schwarz, M. P., & Murray, J. D. 1979, in IAU Symposium, Vol. 84, The Large-Scale Characteristics of the Galaxy, ed. W. B. Burton, 547–556

Mathewson, D. S., Ford, V. L., & Visvanathan, N. 1986, ApJ, 301, 664

Mathewson, D. S., Ford, V. L., & Visvanathan, N. 1988, ApJ, 333, 617

McClure-Griffiths, N. M., Pisano, D. J., Calabretta, M. R., et al. 2009, ApJS, 181, 398

McClure-Griffiths, N. M., Staveley-Smith, L., Lockman, F. J., et al. 2008, ApJ, 673, L143

McGee, R. X. 1964, Australian Journal of Physics, 17, 515

McGee, R. X. & Milton, J. A. 1966, Australian Journal of Physics, 19, 343

Meaburn, J. 1980, MNRAS, 192, 365

Mihos, J. C. & Bothun, G. D. 1997, ApJ, 481, 741

Mihos, J. C., Bothun, G. D., & Richstone, D. O. 1993, ApJ, 418, 82

Minniti, D., Borissova, J., Rejkuba, M., et al. 2003, Science, 301, 1508

Morras, R. 1982, A&A, 115, 249

Nidever, D. L. 2013, ArXiv e-prints

Nidever, D. L., Majewski, S. R., Burton, W., et al. 2013a, in American Astronomical Society Meeting Abstracts, Vol. 221, American Astronomical Society Meeting Abstracts, 404.04

Nidever, D. L., Majewski, S. R., & Burton, W. B. 2008, ApJ, 679, 432

Nidever, D. L., Monachesi, A., Bell, E. F., et al. 2013b, ArXiv e-prints

Nikolaev, S., Drake, A. J., Keller, S. C., et al. 2004, ApJ, 601, 260

Noël, N. E. D., Aparicio, A., Gallart, C., et al. 2009, ApJ, 705, 1260

Olsen, K. A. G. 1999, AJ, 117, 2244

Olsen, K. A. G. & Massey, P. 2007, ApJ, 656, L61

Olsen, K. A. G. & Salyk, C. 2002, AJ, 124, 2045

Olsen, K. A. G., Zaritsky, D., Blum, R. D., Boyer, M. L., & Gordon, K. D. 2011, ApJ, 737, 29

Oort, J. H., Kerr, F. J., & Westerhout, G. 1958, MNRAS, 118, 379

Piatek, S., Pryor, C., & Olszewski, E. W. 2008, AJ, 135, 1024

Pietrzynski, G. & Udalski, A. 2000, Acta Astron., 50, 337

Putman, M. E. 2000, PASA, 17, 1

Putman, M. E., Gibson, B. K., Staveley-Smith, L., et al. 1998, Nature, 394, 752

Putman, M. E., Staveley-Smith, L., Freeman, K. C., Gibson, B. K., & Barnes, D. G. 2003, ApJ, 586, 170

Sandage, A. R. 1953, AJ, 58, 61

Schönrich, R., Binney, J., & Dehnen, W. 2010, MNRAS, 403, 1829

Shapley, H. 1940, Harvard College Observatory Bulletin, 914, 8

Simkin, S. M., van Gorkom, J., Hibbard, J., & Su, H.-J. 1987, Science, 235, 1367

Smart, W. M. & Green, E. b. R. M. 1977, Textbook on Spherical Astronomy

Smecker-Hane, T. A., Cole, A. A., Gallagher, III, J. S., & Stetson, P. B. 2002, ApJ, 566, 239

Stanimirovic, S., Staveley-Smith, L., Dickey, J. M., Sault, R. J., & Snowden, S. L. 1999, MNRAS, 302, 417

Stanimirović, S., Staveley-Smith, L., & Jones, P. A. 2004, ApJ, 604, 176

Staveley-Smith, L., Kim, S., Calabretta, M. R., Haynes, R. F., & Kesteven, M. J. 2003, MNRAS, 339, 87

Staveley-Smith, L., Kim, S., Putman, M., & Stanimirović, S. 1998, in Reviews in Modern Astronomy, Vol. 11, Reviews in Modern Astronomy, ed. R. E. Schielicke, 117

Staveley-Smith, L., Wilson, W. E., Bird, T. S., et al. 1996, PASA, 13, 243

Stetson, P. B. 1987, PASP, 99, 191

Stockton, A. 1974a, ApJ, 190, L47

Stockton, A. 1974b, Nature, 250, 308

Subramaniam, A. 2004, A&A, 425, 837

Subramaniam, A. 2006, A&A, 449, 101

Subramaniam, A. & Prabhu, T. P. 2005, ApJ, 625, L47

Subramaniam, A. & Subramanian, S. 2009, ApJ, 703, L37

Subramanian, S. & Subramaniam, A. 2009, A&A, 496, 399

Subramanian, S. & Subramaniam, A. 2010, A&A, 520, A24

Subramanian, S. & Subramaniam, A. 2013, A&A, 552, A144

Tifft, W. G. 1963, MNRAS, 125, 199

Toomre, A. & Toomre, J. 1972, ApJ, 178, 623

Udalski, A., Soszynski, I., Szymanski, M. K., et al. 2008a, Acta Astron., 58, 89

Udalski, A., Soszyński, I., Szymański, M. K., et al. 2008b, Acta Astron., 58, 329

van der Hulst, J. M. 1979, A&A, 75, 97

van der Kruit, P. C. & Allen, R. J. 1978, ARA&A, 16, 103

van der Marel, R. P. 2001, AJ, 122, 1827

van der Marel, R. P., Alves, D. R., Hardy, E., & Suntzeff, N. B. 2002, AJ, 124, 2639

van der Marel, R. P. & Cioni, M.-R. L. 2001, AJ, 122, 1807

van der Marel, R. P. & Kallivayalil, N. 2014, ApJ, 781, 121

van der Marel, R. P., Kallivayalil, N., & Besla, G. 2009, in IAU Symposium, Vol. 256, IAU Symposium, ed. J. T. van Loon & J. M. Oliveira, 81–92

van Kuilenburg, J. 1972, A&A, 16, 276

van Loon, J. T., Bailey, M., Tatton, B. L., et al. 2013, A&A, 550, A108

Venzmer, M. S., Kerp, J., & Kalberla, P. M. W. 2012, A&A, 547, A12

Wannier, P. & Wrixon, G. T. 1972, ApJ, 173, L119

Weinberg, M. D. 2000, ApJ, 532, 922

Westerlund, B. 1961, Uppsala Astronomical Observatory Annals, 5, 1

Westerlund, B. 1997, The Magellanic Clouds, Cambridge astrophysics series (Cambridge University Press)

Wevers, B. M. H. R., van der Kruit, P. C., & Allen, R. J. 1986, A&AS, 66, 505

Yun, M. S. 1992, PhD thesis, Harvard University, Cambridge, MA.

Yun, M. S., Ho, P. T. P., & Lo, K. Y. 1994, Nature, 372, 530

Yun, M. S., Verdes-Montenegro, L., del Olmo, A., & Perea, J. 1997, ApJ, 475, L21

Zaritsky, D., Harris, J., Thompson, I. B., & Grebel, E. K. 2004, AJ, 128, 1606

Zaritsky, D., Harris, J., Thompson, I. B., Grebel, E. K., & Massey, P. 2002, AJ, 123, 855